Università degli Studi di Genova
Facoltà di Scienze Matematiche, Fisiche e Naturali

Corso di Dottorato di Ricerca in Fisica, ciclo XXX

Tesi di Dottorato di Ricerca

Out-of-equilibrium dynamics of one-dimensional integrable quantum systems

Candidate:
Filippo Maria Gambetta

Supervisor:
Dr. Fabio Cavaliere
External superivisor:
Dr. Niccoló Traverso Ziani

March 2018

ABSTRACT

In this Thesis, we investigate various aspects of integrable one-dimensional systems out-of-equilibrium. In particular, we focus on both transient and asymptotic behavior of some paradigmatic models, such as Luttinger liquids, spin-orbit coupled systems and fermionic chains in the presence of a staggered potential, after a so called quantum quench. The latter is a simple but effective way to drive a system far from equilibrium and consists in varying in time one of its parameters. First, we investigate the time evolution towards the asymptotic state characterizing a Luttinger liquid after a sudden interaction quench. We demonstrate that the quench-induced entanglement results in a universal time-decay $\propto t^{-2}$ in both the spectral and the transport properties of the system. In particular, concerning the latter, we focus on charge and energy currents injected into the Luttinger liquid from an external non-invasive probe. We then investigate the time-evolution of the local particle density of a Luttinger liquid with open boundary conditions after an interaction quench with finite duration. We show that the post-quench dynamics is strongly affected by the interference between two light-cone perturbations arising after both the turning on and turning off of the quench ramp. Finally, we consider quench mechanisms which open a gap in the spectrum of prototypical one-dimensional free fermionic systems, namely a spin-orbit coupled model and a fermionic chain in the presence of a staggered potential. We observe a non-monotonic response in the steady-state value of some characteristic observables as a function of the strength of the quench. By investigating the full dynamical evolution of the associated correlation functions, we explain this behavior in terms of a freezing of the light-cone, which conveys the information through the system, for large quenches. Since the very same phenomenon occurs after an interaction quench in chains of spinless fermions, we argue that our results also apply to more general systems and quench protocols.

LIST OF PUBLICATIONS

The following papers have been published during my Ph.D:

F. M. Gambetta, N. Traverso Ziani, S. Barbarino, F. Cavaliere, and M. Sassetti, "Anomalous Friedel oscillations in a quasihelical quantum dot", Phys. Rev. B **91**, 235421 (2015).

F. Cavaliere, F. M. Gambetta, S. Barbarino, and M. Sassetti, "Crystallization of fractional charges in a strongly interacting quasihelical quantum dot", Phys. Rev. B **92**, 235128 (2015).

F. Cavaliere, F. M. Gambetta, N. Traverso Ziani, and M. Sassetti, "Current noise as a probe for Wigner molecules", Journal of Physics: Condensed Matter **27**, 425301 (2015).

F. M. Gambetta, F. Cavaliere, R. Citro, and M. Sassetti, "Universal transport dynamics in a quenched tunnel-coupled Luttinger liquid", Phys. Rev. B **94**, 045104 (2016).

S. Porta, F. M. Gambetta, F. Cavaliere, N. Traverso Ziani, and M. Sassetti, "Out-of-equilibrium density dynamics of a quenched fermionic system", Phys. Rev. B **94**, 085122 (2016).

A. Calzona, F. M. Gambetta, M. Carrega, F. Cavaliere, and M. Sassetti, "Nonequilibrium effects on charge and energy partitioning after an interaction quench", Phys. Rev. B **95**, 085101 (2017).

A. Calzona, F. M. Gambetta, F. Cavaliere, M. Carrega, and M. Sassetti, "Quench-induced entanglement and relaxation dynamics in Luttinger liquids", Phys. Rev. B **96**, 085423 (2017).

S. Porta, F. M. Gambetta, N. Traverso Ziani, D. M. Kennes, M. Sassetti, and F. Cavaliere, "Nonmonotonic response and light-cone freezing in fermionic systems under quantum quenches from gapless to gapped or partially gapped states", Phys. Rev. B **97**, 035433 (2018).

The following proceedings papers have been published during my Ph.D:

F. Gambetta and S. Porta, "Out-of-equilibrium density dynamics of a spinful Luttinger liquid", Il Nuovo Cimento C **40**, 92 (2017).

The following preprints have been submitted and are still under referral:

A. Calzona, F. M. Gambetta, M. Carrega, F. Cavaliere, and M. Sassetti, *Asymmetries in the spectral density of an interaction-quenched Luttinger liquid*, Submitted as proceedings paper for the conference LT28, 2017.

A. Calzona, F. M. Gambetta, M. Carrega, F. Cavaliere, T. L. Schmidt, and M. Sassetti, *Universal scaling of quench-induced correlations in a one-dimensional channel at finite temperature*, Submitted to SciPost Physics, 2017, arXiv:1711. 02967.

CONTENTS

ACRONYMS

ETH   Eigenstate Thermalization Hypothesis

LRC   Local Relaxation Conjecture

GGE   Generalized Gibbs Ensemble

1D   one-dimensional

2D   two-dimensional

3D   three-dimensional

LL   Luttinger liquid

PBC   period boundary conditions

NESF   non-equilibirum spectral function

OBC   open boundary conditions

SOC   spin-orbit coupled

2DEG   2D degenerate electron gas

SIA   structural inversion asymmetry

SP   staggered potential

KG   Klein-Gordon

DMRG density matrix renormalization group

LC   light cone

INTRODUCTION

The study of non-equilibrium quantum systems is a challenging and long-standing problem in various fields of physics. The importance of such a field clearly emerges when one considers the most obvious definition of non-equilibrium, i.e. the absence of thermodynamic equilibrium. The latter is characterized by the following conditions [1–6]

- a system in thermodynamic equilibrium can be completely described by sets of extensive and intensive variables, which enter in the state equation of the system and do not change in time if the external conditions remain the same;

- if a system in thermodynamic equilibrium is isolated from its environment, *all* its variables remain unchanged.

Even daily experience suggests that these requirements are extremely restrictive and, therefore, non-equilibrium is the rule rather than the exception. Non-equilibrium quantum phenomena are ubiquitous in many diverse fields of physics, ranging from cosmology [7–10] to biology [11, 12], particle physics [8, 13, 14] and condensed matter [15–18]. Concerning the latter, which will be the focus of the present Thesis, they are at the heart of many solid state devices of great technological importance, such as transistors and lasers [19–21]. Moreover, a better understanding of the non-equilibrium behavior of quantum many-particle systems would be of great importance for the realization of new coherent quantum technologies, such as quantum computers [22].

From the theoretical point of view, dealing with non-equilibrium systems is, in general, quite a complex task. Indeed, both classical and quantum systems in thermal equilibrium are completely characterized by their thermal density operator $Z^{-1}e^{-\beta\hat{H}}$, describing the particle distribution in phase or Hilbert space and from which it is possible to evaluate all physical observables [2, 5, 6, 23, 24]. Unfortunately, in a non-equilibrium situation an analogous of this general and powerful approach does not still exist. As a consequence, there are very few tools allowing to deal with non-equilibrium systems on general basis, such as mean field theory or renormalization group in equilibrium, and many concepts of Statistical Mechanics we are used to, such as universality and scaling, must be re-examined case by case.

Nevertheless, the reward for studying non-equilibrium systems surely overcomes the increased difficulties and motivates both theoretical and experimental research in this field: Indeed, by accessing the out-of-equilibrium dynamics of a quantum system it is possible to obtain many more information about its internal structures than looking at its equilibrium properties. This is at the basis, for instance, of the ultrafast spectroscopy technique [25]. Moreover, the phase diagram of non-equilibrium systems is much richer

than the equilibrium one and allows to realize completely new states of matter which cannot exist in equilibrium, such as time crystals [26–31].

Two are the most common and distinct ways for driving a general system out of equilibrium: by a static external drive, such as a voltage bias or a thermal gradients, or by rapidly changing in time one of the parameters of the system. While the former has been extensively investigated in solid state devices, the quantum dynamics arising from the latter procedure, which is known in recent literature as *quantum quench* [32, 33], can hardly be studied in condensed matter systems. Indeed, the decoherence induced by the unavoidable coupling with the external environment present in any solid state device would destroy the unitary quantum evolution of the system after a very short time interval. However, the extraordinary experimental advances in engineering, manipulating and probing cold atomic gases we have been witnessing in the last ten years dramatically renew the interest towards this class of non-equilibrium protocols [34–46]. Indeed, they allow to simulate many condensed matter toy models with a very high degree of fidelity and to tune in a very simple way the parameters of these models, even in a time-dependent fashion. However, the great advantage of studying non-equilibrium phenomena with cold atoms is that they are almost perfectly isolated from the external environment and they thus essentially behave as closed systems on very large time scales. This makes it possible to experimentally realize quantum quenches and to explore their ensuing quantum dynamics.This fact has triggered much theoretical and experimental research on the issue of thermalization of an isolated quantum system driven out of equilibrium [16, 17, 45, 47], namely if, how and with which time scale an out-of-equilibrium system relaxes to a thermal equilibrium state. While in classical mechanics this process is well understood in terms of energy and momentum redistribution due to inter-particle collisions and concepts like ergodicity, chaos and typicality apply [2, 5, 6], the situation in quantum systems is far more subtle. Indeed, the unitary time evolution set by the Schrödinger equation seems to prevent full thermalization. This apparent paradox was already addressed by von Neumann [16, 48, 49], who in is his seminal paper of 1929 developed the intuition of focusing on observables rather than on the state of the system itself. This concept lies at the heart of the Eigenstate Thermalization Hypothesis (ETH) – proposed independently in the 90's by Srednicki and Deutsch [50, 51] – which is so far the most comprehensive theoretical tool to explain why generic isolated quantum systems can be correctly described in terms of standard equilibrium Statistical Mechanics [16].

Concerning the issue of thermalization, integrable quantum systems are of particular interest. Albeit the definition of integrability in Quantum Mechanics is far from being clear [52], as their classical counterparts quantum integrable systems possess an extensive amount of conserved quantities which strongly constrain the time-evolution in a non-equilibrium regime and lead to the breakdown of thermalization [47, 53, 54]. Although a thermal state cannot be reached, ten years ago Rigol and coworkers [54] have shown that

also these systems relax to a steady state after been perturbed away from equilibrium. The latter can successfully be described within a generalized thermal ensemble, the so called Generalized Gibbs Ensemble (GGE), which takes into account the presence of the system conserved quantities [47, 53, 54]. The intense theoretical efforts in understanding the behavior of these peculiar systems allowed Cramer et al. to formulate the Local Relaxation Conjecture (LRC) [55, 56], which complement the ETH and apply for generic quantum systems, integrable or not. Essentially, it states that, although an isolated quantum system cannot thermalize as whole due to the unitarity of its evolution, it behaves as a bath for any of its finite subsystems which, in the long-time limit, relax to a state characterized by the maximum entropy compatible with the constants of motion of the system [16–18, 55–59]. The approach to this state is conveyed by the spreading of information through the system, which occurs in a peculiar light cone (LC) fashion [32, 60] in complete analogy with relativistic quantum field theories.

The scope of the present Thesis is to study how the properties of some paradigmatic one-dimensional (1D) quantum many-body systems are affected by an out-of-equilibrium situation and, conversely, how trails of the intrinsic relaxation process leading to local equilibration emerge in physical observables.

In **Chapter 1** we introduce the main properties and experimental evidences of out-of-equilibrium isolated quantum systems, starting with an overview on quantum quenches and on the issues that immediately raise up when speaking about thermalization in such systems. We then briefly outline the ETH before focusing on the main topics of the Thesis, i.e. integrable quantum systems. After reviewing the seminal experiment of Kinoshita et al. [39], which paved the way to the research in this field, we introduced in some details the LRC and GGE.

In **Chapter 2** we introduce the Luttinger liquid (LL) model and the bosonization technique, which are powerful tools to deal with interacting 1D quantum systems both in and out-of equilibrium. LLs exhibit many peculiar properties, such as power-law correlations, spin-charge separation and fractionalization phenomena [61–63]. The scope of this Chapter is to investigate how these properties are modified in an out-of-equilibrium environment, focusing in particular on the spectral and transport ones after a quench of the inter-particle interaction. We show that the entanglement generated by the quench induces a universal power-law behavior in all these quantities. Although the time-evolution of the non-equilibrium spectral function (NESF) is controlled by a competition between this universal decay and more conventional LL power laws, we show that the former dominates the decay to the steady-state value of tunneling charge and energy currents between the LL and an external non-invasive probe.

In **Chapter 3** we focus on the effects of an interaction quench with finite duration in a finite-size system. In particular, we investigate how the interplay between these two finite scales affects the dynamics of the particle density of a LL with open boundary conditions (OBC). We show that both the turning

on and the turning off of the quench ramp create a pair of LC perturbations which arise from the boundaries and travel ballistically through the system. The post-quench dynamics of the latter is thus strongly affected by the interference between these two LC perturbations. In spite of the finite size of the system, which implies that no true steady state can be reached, we show that for slow quenches the post-quench particle density oscillates in time around the result obtained with a GGE approach. The discrepancy among them decreases as the quench duration is increased with a non-monotonic behavior, with local minima and maxima emerging as a consequence of LCs interference.

In **Chapter 4** we leave the LL model and explore the physics of systems which get (partially-)gapped after changing a parameter of their Hamiltonian. In the first part we study the quench of a magnetic field in a spin-orbit coupled (SOC) system, while in the second one we consider a chain of spinless fermions in which the gap is opened either by the quench of a staggered potential or by switching on inter-particle interactions. In order to characterize the response of the non-interacting models to the quench, we investigate their steady state "magnetization". The latter exhibits a quite surprising non-monotonic behavior as a function of the strength of the quench parameter which can be explained by looking at the dynamics of their associated correlation functions. Indeed, the latter display a competition between a propagation and a freezing regime of the LC-like spreading of information which dramatically affects the steady-state properties of the systems. The very same behavior occurs also after the switching-on of interactions in the fermionic chain and, thus, we argue that it represents a general feature of gap opening quenches.

1

NON–EQUILIBRIUM DYNAMICS OF ISOLATED QUANTUM SYSTEMS

In this Chapter we will discuss some general properties of isolated quantum many-body systems out-of-equilibrium. After a brief introduction on the issue of equilibration, we will describe in details one of the possible method to drive an isolated system far from equilibrium and to study its ensuing coherent dynamics, the so called *quantum quench* protocol [32, 33]. Here, one or more parameters of the Hamiltonian describing an isolated system are varied over a finite interval of time and, then, the system is allowed to evolve freely. This procedure can be easily performed experimentally in cold atomic setups [34–36]. The most natural question one may ask is whether, after this perturbation, the isolated system approaches a steady state and, if so, how this state can be characterized. Then, motivated by recent experiments in cold atomic systems, we will focus on integrable quantum systems. Due to the presence of an extensive number of conserved quantities, they exhibit peculiar properties with respect to the equilibration after a quench, in strong analogy with their classical counterparts. For a more detailed treatment the reader is referred to one of the many excellent reviews existing in the literature [16–18, 40, 43, 45, 47].

In this Chapter and in the following ones we set $\hbar = 1$, with $\hbar$ the (reduced) Planck's constant, unless otherwise specified.

1.1 OUT–OF–EQUILIBRIUM ISOLATED QUANTUM SYSTEMS

Historically, the main focus of many-body quantum theory has been on describing equilibrium properties of nuclear and condensed matter models [23, 24, 64]. This is essentially due to the fact that a system in thermal equilibrium can be completely characterized in terms of its density operator $\hat{\rho} = \hat{Z} e^{-\beta \hat{H}}$, from which all of its physical observables can be computed. This makes it possible to develop some extremely powerful and general theoretical tools, such as renormalization group and mean field approach, and concepts, such as scaling and universalities, which apply to almost all possible equilibrium systems and allow to treat them on a very general and common ground [1, 23, 24, 64].

However, our daily experience suggests that equilibrium is the exception rather than the rule. Indeed, non-equilibrium phenomena are ubiquitous in almost every field of both classical and quantum physics, ranging over very different energy, time and length scales. To cite just few examples, we recall the formation of particles during the reheating following inflation in the early Universe [7, 9, 10], the quark-gluon plasma, characterized by a very short equilibration time, formed in heavy-ion collisions [8, 14], the physics

of ultra-fast spectroscopy in correlated materials [13, 65] and nuclear spins in diamond [66]. So, why in past most of the theoretical research has been focused towards equilibrium systems and so few attention has been devoted to the non-equilibrium realm? The answer is, indeed, rather simple: dealing with systems far from equilibrium is an extremely hard and complex task, since no general approach has been developed so far and the investigation on these systems must be carried out case by case. Moreover, up to ten years ago the investigation of pure quantum non-equilibrium dynamics was far beyond experimental reach.

The study of how isolated quantum systems behave when they are driven far from equilibrium traces back to the early days of Quantum Mechanics [48, 49]. In the 60's some pioneering works by Niemeijer [67], Mazur [68], and Barouch and coworkers [69–71] began to explore the properties of some theoretical toy models out of equilibrium, such as the *XY* model and spin chains. However, due to the impossibility to realize isolated quantum systems in conventional experimental setup, their research remained on a pure academic level. In the last decade things have dramatically changed thanks, in particular, to recent advances in realizing, manipulating and probing cold atomic systems [35, 40, 43, 72]. They have provided a new platform to investigate in real time the coherent dynamics of (nearly-)isolated many-body quantum systems and, as a natural consequence, have also given new impetus to the theoretical research in this field.

The understanding of out-of-equilibrium behavior of quantum systems is of great importance, first of all, from a fundamental point of view. Indeed, as we have said above, all the tools that have proved to be very effective in describing equilibrium physics, such as mean field theory, renormalization group and concepts like universality and scaling, have (yet) no counterparts in the non-equilibrium regime. Thus, due to the complexity of the problem, it is important to focus on out-of-equilibrium properties of simple and solvable models in order to detect possible evidences of general features underlying the dynamics of non-equilibrium quantum systems. Furthermore, due to the presence of non-equilibrium processes in almost every realms of Nature, a better understanding of their general features would shed new light on some fundamental problems in many diverse areas of Physics. This would be of great importance also from the technological point of view, since the development of new coherent quantum technologies requires, of necessity, the ability to coherently manipulate quantum systems in time. Last but not least, non-equilibrium regimes allow to realize new exotic phases of matters, which would be unstable in equilibrium and which exhibit new intriguing properties [26–31]

At the vary basis of every non-equilibrium situation is the issue of *equilibration* in the absence of an external bath. In particular, when an isolated many-body quantum system is driven far from equilibrium, two main questions naturally arise:

- does the system approach a steady state in the long-time limit?

- if so, how can the asymptotic state be described?

The answers to both questions are highly non-trivial and have triggered lots of theoretical work. In the classical case, the relaxation from out-of-equilibrium to equilibrium can be explained in terms of collisions between the particles of a system, which allow for energy and momentum redistribution through the system itself. In more mathematical treatments, the classical equilibration problem is well understood in terms of the properties of flows in phase space and concepts like ergodicity, chaos and mixing [2, 5, 6]. On the other hand, the situation in the quantum realm is far from being clear. Indeed, as we will see in more details in the following, at first glance the relaxation of an out-of-equilibrium isolated quantum system to a steady state seems to be in contradiction with the unitary time evolution set by the Schrödinger equation [16, 73]. Nevertheless, in 1929 von Neumann [48, 49] realized that this fact does not preclude the possibility that some *observables* of the system relax to a stationary value, as both physical intuition and experimental results suggest [42, 46, 59, 74, 75]. As we will see in the following, this shift of focus from the system state/density matrix to its observables turned out to be a key point in the understanding of equilibration properties of isolated quantum systems.

1.2 QUANTUM QUENCHES AND EQUILIBRATION IN ISO– LATED QUANTUM SYSTEMS

In order to inspect in more detail the out-of-equilibrium behavior of isolated quantum systems will we now introduce the concept of a *quantum quench* [15–18, 32, 45, 47], which represents a very simple but effective way to drive a quantum system far from equilibrium and to study its subsequent dynamics. In recent years this procedure has gained greater attention since it can easily be implemented in cold atomic setups [37, 39, 40, 43, 44]. In a quantum quench setup we consider a system described by a local Hamiltonian $\hat{H}(\mathfrak{h}) = \sum_j \hat{\mathcal{H}}_j(\mathfrak{h})$, with $\hat{\mathcal{H}}_j(\mathfrak{h})$ acting non-trivially only on a finite portion of the system. Here, $\mathfrak{h}$ is a parameter of the system describing, for instance, an external field, a coupling constant of the model, or the strength of inter-particle interaction. For $t < 0$ the system is prepared in an equilibrium state with $\mathfrak{h} = h_0$ and associated density matrix $\hat{\rho}_0$, which in most cases coincides with the ground state of the initial Hamiltonian $\hat{H}(h_0)$. At $t = 0$ we start to change in time the parameter value from h_0 to the final value h over a time window of width τ and over the whole system. The entire quenching procedure is schematically shown in Fig 1.1. In particular, if $\tau = 0$ and the parameter is varied instantaneously, the quench is said *sudden*, otherwise we refer to it as a *smooth* quench. In this introductory Chapter we will focus on the simplest sudden quench case only, although similar considerations hold also for the more general one (see, for instance, Chap. 3). Moreover, we will consider a system in the zero-temperature limit. So, let us denote with $|\Psi_0\rangle$ the ground state of $\hat{H}(h_0)$ and with $\hat{\rho}_0 = |\Psi_0\rangle\langle\Psi_0|$ its associated density
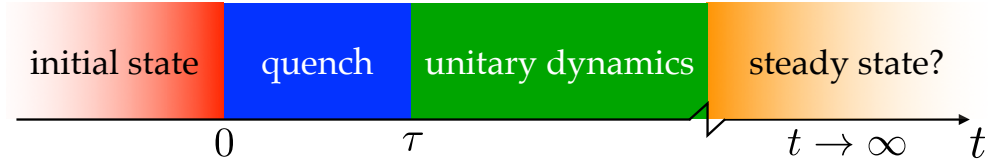
Figure 1.1: Sketch of a quantum quench protocol. At first, the system is prepared in an initial state, usually the ground state of the initial Hamiltonian. Then, at $t = 0$, the quench begins and lasts until $t = \tau$, bringing the system far from equilibrium. Finally, for $t > \tau$ the system is left to evolve unitarily and may reach a steady state for longer times. Figure adapted from Ref. [40].

matrix. After the quench the time evolution of $|\Psi_0\rangle$ is determined by the unitary time evolution operator $\hat{U}(t) = e^{-i\hat{H}(h)t}$ [73, 76],

$$|\Psi(t)\rangle \equiv e^{-i\hat{H}(h)t}|\Psi_0\rangle = \sum_n c_n e^{-iE_n t}|n\rangle, \qquad (1.1)$$

with $\hat{H}(h)|n\rangle = E_n|n\rangle$ the eigenvalue equation of the post-quench regime and $c_n = \langle n|\Psi_0\rangle$. In the realistic case in which $|\Psi_0\rangle$ is not an eigenstate of the final Hamiltonian $\hat{H}(h)$, the procedure described so far is the starting point of a non-equilibrium dynamics.

At this stage, if we try to answer the question "does the system approach a steady state?" we get stuck into an apparent paradox. Indeed, an analogy with classical Statistical Mechanics suggests that every isolated interacting system, after being perturbed from an initial equilibrium configuration, should relax toward a new equilibrium state which can be described by a standard thermodynamic ensemble[1], i.e. one should expected the system to *thermalize*. Here, in the long-time limit, the extra energy and momentum injected into to system by the external perturbation are re-distributed homogeneously among all the particles of the system thanks to inter-particle collisions [2, 5, 6]. The thermalization process in the classical case can be understood even better if one looks at what happens in phase space, by means of the concept of typicality. From the thermodynamic point of view, the latter can be conveniently divided into many regions, each of which containing all the points of the phase space (i.e. the microstates) associated to a given macrostate. The latter is characterized by the values of a certain "complete" set of thermodynamic observables of the system (for example, volume, pressure and temperature in the case of a gas of classical particles). Among all the thermodynamic partitions, the one associated with the thermal equilibrium macrostate, which can be described by standard thermodynamic ensemble, is incredibly larger than any other. Therefore, if a system begins its evolution in one of the small non-equilibrium regions of the phase space (i.e. it has been previously driven out of equilibrium), due to the large discrepancy between volumes of non-equilibrium and equilibrium regions, as time

---

1 Obviously, for an isolated system, the microcanonical ensemble is the most natural choice although, in the thermodynamic limit, one can also equivalently chose either the canonical or the grand canonical ones.

proceeds it will *almost* certainly enter the thermal equilibrium region of the phase space, where it will spend most of the subsequent time. Note that, from this picture the ergodic theorem of classical Statistical Mechanics follows immediately as a consequence of typicality and should not be invoked as a postulate. Indeed, if we introduce the long time average of a given (classical) observable A, evaluated over a trajectory $x(t)$ in phase space,

$$\overline{A} \equiv \lim_{T \to \infty} \int_0^T A(x(t)) dt \qquad (1.2)$$

and the thermodynamic ensemble average of the same observable

$$\langle A \rangle_{\text{ens}} \equiv \int_\Gamma A(x) d\mu, \qquad (1.3)$$

with Γ the whole phase space and $d\mu$ the appropriate measure (microcanonical, canonical or grand-canonical), the ergodic theorem states that [2, 5, 6, 45]

$$\overline{A} = \langle A \rangle_{\text{ens}}. \qquad (1.4)$$

Things in Quantum Mechanics go in a rather different way. To see this, we start by constructing the quantum version of the microcanonical ensemble. In many realistic out-of-equilibrium experimental situations the eigenstates of $\hat{H}(h)$ which significantly contribute to the initial state $|\Psi_0\rangle$ are localized in a narrow energy shell of width $\Delta = [E_0 - \delta, E_0 + \delta]$, centered around the initial state energy $E_0 = \langle \Psi_0 | \hat{H}(h) | \Psi_0 \rangle$. This means that $|\Psi_0\rangle \approx \sum_{n|E_n \in \Delta} c_n |n\rangle$, where the sum is over the eigenstates with energy E_n inside the shell Δ. In these cases a quite natural definition of the microcanonical density matrix of the systems is [16, 45]

$$\hat{\rho}_{\text{mc}} \equiv \frac{1}{\mathcal{N}} \sum_{n|E_n \in \Delta} |n\rangle \langle n|, \qquad (1.5)$$

where $\mathcal{N}$ is the total number of states inside the energy shell Δ and $\{|n\rangle\}$ are the eigenstates whose associated eigenvalues are in Δ. If we now try to extend the implications of the ergodic theorem of classical Statistical Mechanics introduced in Eq. (1.4) to the quantum realm by considering the long-time average of the density matrix associated with the pure state of Eq. (1.1), we obtain

$$\hat{\overline{\rho}} \equiv \lim_{T \to \infty} \frac{1}{T} \int_0^T \hat{\rho}(t) \, dt = \sum_n |c_n|^2 |n\rangle \langle n| \equiv \hat{\rho}_{\text{D}}, \qquad (1.6)$$

where $\hat{\rho}(t) = e^{-i\hat{H}(h)t} \hat{\rho}_0 e^{i\hat{H}(h)t}$ is the time-evolved initial density matrix and $\hat{\rho}_{\text{D}}$ is the density matrix associated with the so called *diagonal ensemble* [45, 54]. In order to have thermalization in the classical sense, the identity $\hat{\rho}_{\text{mc}} = \hat{\overline{\rho}}$ is expected to hold for *almost any* initial states $|\Psi_0\rangle$. However, as one can immediately notice, the latter is satisfied if and only if $|c_n|^2 = 1/\mathcal{N}$, $\forall n$, which, on the contrary, holds for a very limited subset of initial states only. On the other hand, the classical picture we described above and in which thermalization results from the phase-space evolution of the system state towards the large equilibrium region cannot be applied to quantum systems.

Indeed, if a system is initially prepared in a pure state, the unitarity of the time evolution implies that it will remain in a pure state at any subsequent times, i.e. $[\hat{\rho}(t)]^2 = \hat{\rho}(t)$, $\forall t$. Therefore, during its time evolution, the system will explore a very limited fraction of all the possible states, i.e. its dynamics is constrained to a very small region of the Hilbert space, and will never enter into the region of mixed states, which are usually associated with thermal ensembles.

So, to summarize the situation so far, an isolated quantum system driven out-of-equilibrium will never reach a steady state as a whole and, generally, the long-time average of its density matrix never coincides with a thermal one. Therefore, an isolated quantum system will never thermalize in the classical sense.

All the statements above are, however, in contrast with many experiments in which, after an initial perturbation from an equilibrium state, expectation values of many observables of isolated quantum systems relax at later times to a stationary value, in agreement with standard thermodynamic predictions, and fluctuate close to the latter for almost all subsequent times [42, 46, 59, 74, 75]. In modern terminology, this kind of behavior is known as *strong* thermalization and should be compared with *weak* thermalization[2], in which long-time averages are involved [16]. As already realized by von Neumann in 1929 [48, 49], this suggests that the key to address the equilibration problem in Quantum Mechanics requires to shift the focus from the state of system itself to its physical observables. In the context of isolated quantum systems he proved what he called quantum ergodic theorem which encodes the concept of *normal typicality* and, using the word of Goldstein et al., states that [16, 77]

> for a typical finite family of commuting macroscopic observables, every initial wave function from a microcanonical energy shell evolves so that for most times in the long run, the joint probability distribution of these observables obtained from the unitarily time-evolved wave functions close to their micro-canonical distribution.

Even though this theorem represents a milestone in the study of thermalization of isolated quantum systems, it leaves many open problems. Indeed, this theorem does not allow to distinguish between the behavior of non-integrable and integrable systems which, as we shall see in the following, exhibit very different properties with respect to thermalization. Moreover, the typical family of macroscopic observables involved in the theorem does not generally coincide with the physically relevant observables measured in experiments. As we will see in Sec. 1.2.1, both these issues can be properly

---

2 In particular, an observable $\hat{\mathcal{O}}$ of an isolated system is said to thermalize in the weak sense if one obtains

$$\overline{\mathcal{O}} = \lim_{T \to \infty} \frac{1}{T} \int_0^T \langle \hat{\mathcal{O}}(t) \rangle \, dt = \frac{1}{Z_{\text{mc}}} \text{Tr} \left[\hat{\mathcal{O}} \hat{\rho}_{\text{mc}} \right]. \tag{1.7}$$

Note that, in the rest of this Thesis, whenever we refer to equilibration/thermalization we always mean the strong version.

addressed within the ETH, which in short transfers the concept of typicality from the system states to the eigenstates of its Hamiltonian.

Since from the discussion below Eq. (1.6) it follows that after a perturbation from equilibrium the relaxation towards a thermal state is not guaranteed at all, from now on we will distinguish between the concepts of *equilibration* and *thermalization*. In particular, while the latter implies the relaxation towards a thermal-like state which can be described by standard thermodynamics ensemble, the former refers to the more general situation in which a generic, and not necessarily thermal, steady state is reached. Since in Eq. (1.6) we have seen that in the "ergodic sense" the density matrix of the system relaxes to the diagonal ensemble, as a first step it is natural to investigate if and under which assumptions system observables relaxes to their diagonal ensemble predictions.

In particular, following von Neumann's point of view, we say that an observable $\hat{\mathcal{O}}$ *equilibrates* to its diagonal ensemble value [see Eq. (1.6)] if for any $\varepsilon > 0$ there exist a system linear size L, a relaxation time $t_{\rm rel}$ and a recurrence time $t_{\rm rec}$ such that the following relation holds for *almost* every initial state $|\Psi_0\rangle$ and times $t_{\rm rel} < t < t_{\rm rec}$ [17]

$$\left| \langle \hat{\mathcal{O}}(t) \rangle - \langle \hat{\mathcal{O}} \rangle_{\rm D} \right| < \varepsilon, \tag{1.8}$$

with $\langle \hat{\mathcal{O}} \rangle_{\rm D} = {\rm Tr}[\hat{\mathcal{O}}\hat{\rho}_{\rm D}]$ the diagonal ensemble average and

$$\langle \hat{\mathcal{O}}(t) \rangle = \langle \Psi(t) | \hat{\mathcal{O}} | \Psi(t) \rangle = \underbrace{\sum_n |c_n|^2 \mathcal{O}_{nn}}_{\langle \hat{\mathcal{O}} \rangle_{\rm D}} + \underbrace{\sum_{n \neq m} c_m^* c_n \mathcal{O}_{mn} e^{i(E_m - E_n)t}}_{\delta\mathcal{O}(t)}, \tag{1.9}$$

where we have introduced the shorthand notation $\mathcal{O}_{nm} \equiv \langle n | \hat{\mathcal{O}} | m \rangle$. Here, for the sake of simplicity, we assumed that no degeneracies in the spectrum of the Hamiltonian are present, as one expects for a large but finite system in the absence of special symmetries. Note that the definition in Eq. (1.8) takes into account the presence of recurrences due the Poincaré recurrence theorem (and its quantum version) [78–80], which implies the existence of a finite recurrence time $t_{\rm rec}$ for every finite system (see Appendix A for details). Note that $t_{\rm rec}$ can be made large enough by considering a sufficiently large system size L. Anyhow, even for moderately small systems with non-commensurate spectrum, $t_{\rm rec}$ is so large that recurrences do not occur during experimentally accessible times. Note that, if an observable equilibrates in the strong sense specified above it will remain arbitrarily close to its equilibration value $\langle \hat{\mathcal{O}} \rangle_{\rm D}$ for almost all subsequent times but this does not prevent the instantaneous value of $\langle \hat{\mathcal{O}}(t) \rangle$ to exhibit fluctuations for small interval of times and with exponentially small (in the system size) probability.

Let us now go back to Eq. (1.9). In order to have equilibration to the diagonal ensemble the time dependent part of $\langle \hat{\mathcal{O}}(t) \rangle$ must vanish in the long-time limit, i.e. $\delta\mathcal{O}(t) \to 0$ for $(t_{\rm rec} \gg)t \gg t_{\rm rel}$. This requires that all the terms of the sum interfere destructively with each other. This is not at all a trivial assumption. Indeed, since energy levels are extensive quantities while the dimension of the Hilbert space is exponentially large in the system size,

the eigenstates of $\hat{H}(\mathfrak{h})$ become more dense – and thus the gaps get smaller – as the system size is increased [16, 81]. This could lead to an exponentially long waiting time in order to see the relaxation of $\langle \hat{\mathcal{O}}(t) \rangle$ to its diagonal ensemble average or, even worse, to non-diagonal contributions to the time average of $\langle \hat{\mathcal{O}}(t) \rangle$ which would breakdown the equilibration towards the latter. Since these statements are in contrast with what is usually seen in experiments [42, 46, 59, 74, 75], in which many observables display a fast equilibration to $\langle \hat{\mathcal{O}} \rangle_D$, a change of perspective is necessary. In particular, some hypotheses on the structure of the off-diagonal matrix elements $\mathcal{O}_{mn}$ are required. Indeed, we can rewrite $\delta\mathcal{O}(t)$ as

$$\delta\mathcal{O}(t) = \int_{-\infty}^{\infty} e^{-i\Omega t} \mathcal{F}_{\mathcal{O}}(\Omega) \, d\Omega, \qquad (1.10)$$

with $\mathcal{F}_{\mathcal{O}}(\Omega) = \sum_{n \neq m} c_m^* c_n \mathcal{O}_{mn} \delta(\omega - E_n + E_m)$. In the thermodynamic limit[3], if the spectrum of the system is a smooth continuous function and the weights $c_m^* c_n \mathcal{O}_{mn}$ make $\mathcal{F}_{\mathcal{O}}(\Omega)$ integrable, the Riemann-Lebesgue theorem guarantees that $\delta\mathcal{O}(t) \to 0$ for $t \to \infty$ [81–83]. This ensures that equilibration to the diagonal ensemble is achieved in the strong sense and is entirely due to destructive interference (dephasing) induced by the oscillating factor $e^{-i\Omega t}$. Note that, for finite size systems, $\mathcal{F}_{O}(\Omega)$ is an infinite sum of Dirac's delta and, thus, it is no more an integrable function. This is compatible with the emergence of a recurrence time t_{rec}, although one expects the system to be almost equilibrated in the usually large time interval $t_{rel} < t < t_{rec}$. Unfortunately, the above argument leaves completely outside from the discussion an estimate of the relaxation time. This is still an open and debated issue and generally, it strongly depends on the specific observable considered, the initial pre-quench state and the details of the post-quench Hamiltonian. The only clue about this very complex problem comes from numerical simulations in lattice systems, which confirm that relaxation times to a steady state are always not exponentially large [16].

In this Section we have shown that if one focuses on system observables equilibration can occur, under certain assumptions, also in isolated quantum systems. However, one of the main points of Statistical Mechanics remains still unclear: is it possible to characterize the equilibrated state by means of few macroscopic parameters, such as temperature and particle number as in standard Thermodynamics? Indeed, Eq. (1.8) establishes the convergence of the expectation value of a generic observable $\hat{\mathcal{O}}$ to its diagonal ensemble prediction. The latter is obtained through the diagonal density matrix $\hat{\rho}_D = \sum_n |c_n|^2 |n\rangle\langle n|$, which basically contains all the information about the initial state and requires the knowledge of an exponentially large (in system size) number of parameters – namely all the coefficients c_n. However, this huge amount of needed information is in sharp contrast with experiments, in which also isolated quantum systems can be effectively described by standard ensembles of Statistical Mechanics.

---

3 Note that, in this case, $t_{rec} \to \infty$.

1.2.1 Thermalization and the Eigenstate Thermalization Hypothesis

A cornerstone in answering to the question raised in closing the previous Section for the case of a general non-integrable many-body quantum system was laid by Deutsch [50] and Srednicki [51, 84, 85] 20 years ago. Here, we only briefly sketch their argument, since it will not be the focus of this Thesis, and the reader is referred to Ref. [16] for a more detailed treatment. As stated above, the starting point is that one expects that generally, after relaxation, the system approaches a thermal state described by one of the well-known thermodynamics ensemble. Again, since we are dealing with isolated systems, the more appropriate choice would definitely be the micro-canonical one, although in the thermodynamic limit all the ensembles are equivalent. Therefore, by adapting the definition of Eq. (1.8) to this case, we say that an observable $\hat{\mathcal{O}}$ *thermalize* if for any $\varepsilon > 0$ there exist a system linear size L and a relaxation time t_{rel} such that the following relation holds for *almost* every initial state $|\Psi_0\rangle$ and times $t_{\mathrm{rel}} < t < t_{\mathrm{rec}}$

$$\left| \langle \hat{\mathcal{O}}(t) \rangle - \langle \hat{\mathcal{O}} \rangle_{\mathrm{mc}} \right| < \varepsilon, \tag{1.11}$$

with $\langle \hat{\mathcal{O}} \rangle_{\mathrm{mc}} = \mathrm{Tr}[\hat{\mathcal{O}} \hat{\rho}_{\mathrm{mc}}]$ and $\hat{\rho}_{\mathrm{mc}}$ introduced in Eq. (1.5). From the above discussions, it should be clear that Eq. (1.11) does not hold for any observable $\hat{\mathcal{O}}$ and that the structure of the matrix elements of the various observables play a crucial role in equilibration and thermalization processes. This observation lies at the heart of the ETH, developed independently in the 90's by Deutsch [50] and Srednicki [51, 84, 85] and numerically observed for the first time in a realistic quantum system in 2008 by Rigol *et al.* [53]. The ETH is an ansatz for the matrix elements of an observable on the basis of the eigenstates E_n of the Hamiltonian governing the dynamics of the system, i.e., $\hat{H}(h)$ in the notation of Sec. 1.2. It can be stated as

$$\mathcal{O}_{mn} = \mathcal{O}(\bar{E}) \delta_{mn} + e^{-S(\bar{E})/2} f_{\mathcal{O}}(\bar{E}, \omega) R_{mn}, \tag{1.12}$$

where the shorthand $\mathcal{O}_{mn}$ has been introduced in Eq. (1.9), $\bar{E} = (E_m + E_n)/2$, $\omega = E_n - E_m$, and $S(E) = k_B \mathrm{Tr}[\hat{\rho} \ln(1/\hat{\rho})]$, with k_B the Boltzmann's constant, is the thermodynamic entropy of the system at energy E. Here, $\mathcal{O}(\bar{E})$ and $f_{\mathcal{O}}(\bar{E}, \omega)$ are smooth functions, with $\mathcal{O}(\bar{E}) = \langle \hat{\mathcal{O}} \rangle_{\mathrm{mc}}$, and R_{mn} a random real or complex number with zero mean and unit variance. Physically, the content of the ETH hypothesis is the following: If the matrix elements of an observable, evaluated on the basis of the eigenstate of the Hamiltonian governing the system dynamics, weakly fluctuates across different eigenstates close in energy (encoded in smoothness of $\mathcal{O}(\bar{E})$ and $f_{\mathcal{O}}(\bar{E}, \omega)$) they can be equivalently evaluated by an ensemble average. This means that, in essence, eigenstates close in energy are typical, i.e. they show the same macroscopic behavior. Although a rigorous proof is still lacking, numerical simulations in different lattice models showed that ETH holds for few-body observables of generic non-integrable quantum systems (which are also the experimentally relevant ones) [16]. The ansatz of Eq. (1.12) is an extension of the prediction of Random Matrix Theory [16, 86] and, for quantum systems with a

chaotic classical counterpart, correctly reproduces results obtained in their semi-classical limit [16, 51, 84, 85]. We can now prove that if an observable $\hat{\mathcal{O}}$ satisfies the ansatz in Eq. (1.12) then it thermalizes in the (strong) sense described above. Indeed, if we consider the long-time average of $\langle \hat{\mathcal{O}}(t) \rangle$ one gets

$$\overline{\mathcal{O}} \equiv \lim_{T \to \infty} \frac{1}{T} \int_0^T \langle \hat{\mathcal{O}}(t) \rangle \, dt = \sum_n |c_m|^2 \mathcal{O}_{nn} \approx \langle \hat{\mathcal{O}} \rangle_{\mathrm{mc}} + \frac{1}{2} (\delta E)^2 \langle \hat{\mathcal{O}} \rangle''_{\mathrm{mc}}, \quad (1.13)$$

where in the last step we employed Eq. (1.12). Here, we assumed that the energy fluctuations

$$\delta E = \sqrt{\langle \Psi_0 | [\hat{H}(h)]^2 | \Psi_0 \rangle - [\langle \Psi_0 | \hat{H}(h) | \Psi_0 \rangle]^2} \qquad (1.14)$$

around the energy $E_0 = \langle \Psi_0 | \hat{H}(h) | \Psi_0 \rangle$ are sufficiently small and well described by a gaussian distribution, as usually happens in Statistical Mechanics and in numerical simulations in lattice systems. To prove that thermalization occurs in the strong sense, we now evaluate the time fluctuations of $\langle \hat{\mathcal{O}}(t) \rangle$ around $\overline{\mathcal{O}} \approx \langle \hat{\mathcal{O}} \rangle_{\mathrm{mc}}$. Using the ETH ansatz of Eq. (1.12) it is possible to show that [16]

$$\lim_{T \to \infty} \frac{1}{T} \int_0^T [\langle \hat{\mathcal{O}}(t) \rangle]^2 \, dt - \overline{\mathcal{O}}^2 < \max[|\mathcal{O}_{mn}|^2] \propto e^{-S(\bar{E})}. \qquad (1.15)$$

Thus, since the thermodynamic entropy is an extensive quantity, these fluctuations are exponentially small in system size. This means that, after a relaxation period, the value of $\langle \hat{\mathcal{O}}(t) \rangle$ stays very close to its thermal value for most of the time, i.e. the observable thermalizes in the strong sense. Therefore, although the microcanonical and the diagonal density matrices of Eqs. (1.5) and (1.6) are profoundly different, if ETH holds for the observable considered and the initial state $|\Psi_0\rangle$ is such that the distribution of c_n is sufficiently localized around E_0, they lead to the same expectation value after relaxation. The only information about $|\Psi_0\rangle$ that survives is thus its energy, consistently with the fact that in non-integrable quantum system energy is the only conserved quantity after the quench. Since in the thermodynamic limit all statistical ensembles are equivalent, one can, in principle, use in Eq. (1.13) the canonical ensemble instead of the microcanonical one. In this case, the initial energy E_0 is converted into an inverse temperature β, defined by the identity $\mathrm{Tr}[e^{-\beta \hat{H}(h)} \hat{H}(h)] = E_0$.

By inspecting Eq. (1.9) and (1.13), one may note that equilibration (or thermalization) in a quantum system is dramatically different from the collisional picture of Classical Mechanics. Indeed, it consists essentially in the dephasing process of the contribution $\delta \mathcal{O}(t)$. Therefore, in a sense, the equilibrated (or thermalized) state is already encoded in the initial one, with the time evolution simply revealing it through dephasing [16, 53], and it is not the result of exchange of energy and momentum among the particles of the system, as occurs in classical Statistical Mechanics.
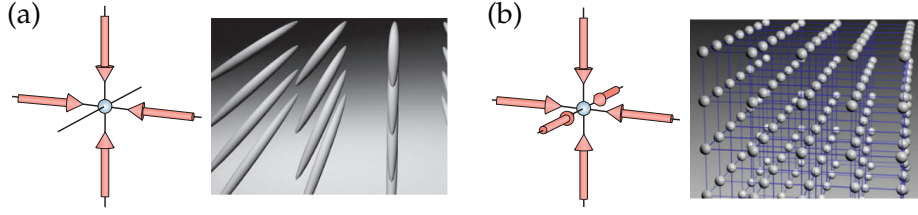
Figure 1.2: Optical lattices can be obtained by employing counter-propagating pair of laser beams. In particular, two orthogonal standing waves created by two different pairs of laser beams result in a 2D square lattice of 1D tubes [Panel (a)]. On the other hand, the interference of three pairs of laser beams can be used to realize a 3D cubic lattice in which each site can be described by a harmonic trapping potential [Panel (b)]. By varying the angle between pairs of beams more complex lattice can be created. Figure taken from Ref. [34].

1.3 EXPERIMENTS: ULTRACOLD ATOMIC SYSTEMS

As we have seen in the previous Section, the problem of thermalization/equilibration in isolated quantum systems has been addressed since long ago. However, only recently the interest towards a better understanding of non-equilibrium phenomena has emerged. This is due to the spectacular experimental developments in the field of ultracold atoms, which allow to realize and simulate a wide variety of well-known theoretical many-body quantum systems [34–36], such as the Bose-Hubbard model [34, 37], Luttinger liquids [87, 88] and Lieb-Liniger gases [41, 89]. Cold-atom setups consist of very dilute clouds of up to 10^7 atoms confined by magnetic traps on atom chips [90, 91] or by optical means, such as optical dipole traps [92] and optical lattices [34]. In order to enter the quantum regime, the de Broglie wavelength $\lambda_{dB} = 2\pi\hbar/\sqrt{mk_BT}$, with m the particle mass and T the temperature, should be comparable with the inter-particle spacing $n^{-1/3}$, with n the particle density. Here, we have temporarily the Planck's constant, $\hbar$. This results in the condition

$$n\lambda_{dB}^3 = n\left(\frac{2\pi\hbar^2}{mk_BT}\right)^{\frac{3}{2}} \lesssim 1. \tag{1.16}$$

Since cold atomic systems usually have very low densities (typically $n \sim 10^{20}$ m^{-3}), rather small temperatures, of the order of $T \sim 10^{-8}$ K, are required in order to satisfy Eq. (1.16). They can be reached by using a combination of laser and evaporative cooling [93]. The main strengths of ultracold atomic systems are their almost perfect isolation from the external environment, which ensures a very long quantum-coherence time, and their high degree of tunability. In optical lattices, for example, the shape and dimensionality of the systems can be controlled with great precision by means of counter-propagating laser beams, as shown in Fig. 1.2. This is made possible by the so called Stark shift, which prescribes that an atom inside an electromagnetic wave with intensity $I(\mathbf{r})$ feels a potential $V(\mathbf{r}) \propto I(\mathbf{r})$ [92]. Using the interference pattern resulting from pairs of counter-propagating

laser beams allows to create arrangements of sites very similar to crystalline structures with various shapes and dimensionality, enabling to simulate lattice condensed matter models with a high degree of fidelity. However, the great advantage of cold atoms – especially for the study of non-equilibrium phenomena – is the possibility to tune the physical parameters of the simulated systems, often in regimes unachievable in their condensed matter counterparts and even in a time-dependent fashion. For example the depth of the lattice potential can be adjusted by simply varying the intensity of the laser beams. Moreover, if the latter is changed in an anisotropic fashion, the dimensionality of the system can also be modified, allowing to turn a 3D lattice into an ensemble of 1D ones within the same experimental setup.

Another very intriguing property of cold atoms is that, due to the internal structure of the atoms themselves, scattering and interaction properties of the system can be tuned over a wide range by exploiting magnetic Feshbach resonances [40, 94, 95]. The latter occur when the state of two free and colliding atoms becomes resonant with a molecular bound state. By applying and fine-tuning an external magnetic field the energies of these two states can be shifted, resulting in a variation of the s-wave scattering length in accordance to $a(B) = a_{\mathrm{bg}}[1 - \Delta/(B - B_0)]$. Here, a_{bg} is the background scattering length away from the resonance, while Δ and B_0 are the width and the position of the resonance, respectively.

The interplay between the possibility of modifying in a simple and real-time way their physical parameters and the high degree of isolation from the environment make cold atomic gases an ideal playground to experimentally investigate the out-of-equilibrium dynamics of isolated quantum systems [40, 43]. Furthermore, their low density and extremely low temperature result in very long dynamical time scales, allowing for a real-time monitoring of the quantum non-equilibrium evolution [37, 39, 96].

1.4 EQUILIBRATION IN INTEGRABLE QUANTUM SYSTEMS

In Sec. 1.2 we have seen that, if ETH holds, the only information of the initial state that survives the thermalization process is the energy. It is thus interesting to ask how previous discussions get modified if other conserved quantities are present and, in particular, if a steady state can be reached anyhow. This happens, for example, in integrable quantum systems, which will constitute the main topic of this Thesis. The concept of quantum integrability is a quite subtle one. A rigorous definition relies on the absence of diffraction in scattering between elementary excitations of the system [52, 97] and its relationship with the presence of conserved quantities, as in classical systems, is still unclear. Nevertheless, for the the purposes of this Thesis, in the following we can safely assume that an integrable quantum model is defined as a system which possesses an *extensive* number of *local* conserved quantities $\{\hat{I}_\alpha\}$ satisfying the conditions

$$\left[\hat{H}(h), \hat{I}_\alpha\right] = 0 \quad \forall \alpha \quad \text{and} \quad \left[\hat{I}_\alpha, \hat{I}_\beta\right] = 0 \quad \forall \alpha, \beta. \tag{1.17}$$

By analogy with their classical counterparts, after being perturbed far from equilibrium, one expects these systems to show a dramatically different behavior from generic non-integrable ones with respect to the equilibration issue, since they will hardly relax to a thermal-like state. This is due to the fact that they retain a strong memory of the initial state, encoded in the set of integrals of motion $\{\hat{I}_\alpha\}$, which strongly constrain the subsequent non-equilibrium dynamics of the system. A common question that maybe has come to the reader's mind at this point is: Why should the conserved quantities $\hat{I}_\alpha$ be local? The answer to this question is rather simple: Any Hamiltonian possesses at least the same number of conserved quantities as the dimension of the Hilbert space spanned by its eigenstates $\{|n\rangle\}$. Indeed, all the one-dimensional projectors over the latter, namely $\hat{P}_n = |n\rangle\langle n|$ (assuming, for the sake of simplicity, no degeneracies), satisfy the relations $[\hat{H}, \hat{P}_n] = [\hat{P}_n, \hat{P}_m] = 0$ and are thus conserved quantities in the sense of Eq. (1.17) but they are by no means local. Since these highly non-local conservation laws exist for any Hamiltonian, one expects that they do not play an important role in the behavior of the system. On the other hand, local integrals of motion are peculiar to specific systems and, as we will see in the quantum Newton's cradle experiment described in Sec. 1.4.1, deeply affect their quantum dynamics.

In our days integrable systems are far from being an academic idealization: Cold atomic setups offer the possibility to simulate with a high degree of fidelity integrable models on long and experimentally accessible time scales, with only very small integrability-breaking perturbations. In recent years they allowed to investigate the relation between integrability, many-body dynamics and equilibration. As a prominent example, in the next Section we will describe in some details the pioneering experiment by Kinoshita et al. [39], which paved the way to both experimental and theoretical research in the properties of out-of-equilibrium integrable quantum systems. Furthermore, integrable systems have played a fundamental role in the understanding of quantum non-equilibrium dynamics, essentially due to the fact that analytical results can be derived for the time behavior of many observables.

1.4.1 The quantum Newton's cradle

A decade ago, in a pioneering work about the study of thermalization in a 1D Bose gas, Kinoshita et al. [39] observed for the first time an isolated and interacting many-body system with many degrees of freedom that relaxes towards a non-thermal steady state. They prepared a Bose-Einstein condensate of ^{87}Ru loaded into a 2D optical lattice similar to the one shown Fig. 1.2(a), with the confinement along the tubes provided by a crossed dipole trap. In their setup the lowest transverse excitation energy $\hbar\omega_\perp$ is much larger than any other energy scale involved and, thus, the dynamics of the system is strictly 1D along the longitudinal direction. The strength of inter-particle interactions is described by the parameter $\gamma = mg/\hbar n_{1D}$, with m the mass

of the atoms, $g = 4a\omega_\perp$, a the 3D Bose gas scattering length and n_{1D} the 1D particle density inside each tube. The effective inter-particle strength can thus be tuned over a wide range of values by both acting on n_{1D} and on the confining potential. In particular, both the strongly interacting regime $\gamma \gg 1$, in which 1D bosons interact locally like non-interacting fermions (Tonks-Girardeau limit), and the intermediate coupling regime can be addressed [38, 39].

The non-equilibrium regime, i.e. the quantum quench, is obtained by pulsing an optical phase grating over the system [44]. The latter depletes the zero-momentum mode and put the atomic cloud in a superposition of states with momentum $\pm 2\hbar k_0$, with k_0 the wave-vector of the pulsed light. The energy transferred to each 1D tube is far below the transverse excitation one, $\hbar\omega_\perp$, and thus the dynamics of the system remains purely 1D during all the subsequent evolution. After the pulse each 1D Bose system starts an oscillatory motion with period τ, determined by the strength of the crossed dipole trap, which strongly resembles the one of a classical Newton's cradle. This behavior can be seen from Panel (a) of Fig. 1.3, which shows a time series of time-of-flight images of the system [93, 98]. In this technique the condensate is left to evolve for a variable time t. Then, the crossed dipole trap is turned off so that the system can expand freely. Finally, an absorption or fluorescence measurement of the position of each atom allows the reconstruction of the out-of-equilibrium momentum distribution $f(p)$ of the original confined condensate. Panel (a) of Fig. 1.3 shows the evolution in real-time of the momentum distribution function $f(p)$ of a 1D Bose gas after the quench. The oscillatory motion of the system clearly emerges. Note that, whenever the two clouds with opposite momentum meet, many inter-atomic collisions occurs and, in a classical gas, would be responsible of energy and momentum redistribution leading to thermalization.

The green curves of Panel (b) of Fig. 1.3 represent the time average of the momentum distribution function over the first oscillation period τ of Panel (a) for various interaction strength γ. Interestingly, after $10 - 15$ periods, $f(p)$ stops to change qualitatively and, therefore, reaches a stationary regime. The differences between blue and red curves in Fig. 1.3(b), which show $f(p)$ for different large times, are only due to heating and loss effects. Indeed, by rescaling the curves taking into account the presence of these effects, Kinoshita et al. obtained a good overlap between them in all the cases [39]. Therefore, even after thousands of inter-atomic collisions, $f(p)$ does not approach a Gaussian thermal shape but, on the contrary, it relaxes to a steady non-thermal regime. Note that the larger the interaction the more the momentum distribution differs from a Gaussian profile. Kinoshita et al. ascribed the absence of thermalization of a 1D Bose gas to the fact that its strongly interacting (Tonks-Girardeau) limit is described by an integrable model and its dynamics is thus affected by the presence of an extensive set of conservation laws. In order to verify that these results are due exclusively to integrability, they performed the same experiment in a 3D non-integrable Bose gas, obtained without turning on the 2D optical lattice. As expected,
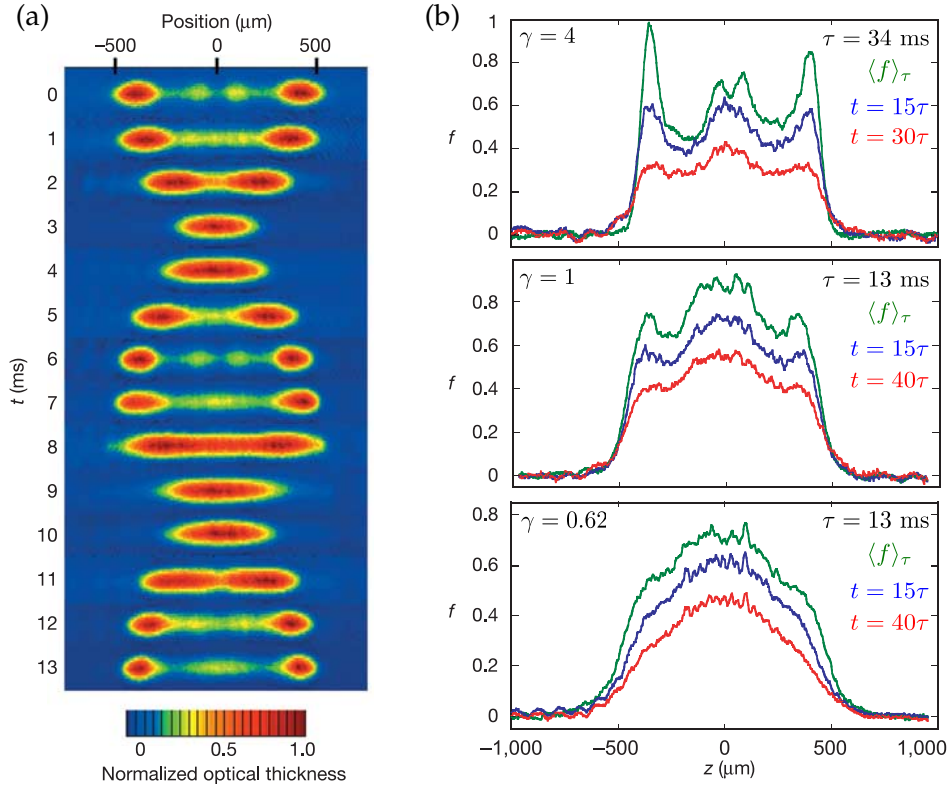
Figure 1.3: In Panel (a) we show the time evolution of the momentum distribution function $f(p)$ of a 1D Bose gas, obtained by a time-of-flight measurement. Note that on the $x-$axis the position of each atoms is proportional to its momentum. Panel (b) displays the averaged momentum distribution functions over the first period, $\langle f \rangle_\tau$ (green), and two snapshots of $f(p)$ for larger times (blue and red) for three different values of the interaction parameter γ: $\gamma = 4$ (top), $\gamma = 1$ (middle), and $\gamma = 0.62$ (bottom). After $10 - 15$ oscillation periods τ, $f(p)$ settles to a stationary regime which, especially for strong inter-particle interactions (top and middle panels), strongly differs from the Gaussian profile expected for a thermalized system. Figure taken from Ref. [39].

they obtained that in the latter system the three-dimensional momentum distribution $f(\boldsymbol{p})$ approaches a more conventional Gaussian profile after a few periods of oscillation.

In their groundbreaking experiment Kinoshita et al. thus demonstrated that weak non-integrabilities, such as anharmonicity of the trap or intermediate inter-particle interactions, are not sufficient to make the system thermalize over a very long time interval, showing that cold atoms allow to successfully investigate the peculiar equilibration properties of quantum integrable systems. Of course, this experiment has triggered a huge amount of theoretical research on the non-equilibrium behavior of integrable quantum models and laid the foundation of all the current understanding of their dynamics.

1.4.2 Local equilibration and the generalized Gibbs ensemble

Summarizing the discussion of Sec. 1.2, we have shown that an isolated quantum system driven far from equilibrium cannot reach a steady state in its entirety. We have then seen that, on the other hand, in a generic non-integrable system if one focuses on physical observables satisfying some assumptions (namely, their energy-eigenstate matrix elements obey Eq. (1.12)) the latter reaches a thermal steady-state value and remain close to it most of the sequent time, i.e. it thermalizes in the strong sense. However, some points still remain rather obscure. For instance, the condition set by Eq. (1.12) is quite abstract and it does not involve any general properties of observable themselves. It is thus difficult to say if a certain observable will thermalize or not without explicitly evaluate its energy-eigenstate matrix elements. One may ask if there exist some general features which ensure thermalization. Starting from this point, we can reasonably assume that, if one focuses on a small and finite portion of the system, the rest of the system itself will play the role of a bath and each finite subsystem relax, in a sense that will be specified in the following, to an equilibrated state. It is then natural to guess that *local* observables, acting on small and finite portion of the system, are promising candidate to exhibit equilibration. In this picture, the emergence of a steady state is the result of nothing but pure quantum coherent dynamics and no external bath is required.

As one of its main successes, research in integrable quantum models has put on solid ground the qualitative arguments outlined in the previous paragraph, showing that indeed equilibration in generic quantum systems, both integrable and non-integrable, occurs *locally* in space and is strictly connected to the way information spread after the system is driven far from equilibrium [55–58, 99]. This has been done for the first time in 2008 in the context of quantum quenches in the Hubbard model from the Mott to the superfluid phases by Cramer et al. [55, 56], which proposed the LRC. Basically, this conjecture states that any quantum systems driven far from equilibrium relaxes to a state which appears locally indistinguishable from a stationary (equilibrated) state. Rigorously, the LRC can be stated in the following way.

First of all, we consider a finite subsystem A of the system itself, denote with B its complement, and focus on its reduced density matrix [18]

$$\hat{\rho}_A(t) = \text{Tr}_B[\hat{\rho}(t)]. \qquad (1.18)$$

We say that the system *locally equilibrates* if, in the thermodynamic limit, the following limit exists

$$\lim_{t \to \infty} \lim_{L \to \infty} \hat{\rho}_A(t) = \hat{\rho}_A(\infty) \qquad (1.19)$$

for any finite subsystem A. Then, if the system locally equilibrates, we can define the steady state towards which the system relaxes as the one associated with the global time-independent density matrix $\hat{\rho}^{\text{ss}}$ satisfying the identity

$$\lim_{L \to \infty} \text{Tr}_B[\hat{\rho}^{\text{ss}}] = \hat{\rho}_A(\infty) \qquad (1.20)$$

for any finite subsystem A[4]. Note that, if a system relaxes in the sense specified above, all its local observables equilibrate in the strong sense of Eq. (1.8), with $\langle \hat{O} \rangle_{\text{D}}$ substituted with $\text{Tr}[\hat{O}\hat{\rho}^{\text{ss}}]$, and no time-averaging procedure is required. At this point, it is convenient to introduce the following definition: Two density matrices $\hat{\rho}_1$ and $\hat{\rho}_2$ – and the two statistical ensembles they potentially describe – are said to be *locally equivalent*, in symbols

$$\hat{\rho}_1 \overset{\text{loc}}{=} \hat{\rho}_2, \qquad (1.22)$$

if

$$\lim_{|B| \to \infty} \text{Tr}_B[\hat{\rho}_1] = \lim_{|B| \to \infty} \text{Tr}_B[\hat{\rho}_2], \qquad (1.23)$$

for any finite subsystem A, being $|B|$ the volume of its complement B.

Importantly, Cramer et al. [55] demonstrated that the steady state to which their quenched Bose-Hubbard model relaxes after the quench is characterized by having the maximum thermodynamic entropy $S = k_B \text{Tr}[\hat{\rho} \ln(1/\hat{\rho})]$ compatible with the constraints imposed by the conservation laws of the system. Shortly after, the LRC has been extended to systems initially prepared in gaussian [57] and non-gaussian [58] states with the post-quench evolution governed by quadratic Hamiltonians. It is very important to point out that, although the LRC states that the system looks locally equilibrated, due to the unitary quantum dynamics, the full memory of the initial state is conserved in the entire system at any time.

The framework set by the LRC is extremely general and describes both systems which thermalize and systems which, on the contrary, relax to non-thermal steady states as integrable models. We now analyze implications of

---

4 The above statement can also easily be translated to the finite-size systems, in analogy with the definitions of equilibration/thermalization of observables we gave in previous Sections. In particular, we say that a system locally equilibrates to the steady state described by $\hat{\rho}^{\text{ss}}$ if, for any $\varepsilon > 0$, there exists a system linear size L, a relaxation time t_{rel}, and a recurrence time t_{rec} such that the following relation holds for *almost* all times $t_{\text{rel}} < t < t_{\text{rec}}$

$$\|\hat{\rho}_A(t) - \hat{\rho}_A^{\text{ss}}\|_{\text{tr}} < \varepsilon, \qquad (1.21)$$

with $\hat{\rho}_A^{\text{ss}} = \text{Tr}_B[\hat{\rho}^{\text{ss}}]$, for any finite subsystem A. Here, $\|M\|_{\text{tr}} = \sum_i \sigma_i(M)$ denotes the trace norm of the matrix M, with $\sigma_i(M)$ its eigenvalues.

this conjecture in the typical quantum quench protocol described in Sec. 1.2. We start from the general case in which energy is the only conserved quantity of the system. According to the LRC and since in this case the state which maximizes the entropy is a thermal one, the system relaxes to a locally thermal state:

$$\hat{\rho}^{ss} \stackrel{\text{loc}}{=} \hat{\rho}_{mc} \stackrel{\text{loc}}{=} \hat{\rho}_{c}, \qquad (1.24)$$

where the microcanonical density matrix $\hat{\rho}_{mc}$ is defined in Eq. (1.5) and $\hat{\rho}_{c} = Z_{c}^{-1} e^{-\beta_{eff}\hat{H}(h)}$ is the canonical one. Here, $Z_{c} = \text{Tr}\left[e^{-\beta_{eff}\hat{H}(h)}\right]$ and the effective inverse temperature β_{eff} is fixed by $\text{Tr}[e^{-\beta_{eff}\hat{H}(h)}\hat{H}(h)] = E_0$. Thus, the LRC leads to the same results of the ETH[5].

On the other hand, the conjecture gives precise indications to understand what happens if additional local conservation laws are present. Of particular interest in this sense is the case of integrable quantum systems introduced in Eq. (1.17) which, due to the presence of an extensive set of integrals of motion $\{\hat{I}_\alpha\}$ constraining their dynamics, will generally never thermalize. Nevertheless, the LRC suggests that also these systems locally relax to a stationary state $\hat{\rho}^{ss}$, characterized by the maximum entropy compatible with the conservation of $\{\hat{I}_\alpha\}$. This is in complete agreement with what Rigol et al. found in 2007 studying the quench of a hard-core boson gas [54]. Here, generalizing the information theory approach to Statistical Mechanics developed by Jaynes [100, 101] and looking for a steady state which maximizes the entropy, they conjectured that the density matrix describing the asymptotic state of the system is locally equivalent to the one obtained within the GGE [47, 53, 54],

$$\hat{\rho}^{ss} \stackrel{\text{loc}}{=} \hat{\rho}_{GGE} = \frac{1}{Z_{GGE}} e^{-\sum_\alpha \lambda_\alpha \hat{I}_\alpha}, \qquad (1.25)$$

where $Z_{GGE} = \text{Tr}\left[e^{-\sum_\alpha \lambda_\alpha \hat{I}_\alpha}\right]$ and the Lagrange multipliers λ_α, which contain the information about the initial state $|\Psi_0\rangle$, are fixed by the requirement

$$\langle\Psi_0|\hat{I}_\alpha|\Psi_0\rangle = \text{Tr}[\hat{I}_\alpha\hat{\rho}_{GGE}] = \frac{1}{e^{\lambda_\alpha} \pm 1}, \qquad \forall \alpha, \qquad (1.26)$$

with $+$ $(-)$ for fermionic (bosonic) systems. Note that $\hat{\rho}_{GGE}$ looks very similar to a standard thermodynamic density matrix in which, however, one has taken into account the presence of all conserved quantities $\hat{I}_\alpha$.

The GGE approach has been theoretically verified in many 1D integrable quantum systems: from continuum models (e.g., Luttinger liquids [15, 33, 102] and the sine-Gordon model [15, 103]) to lattice ones (such as the Hubbard model [55, 104] and transverse quantum Ising chain [18, 105–107]). In addition, Barthel and Schollwöck [57] rigorously proved that systems described by quadratic bosonic or fermionic Hamiltonians and prepared in Gaussian states locally relax to a GGE, in which the proper integrals of motion to be considered in Eq. (1.25) are the occupation numbers $\hat{I}_\alpha = \hat{\eta}_\alpha^\dagger \hat{\eta}_\alpha$ of the eigenstates of the final Hamiltonian $\hat{H}(h) = \sum_\alpha \varepsilon_\alpha \hat{\eta}_\alpha^\dagger \hat{\eta}_\alpha$. Here, $\hat{\eta}_\alpha^\dagger$ are

---

5 Note that actually ETH is a bit more powerful than the LRC. Indeed for local observables the ETH always holds, but the opposite is not true [16, 47]. However, this shortcoming is largely compensated by the generality of the LRC.

bosonic or fermionic operators which diagonalize $\hat{H}(h)$ and ε_α the associated single-particle energies. As one immediately realizes, however, this latter statement seems to be in contradiction with the requirement of locality for the set of quantities $\{\hat{I}_\alpha\}$. Indeed, the eigenstate occupation numbers $\hat{\eta}_\alpha^\dagger \hat{\eta}_\alpha$ are not local at all.

Moreover, in order for the GGE to be considered as a legitimate thermodynamic ensemble, it must ensure the statistical independence of macroscopic subsystems. This would be the case if the conserved quantities $\{\hat{I}_\alpha\}$, which as noted before appear in Eq. (1.25) in the traditional thermodynamic form $e^{-\lambda_\alpha \hat{I}_\alpha}$, were extensive (like, for example, the Hamiltonian and particle-number operators in usual thermodynamic ensembles). The key point to solve both these issues at once is that it is always possible to construct new local and extensive conserved quantities $\{\hat{\mathcal{I}}_\beta\}$ by a *linear* transformation of the original set $\{\hat{I}_\alpha\}$, $\hat{\mathcal{I}}_\beta = \sum_\alpha L_{\beta\alpha} \hat{I}_\alpha$. Therefore, $\hat{\rho}_{\text{GGE}}$ can be expressed equivalently by means of both sets of conserved quantities:

$$\hat{\rho}_{\text{GGE}} = \frac{1}{Z_{\text{GGE}}} e^{-\sum_\alpha \lambda_\alpha \hat{I}_\alpha} = \frac{1}{\mathcal{Z}_{\text{GGE}}} e^{-\sum_\beta \mu_\beta \hat{\mathcal{I}}_\beta}, \tag{1.27}$$

with $\mathcal{Z}_{\text{GGE}} = \text{Tr}\left[e^{-\sum_\beta \mu_\beta \hat{\mathcal{I}}_\beta}\right]$. Finally, to complete the raise of the GGE to a true ensemble, we also note that with the above discussion we have demonstrated that the GGE also fulfills the thermodynamic requirement of "describing a system by means of few macroscopic parameters" [5, 47]. Indeed, the diagonal ensemble density matrix defined in Eq. (1.6) contains an *exponentially* large (in system size) number of parameters, namely the coefficients c_n of the projections of the initial state $|\Psi_0\rangle$ on the final Hamiltonian eigenstates $\{|n\rangle\}$. On the other hand, the GGE requires the knowledge of an *algebraically* large (in system size) number of parameters, i.e. the Lagrange multipliers λ_α (or, equivalently, μ_β). Therefore, the GGE approach makes use of an exponentially smaller amount of "information" about the system than the diagonal ensemble one and thus, in the language of Thermodynamics, it describes macrostates of the system [47, 99].

1.4.3 Relaxation dynamics and the light–cone effect

So far our attention has been devoted to understand if and in what sense an isolated quantum system driven far from equilibrium can relax to a steady state. However, our previous discussions have completely left out to say how this possible state is approached. This issue is far more complicated than the characterization of the steady state itself since, in general, strongly depends on details of the model. Nevertheless, the studies of quantum quenches in integrable systems have contributed to reveal some general feature of the relaxation dynamics towards a steady state. The key concept, first introduced by Calabrese and Cardy in 2006 [32, 60], is the so called *light-cone effect*. In their work, Calabrese and Cardy studied how correlation functions of a generic quantum system evolve after a quench towards a critical Hamiltonian, focusing in particular on a 1D system with a linear dispersion relation,

$\omega(k) = v|k|$. In simple terms, their main result can be stated in the following way. Let us consider a quenched 1D model and look at a generic two-point connected correlation function of a local observable $\hat{\mathcal{O}}(r)$ evaluated at time t in two different positions, r_1 and r_2,

$$C_{\hat{\mathcal{O}}}(r_1, r_2; t) = \langle \Psi(t)|\hat{\mathcal{O}}(r_1)\hat{\mathcal{O}}(r_2)|\Psi(t)\rangle$$
$$- \langle \Psi(t)|\hat{\mathcal{O}}(r_1)|\Psi(t)\rangle\langle \Psi(t)|\hat{\mathcal{O}}(r_2)|\Psi(t)\rangle. \qquad (1.28)$$

Here, $|\Psi(t)\rangle = e^{-i\hat{H}(h)t}|\Psi_0\rangle$ is the time-evolved initial state $|\Psi_0\rangle$. After the quench (i.e. for $t > 0$) the behavior of $C_{\hat{\mathcal{O}}}(r_1, r_2; t)$ can always be qualitatively described by

$$C_{\hat{\mathcal{O}}}(r_1, r_2; t) \sim \begin{cases} f_{\hat{\mathcal{O}}}(t)C_{\hat{\mathcal{O}}}(r_1, r_2; t = 0) & \text{for } t \lesssim \frac{|r_1 - r_2|}{2v_{\max}}, \\ C_{\hat{\mathcal{O}}}^{\text{ss}}(r_1, r_2) & \text{for } t \gtrsim \frac{|r_1 - r_2|}{2v_{\max}}, \end{cases} \qquad (1.29)$$

with $C_{\hat{\mathcal{O}}}(r_1, r_2; t = 0)$ the value of the two-point correlation function before the quench, $f_{\hat{\mathcal{O}}}(t)$ a smooth monotonic function of time and $C_{\hat{\mathcal{O}}}^{\text{ss}}(r_1, r_2)$ the post-quench steady-state correlation function, depending on both the model and the quench protocol [32, 33]. Here, $v_{\max}$ is the maximum velocity of elementary excitations of the post-quench Hamiltonian $\hat{H}(h)$,

$$v_{\max} = \max_{\{k\}} \frac{d\omega(k)}{dk}. \qquad (1.30)$$

From Eq. (1.29) it follows that all significant changes in $C_{\hat{\mathcal{O}}}(r_1, r_2; t)$ occur in a neighborhood of $t^* = |r_1 - r_2|/(2v)$. Calabrese and Cardy developed an intuitive and physical picture, illustrated in Fig. 1.4, to explain this behavior in terms of the propagation of entangled quasi-particles, which holds also for systems with a more general dispersion relation $\omega(k)$. In particular, since the state $|\Psi_0\rangle$ is a highly excited state with respect to the post-quench Hamiltonian $\hat{H}(h)$, the quench performed at $t = 0$ generates in each point of space an extensive amount of quasi-particle excitations which start to propagate through the system in all possible directions (right or left in the 1D we are considering). Quasi-particles which originate from the same point are entangled and "encode" the information about the quench[6]. Within this picture, if at time $t > 0$ no entangled pairs of counter-propagating quasi-particles have reached *both* r_1 and r_2, the two-point correlation function $C_{\hat{\mathcal{O}}}(r_1, r_2; t)$ would not deviate significantly from its initial value. In particular, the first couple of entangled excitations simultaneously arrives at the points r_1 and r_2 at the time

$$t^* = \frac{|r_1 - r_2|}{2v_{\max}} \qquad (1.31)$$

and begin to induce quantum correlations between the two points. This results in a dramatic variation of $C_{\hat{\mathcal{O}}}(r_1, r_2; t)$. For the simple case of a linear dispersion relation considered in Eq. (1.29), one gets $d\omega(k)/(dk) = v, \forall k$, i.e.

---

6 Note that, if the initial state has a finite correlation length χ, this statement holds for all quasi-particles created within χ [32].
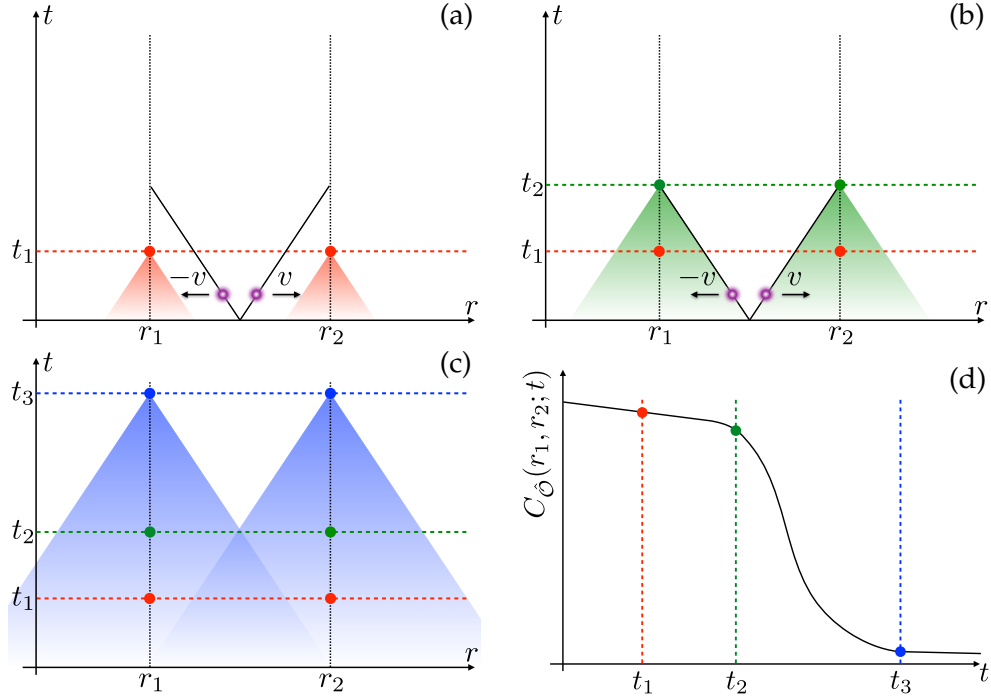
Figure 1.4: Light-cone dynamics of a two-point correlation function $C_{\hat{\mathcal{O}}}(r_1, r_2; t)$ of a generic local observable $\hat{\mathcal{O}}(r)$ after a quantum quench. At the instant of the quench, $t = 0$, quasi-particle excitations are generated from every point of the system and start propagating with maximum group velocity $v_{\max} = v$ in opposite directions. (a) At time $t = t_1$, only quasi-particles generated inside the red cones have reached the points r_1 and r_2: The behavior of $C_{\hat{\mathcal{O}}}(r_1, r_2; t)$ looks very similar to the pre-quench one [red dotted line in Panel (d)]. (b) At time $t = t_2 = t^*$, the first pair of quasi-particle excitations have traveled the distance $|r_1 - r_2|$: The correlation function begins to feel the quench and this results in a rapid variation of its value [green dotted line in Panel (d)]. (c) The transient regime, in which $C_{\hat{\mathcal{O}}}(r_1, r_2; t)$ continues to change, lasts approximately until $t = t_3 = |r_1 - r_2|/v$, when all the quasi-particles generated inside the interval $[r_1, r_2]$ has left this region. For $t > t_3$, $C_{\hat{\mathcal{O}}}(r_1, r_2; t)$ settles to its final steady state value [blu dot in Panel (d)].
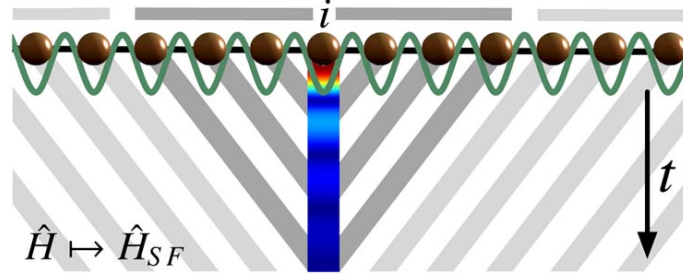
Figure 1.5: Schematic picture of the relaxation process in a quenched Bose-Hubbard model according to the LRC. At a given time t, the lattice site i is only affected by the information transfered from the neighbor lattice sites which are contained inside the gray light cones, while contributions due to sites outside the latter are exponentially suppressed. The incommensurate influence of information coming from different sites leads to the relaxation to the maximum entropy state in the long-time limit. Figure taken from Ref. [55]

all quasi-particle excitations move with the same velocity. When all quasi-particles generated in the region between r_1 and r_2 have moved outside this region, that is for $t > |r_1 - r_2|/v$, $C_{\hat{\mathcal{O}}}(r_1, r_2; t)$ quickly approaches its final stationary value. Note that in the case of a general dispersion relation $\omega(k)$, where lots of excitations move slower than $v_{\max}$, this relaxation process can be quite slow, especially if there exist some values of k' such that $\omega(k') \to 0$.

The propagation of entangled quasi-particles has a huge impact also on the one-point local observables $\langle \hat{\mathcal{O}}(r) \rangle$ we considered in previous Sections and, indeed, lies at the basis of the LRC. Here, as shown in Fig. 1.5, local relaxation is basically due to the cumulative effects of the incoherent passage of excitations at the point r, which leads to an averaging process resulting in the local equilibration of the neighborhood of r (and, therefore, of the average of a local observable $\langle \hat{\mathcal{O}}(r) \rangle$) to the maximum entropy ensemble [32, 55, 56, 58] [see also Sec. 1.4.2].

LIEB–ROBINSON BOUND The light-cone build-up of correlations through a quantum system after a quench is strictly connected with the so called Lieb-Robinson bound [18, 108, 109], which implements in non-relativistic quantum systems the principle of causality by setting a bound on the velocity of propagation of information in quantum models with short range interactions. In particular, Lieb and Robinson showed that the following causal structure in the commutator between two local operators evaluated at different times is satisfied

$$\| \left[\hat{\mathcal{O}}_A(t), \hat{\mathcal{O}}_B(0) \right] \| \leq c \min(|A|, |B|) \| \hat{\mathcal{O}}_A \| \| \hat{\mathcal{O}}_B \| e^{-\frac{L-vt}{\xi}}. \tag{1.32}$$

Here, $\hat{\mathcal{O}}_A$ and $\hat{\mathcal{O}}_B$ are local operators acting on two finite subsystems A and B, the latter being separated by a distance L. Here, $\| \cdot \|$ denotes the trace norm of an operator introduced in footnote 4, $|A|$ is the volume of subsystem A, and c, v, and ξ are constants. Bravyi et al. demonstrated that Eq. (1.32) has important consequences in the time-evolution of correlation functions

after a quantum quench in systems initially prepared in a state $|\psi_0\rangle$ with finite correlation length χ [110]. It is indeed possible to show that

$$\langle\Psi_0|\hat{\mathcal{O}}_A(t)\hat{\mathcal{O}}_B|\Psi_0\rangle - \langle\Psi_0|\hat{\mathcal{O}}_A(t)|\Psi_0\rangle\langle\Psi_0|\hat{\mathcal{O}}_B(t)|\Psi_0\rangle \leq \bar{c}(|A| + |B|)e^{-\frac{L-2vt}{\chi+2\xi}}$$

(1.33)

Physically, this means that if subsystems A and B are initially uncorrelated, their correlation remains exponentially small up to times $t > L/2v$ and, thus, behave exactly as depicted in Fig. 1.4.

1.4.4 Experimental observation of the GGE and LC dynamics

After being numerically tested in a variety of different systems [47, 54], local relaxation towards the GGE has recently been seen experimentally by the Schmiedmayer's group in Vienna [40, 41, 43]. The experimental setup they used consists of a single 1D Bose gas realized with a magnetic trap on an atom chip [91]. As shown in Fig. 1.6(a), the application of an external radiofrequency electromagnetic field allows to suddenly turn the transverse harmonic trapping potential into a double-well one [111]. This procedure splits the gas in two independent 1D condensates and, at the same time, injects energy inside the system, thus realizing a true quantum quench. Each of the two gases can be described in terms of density fluctuations $\delta\rho_i(z)$ around their mean density n_{1D}, with $i = \{1,2\}$ and z the axial coordinate, and of fluctuating phases $\theta_i(z)$; see Fig. 1.6(a).

After the quench, the setup is allowed to evolve coherently for a certain time t. Then, all the trapping potentials are turned off and the gas begins to expand freely. The relative local phase difference $\varphi(z;t) = \theta_1(z;t) - \theta_2(z;t)$ is extracted from a matter-wave interference pattern, measured by an absorption imaging technique [113, 114]. A typical result is shown in Fig. 1.6(b). This allows to immediately evaluate from experimental data the time-dependent $N-$point phase correlation function,

$$C(z_1, z_2, ..., z_N; t) \sim \langle\Psi_1(z_1;t)\Psi_2^\dagger(z_1;t)\Psi_1^\dagger(z_2;t)\Psi_2(z_2;t)...\Psi_1^\dagger(z_N;t)\Psi_2(z_N;t)\rangle$$
$$\sim \langle e^{i\varphi(z_1;t)-i\varphi(z_2;t)+...-i\varphi(z_N;t)}\rangle,$$

(1.34)

where $\Psi_i(z)$, with $i \in \{1,2\}$, denotes the bosonic field operator acting on the $i-$th split condensate and the brackets denotes the quantum average over the initial state.

In Refs. [41] and [42] Langen et al. focused in particular on the behavior of the 2-point phase correlation function, $C(z_1, z_2; t)$, whose behavior in time is shown in Fig. 1.7. Immediately after the splitting of the system one finds $C(z_1, z_2; 0) \approx 1$ for any z_1, z_2. This signals the long-range phase coherence created by the splitting procedure. For $t > 0$ the two regimes of correlations build-up introduced in Eq. (1.29) can be clearly observed. Indeed, for relative distances $\bar{z} = z_1 - z_2$ such that $\bar{z} < \bar{z}_c = 2vt$, with v is the speed of phononic excitations in the system, the correlation function $C(z_1, z_2; t)$ features the exponential decay associated with the equilibrated regime [green curve in Fig. 1.7(a)] and stops changing significantly. On the other hand, for distances
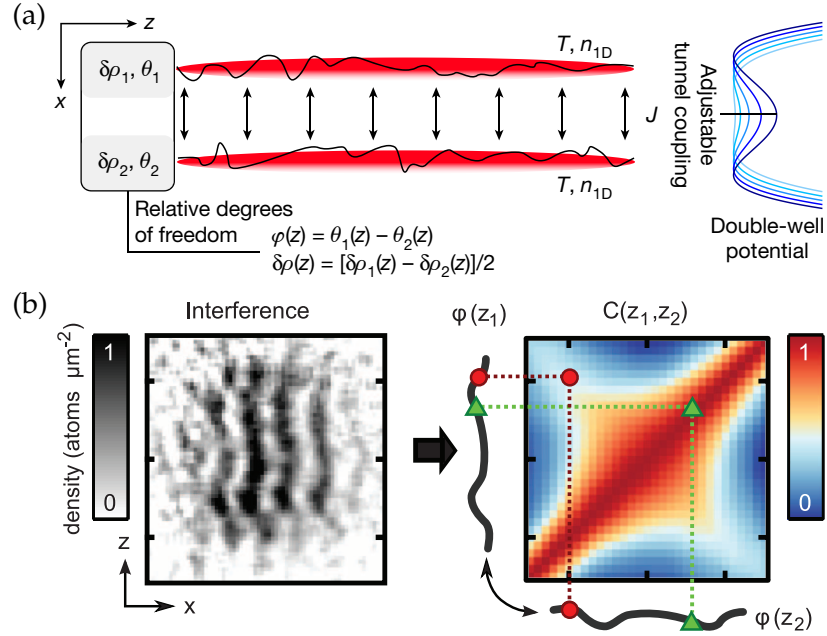
Figure 1.6: In Panel (a) is shown a sketch of the experimental setup used in Ref. [41]. The initial harmonic confining potential can be deformed in a double-well potential by the application of an external field. The system is then split in two 1D gases, which can be described in terms of density fluctuations $\delta\rho_i$ and phase θ_i (with $i \in \{1,2\}$). For small value of tunneling parameter J the two systems evolve independently from each other. After a time interval t the trapping potential is released and a matter-wave interference pattern between the two gases is measured by an absorption imaging technique [Panel (b), left]. The relative phase $\phi(z) = \theta_1 - \theta_2$ can then be extracted from the interference pattern and directly employed for evaluating the 2−point correlation function $C(z_1, z_2)$ [Panel (b), right]. Green triangles corresponds to a diagonal contribution of the correlation function, i.e. with $z_1 = z_2$, while red circles indicate an anti-diagonal one, i.e. with $z_1 = -z_2$. The latter contribution is strongly suppressed in thermal equilibrium and a large value signals an out-of-equilibrium regime. Figures taken from Refs. [112] [Panel (a)] and [41] [Panel (b)].
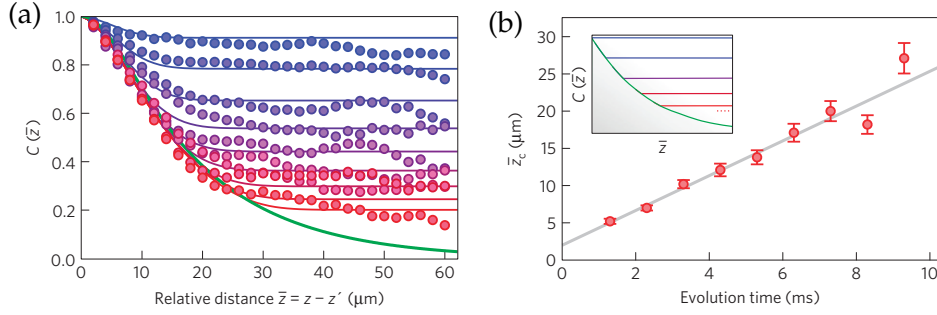
Figure 1.7: Time evolution of the phase correlation function $C(z_1, z_2; t)$. In Panel (a) different snapshots of $C(z_1, z_2; t)$ as a function of the relative distance $\bar{z} = z_1 - z_2$ are shown, with t increasing from 1 ms to 9 ms in steps of 1 ms from top to bottom. Filled circles correspond to experimental data, while solid lines are obtained by a theoretical Luttinger liquid model. See Ref. [42] for details. The green solid line corresponds to the asymptotic prediction for $C(z_1, z_2; t)$, $C^{SS}(z_1, z_2)$. The light-cone spreading of correlations is clearly visible: For any $t > 0$, $C(z_1, z_2; t)$ is very close to its asymptotic value in the region $\bar{z} < \bar{z}_c = 2ct$, while it remains qualitative similar to pre-quench correlation function on larger relative distances. The velocity of phononic excitations v is determined by a fit of the cross-over distance $\bar{z}_c$ as a function of time, as shown in Panel (b). The latter parameter is extracted from the intersection between $C(z_1, z_2; t)$ and its theoretical asymptotic profile, as schematically shown in the inset of Panel (b). Figures taken from Ref. [42].

$\bar{z} > \bar{z}_c$, $C(z_1, z_2; t)$ remains nearly constant over the whole system, which thus retains the initial long-range phase coherence on large distances. The smooth and monotonic decrease in time observed can be explained in terms of the function $f_{\hat{O}}(t)$ introduced in Eq. (1.29). The "Vienna experiment" is therefore a beautiful demonstrations of the local emergence of equilibration, induced by light-cone-like spreading of correlations through the system, and thus confirms the LRC. A very similar behavior have also been observed by Cheneau et al. in the context of quantum quenches in the Bose-Hubbard model [115].

We can now turn our attention to the asymptotic behavior of $C(z_1, z_2; t)$, denoted by $C^{SS}(z_1, z_2)$, looking for an experimental confirmation of the GGE conjecture [41]. Indeed, the two 1D gases obtained after the quench in the setup discussed so far are a very close realization of the Lieb-Lininger model [89, 116], one of the most well-known integrable systems, and they behave as if they were completely integrable over a very long time scale [39, 42, 87]. Deviations from thermalization are therefore expected. Unfortunately, the sudden splitting protocol employed in the experiment just described results in an equipartition of the injected energy among all the conserved quasi-particle modes associated with the degrees of freedom of the systems, with $\varepsilon_{\text{split}} = k_B T_{\text{eff}}$ and T_{eff} an effective temperature. This implies that the state corresponding to $C^{SS}(z_1, z_2)$ shown in Fig. 1.7(a) is indistinguishable from a thermal one and the emergence of the GGE can not thus be captured. This issue has been resolved by Langen et al. by varying the speed of the

quench protocol. In this way it has been possible to create an imbalance in the occupations of different quasi-particle modes [41], which results in a relaxation of the system towards a non-thermal steady state. This can be seen in Fig. 1.8 from the presence of higher values of correlation outside the region $z_1 = z_2$ and, in particular, along the anti-diagonal $z_1 = -z_2$. As said above, this is a hallmark of an out-of-equilibrium regime. Langen et al. found an excellent agreement between their experimental data and a GGE calculation in which at least ten lowest-energy occupation numbers of the quasi-particle modes of the system degrees of freedom have been considered. Their values have been obtained by fitting the occupation numbers of the steady state two-point correlation function $C^{SS}(z_1, z_2)$. As can be seen from the bottom row plot in Fig. 1.8, the local χ^2 of the fitting procedure is indeed very small, thus confirming the goodness of the GGE approach. Moreover, the occupation numbers obtained by the fitting procedure allows also for an accurate description of the dynamics of the system [41].

Since the GGE is expected to reproduce well the behavior of local quantities only, Langen et al. looked for possible deviations by measuring higher-order (and, then, lesser local) correlation functions. However, also for this quantities they found an excellent agreement between the experimental data and the theoretical model based on the GGE, with the same Lagrange multipliers obtained from the fit on $C^{SS}(z_1, z_2)$. Results for some cuts of $4-$, $6-$ and $10-$point correlation functions are shown in Panel (b) of Fig. 1.8.

1.4.5 Pre-thermalization in nearly-integrable systems

We conclude this introductory Chapter by a final remark on the experimental relevance of integral quantum models. Indeed, non-integrable perturbations, however small, always exist in real systems. One therefore should expect that every experimental setup driven out of equilibrium will eventually relax to a thermal state at some point. However, if the non-integrability perturbation is sufficiently small, it is natural to suppose that initially the relaxation process is essentially governed by the integrable contribution of the Hamiltonian of the system, which leads the latter towards an approximate stationary state described by the GGE. Non-integrability enters in the dynamics only at a larger time scale and finally makes the system relax to a true thermal state. The intermediate quasi-stationary state reached after the first step of the relaxation process is now known as *pre-thermalization* regime and it has been introduced for the first time by Berges et al. in the field of cosmology [8]. In general, the relaxation of a quantum system prepared in an out-of-equilibrium state involves three different processes, each of which with its characteristic time-scale [8, 43, 117]:

1. *kinetic pre-thermalization* represents the first stage of relaxation and is caused by the fast dephasing between the post-quench Hamiltonian eigenmodes;
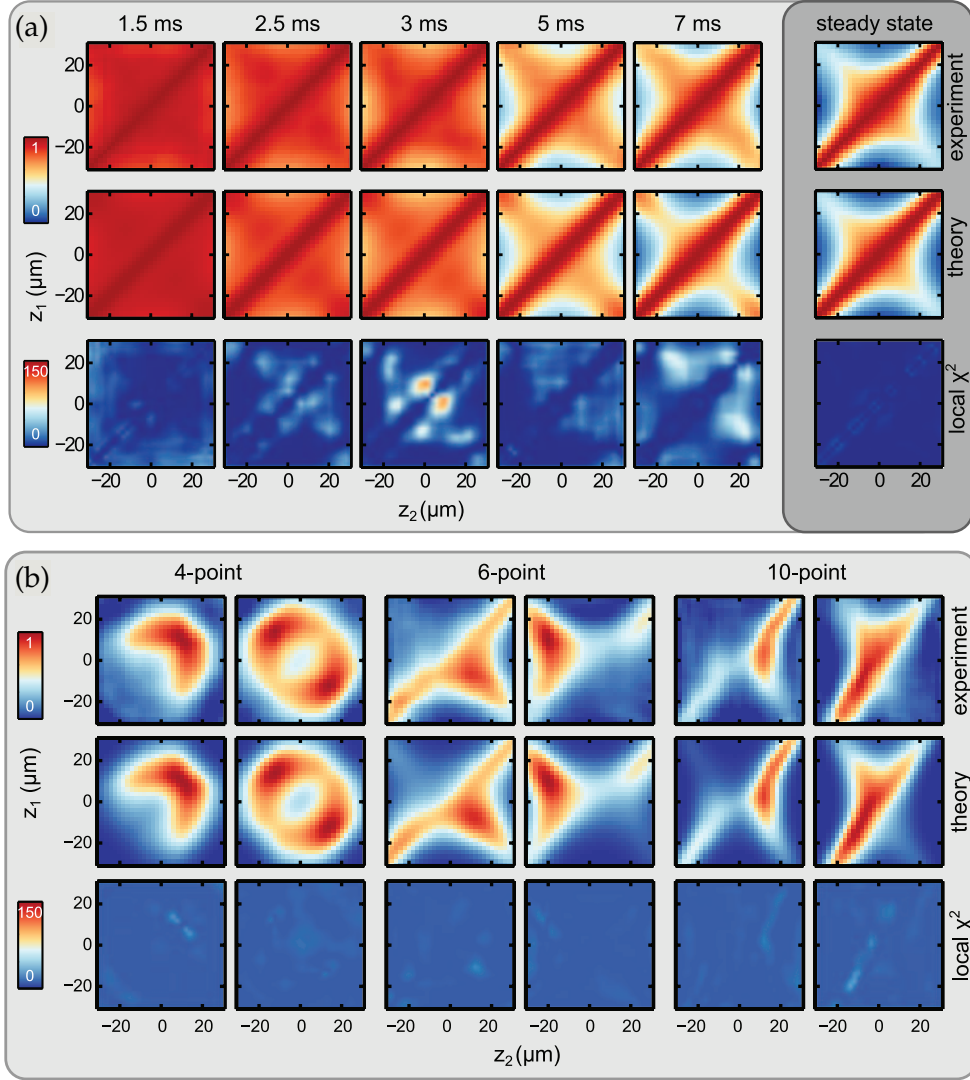
Figure 1.8: Comparison between experimental measured $N-$point phase correlation functions and theoretical predictions obtained within a GGE approach in which the first ten lowest-energy occupation numbers have been considered and fitted. In Panel (a) the two-point correlation function $C(z_1, z_2; t)$ is shown. The agreement between the asymptotic data and the theoretical model is almost perfect (last column). Note that the occupation numbers obtained by the fitting procedure in the steady state regime allows also for an accurate description of the system dynamics. In Panel (b) some cuts of asymptotic 4-, 6- and 10-point correlation function are reported. From left to right $C^{SS}(z_1, 10, z_2, 10)$, $C^{SS}(z_1, -12, z_2, 14)$, $C^{SS}(z_1, 10, 10, z_2, -20, 10)$, $C^{SS}(z_1, -8, 8, z_2, -24, -20)$, $C^{SS}(z_1, 4, 10, z_2, -8, z_2, -22, -18, 10, -4)$, and $C^{SS}(z_1, -22, -8, z_2, -22, -26, -22, z_2, -26, -24)$. The GGE predictions are evaluated with the same occupation numbers obtained in the fitting procedure on the $2-$point correlation function. The excellent agreement between experimental and theoretical results also for more complex correlation functions confirms the validity of the GGE approach. Figures taken from Ref. [41].
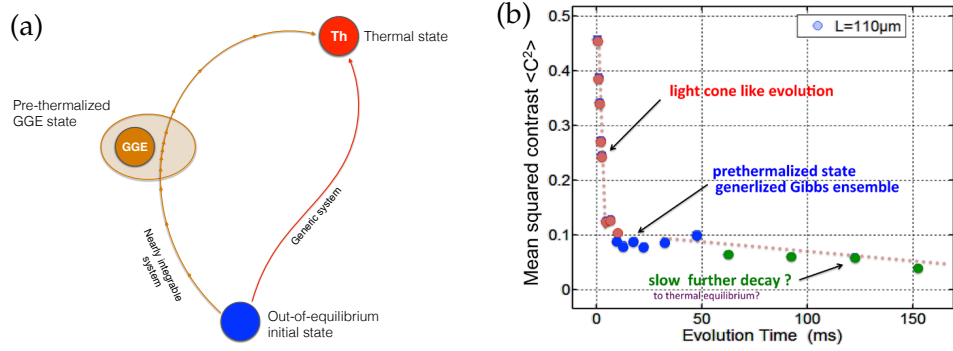
Figure 1.9: In Panel (a) we show two possible scenarios for the relaxation of a quantum system initially prepared in an out-of-equilibrium state, according to the three different steps described in the text. For a generic quantum system, the time scales associated with the various processes are comparable and a direct relaxation towards a thermal state is observed. On the contrary, in a nearly-integrable quantum systems the characteristic time scales differ by orders of magnitude and after the quantum dephasing the system reaches a metastable pre-thermalized state described by the GGE. Relaxation to a thermal state comes into play only at larger times, thus allowing to experimentally access and probe the pre-thermal GGE state. An example of this behavior is shown in Panel (b), in which we display the time evolution of the integrated mean squared contrast $\langle \mathscr{C}^2 \rangle$ of the interference pattern of the setup described in Fig. 1.6. After a fast relaxation, $\langle \mathscr{C}^2 \rangle$ approaches a pre-thermalized GGE state, with the true thermalization process setting in only on larger times. Figure in Panel (b) is taken from Ref. [43]

2. at larger times inter-particle interactions leads to a *loss of the memory of initial conditions* and different initial state with the same energy and number of particles features the same transient behavior;

3. at even larger times true *thermalization* sets in and the system relax to a thermal state.

While the first step is induced by pure quantum effects and it is not affected by possible dynamical constraints due to conserved quantities, the time scales of step 2 and 3 strongly depends on the degree of integrability of the system. In particular, these processes are completely inhibited in a fully integrable model while they are dramatically slowed down in a nearly-integrable one. The latter is indeed the case of the experiments with cold atoms we have described in Secs. 1.4.1 and 1.4.4 [see the cartoon in Fig. 1.9(a)]. Here, after the fast quantum dephasing the system settles to a metastable, pre-thermalized state, which can be properly described by the GGE. Then, it remains close to this state for an experimentally relevant range of time allowing to probe its properties. Finally, true thermalization sets in on time scales which can be order of magnitude greater than the one associated with step 1.

The relaxation behavior discussed so far has been beautifully observed by Langen et al. in the time-evolution of the integrated mean squared contrast

$\langle \mathscr{C}^2 \rangle$ of the interference pattern between the nearly-integrable 1D split condensates described in Fig. 1.6 [41, 87]. As can be seen in Panel (b) of Fig. 1.9, after a fast decreasing induced by quantum dephasing, which is responsible for the LC build-up of correlations examined in Sec. 1.4.4, $\langle \mathscr{C}^2 \rangle$ approaches a quasi-stationary pre-thermal state which retains a strong memory of initial conditions and can be described by the GGE. However, due to the presence of weak integrability-breaking perturbations, such as small anharmonicities in the trapping potential, three-body collisions or phonon-phonon scattering, on longer time scales the system undertakes a further relaxation which slowly drives it towards a thermal state, as it has been very recently investigate in Ref. [118]. Importantly, the time scales of the two relaxation processes are well separated and this makes cold atomic setups an ideal playground to experimentally investigate the GGE physics over a wide time interval.

2 | TRANSPORT PHENOMENA IN A QUENCHED LUTTINGER LIQUID

In this Chapter we investigate how the peculiar features of out-of-equilibrium integrable systems affect their spectral and transport properties. In the first part of the Chapter we briefly introduce the LL model and the bosonization technique, which are very effective tools to investigate the low-energy physics of gapless 1D fermionic systems in equilibrium. Although in two- and three-dimensions they are well described by the Fermi liquid theory [19], where inter-particle interactions can be taken into account by reformulating the problem in terms of quasi-particles with renormalized parameters [19, 119], in 1D this picture fails. This is due to the reduced phase space available, which results in the fact that the low-energy excitations exhibit a collective and bosonic nature. As a consequence, 1D systems have very peculiar and intriguing properties, such as charge and spin fractionalization [120–131]. In this Chapter we focus on LL models with period boundary conditions (PBC), which are suitable for inspecting system properties in the thermodynamic limit. Finite-size effects will be addressed in the following Chapter, in which we will discuss LLs in the presence of OBC.

In the second part of the Chapter, we analyze how the unusual equilibrium spectral and transport properties of a Luttinger liquid – characterized by power-law behavior with interaction-dependent exponent [61, 62, 132] – are modified in the presence of a quantum quench of the inter-particle interaction. We demonstrate that the latter generates entanglement between right- and left-moving density excitations, encoded in their cross-correlators, which vanishes in the steady state inducing a *universal* power-law decay, i.e. independent of any quench parameters. In order to highlight the presence of entanglement, we focus on the time evolution of the NESF and identify in its long-time behavior a universal contribution $\propto t^{-2}$, precisely due to the entanglement dynamics of cross-correlators. Due to the role played by spectral properties in describing the general behavior of a quantum system, one would also expect signatures of the latter in the long-time evolution of other system observables. We therefore explore the transient dynamics of transport properties, which are strictly related to the NESF. In particular, we consider the injection process from an external probe and the subsequent dynamics of the LL after the quench, studying the injected charge and energy current as a function of time. We demonstrate that, for these quantities, the universal character clearly emerges as the dominant contribution to their long-time behavior. Finally, we find that the latter is even more evident in the energy fractionalization ratio [122, 133, 134], which thus represents a very promising tool to probe the relaxation effects induced by the vanishing of entanglement.

This Chapter is based on the results obtained in Refs. [135, 136].

2.1 THE LUTTINGER LIQUID MODEL: A DIGEST

In this Section we will outline the main features of the Luttinger liquid model, which allows to treat analytically interacting 1D systems. For a more detailed and complete treatment the reader is referred to one of the extensive reviews and books present in the literature [61–63, 137]. The validity of the LL model as a low energy theory for 1D systems of fermions, bosons and spins, has been recently demonstrated in a large number of experiments, for instance by means of anomalous tunneling effects [144, 145], by observing spin-charge separation [120, 125] and charge fractionalization [126, 131]. Moreover, the LL theory represents a very useful tool for the study of a wide range of 1D systems, including edge channels of integer [146] and fractional [147] quantum Hall effects and of two dimensional topological insulators [148–150], weakly interacting quantum wires [144], carbon nanotubes [145, 151–153], spin chains [154, 155] and Wigner crystals [156–159].

Our starting point is an interacting 1D fermionic system with length L and containing N particles. For the sake of simplicity in this Thesis we will focus on the spinless case, describing e.g. polarized fermion, since it already contains all the interesting non-equilibrium physics. The model Hamiltonian can be written as [1, 19]

$$\hat{H} = \hat{H}_0 + \hat{H}_{\text{int}}, \tag{2.1}$$

where $\hat{H}_0$ is the kinetic contribution,

$$\hat{H}_0 = \int_{-L/2}^{L/2} dx \, \hat{\Psi}^\dagger(x) \varepsilon(-i\partial_x) \hat{\Psi}(x), \tag{2.2}$$

while $\hat{H}_{\text{int}}$ takes into account inter-particle interactions

$$\hat{H}_{\text{int}} = \frac{1}{2} \int_{-L/2}^{L/2} dx \int_{-L/2}^{L/2} dy \, \hat{\Psi}^\dagger(x) \hat{\Psi}^\dagger(y) V(x-y) \hat{\Psi}(y) \hat{\Psi}(x). \tag{2.3}$$

Here, $\hat{\Psi}(x)$ is the Fermi field operator destroying a fermion at the position x, $\varepsilon(k)$ is the single-particle spectrum and $V(x-y)$ is a two-particle interaction potential. In this Section we assume for the system PBC, i.e.

$$\hat{\Psi}(x) = \hat{\Psi}(x+L). \tag{2.4}$$

It is convenient to begin discussing the non-interacting case, $\hat{H} = \hat{H}_0$. Here, single-particle energy levels and wave functions are

$$\varepsilon(k) = \frac{k^2}{2m}, \qquad \psi_k(x) = \frac{1}{\sqrt{L}} e^{ikx}, \tag{2.5}$$

respectively, with discretized momentum $k = 2\pi n/L$ (n being an integer). In the zero-temperature ground state of the system, denoted by $|F\rangle$, energy levels are filled up to the Fermi wave-vector $k_F = 2\pi N/L$, corresponding to the Fermi energy $E_F = k_F^2 (2m)^{-1}$.
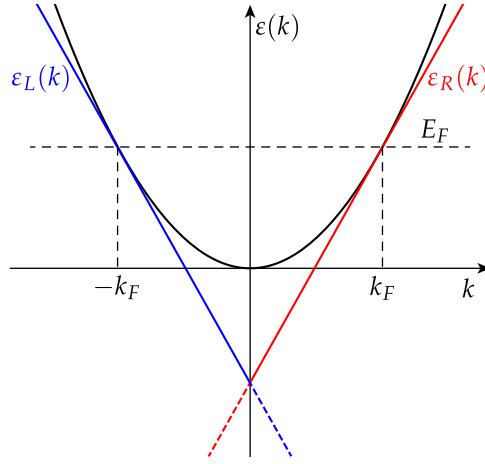
Figure 2.1: Linearization procedure of the original single-particle spectrum $\varepsilon(k)$ (black curve) around the Fermi energy E_F in the LL model. Red and blue lines represent the dispersion relation of right and left branches, respectively, with dashed regions signaling the infinite number of occupied fictitious states with negative energies introduced in the LL model.

LINEARIZATION The key point of the LL model [61–63, 138] lies in the linearizion of the spectrum around the two Fermi points $k = \pm k_F$, as shown in Fig. 2.1. This process gives rise to two different energy branches,

$$\varepsilon_r(k) = E_F + v_F(\epsilon_r k - k_F) \tag{2.6}$$

associated with right-moving ($r = R$, $\epsilon_R = 1$) and left-moving ($r = L$, $\epsilon_L = -1$) fermions. Here, $v_F = d\varepsilon(k)/dk|_{+k_F}$ is the Fermi velocity while the Fermi energy reads $E_F = v_F k_F$. Then, to make the model soluble, both the branches are extended to $k \in (-\infty, \infty)$. This procedure introduces an infinite number of occupied fictitious single-particle states with negative energies, which should be taken into account when physical observables of the system are considered. This can be properly done by looking at *normal ordered* operators,

$$: \hat{O} := \hat{O} - \langle R|\hat{O}|R\rangle, \tag{2.7}$$

with a $|R\rangle$ a reference state, instead of the bare one. The state $|R\rangle$ is usually chosen to be the ground state of $\hat{H}_0$, $|F\rangle$. Right- and left-movers can thus be regarded as two different fermionic species, each of them described by the associated Fermi field operator

$$\hat{\Psi}_r(x) = \frac{1}{\sqrt{L}} \sum_{k=-\infty}^{\infty} e^{i\epsilon_r k x} \hat{c}_{r,k}, \tag{2.8}$$

with $\hat{c}_{r,k}$ the fermionic annihilation operator destroying a $r-$moving fermion with momentum k. These fields (and the associated annihilation and creation operators in momentum space) satisfy usual anti-commutation relations,

$$\left\{\hat{\Psi}_r(x), \hat{\Psi}_{r'}(y)\right\} = \left\{\hat{\Psi}_r^\dagger(x), \hat{\Psi}_{r'}^\dagger(y)\right\} = 0, \tag{2.9a}$$

$$\left\{\hat{\Psi}_r(x), \hat{\Psi}_{r'}^\dagger(y)\right\} = \delta_{r,r'}\delta(x-y). \tag{2.9b}$$

BOSONIZATION   At this point the bosonization technique sets in, allowing to express the Fermi fields of Eq. (2.8) in terms of bosonic excitations [61–63, 138–140],

$$\hat{\Psi}_r(x) = \frac{\hat{F}_r}{\sqrt{2\pi a}} e^{i\epsilon_r k_F x} e^{-i\hat{\Phi}_r(x)}, \tag{2.10}$$

where a is a small-length cutoff of the order of the inverse of the Fermi wave-vector, $a \sim k_F^{-1}$, and

$$\hat{\Phi}_r(x) = i \sum_{q>0} \sqrt{\frac{2\pi}{qL}} e^{-aq/2} \left(e^{i\epsilon_r qx} \hat{b}_{r,q} - e^{-i\epsilon_r qx} \hat{b}_{r,q}^\dagger \right) \tag{2.11}$$

is a bosonic field operator, with $q = 2\pi n_q/L$ (n_q being a positive integer). The bosonic creation and annihilation operators, $\hat{b}_{r,q}^\dagger$ and $\hat{b}_{r,q}$, introduced in Eq. (2.11) satisfy usual commutation relations,

$$\left[\hat{b}_{r,q}^\dagger, \hat{b}_{q',r'}^\dagger \right] = \left[\hat{b}_{q,r}, \hat{b}_{r',q'} \right] = 0, \tag{2.12a}$$

$$\left[\hat{b}_{r,q}, \hat{b}_{r',q'}^\dagger \right] = \delta_{r,r'} \delta_{q,q'}, \tag{2.12b}$$

and are related to the original fermionic operators of Eq. (2.8) by

$$\hat{b}_{r,q} = \sqrt{\frac{2\pi}{Lq}} \sum_k \hat{c}_{r,k-q}^\dagger \hat{c}_{r,k}, \qquad \hat{b}_{r,q}^\dagger = \sqrt{\frac{2\pi}{Lq}} \sum_k \hat{c}_{r,k+q}^\dagger \hat{c}_{r,k}. \tag{2.13}$$

Therefore, they describe particle-hole excitations of the system and can be interpreted as density fluctuations.

Finally, in Eq (2.10) we have introduced the so called Klein factors. They satisfy the algebra [61–63]

$$\left\{ \hat{F}_r, \hat{F}_{r'}^\dagger \right\} = 2\delta_{r,r'}, \tag{2.14a}$$

$$\left\{ \hat{F}_r, \hat{F}_{r'} \right\} = \left\{ \hat{F}_r, \hat{F}_{r'} \right\} = 0, \qquad \text{for } r \neq r' \tag{2.14b}$$

and ensure that anticommutation relations of Eq. (2.9) still hold. Moreover, they are unitary operators, i.e. $\hat{F}_r^\dagger = \hat{F}_r^{-1}$, commute with the bosonic operators $\hat{b}_{r,q}^{(\dagger)}$ and satisfy the following commutation relation with the r−branch number operators $\hat{N}_r = \sum_k : \hat{c}_{r,k}^\dagger \hat{c}_{r,k} :$

$$\left[\hat{F}_r, \hat{N}_{r'} \right] = \delta_{r,r'} \hat{F}_r, \qquad \left[\hat{F}_r^\dagger, \hat{N}_{r'} \right] = -\delta_{r,r'} \hat{F}_r^\dagger. \tag{2.14c}$$

From the Eqs. (2.11) and (2.12) one readily obtains the following important commutation rule for the bosonic field

$$\left[\hat{\Phi}_r(x), \hat{\Phi}_{r'}(y) \right] \to i2\pi r \delta_{r,r'} \left[\frac{1}{\pi} \arctan\left(\frac{x-y}{a} \right) - \frac{x-y}{L} \right] \quad \text{for } L \to \infty$$

$$\to i2\pi r \delta_{r,r'} \left[\frac{1}{\pi} \frac{\text{sgn}(x-y)}{2} - \frac{x-y}{L} \right] \quad \text{for } a \to 0^+. \tag{2.15}$$

We now quote the bosonized version of some important operators [61–63, 137, 138]. Note that, as said in Eq. (2.7), in the LL picture they should always be regarded as normal ordered operators. Let us start from the kinetic contribution to the Hamiltonian of the linearized system,

$$
\begin{aligned}
\hat{H}_0 &= \sum_r v_F \int_{-L/2}^{L/2} dx\, \hat{\Psi}_r^\dagger(x)(-ir\partial_x)\hat{\Psi}_r(x) \\
&= \sum_r \sum_k v_F(k - rk_F) : \hat{c}_{r,k}^\dagger \hat{c}_{r,k} : \\
&= \sum_r \sum_{q>0} v_F q\, \hat{b}_{r,q}^\dagger \hat{b}_{r,q} + \hat{H}_{0,N}
\end{aligned}
\tag{2.16a}
$$

$$
= \frac{v_F}{4\pi} \sum_r \int_0^L dx : \left[\partial_x \hat{\Phi}_r(x)\right]^2 : + \hat{H}_{0,N},
\tag{2.16b}
$$

where $\hat{H}_{0,N} = \frac{\pi v_F}{L} \sum_r \hat{N}_r(\hat{N}_r + 1)$ is the zero-mode contribution. Note that the term linear in $\hat{N}_r$ can be removed by a shift of the chemical potential and will thus be neglected.

Another very important operator is the particle density operator, which is defined as

$$
\hat{\rho}_r(x) =: \hat{\Psi}_r^\dagger(x)\hat{\Psi}_r(x) := \frac{1}{L}\sum_{k,k'} e^{i\epsilon_r(k-k')x} : \hat{c}_{r,k'}^\dagger \hat{c}_{r,k} :
$$

$$
= \frac{\hat{N}_r}{L} - \frac{r}{2\pi}\partial_x \hat{\Phi}_r(x)
\tag{2.17a}
$$

$$
= \frac{\hat{N}_r}{L} + \frac{1}{2\pi}\sum_{q>0}\sqrt{\frac{2\pi q}{L}}\left(e^{irqx}\hat{b}_{r,q} + e^{-irqx}\hat{b}_{r,q}^\dagger\right)
\tag{2.17b}
$$

INTERACTIONS At this point, we have introduced all the tools needed to include also the inter-particle interaction contribution of Eq. (2.3). In the following we will consider point-like interactions described by a potential of the form

$$
V(x - y) = V_0\delta(x - y)
\tag{2.18}
$$

and will focus on density-density interaction terms [61–63, 137, 138]. In this case $\hat{H}_{\text{int}}$ can be decomposed as

$$
\hat{H}_{\text{int}} = \hat{H}_{\text{int}}^{(4)} + \hat{H}_{\text{int}}^{(2)},
\tag{2.19a}
$$

with

$$
\hat{H}_{\text{int}}^{(4)} = \pi g_4 \sum_r \int_{-L/2}^{L/2} dx : \hat{\rho}_r(x)\hat{\rho}_r(x) :,
\tag{2.19b}
$$

$$
\hat{H}_{\text{int}}^{(2)} = 2\pi g_2 \int_{-L/2}^{L/2} dx : \hat{\rho}_R(x)\hat{\rho}_L(x) :,
\tag{2.19c}
$$

describing intra- and inter-branch interactions, respectively. Note that the presence of point-like interactions results in the fact that g_2 and g_4 are q−independent. On the other hand, in the general case of interactions with

finite range, one would have $g_2(q)$ and $g_4(q)$. However, as long as one is interested in the low-energy properties of the model and if $g_2(q \to 0)$ and $g_4(q \to 0)$ are finite, the two cases asymptotically describe the same physics [61].

By using Eqs. (2.11) and (2.17) one can rewrite the total Hamiltonian $\hat{H} = \hat{H}_0 + \hat{H}_{\text{int}}^{(2)} + \hat{H}_{\text{int}}^{(4)}$ as

$$\hat{H} = \hat{H}_{\text{bos}} + \hat{H}_N, \tag{2.20}$$

with

$$\hat{H}_{\text{bos}} = \sum_{q>0} q \left[(v_F + g_4) \sum_r \hat{b}_{r,q}^\dagger \hat{b}_{r,q} + g_2 \left(\hat{b}_{R,q} \hat{b}_{L,q} + \hat{b}_{R,q}^\dagger \hat{b}_{L,q}^\dagger \right) \right], \tag{2.21a}$$

$$\hat{H}_N = \left(1 + \frac{g_4}{v_F} \right) \frac{v_F \pi}{L} \sum_r \hat{N}_r^2 + \frac{2\pi g_2}{L} \hat{N}_R \hat{N}_L, \tag{2.21b}$$

the bosonic and the zero-mode contribution, respectively. The former can be diagonalized by means of the following Bogolubov transformation

$$\hat{B}_{+,q} = A_+ \hat{b}_{R,q} + A_- \hat{b}_{L,q}^\dagger \qquad \hat{B}_{-,q}^\dagger = A_- \hat{b}_{R,q} + A_+ \hat{b}_{L,q}^\dagger, \tag{2.22}$$

with

$$A_\pm = \frac{1}{2} \left(\frac{1}{\sqrt{K}} \pm \sqrt{K} \right). \tag{2.23}$$

In the last step we have introduced the *Luttinger parameter*

$$K \equiv \sqrt{\frac{v_F - g_2 + g_4}{v_F + g_2 + g_4}}, \tag{2.24}$$

which describes the strength of the inter-particle interaction. In particular, $K = 1$ in the non-interacting case, while $K < 1$ ($K > 1$) in the presence of repulsive (attractive) interactions. In terms of the new bosonic operators $\hat{B}_{\eta,q}$, with $\eta = \pm$, introduced in Eq. (2.22), $\hat{H}_{\text{bos}}$ reads

$$\hat{H}_{\text{bos}} = u \sum_{\eta=\pm} \sum_{q>0} q \hat{B}_{\eta,q}^\dagger \hat{B}_{\eta,q}, \tag{2.25}$$

with

$$u = \sqrt{(v_F + g_4)^2 - (g_2)^2} \tag{2.26}$$

the renormalized velocity of elementary excitations of the system. On the other hand, by introducing the operators

$$\hat{N} = \hat{N}_R + \hat{N}_L, \tag{2.27}$$

$$\hat{J} = \hat{N}_R - \hat{N}_L, \tag{2.28}$$

associated with the total number of particles and the imbalance between right- and left-movers in the system, the zero-mode Hamiltonian in Eq. (2.21b) can be written as

$$\hat{H}_N = \frac{\pi u}{2L} \left(\frac{1}{K} \hat{N}^2 + K \hat{J}^2 \right). \tag{2.29}$$

In the rest of this Chapter we will consider the limit $L \to \infty$ and, thus, we will neglect this contribution.

CHIRAL FIELDS   In the presence of interactions the fields $\hat{\phi}_r(x)$ are not associated with right or left moving excitations anymore. Indeed, the total Hamiltonian $\hat{H}$ is not diagonal in the bosonic operators $\hat{b}_{r,q}$. In order to obtain new bosonic fields with the same *chiral* features of the non-interacting ones, we introduced the bosonic fields associated with operators $\hat{B}_{\eta,q}$,

$$\hat{\phi}_\eta(x) = i \sum_{q>0} \sqrt{\frac{2\pi}{qL}} e^{-aq/2} \left(\hat{B}_{\eta,q} e^{i\eta qx} - \hat{B}_{\eta,q}^\dagger e^{-i\eta qx} \right). \tag{2.30}$$

Indeed, the Heisenberg equation of motions for the bosonic operators $\hat{B}_{\eta,q}$ reads

$$\partial_t \hat{B}_{\eta,q}(t) = -i \left[\hat{B}_{\eta,q}, \hat{H}_{\text{bos}} \right] = -iu|q|\hat{B}_{\eta,q} \tag{2.31}$$

from which it follows that

$$\hat{B}_{\eta,q}(t) = e^{-iu|q|t} \hat{B}_{\eta,q}(0). \tag{2.32}$$

Therefore, the fields $\hat{\phi}_\eta(x)$ exhibit a chiral evolution with time,

$$\hat{\phi}_\eta(x,t) = \hat{\phi}_\eta(x - \eta ut), \tag{2.33}$$

and thus describe really right ($\eta = +$) and left ($\eta = -$) moving excitations. Note that the following operational relation between the original fields $\hat{\Phi}_r(x)$ and the chiral ones $\hat{\phi}_\eta(x)$ holds

$$\hat{\Phi}_r(x) = \sum_{\eta=\pm} A_{(\epsilon_r \eta)} \hat{\phi}_\eta(x), \tag{2.34}$$

with $A_{(\epsilon_r \eta)}$ given in Eq. (2.23). Moreover, the bosonic Hamiltonian of Eq. (2.25) can be written in terms of the new chiral fields as

$$\hat{H}_{\text{bos}} = \sum_{\eta=\pm} \int_{-L/2}^{L/2} dx \, \hat{\mathcal{H}}_\eta(x), \tag{2.35}$$

with

$$\hat{\mathcal{H}}_\eta(x) = \frac{u}{4\pi} : \left[\partial_x \hat{\phi}_\eta(x) \right]^2 : \tag{2.36}$$

the chiral-dependent Hamiltonian density. The sectors $\eta = +$ and $\eta = -$ are thus totally decoupled.

We finally introduce the chiral particle density operator,

$$\hat{\rho}_\eta(x) = -\eta \frac{\sqrt{K}}{2\pi} \partial_x \hat{\phi}_\eta(x), \tag{2.37}$$

which allows studying the flow of particle in the η direction. Note that the following relations between the densities $\hat{\rho}_r(x)$ and $\hat{\rho}_\eta(x)$, hold

$$\hat{\rho}(x) = \hat{\rho}_+(x) + \hat{\rho}_-(x) = \hat{\rho}_R(x) + \hat{\rho}_L(x), \tag{2.38a}$$

$$\hat{\rho}_\eta(x) = \left(\frac{1+\eta K}{2} \right) \hat{\rho}_R(x) + \left(\frac{1-\eta K}{2} \right) \hat{\rho}_L(x), \tag{2.38b}$$

$$\hat{\rho}_r(x) = \frac{\epsilon_r}{K} \left[\left(\frac{1+\epsilon_r K}{2} \right) \hat{\rho}_+(x) - \left(\frac{1-\epsilon_r K}{2} \right) \hat{\rho}_-(x) \right]. \tag{2.38c}$$

Moreover, since in the non-interacting case $K = 1$, one finds

$$\hat{\rho}_+(x) = \hat{\rho}_R(x), \qquad \hat{\rho}_-(x) = \hat{\rho}_L(x), \tag{2.39}$$

as expected.

In the rest of the Chapter the normal ordering notation will be assumed implicitly whenever is necessary.

2.1.1 Lesser Green function

We are now able to evaluate all correlation functions of a LL with the aid of the bosonization technique. Looking ahead, we briefly study here the equal-position $r-$branch lesser Green function of a LL in equilibrium,

$$G_r^<(\tau) = i\langle \hat{\Psi}_r^\dagger(x,0)\hat{\Psi}_r(x,\tau)\rangle, \tag{2.40}$$

with the average performed over the ground state of $\hat{H}$. Indeed, as we will seen in the following, this Green function allows to inspect spectral and transport properties of both equilibrium and out-of-equilibrium LLs. Using Eq. (2.10), Eq. (2.34), the Baker-Hausdorff-Campbell formula [63]

$$e^{\hat{A}}e^{\hat{B}} = e^{\hat{A}+\hat{B}}e^{\frac{1}{2}[\hat{A},\hat{B}]}, \tag{2.41}$$

which is valid if the commutator $[\hat{A}, \hat{B}]$ is a $c-$number, and the identity

$$\langle e^{\hat{A}} \rangle = e^{\frac{1}{2}\langle \hat{A}^2 \rangle}, \tag{2.42}$$

which holds if $\hat{A}$ is a linear combination of operators $\hat{B}_{\eta,q}$ and $\hat{B}_{\eta,q}^\dagger$ [63], we can rewrite Eq. (2.40) as

$$G_r^<(\tau) = \frac{i}{2\pi a}\exp\left\{\frac{1}{2}\left[A_{\epsilon_r}^2\mathcal{D}_+(0,\tau) + A_{-\epsilon_r}^2\mathcal{D}_-(0,\tau)\right]\right\}. \tag{2.43}$$

Here, we introduced the equilibrium bosonic correlators

$$\mathcal{D}_\alpha(\xi,\tau) = 2\langle \hat{\phi}_\alpha(0,0)\hat{\phi}_\alpha(\xi,\tau)\rangle - 2\langle \hat{\phi}_\alpha(0,0)\hat{\phi}_\alpha(0,0)\rangle, \tag{2.44}$$

where we explicitly used the space and time-translational invariance of the system. In the zero-temperature case these correlators can be easily evaluated using Eq. (2.30), from which one obtains [61–63, 137, 138]

$$\langle \hat{\phi}_\alpha(0,0)\hat{\phi}_\alpha(\xi,\tau)\rangle = \ln\left[\frac{L}{2\pi}\frac{1}{a+i\alpha\xi - iu\tau}\right] \tag{2.45}$$

and then, after some algebra,

$$\mathcal{D}_\alpha(\xi,\tau) = 2\ln\left[\frac{a}{a+i\alpha\xi - iu\tau}\right]. \tag{2.46}$$

Using the above results, one finally finds for the lesser $r-$branch Green function of Eq. (2.43) the following result

$$G_r^<(\tau) = \frac{i}{2\pi a}\left[\frac{a}{a - iu_f\tau}\right]^{\nu_{nq}}, \tag{2.47}$$

regardless of the branch index r, with

$$\nu_{\mathrm{nq}} = \frac{1}{2}(K + K^{-1}) \tag{2.48}$$

an interaction-dependent exponent. On the other hand, in the presence of a finite temperature T (setting $k_B = 1$) one gets

$$\langle \hat{\phi}_\alpha(0,0)\hat{\phi}_\alpha(\xi,\tau)\rangle_T = \langle \hat{\phi}_\alpha(0,0)\hat{\phi}_\alpha(\xi,\tau)\rangle_{T\to 0} + W_\alpha(\xi,\tau;T), \tag{2.49}$$

with $\langle \hat{\phi}_\alpha(0,0)\hat{\phi}_\alpha(\xi,\tau)\rangle_{T\to 0}$ representing the zero-temperature result of Eq. (2.45) and

$$W_\alpha(\xi,\tau;T) = \lim_{\gamma\to 0}\left[-\frac{1}{\gamma}\left(\frac{2aT}{u}+1\right) + 2\ln\frac{\pi}{2} \right.$$
$$\left. + \ln\left|\Gamma\left(1 + \frac{aT}{u} + i\frac{\xi - \alpha u\tau T}{u}\right)\right|^2 \right]. \tag{2.50}$$

Substituting Eq. (2.49) in Eq. (2.44) leads to

$$\mathcal{D}_{\alpha,\alpha}(\xi,\tau;T) = 2\ln\left[\frac{a}{a + i\alpha\xi - iu\tau}\right]$$
$$+ 2\ln\left[\frac{|\Gamma\left(1 + aTu^{-1} + i(\xi - \alpha u\tau)Tu^{-1}\right)|^2}{\Gamma(1 + aTu^{-1})^2}\right]. \tag{2.51}$$

Finally, recalling Eq. (2.43), the lesser Green function at finite temperature is given by [19, 141]

$$G_r^<(\tau;T) = \frac{i}{2\pi a}\left(\frac{a}{a - iu\tau}\right)^{\nu_{\mathrm{nq}}}\left[\frac{|\Gamma(1 + aTu^{-1} - iT\tau)|^2}{\Gamma^2(1 + aTu^{-1})}\right]^{\nu_{\mathrm{nq}}}. \tag{2.52}$$

2.1.2 Equilibrium spectral function of a Luttinger liquid

From the lesser Green functions obtained in Eqs. (2.47) and (2.52) one can immediately evaluate the lesser spectral functions of an equilibrium LL at zero and at finite temperature, respectively. Indeed, they are basically defined as the Fourier transform of the associated Green function. In particular, for the zero temperature case we get

$$A_r^<(\omega) = \frac{1}{2\pi}\int_{-\infty}^{\infty} e^{i\omega\tau}(-i)G_r^<(\tau)\, d\tau$$
$$= \frac{1}{\pi u}\frac{e^{-|\omega a/u|}}{\Gamma(\nu_{\mathrm{nq}})}\left|\frac{\omega a}{u}\right|^{\nu_{\mathrm{nq}}-1}\theta(-\omega). \tag{2.53}$$

Note that for $\omega \to 0^-$, one obtains $A_r^<(\omega) \sim |\omega|^{\nu_{\mathrm{sq}}}$, i.e. $A_r^<(\omega)$ vanishes with a typical LL-like power law with an interaction-dependent exponent [61, 62]. Concerning the case with finite temperature T, we have

$$A_r^<(\omega;T) = \frac{1}{2\pi}\int_{-\infty}^{\infty} e^{i\omega\tau}(-i)G_r^<(\tau;T)\, d\tau. \tag{2.54}$$

Although no analytical expression can be obtained in the general case, in the limit of small temperature and frequency $T, \omega \ll au^{-1}$, Eq. (2.54) can be approximated as [19, 141]

$$A_r^<(\omega; T) \approx \frac{1}{8\pi^3 aT} \left(\frac{2\pi aT}{u} \right)^{\nu_{\mathrm{nq}}} e^{\frac{\omega a}{u} - \frac{1}{\omega T}} \mathcal{B} \left(\frac{\nu_{\mathrm{nq}}}{2} + i\frac{\omega}{2\pi T}, \frac{\nu_{\mathrm{nq}}}{2} - i\frac{\omega}{2\pi T} \right),$$
(2.55)

where $\mathcal{B}$ is the Euler Beta function [142]. In particular, for $\omega \to 0$, one has $A_r^<(\omega; \beta) \sim a(T) + b(T)\omega$, with a and b temperature-depending coefficients. In this case, $A_r^<(\omega; T)$ does not vanish for $\omega = 0$ and, in sharp contrast with the zero-temperature case, exhibits a linear dependence on ω for $\omega \to 0$, regardless the Luttinger parameter.

Both zero- and finite-temperature spectral functions are shown in Fig. 2.3, where they are compared with the one obtained in a non-equilibrium regime.

2.1.3 Fractionalization phenomena in a Luttinger liquid

One of the most intriguing feature of LLs is the charge fractionalization [123, 143], which has been recently experimentally observed [126, 127, 131]. For the sake of simplicity, let us imagine to inject into an interacting spinless LL a single right-moving fermion with charge q at the position x_0. If we denote the initial ground state of the LL by $|F\rangle$, the injection process is modeled as $\hat{\Psi}_R^\dagger(x_0)|F\rangle$. Since, combining Eqs. (2.10), (2.34) and (2.33), we have

$$\hat{\Psi}_R(x_0) \sim e^{A_+ \hat{\phi}_+(x_0)} e^{A_- \hat{\phi}_-(x_0)},$$
(2.56)

one immediately realizes that as a result of the injection event two perturbations are created inside the system, one moving in the $\eta = +$ direction and the other moving in the $\eta = -$ one. To see this in a more formal way, we start from the following identity

$$\left[\hat{\rho}_r(x), \hat{\Psi}_R^\dagger(x_0) \right] = \delta_{r,R} \delta(x - x_0) \hat{\Psi}_R^\dagger(x_0),$$
(2.57)

which can be obtained from the fermionic anticommutation rules of Eq. (2.9) and encodes the fact that the field $\hat{\Psi}_R^\dagger(x_0)$ actually creates a right-moving fermion. In order to study what happens to the injected charge at later time, we need to focus on the following time-dependent commutator

$$\left[\hat{\rho}(x, t), \hat{\Psi}_R^\dagger(x_0, 0) \right].$$
(2.58)

Recalling Eqs. (2.38a), (2.37) and (2.33), one has

$$\hat{\rho}(x, t) = \hat{\rho}_+(x, t) + \hat{\rho}_-(x, t) = \hat{\rho}_+(x - ut, 0) + \hat{\rho}_-(x + ut, 0).$$
(2.59)

Finally, plugging this result in Eq. (2.38c), we find

$$\left[\hat{\rho}(x, t), \hat{\Psi}_R^\dagger(x_0, 0) \right] = \left[\frac{1 + K}{2} \delta(x + ut - x_0) \right.$$

$$\left. + \frac{1 - K}{2} \delta(x - ut - x_0) \right] \hat{\Psi}_R^\dagger(x_0, 0).$$
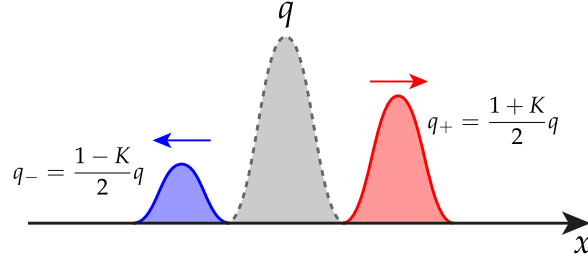(2.60)

Figure 2.2: Schematic representation of the fractionalization phenomenon. A right-moving fermion with charge q is injected into an interacting LL with Luttinger parameter K. As a consequence of inter-particle interactions, the original charge q splits in two packets with charge q_+ and q_-, moving to the right and to the left, respectively.

The above equation means that the injection of a right-moving fermion with charge q leads to the creation of a pair of counter-propagating excitations, one moving in the $\eta = +$ channel and the other in the $\eta = -$ one, with fractional charges

$$q_+ = \frac{1}{2}(1 + K)q, \qquad (2.61)$$

$$q_- = \frac{1}{2}(1 - K)q, \qquad (2.62)$$

respectively. This phenomenon is known in literature as charge fractionalization [123, 143], and is schematically shown in Fig. 2.2. Note that Eq. (2.60) is an identity among operators, implying that the charge of the two counter-propagating excitations is truly fractional and it is not due to quantum averaging [143]. As we shall see at the end of this Chapter (see Sec. 2.4.2), a very similar phenomenon also occurs if one looks at the behavior of the energy injected into an interacting LL [134].

2.2 QUENCH IN LUTTINGER LIQUIDS

In the previous Section we have seen that the LL paradigm allows to include the main effects of inter-particle interactions and to easily compute equilibrium correlation functions. In the last decade LLs also became an ideal platform for studying the out-of-equilibrium behavior of interacting quantum many-body systems. Indeed, they offer the possibility to compute analytically the system correlation functions also in an out-of-equilibrium regime and, since the LL model is integrable (see Sec. 2.2.1 for further details), they allow to investigate the peculiar physics of integrable quantum systems described in Sec. 1.4. In particular, sudden interaction quenches in LLs have provided the first analytical confirmations of the GGE conjecture [33] and allowed for very neat signatures of the light-cone effect [160, 161]. After these results, many theoretical research has been done in order to study in details the effects of the post-quench relaxation dynamics and of

the steady state reached in the long-time limit on the peculiar properties of LLs [162–166].

Moreover, the possibility of addressing different quenching protocols, as we shall see in more detail in Chap. 3, allowed a better understanding of the crossover from adiabatic to sudden quenches [167–169]. An even more interesting point about quantum quenches in LLs is that, when the LL picture is applicable, its predictions are universal (although some conditions of locality in the mapping to the LL model are required) [15, 170, 171]: The long wavelength and low temperature results are in good agreement with numerical data obtained inspecting spin and fermionic lattice models. The power of the LL as a tool for studying 1D equilibrium systems is hence to some extent transferred to non-equilibrium situation.

Following the general discussion of Sec. 1.4.2, a typical interaction quench in a LL can be described as follows. The system is prepared in the ground state $|0_i\rangle$ of the initial Hamiltonian $\hat{H}_i$, characterized by the Luttinger parameter K_i. At $t = 0$ the system is brought out of equilibrium by suddenly changing the strength of inter-particle interaction from K_i to K_f. After that, for $t > 0$, the system is allowed to unitarily evolve under the influence of the final Hamiltonian $\hat{H}_f$ [15, 33]. Performing the limit $L \to \infty$ and neglecting the zero-mode contribution, we have

$$\hat{H}_\mu = \sum_{\eta=\pm} \sum_{q>0} u_\mu q \hat{B}^\dagger_{\nu,\eta,q} \hat{B}_{\nu,\eta,q} \tag{2.63a}$$

$$= \frac{u_\mu}{4\pi} \sum_{\eta=\pm} \int_{-\infty}^{\infty} \left[\partial_x \hat{\phi}_{\mu,\eta}(x)\right]^2 dx, \tag{2.63b}$$

with $\mu \in \{i, f\}$ and

$$\hat{\phi}_{\mu,\eta}(x) = i \sum_{q>0} \sqrt{\frac{2\pi}{qL}} e^{-aq/2} \left(\hat{B}_{\mu,\eta,q} e^{i\eta qx} - \hat{B}^\dagger_{\mu,\eta,q} e^{-i\eta qx}\right). \tag{2.64}$$

In order to evaluate all the possible time-dependent quantum averages is convenient to move to Heisenberg picture and perform the averages over the ground state of the initial Hamiltonian. In this case, the time evolution of the final bosonic operators $\hat{B}_{f,\eta,q}$ – see Eq. (2.32) – is simply

$$\hat{B}_{\nu,\eta,q}(t) = e^{iu_f|q|t} \hat{B}_{\nu,\eta,q}(0). \tag{2.65}$$

We can then exploit the canonical transformation connecting final and initial bosonic operators [135, 136, 172],

$$\hat{B}_{f,\eta,q} = \theta_\eta \hat{B}_{i,+,q} - \theta_{-\eta} \hat{B}^\dagger_{i,-,q} \tag{2.66a}$$

$$\hat{B}^\dagger_{f,\eta,q} = \theta_\eta \hat{B}^\dagger_{i,+,q} - \theta_{-\eta} \hat{B}_{i,-,q}, \tag{2.66b}$$

with

$$\theta_\pm = \frac{1}{2} \left[\sqrt{\frac{K_i}{K_f}} \pm \sqrt{\frac{K_f}{K_i}}\right]. \tag{2.67}$$

Note that this transformation also results in the following identity between the chiral fields before and after the quench,

$$\hat{\phi}_{f,\eta}(x) = \sum_{\ell=\pm} \theta_{(\ell\eta)}\hat{\phi}_{i,\ell}(x). \tag{2.68}$$

2.2.1 Generalized Gibbs ensemble for a quenched Luttinger liquid

Since $\hat{H}_f$ is a quadratic bosonic Hamiltonian, from the work of Barthel and Schollwöck [57] sketched in Sec. 1.4.2 it follows that the quenched LL described so far will locally relax to a GGE. In particular, its associated density matrix is given by

$$\hat{\rho}_{\text{GGE}} = \frac{1}{Z_{\text{GGE}}}e^{-\sum_\eta \sum_{q>0}\lambda_{\eta,q}\hat{I}_{\eta,q}}, \tag{2.69}$$

with $Z_{\text{GGE}} = \text{Tr}\left[\exp(-\sum_\eta \sum_{q>0}\lambda_q\hat{I}_{\eta,q})\right]$. Here, the conserved quantities needed to build the GGE are the occupation numbers of the modes diagonalizing $\hat{H}_f$, namely

$$\hat{I}_{\eta,q} = \hat{B}_{f,\eta,q}^\dagger \hat{B}_{f,\eta,q}. \tag{2.70}$$

The Lagrange multipliers $\lambda_{\eta,q}$ are determined by imposing that the integral of motions $\hat{I}_{\eta,q}$ are conserved and equal to their value at $t = 0$,

$$\langle\hat{I}_{\eta,q}(t=0)\rangle_i = \langle\hat{I}_{\eta,q}\rangle_{\text{GGE}} = \frac{1}{e^{\lambda_{\eta,q}}-1}, \qquad \forall\eta,q. \tag{2.71}$$

2.3 QUENCH-INDUCED ENTANGLEMENT AND RELAXATION DYNAMICS IN LUTTINGER LIQUIDS

In the following we will study how the spectral and transport properties of a spinless LL are affected by the quantum quench protocol described in the previous Section. For the sake of simplicity we focus on the Galilean invariant case only, with $g_{\mu,2} = g_{\mu,4} \equiv g_\mu$, where the mode velocities simplify to $u_\mu = v_F/K_\mu$ and $K_\mu = [1 + g_\mu/(\pi v_F)]^{-1/2}$ [61–63]. The more general case with $g_{\mu,2} \neq g_{\mu,4}$ can be obtained straightforwardly without any significant change.

To investigate the dynamics induced by the quench, it is useful to express the initial state $|0_i\rangle$ in terms of *final* chiral fields $\hat{\phi}_{f,\eta}(x)$. One obtains [173, 174]

$$|0_i\rangle \propto \exp\left\{\sigma \int_{-\infty}^{\infty}[\partial_x\hat{\phi}_{f,+}(x)]\hat{\phi}_{f,-}(x)\,dx\right\}|0_f\rangle, \tag{2.72}$$

with $\sigma = (2\pi)^{-1}\theta_-/\theta_+$ and $|0_f\rangle$ the ground state of $\hat{H}_f$. Equation (2.72) implies that the bosonic chiral fields $\hat{\phi}_{f,+}(x)$ and $\hat{\phi}_{f,-}(x)$ are strongly correlated and, from their perspective, the initial state of the system is strongly entangled. It is thus interesting to inspect how the evolution of this entanglement

affects the dynamics of the system itself. To this end, since $|0_i\rangle$ is a gaussian state, we can focus on two-point correlators

$$
\begin{aligned}
D_{\alpha,\beta}(\xi;t,\tau) \equiv\ & 2\langle\hat{\phi}_{f,\alpha}(x-\xi,t-\tau)\hat{\phi}_{f,\beta}(x,t)\rangle_i \\
& - \langle\hat{\phi}_{f,\alpha}(x-\xi,t-\tau)\hat{\phi}_{f,\beta}(x-\xi,t-\tau)\rangle_i \\
& - \langle\hat{\phi}_{f,\alpha}(x,t)\hat{\phi}_{f,\beta}(x,t)\rangle_i,
\end{aligned}
\tag{2.73}
$$

which fully characterize the system and generalize the ones defined in Eq. (2.44). Here, $\langle\dots\rangle_i$ denotes quantum average on the pre-quench ground state $|0_i\rangle$. Note that, in contrast with the equilibrium case of Eq. (2.44), after the quench time-translational invariance is lost and both an absolute (t) and a relative (τ) time coordinates are thus required. On the other hand, space-translational invariance is preserved and two-point correlators only depends on the relative coordinate ξ. In the absence of the quench [i.e. for $\sigma = 0$ in Eq. (2.72)] quantum averages in Eq. (2.73) would be evaluated on the corresponding ground state $|0_f\rangle$, resulting in $D_{\alpha,\beta}(\xi;t,\tau) \equiv \mathcal{D}_\alpha(\xi;\tau)\delta_{\alpha,\beta}$, with $\mathcal{D}_\alpha(\xi;\tau)$ given in Eq. (2.44). As we have seen, in this latter case, due to time-translational invariance two-point correlators only depends on the relative temporal coordinate τ and fields with opposite chirality are not entangled, as expected in an equilibrium regime.

After rather long but straightforward calculations the out-of-equilibrium two-point correlators of Eq. (2.73) evaluate to

$$
D_{\alpha,\beta}(\xi;t,\tau) \equiv \vartheta(t-\tau)D^A_{\alpha,\beta}(\xi;t,\tau) + \vartheta(\tau-t)D^B_{\alpha,\beta}(\xi;t,\tau),
\tag{2.74}
$$

where

$$
D^A_{\alpha,\beta}(\xi;t,\tau) = \sum_{\eta=\pm} \theta_{(\eta\alpha)}\theta_{(\eta\beta)} \ln\left\{ \frac{[a-i\eta(\beta-\alpha)u_ft][a-i\eta(\beta-\alpha)u_f(t-\tau)]}{[a-i\eta(-\xi+(\beta-\alpha)u_ft+\alpha u_f\tau)]^2} \right\}
\tag{2.75}
$$

and

$$
D^B_{\alpha,\beta}(\xi;t,\tau) = \sum_{\eta=\pm} \theta_{\eta\alpha}\theta_{\eta\beta} \ln\left\{ \frac{a[a-i\eta(\beta-\alpha)u_ft]}{[a-i\eta(-\xi-(\eta u_i-\alpha u_ft+\eta u_i\tau)]^2} \right\}.
\tag{2.76}
$$

Here, the averages are computed by recalling that $\hat{\phi}_{f,\eta}(x,t) = \hat{\phi}(x-\eta u_ft)$ for $t > 0$ while $\hat{\phi}_{i,\eta}(x,t) = \hat{\phi}(x-\eta u_it)$ for $t < 0$. Moreover, we have exploited the canonical transformation between initial and final chiral fields given in Eq. (2.68) and the equilibrium results of Eq. (2.45), which in this context reads

$$
\langle\hat{\phi}_{i,\alpha}(x)\hat{\phi}_{i,\beta}(y)\rangle_i = \delta_{\alpha,\beta} \ln\left[\frac{L}{2\pi}\frac{1}{a-i\alpha(x-y)} \right].
\tag{2.77}
$$

To investigate the dynamics induced by entanglement, we now focus on the long-time behavior of two-point correlators $D_{\alpha,\beta}(\xi;t,\tau)$, defined by $t \gg \tau, \xi/u_f$. In this case, one needs to look at the term $D^A_{\alpha,\beta}(\xi;t,\tau)$ only. In particular, for $\alpha = \beta$ one gets

$$
D^A_{\alpha,\alpha}(\xi;t,\tau) = \sum_{\eta=\pm} \theta^2_{(\eta\alpha)} \ln\left[\frac{a}{a+i\eta(\xi-\alpha u_f\tau)} \right] \equiv D^A_\alpha(\xi;\tau).
\tag{2.78}
$$

The breaking of time-translational invariance does not affect auto-correlators, although they are different from their equilibrium counterparts of Eq. (2.46). Moreover, one can easily check that Eq. (2.78) coincides with the steady-state result obtained within the GGE defined in Eq. (2.69).

On the other hand, cross-correlators exhibit an explicit time dependence,

$$D^A_{\alpha,-\alpha}(\xi; t, \tau) = \theta_+ \theta_- \ln \left\{ \frac{(a^2 + 4u_f^2 t^2)[a^2 + 4u_f^2 (t - \tau)^2]}{[a^2 + (-\xi - \alpha u_f (2t - \tau))^2]^2} \right\}, \qquad (2.79)$$

encoding the entanglement and its decay in time between bosonic fields $\hat{\phi}_{f,+}(x)$ and $\hat{\phi}_{f,-}(x)$. Note that cross-correlators are different from zero at any finite time t while $D_{\alpha,-\alpha}(\xi; t, \tau) \to 0$ for $t \to \infty$. By expanding Eq. (2.79) in Taylor series in the long-time limit $t \gg \tau, \xi/u_f$ one obtains that they vanish with integer power laws only, whose exponents are thus independent of the quench parameters. In particular, in the local case $\xi = 0$ – on which we will focus in the following – one has

$$D_{\alpha,-\alpha}(0; t, \tau) = \sum_{n=2}^{\infty} \frac{d_n(\tau)}{t^n}, \qquad (2.80)$$

with coefficients $d_n(\tau)$ independent of the chirality. Therefore, in the long-time limit, cross-correlators decay with a leading power-law behavior $\propto t^{-2}$. The fact that $D_{\alpha,-\alpha}(\xi; t, \tau)$ are finite is a hallmark of the quench-induced entanglement between the two counter-propagating bosonic fields and will significantly affect the long-time relaxation of the system towards its steady-state. Due to their algebraic long-ranged behavior, one would expect observable signature of their decay also in system properties.

We would like to stress here that, although in the above discussion we focused on a fermionic LL, results obtained so far hold also for any 1D system that can be described in terms of the Hamiltonians in Eq. (2.63), both fermionic and bosonic.

2.3.1 Time–dependent spectral function

We now discuss the influence of quench-induced cross-correlations on the spectral properties of the system. Using the bosonization technique described in Sec. 2.1 we first investigate how the decay of entanglement between opposite chiral excitations influences the dynamics of the local lesser Green function.

$$G^<(t, t - \tau) \equiv i \langle \hat{\psi}^\dagger(x, t - \tau) \hat{\psi}(x, t) \rangle_i. \qquad (2.81)$$

Again, in contrast with the equilibrium case of Eq. (2.40) and due to breaking of time-translational invariance, the two time coordinates t and τ are required. Since particle number is conserved, we can write

$$G^<(t, t - \tau) = G^<_R(t, t - \tau) + G^<_L(t, t - \tau), \qquad (2.82)$$

where $G_r^<(t, t - \tau)$ denotes the $r-$channel lesser Green function. Following the same steps as in Sec. (2.1.1) and using Eq. (2.73), we obtain

$$G_r^<(t, t - \tau) = \frac{i}{2\pi a} e^{\frac{1}{2}\left\{A_{f,\epsilon_r}^2 D_+(0;\tau) + A_{f,-\epsilon_r}^2 D_-(0;\tau) + A_{f,+}A_{f,-}\left[D_{+-}(0;t,\tau) + D_{-+}(0;t,\tau)\right]\right\}},$$

(2.83)

with [see Eq. (2.23)]

$$A_{f,\pm} = \frac{1}{2}\left(\frac{1}{\sqrt{K_f}} \pm \sqrt{K_f}\right).$$

(2.84)

Recalling the decomposition of the two-point bosonic correlation function of Eq. (2.74) and the results of Eqs. (2.75) and (2.76), one gets

$$G_r^<(t, t - \tau) = \begin{cases} G_{r,\infty}^<(\tau)\mathcal{U}(t, \tau) & \text{for } \tau \leq t, \\ \mathcal{G}_r^<(t, \tau)\mathscr{U}(t) & \text{for } \tau > t, \end{cases}$$

(2.85)

where we have introduced

$$G_{r,\infty}^<(\tau) = \frac{i}{2\pi a}\left[\frac{a}{a + iu_f\tau}\right]^{\nu_+}\left[\frac{a}{a - iu_f\tau}\right]^{\nu_-},$$

(2.86a)

$$\mathcal{U}(t, \tau) = \left\{\frac{[a^2 + u_f^2(2t - \tau)^2]^2}{(a^2 + 4u_f^2 t^2)[a^2 + 4u_f^2(t - \tau)^2]}\right\}^\gamma,$$

(2.86b)

$$\mathcal{G}_r^<(t, \tau) = \frac{i}{2\pi a}\prod_{\ell = \pm}\left\{\frac{a}{a + i[(u_i + \ell u_f)t - u_i\tau]}\right\}^{\nu_\ell - 2\gamma},$$

(2.86c)

$$\mathscr{U}(t) = \left(\frac{a^2}{a^2 + 4u_f^2 t^2}\right)^\gamma,$$

(2.86d)

with $\nu_\pm = \theta_\mp^2(A_+^2 + A_-^2)$ and $\gamma = -A_+A_-\theta_+\theta_-$. In particular, for the quench protocols we are considering with $K_i > K_f$ one always finds $\gamma > 0$. In the above equations $G_{r,\infty}^<(\tau)$ represents the steady-state $r-$channel lesser Green function and coincides with the GGE results, while $U(t, \tau)$ features the explicit time dependence encoded in the cross-correlators $D_{\alpha,-\alpha}(0;t,\tau)$. Furthermore, note that $\mathcal{U}(t, \tau)$ does not depend on the channel index r and $\mathcal{U}(t, \tau) \to 1$ for $t \to \infty$.

Importantly, the presence of cross-correlators $D_{\alpha,-\alpha}(0;t,\tau)$ in the function $\mathcal{U}(t, \tau)$ leads to a universal power-law decay of $G_r^<(t, t - \tau)$ in the long-time limit $t \gg \tau$. Indeed, by expanding $\mathcal{U}(t, \tau)$ in Taylor series for $\tau/t \ll 1$, we obtain

$$G_r^<(t, t - \tau) = G_{r,\infty}^<(\tau)\left[1 + \sum_{n=2}^\infty \frac{g_n(\tau)}{t^n}\right].$$

(2.87)

Since in the local case we are addressing here $G_r^<(t, t - \tau)$ does not explicitly depend on the index r, one readily obtains the long-time limit expansion of the full lesser Green function

$$G^<(t, t - \tau) = G_\infty^<(\tau)\left[1 + \sum_{n=2}^\infty \frac{g_n(\tau)}{t^n}\right]$$

(2.88a)

$$\approx G_\infty^<(\tau)\left(1 + \frac{\gamma\tau^2}{2t^2}\right),$$

(2.88b)

with $G_\infty^<(\tau) = 2G_{r,\infty}^<(\tau)$. Therefore, in the long-time limit, $G^<(t, t-\tau)$ approaches its asymptotic value $G_\infty^<(\tau)$ with a power-law decay $\propto t^{-2}$, directly induced by the relaxation of cross-correlators $D_{\alpha,-\alpha}(\xi; t, \tau)$ found in Eq. (2.80).

The long-time behavior of Eq. (2.88b) immediately reflects on spectral properties of the system, as one can see by inspecting the time evolution of the local (lesser) NESF [163, 175, 176]

$$A^<(\omega, t) \equiv \frac{1}{2\pi} \int_{-\infty}^{\infty} e^{i\omega\tau}(-i)G^<(t, t-\tau)\, d\tau. \qquad (2.89)$$

In order to investigate the long-time behavior of this quantity, we note that the main features of the integrand function, i.e. $G^<(t, t-\tau)$, are localized into three well-separated regions of time. Indeed, recalling Eqs. (2.85) and (2.86), $G_\infty^<(\tau)$ has two branch points in $\tau = \pm ia/u_f$, $U(t, \tau)$ has two branch points in $\tau = t + ia/(2u_f)$ and, finally, $\mathscr{G}_r^<(t, \tau)$ has two further branch points in $\tau = (1 + u_f/u_i)t - ia/u_i$. Apart from these points, $G^<(t, t-\tau)$ is a smooth and slowly varying function of τ. Due to the presence of the oscillating phase term $e^{i\omega\tau}$, one can conclude that the main contributions to the integral come from the singular parts of $G^<(t, t-\tau)$ only. We can thus write

$$A^<(\omega, t) \approx A_0^<(\omega, t) + A_t^<(\omega, t) + A_{(1+u_f/u_i)t}^<(\omega, t), \qquad (2.90)$$

with $A_0^<(\omega, t)$, $A_t^<(\omega, t)$, and $A_{(1+u_f/u_i)t}^<(\omega, t)$ the contributions stemming from regions around $\tau \sim 0$, $\tau \sim t$, and $\tau \sim (1 + u_f/u_i)t$ respectively. At first, let us focus on $A_0^<(\omega, t)$. To this end, we can use the long-time expansion of $G^<(t, t-\tau)$ obtained in Eq. (2.88b), retaining only the lowest order contributions in t/τ. Since we are interested in the region near $\tau \sim 0$ and thanks to the presence of the oscillating factor we can safely set $t \to \infty$ in the integration domain, obtaining to the leading order

$$A_0^<(\omega, t) \approx A_\infty^<(\omega) - \frac{\gamma}{2t^2} \frac{d^2}{d\omega^2} A_\infty^<(\omega). \qquad (2.91)$$

Here,

$$
\begin{aligned}
A_\infty^<(\omega) &= \frac{1}{2\pi} \int_{-\infty}^{\infty} e^{i\omega\tau}(-i)G_\infty^<(\tau)\, d\tau \\
&= \frac{1}{\pi u_f} e^{-|\omega a/u_f|} \left|\frac{\omega a}{u_f}\right|^{\nu_+ + \nu_- - 1} \left[\frac{U(\nu_+, \nu_+ + \nu_-, -2\omega a/u_f)}{\Gamma(\nu_-)} \theta(-\omega)\right. \\
&\quad \left. + \frac{U(\nu_-, \nu_+ + \nu_-, 2\omega a/u_f)}{\Gamma(\nu_+)} \theta(\omega)\right]
\end{aligned}
\qquad (2.92)
$$

is the asymptotic value of $A^<(\omega, t)$, with $U(a, b, z)$ the Tricomi confluent hypergeometric function and $\Gamma(z)$ the Gamma function [142]. Similarly, using the complete Taylor series expansion of Eq. (2.88a), we get

$$A_0^<(\omega, t) = A_\infty^<(\omega) + \sum_{n=2}^{\infty} \frac{\mathcal{A}_n(\omega)}{t^n}, \qquad (2.93)$$

Here, we have introduced the coefficients

$$\mathcal{A}_n = \int_{-\infty}^{\infty} G_{\infty}^{<}(\tau) g_n(\tau) \, d\tau, \tag{2.94}$$

with $g_n(\tau)$ defined in Eq. (2.88a). In particular, $\mathcal{A}_2 = -\gamma/2(d^2/d\omega^2)A_{\infty}^{<}(\omega)$. Therefore, the universal power-law decay of the system lesser Green function found in Eq. (2.88b) results in an analogous behavior in the $\tau \sim 0$ contribution $A_0^{<}(\omega, t)$.

Let us now discuss the region around $\tau \sim t$. From Eq. (2.85) it follows that both the contributions arising from $\tau \leq t$ and from $\tau > t$ should be taken into account. After the change of variable $y = t - \tau$, the long-time limit is obtained by expanding the integrand to the lowest order in $y/t \ll 1$. We get

$$A_t^{<}(\omega, t) \approx \frac{1}{2\pi^2 a} \frac{e^{i\frac{\pi}{2}(\nu_- - \nu_+)}}{4^{2\gamma}} \left(\frac{a}{u_f}\right)^{\nu_+ + \nu_-} \frac{e^{i\omega t}}{t^{\nu}}$$
$$\times \left\{ \int_0^{\infty} e^{-i\omega y} \frac{1}{[a^2/(2u_f)^2 + y^2]^{\gamma}} \, dy + \frac{2^{2\gamma}}{i\omega} \left(\frac{u_f}{a}\right)^{2\gamma} \right\}, \tag{2.95}$$

where the first term in curly brackets stems from the region $\tau \leq t$ while the second one is due to the regime $\tau > t$. Here,

$$\nu \equiv \nu_+ + \nu_- - 2\gamma = \frac{K_f^4 + K_i^2 + 3K_f^2(1 + K_i^2)}{8K_f^2 K_i} \geq 1. \tag{2.96}$$

Finally, we focus on the contribution arising from $\tau \sim (1 + u_f/u_i)t$. By performing the change of variable $z = -u_i(t - \tau) - u_f t$ and retaining only the lowest order in $z/t \ll 1$ in the integrand function, one obtains

$$A_{(1+u_f/u_i)t}^{<}(\omega, t) \approx \frac{\theta(\omega)}{2\pi a} \left(\frac{a}{2u_f}\right)^{\nu_-} \left(\frac{a}{u_i}\right)^{\nu_+ - 2\gamma} \frac{e^{i(1+u_f/u_i)\omega t}}{t^{\nu_-}}$$
$$\times \frac{e^{-i\frac{\pi}{2}(\nu_- - 2\gamma)} e^{-a|\omega|/u_i}}{u_i \Gamma(\nu_+ - 2\gamma)} |\omega|^{\nu_+ - 2\gamma - 1}. \tag{2.97}$$

Since, for quenches with $K_i > K_f$ one always has $\nu < \nu_-$, in the long-time limit this latter contribution is sub-leading with respect to $A_t^{<}(\omega, t)$.

Collecting all the results of Eqs. (2.93), (2.95) and (2.97) we finally obtain

$$A^{<}(\omega, t) = A_{\infty}^{<}(\omega) + \sum_{n=2}^{\infty} \frac{\mathcal{A}_n(\omega)}{t^n} + \frac{M^A(\omega, t)}{t^{\nu}}, \tag{2.98}$$

where $\mathcal{A}_n(\omega) = 2\pi^2\nu \int_{-\infty}^{\infty} G_{\infty}^{<}(\tau) g_n(\tau) \, d\tau$, with $g_n(\tau)$ defined in Eq. (2.88a), and to the leading order in the long-time limit[1]

$$M^A(\omega) \approx \frac{1}{2\pi^2 a} \frac{e^{i\frac{\pi}{2}(\nu_- - \nu_+)}}{4^{2\gamma}} \left(\frac{a}{u_f}\right)^{\nu_+ + \nu_-} e^{i\omega t}$$
$$\times \left\{ \int_0^{\infty} e^{-i\omega y} \frac{1}{[a^2/(2u_f)^2 + y^2]^{\gamma}} \, dy + \frac{2^{2\gamma}}{i\omega} \left(\frac{u_f}{a}\right)^{2\gamma} \right\}, \tag{2.99}$$
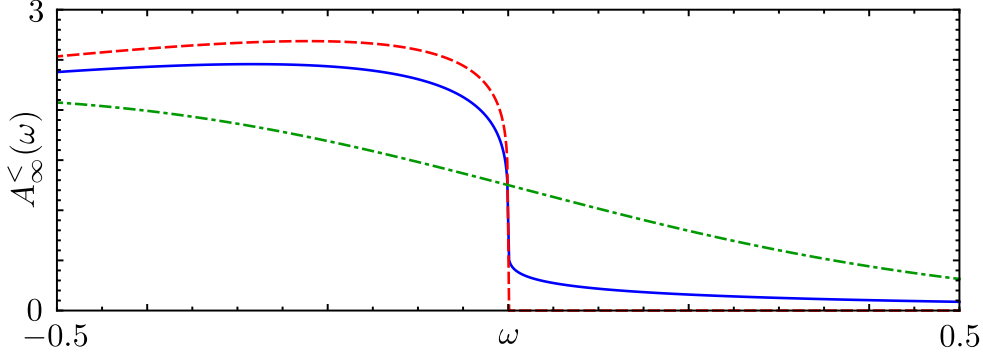
Figure 2.3: Plot of the asymptotic spectral function $A_\infty^<(\omega)$ [units $(2\pi^2 v_F)^{-1}$] as a function of ω (units $v_F a^{-1}$). The blue solid line shows the quenched case with $K_i = 0.9 \to K_f = 0.6$. The red dashed and the green dash-dotted ones correspond to the zero-temperature and finite-temperature regimes in the absence of quench discussed in Eqs. (2.53) and (2.54), respectively. In the latter case, the effective temperature $T_{\text{eff}}^{-1} = 1.89 \ a v_F^{-1}$) has been fixed by equating the average thermal energy with the one injected during the quench.

Although the main focus of this Chapter is to study the time evolution of system properties induced by the decay of entanglement, we briefly address here the behavior of the asymptotic post-quench spectral function $A_\infty^<(\omega)$, shown in Fig. 2.3. It contains many interesting features, especially in the region $\omega \to 0$ [135, 163]. In particular, using the following asymptotic expansions of the Tricomi hypergeometric function [142]

$$U(a,b,z) \approx \frac{\Gamma(b-1)}{\Gamma(a)} + \frac{(1+a-b)\Gamma(b-1)}{(2-b)\Gamma(a)}z + \frac{\Gamma(1-b)}{\Gamma(a-b+1)}z^{b-1}, \quad (2.100)$$

valid for $z \to 0$, we obtain the following expansion near $\omega \sim 0$

$$A_\infty^<(\omega) \approx \frac{4\pi K_f}{2^{\nu_+ + \nu_-}} \left[C_0^A + C_1^A(\omega)(2k_f|\omega|) + C_2^A(\omega)(2k_f|\omega|)^{\nu_+ + \nu_- - 1} \right]. \quad (2.101)$$

Here, we have the following coefficients

$$C_0^A = \frac{\Gamma(\nu_+ + \nu_- - 1)}{\Gamma(\nu_+)\Gamma(\nu_-)}, \quad (2.102a)$$

$$C_1^A(\omega) = \frac{\Gamma(\nu_+ + \nu_- - 1)}{\Gamma(\nu_+)\Gamma(\nu_-)} \left[\frac{(1-\nu_+)\theta(\omega)}{2 - \nu_+ - \nu_-} + \frac{(1-\nu_-)\theta(-\omega)}{2 - \nu_+ - \nu_-} - \frac{1}{2} \right], \quad (2.102b)$$

$$C_2^A(\omega) = \frac{\Gamma(1 - \nu_+ - \nu_-)}{\pi} \left[\sin(\pi\nu_+)\theta(-\omega) + \sin(\pi\nu_-)\theta(-\omega) \right]. \quad (2.102c)$$

From the above equation it clearly emerges that $A_\infty^<(\omega = 0) \neq 0$, which is quite similar to what happens in a finite temperature LL at equilibrium [19, 141], as we have seen in Eq. (2.54). Interestingly, $A_\infty^<(\omega)$ exhibits two different regimes depending on the value of $\nu_+ + \nu_-$. In particular, for small

---

1 Note that the function $\mathcal{M}^A(\omega, t)$ also contains all the corrections deriving from having set $t \to \infty$ in the integration domain in Eq. (2.94), which are sub-leading contributions with respect to the expansion in Eq. (2.99).

quenches one finds $1 \leq \nu_+ + \nu_- < 2$ and, therefore, $A_\infty^<(\omega)$ approaches $\omega = 0$ with a power law $\propto |\omega|^{\nu_+ + \nu_- - 1}$. This resembles the typical power-law behavior we found in Eq. (2.53) for a zero-temperature LL in equilibrium, albeit with a different exponent [61, 62, 138]. On the other hand, when $\nu_+ + \nu_- > 2$, the leading contribution to $A_\infty^<(\omega)$ is $\propto |\omega|$, with the details of quench affecting the prefactor only. In Fig. 2.3 we compare the quenched spectral function with the zero and finite temperature ones, obtained in Eqs. (2.53) and (2.54). In the latter case, the effective inverse temperature, T_{eff}, has been chosen in such a way that the average thermal energy of the non-quenched system is equal to the energy injected into the quenched one [18, 163, 177],

$$\langle \hat{H}_f \rangle_i = \frac{\text{Tr}\left[\hat{H}_f e^{-\hat{H}_f/T_{\text{eff}}} \right]}{\text{Tr}\left[e^{-\hat{H}_f/T_{\text{eff}}} \right]}, \qquad (2.103)$$

which results in

$$T_{\text{eff}}^{-1} = \sqrt{\frac{2}{3}} \pi K_f \frac{\sqrt{K_i K_f}}{|K_i - K_f|}. \qquad (2.104)$$

For the parameters of the quench reported in Fig. 2.3 we have $1 \leq \nu_+ + \nu_- < 2$ and the two main features of the quenchd spectral function $A_\infty^<(\omega)$, namely the fact that $A_\infty^\omega(0) \neq 0$ and the power-law behavior near $\omega \sim 0$, are clearly visible.

After this digression, we can now focus on the time decay of $A^<(\omega, t)$ towards the asymptotic value discussed above. Looking back to Eq. (2.98) we can see that two distinct contributions are present. The first one contains only integer power laws of time, $\propto t^{-n}$ (with $n \geq 2$), and is entirely due to the decay of $G^<(t, t - \tau)$ found in Eq. (2.88a). The leading contribution to this term is thus a *universal* power-law decay $\propto t^{-2}$, regardless of quench parameters. On the other hand, the second contribution contains the function $\mathcal{M}^A(\omega, t)$ which, to the leading order in $1/t$, is an oscillating function with constant amplitude, as can be seen from Eq. (2.99). In the long-time limit, it decays with a LL-like *non-universal* power law $\propto t^{-\nu}$, with ν strongly dependent on the quench parameters K_i and K_f. However, since for any reasonable quench one finds $1 \leq \nu < 2$, it turns out that the universal power-law behavior, which directly originates from the decay of entanglement between bosonic excitations $\hat{\phi}_{f,+}(x)$ and $\hat{\phi}_{f,-}(x)$, is hardly visible in the transient of the NESF: The long-time decay of $A^<(\omega, t)$ is governed by the non-universal contribution $\propto t^{-\nu}$, with the universal one being a sub-leading term. This is illustrated in Fig. 2.4, which shows the real part of the deviation of the lesser NESF from its steady-state value, $|\Delta A^<(\omega, t)| = |A^<(\omega, t) - A_\infty^<(\omega)|$, at large times and for two different interaction quenches. Here, the oscillating behavior due to $\mathcal{M}^A(\omega, t)$ decays with non-universal power law $\propto t^{-\nu}$ (see solid black lines) while no evidence of the universal behavior $\propto t^{-2}$ is present. Despite the sub-leading character of the universal contribution to the behavior of the NESF in Eq. (2.98), in the next Section we will demonstrate that it controls the long-time behavior of charge and energy currents in a transport setup.
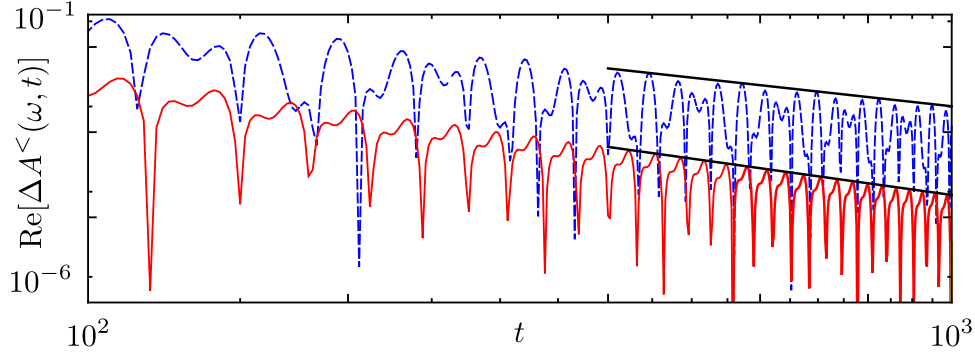
Figure 2.4: Plot of $|\text{Re}[\Delta A^<(\omega, t)]|$ [units $(2\pi^2 v_F)^{-1}$] as a function of time t [units $a v_F^{-1}$] with $\omega = -0.1\, a^{-1} v_F$ for the quenches $K_i = 0.9 \rightarrow K_f = 0.7$ (blue, dashed) and $K_i = 0.8 \rightarrow K_f = 0.4$ (red, solid). Here, solid black lines represent the power-law behavior $\propto t^{-\nu}$ for the two different cases.

2.4 TRANSIENT DYNAMICS OF TRANSPORT PROPERTIES

Motivated by recent transport experiments in cold atomic systems [178–181], we now investigate the effects of a quantum quench on the transport properties of the system considered so far. To do so, we assume that immediately after the quench, the LL (hereafter dubbed *the system*) is locally tunnel-coupled to a 1D non-interacting *probe*, as sketched in Fig. 2.5. The probe is described by the Hamiltonian

$$\hat{H}_p = v_F \int_{-\infty}^{\infty} \hat{\chi}^\dagger(x)(-i\partial_x)\hat{\chi}(x)\, dx, \tag{2.105}$$

with $\hat{\chi}(x)$ its fermionic field. The probe is subject to a bias voltage V measured with respect to the Fermi level of the system. We assume a local tunneling at x_0 which breaks inversion parity, focusing, e.g., on the injection in the system $R-$channel only [136, 172, 182–184],

$$\begin{aligned} \hat{H}_T(t) &= \hat{H}_T^+(t) + \hat{H}_T^-(t) \\ &\equiv \vartheta(t)\lambda \left[\hat{\psi}_R^\dagger(x_0)\hat{\chi}(x_0) + \hat{\chi}^\dagger(x_0)\hat{\psi}_R(x_0) \right], \end{aligned} \tag{2.106}$$

where λ is the tunneling amplitude and $\vartheta(t)$ is the Heaviside step function. Although this parity-breaking injection mechanism is not an essential requirement for what follows, it also allows to study the peculiar fractionalization properties of LLs in the presence of a quantum quench. The whole setup is assumed to be in its ground state before the quench, with $\hat{\rho}(0)$ the associated zero-temperature total density matrix.

2.4.1 Tunneling charge current

We concentrate at first on the chiral charge current, defined as

$$I_\eta(V, t) = -q\partial_t \int_{-\infty}^{\infty} \langle \delta\hat{n}_\eta(x, t) \rangle\, dx \tag{2.107}$$
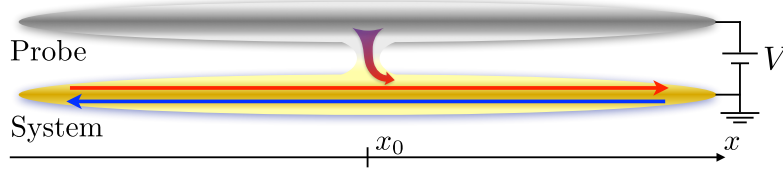
Figure 2.5: Scheme of the system, modeled as a pair of counter-propagating channels, and the probe, biased with a dc voltage V with respect to the system. At $x = x_0$, the probe injects $R-$moving particles only.

with q the charge of a single fermion and the average performed with respect to $\hat{\rho}(0)$. Here,

$$\hat{n}_\eta(x,t) = -\eta\sqrt{\frac{K_f}{2\pi}}\partial_x\hat{\phi}_{f,\eta}(x - \eta u_f t),\qquad (2.108)$$

are the chiral particle densities introduced in Eq. (2.37) while

$$\langle\delta\hat{\mathcal{O}}(x,t)\rangle = \mathrm{Tr}\{\hat{\mathcal{O}}(x,t)[\hat{\rho}(t) - \hat{\rho}(0)]\}\qquad (2.109)$$

represents the average variation, induced by the tunneling, of a given operator $\hat{\mathcal{O}}(x,t)$. For a generic Hermitian and particle-number conserving operator $\hat{\mathcal{O}}(x,t)$, working in the interaction picture with respect to the tunneling Hamiltonian $\hat{H}_T(t)$ [73, 76] and to the lowest order in the tunneling amplitude λ [122, 135, 172], a direct calculation leads to [see Appendix B and, in particular, Eq. (B.13)]

$$\langle\delta\hat{\mathcal{O}}(x,t)\rangle = 2\mathrm{Re}\int_0^t d\tau_1 \int_0^{\tau_1} d\tau_2\,\mathrm{Tr}\Big\{\hat{\rho}(0)\hat{H}_t^+(\tau_2)\left[\hat{\mathcal{O}}(x,t),\hat{H}_t^-(\tau_1)\right]$$
$$+ \hat{\rho}(0)\hat{H}_t^-(\tau_2)\left[\hat{\mathcal{O}}(x,t),\hat{H}_t^+(\tau_1)\right]\Big\}.\qquad (2.110)$$

Note that, if $\hat{\mathcal{O}}(x,t)$ is an operator acting only on the system, as in the case we are considering, it commutes with the Fermi field of the probe, $\hat{\chi}(x)$. In order to evaluate Eq. (2.107), we substitute $\hat{\mathcal{O}}(x,t) = \hat{n}_\eta(x,t)$ in Eq. (2.110). As a first step, we calculate the correlators of the non-interacting probe. Note that its chemical potential is shifted by the bias energy qV with respect to the Fermi level of the system. In the zero-temperature case we obtain

$$\langle\hat{\chi}^\dagger(x_0,\tau_2)\hat{\chi}(x_0,\tau_1)\rangle = iG_p^>(\tau_1 - \tau_2)e^{iqV(\tau_2-\tau_1)},\qquad (2.111)$$

$$\langle\hat{\chi}(x_0,\tau_2)\hat{\chi}^\dagger(x_0,\tau_1)\rangle = iG_p^>(\tau_1-\tau_2)e^{-iqV(\tau_2-\tau_1)},\qquad (2.112)$$

where the probe local greater Green function is

$$G_p^>(\tau) = -\frac{i}{2\pi a}\frac{a}{a - iv_F\tau}.\qquad (2.113)$$

Then, we focus on the commutator found in Eq. (2.110), which gives

$$\left[\hat{n}_\eta(x,t),\hat{\psi}_R^\dagger(x_0,\tau)\right] = \frac{\sqrt{K_f}A_\eta}{\pi}\left[\frac{a}{a^2 + (z_{f,\eta} - \bar{z}_{f,\eta})^2}\right]\hat{\psi}_R^\dagger(x_0,\tau),\qquad (2.114)$$

with generalized coordinates $z_{f,\eta} = x - \eta u_f t$ and $\bar{z}_{f,\eta} = x_0 - \eta u_f \tau$. Finally, noting that

$$\langle \psi_R^\dagger(x_0, \tau_2) \psi_R(x_0, \tau_1) \rangle = \langle \psi_R(x_0, \tau_2) \psi_R^\dagger(x_0, \tau_1) \rangle = -i G_R^<(\tau_1, \tau_2), \quad (2.115)$$

with $G_R^\lessgtr(\tau_1, \tau_2) = G^<(\tau_1, \tau_2)/2$ given in Eq. (2.85), we obtain

$$I_\eta(V, t) = I_\eta^0 \, \mathrm{Re}\left[\int_0^t G^<(t, t - \tau) G_p^>(\tau) i \sin(qV\tau) \, d\tau \right], \quad (2.116)$$

where $I_\eta^0 = -q|\lambda|^2(1 + \eta K_f)$. In the above equation $G^<(t, t - \tau)$ is always in the regime $\tau \le t$, where $G^<(t, t - \tau) = G_\infty^\lessgtr(\tau) \mathcal{U}(t, \tau)$, as we have found in Eq. (2.85). Moreover, the chirality η affects the pre-factor I_η^0 only and, therefore, $I_+(V, t) \propto I_-(V, t)$, with $I_+(V, t) \ge I_-(V, t)$. This implies that the charge fractionalization ratio

$$R_\eta^Q = \frac{I_\eta(V, t)}{I(V, t)}, \quad (2.117)$$

with $I(V, t) = \sum_\eta I_\eta(V, t)$ the total charge current, is a constant at any time and, in particular,

$$R_\eta^Q = \frac{1 + \eta K_f}{2}. \quad (2.118)$$

The same expression holds for a non-quenched system with Luttinger parameter K_f [121]: charge fractionalization has no memory at all of the initial pre-quench state. Furthermore, we note that the ratio R_η^Q has natural bounds, $1/2 \le R_\eta^Q \le 1$. The physical origin of this behavior and the fact that R_η^Q is memoryless and insensitive to K_i traces back to the absence of charge transfer between R and L branches. Indeed, the inter-particle interaction can only create fluctuations of particle density but the total number of particles on each channel is conserved. Since in our scheme particles are injected solely in the R channel, only this one will actively contribute to the net charge current, no matter how the injection is carried out or how the system is prepared before the injection. Moreover, as long as only one channel is concerned, it has been shown [121, 185] that charge fractionalization phenomena are completely controlled by the equation of motion of its field operators. Therefore their dynamics depend only on the final (post-quench) Hamiltonian and this explains why R_η^Q does not depend on K_i.

We now turn to the long-time behavior of Eq. (2.116). We follow the same steps illustrated in Sec. 2.3.1 leading to Eq. (2.98). In this case things are a little simpler, since one has to consider $G^<(t, t - \tau)$ only in the regime $\tau \le t$. Moreover, the Green function of the probe $G_p^>(\tau)$ is a smooth and slowly varying function, apart from a simple pole in $\tau \pm ia/v_F$, which is very close to the branch point of $G^<(t, t - \tau)$. Therefore, in the long-time limit Eq. (2.116) can be written as

$$I_\eta(V, t) \approx I_{\eta,0}(V, t) + I_{\eta,t}(V, t), \quad (2.119)$$

with $I_{\eta,0}(V, t)$ and $I_{\eta,t}(V, t)$ the main contributions to the integral stemming from regions near $\tau \sim 0$ and $\tau \sim t$, respectively. They can be evaluate

following the same procedure described below Eq. (2.90), leading to the final result

$$I_\eta(V,t) = I_\eta^\infty(V) + \sum_{n=2}^\infty \frac{\mathcal{I}_{\eta,n}(V)}{t^n} + \frac{\mathcal{M}_\eta^I(V,t)}{t^{\nu+1}}. \tag{2.120}$$

Here,

$$I_\eta^\infty(V) = I_\eta^0 \text{Re}\left[\int_0^\infty G_\infty^<(\tau) G_p^>(\tau) i\sin(qV\tau)\,d\tau\right] \tag{2.121a}$$

is the asymptotic tunneling current, while

$$\mathcal{I}_{\eta,n}(V) = I_\eta^0 \text{Re}\left[\int_0^\infty g_n(\tau) G_p^>(\tau) i\sin(qV\tau)\,d\tau\right], \tag{2.121b}$$

$$\mathcal{M}_\eta^I(V,t) \approx -\frac{I_\eta^0}{4\pi^2 a v_F}\left(\frac{a}{u_f}\right)^{\nu_++\nu_-}\frac{\cos\left[\frac{\pi}{2}(\nu_+-\nu_-)\right]}{4^{2\gamma}}$$
$$\times \int_0^\infty \frac{\sin[qV(t-y)]}{[a^2/(2u_f)^2+y^2]^\gamma}\,dy, \tag{2.121c}$$

where the coefficients $g_n(\tau)$ have been defined in Eq. (2.88a) and in $\mathcal{M}_\eta^I(V,t)$ we retained only the leading order in $y/t \ll 1$. In particular,

$$\mathcal{I}_{\eta,2}(V) = -\frac{\gamma}{2q^2}\frac{d^2}{dV^2}I_\eta^\infty(V). \tag{2.122}$$

The tunneling current $I_\eta(V,t)$ exhibits the same structure of the spectral function $A^<(\omega,t)$ we found in Eq. (2.98). In particular, Eq. (2.120) consists of three contributions: the steady state value $I_\eta^\infty(V)$ and two transient terms, one containing only integer power laws of time, $\propto t^{-n}$, stemming from the long-time expansion of $G^<(t,t-\tau)$ in Eq. (2.88b), and one displaying a more conventional LL-like non-universal power-law behavior. However, in contrast with the NESF, this latter contribution decays as $t^{-\nu-1}$. Since $\nu+1 \geq 2$, the relaxation dynamics of $I_\eta(V,t)$ is thus governed by the universal decay $\propto t^{-2}$, which does not depend on the quench parameters and traces back to the behavior of cross-correlators $D_{\alpha,-\alpha}(0;t,\tau)$. Thus, the long-time dynamics of the chiral charge current directly reveals the entanglement between chiral bosonic fields $\hat\phi_{f,+}(x)$ and $\hat\phi_{f,-}(x)$ and its relaxation.

In Fig. 2.6 we show the behavior of the asymptotic total tunneling current $I^\infty(V) = \sum_\eta I_\eta^\infty(V)$ and compare it with the non-quenched zero temperature case. The main feature of the quenched tunneling current is that $I^\infty(V) \sim V$ for $V \to 0$. This is in sharp contrast with the non-quenched one, in which $I^\infty(V)$ is characterized by a power-law decay $V^{\nu_{nq}}$ for $V \to 0$ [132]. This is a quite expected behavior since, in essence, $A_\infty^<(V) \propto \partial_V I^\infty(V)$ with $A_\infty^<(0) \neq 0$.

The time evolution of $I_\eta(V,t)$ during the transient is displayed in Fig. (2.7). For long times the universal power-law behavior $\propto t^{-2}$ emerges, but on intermediate times it is hidden by marked oscillations arising from the non-universal power law $\propto t^{-\nu-1}$. This is due essentially to the following two reasons. First, for the quench considered in Fig. (2.7) (which is a rather
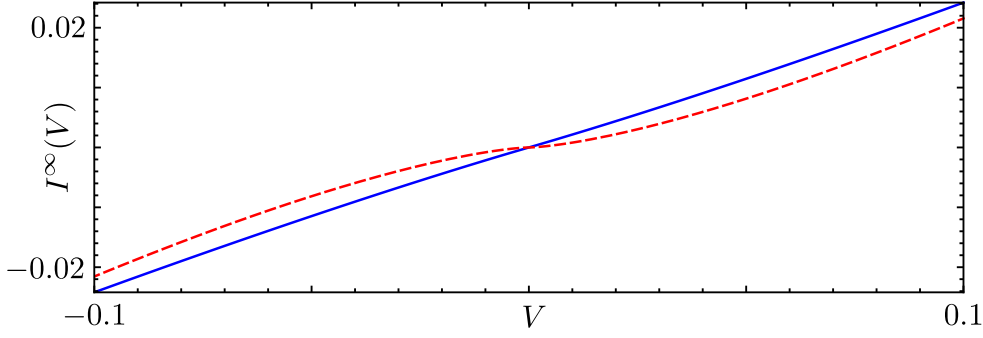
Figure 2.6: Asymptotic total charge current $I^\infty(V)$ [units $q|\lambda|^2(\pi^2 v_F)^{-1}$] as a function of V [units $v_F(qa)^{-1}$] for a quenched LL with $K_i = 0.8 \to K_f = 0.4$ (solid blue) and for a non-quenched zero-temperature LL with $K = 0.4$ (dashed green). In the presence of the quench $I(V)$ exhibits a behavior $\propto V$ for $V \to 0$. This is in sharp contrast with the non-quenched case, where a more common LL-like power-law decay $\propto V^{\nu_{eq}}$ emerges.

strong one) one finds $\nu = 2.4$: it could thus be difficult to distinguish between universal and non-universal power laws. Second, as can be seen from the inset of Fig. 2.7, coefficients of the transient terms in Eq. (2.120) are such that $|\mathcal{I}_{\eta,2}(V)| \ll |\mathcal{M}_\eta^I(V,t)|$ for any reasonable quench. This implies that the universal behavior is always at a great disadvantage compared to the non-universal one and explains why one has to wait very long times to observe the leading power-law decay $\propto t^{-2}$.

2.4.2 Tunneling energy current

As we have seen in the previous Section charge current may not be the best tool to investigate the universal dynamics induced by the entanglement between bosonic excitations. Now, we will focus on another important transport property of the system which, as we shall see below, allows for a neat observability of the power-law behavior $\propto t^{-2}$, namely the tunneling energy current [122, 134, 136]. It is defined as

$$P_\eta(V,t) = \partial_t \int_{-\infty}^{\infty} \langle \delta \hat{\mathcal{H}}_\eta(x,t) \rangle \, dx, \tag{2.123}$$

with the Hamiltonian density [see also Eq. (2.36)]

$$\hat{\mathcal{H}}_\eta(x,t) = \frac{u_f}{2} [\partial_x \hat{\phi}(x - \eta u_f t)]^2. \tag{2.124}$$

As in Eq. (2.107), the symbol δ means that we are looking to the average variation of $\hat{\mathcal{H}}_\eta(x,t)$ induced by the tunneling. Following the same procedure of the previous Section, we begin by substituting $\hat{\mathcal{O}}(x,t) = \hat{\mathcal{H}}_\eta(x,t)$ in Eq. (2.110). The commutator we need to evaluate is now

$$\left[\hat{\mathcal{H}}_\eta(x,t), \hat{\psi}_R^\dagger(x_0,\tau) \right] = -\frac{\eta u_f A_\eta}{\sqrt{2\pi}} \left[\frac{a}{a^2 + (z_{f,\eta} - \bar{z}_{f,\eta})^2} \right]$$
$$\times \partial_x \left\{ \hat{\phi}_\eta(z_{f,\eta}), \hat{\psi}_R^\dagger(x_0,\tau) \right\}, \tag{2.125}$$
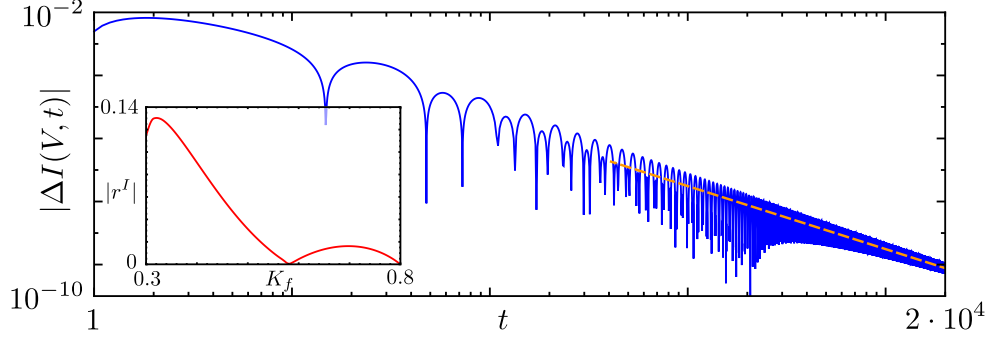
Figure 2.7: Time evolution of the total tunneling current $|\Delta I(V,t)|$ [units $q|\lambda|^2(2\pi^2 v_F)^{-1}$] as a function of t (units av_F^{-1}) for the quench $K_i = 0.8 \rightarrow K_f = 0.4$ (solid blue). The dashed orange line represents the universal power law t^{-2}. The presence of the non universal power-law decay $t^{-\nu-1}$ results in marked oscillations and the universal behavior emerges only at very long times. *Inset*: ratio $|r^I| = |\mathcal{I}_{\eta,2}/\mathcal{M}_\eta^I(V,t^*)|$ between coefficients of the leading terms of the Eq. (2.120) as a function of the post-quench Luttinger parameter K_f for $K_i = 0.8$. Here, t^* is such that $\mathcal{M}_\eta^I(V,t^*)$ is maximum. Clearly, for any reasonable quench, $|\mathcal{I}_{\eta,2}| \ll |\mathcal{M}_\eta^I(V,t)|$ and therefore the universal power-law contribution is hard to be observed. Here, $V = 0.1\, v_F(qa)^{-1}$.

with $z_{f,\eta} = x - \eta u_f t$ and $\bar{z}_{f,\eta} = x_0 - \eta u_f \tau$. From the above equation it emerges that quantum averages of the form

$$\langle \hat{\psi}_R^\dagger(x_0,\tau_2)\hat{\phi}_\eta(z_\eta)\hat{\psi}_R(x_0,\tau_1)\rangle \tag{2.126}$$

have to be computed. This can be done by using the bosonization formula of Eq. (2.10), the relation

$$\hat{\phi}_\eta(z_\eta) = -i\partial_y e^{iy\hat{\phi}_\eta(z)}\Big|_{y=0} \tag{2.127}$$

and the identities introduced in Eqs. (2.41) and (2.42). We obtain

$$P_\eta(V,t) = P^0 \operatorname{Re}\left\{\int_0^t G^<(t,t-\tau)\mathcal{F}_\eta(t,\tau)G_P^>(\tau)\cos(qV\tau)\,d\tau\right\}, \tag{2.128}$$

with $P^0 = 2|\lambda|^2 u_f$ and

$$\mathcal{F}_\eta(t,\tau) = A_\eta^2 \mathcal{F}_1(\tau) - \gamma\mathcal{F}_2(t,\tau), \tag{2.129a}$$

$$\mathcal{F}_1(\tau) = \frac{\theta_+^2}{a - iu_f\tau} - \frac{\theta_-^2}{a + iu_f\tau}, \tag{2.129b}$$

$$\mathcal{F}_2(t,\tau) = \frac{2iu_f(2t-\tau)}{a^2 + u_f^2(2t-\tau)^2} - \frac{4iu_f t}{a^2 + 4u_f^2 t^2}. \tag{2.129c}$$

At first glance, one immediately sees that, in sharp contrast with the charge current, $P_\eta(V,t)$ exhibits a non-trivial dependence on the chirality index η. In particular, it can be decomposed in a chirality-dependent contribution and in a chirality-independent one,

$$P_\eta(V,t) = A_\eta^2 P_1(V,t) + \gamma P_2(V,t). \tag{2.130}$$

As we will discuss later in the Chapter, this will result in some intriguing fractionalization phenomena and allows for a very neat detection of the universal power-law decay $\propto t^{-2}$. In passing, we note that also the energy current $P_\eta(V, t)$ can be understood in terms of the spectral properties of the system itself. Indeed, it is possible to show that [136]

$$G^<(t, t - \tau)\mathcal{F}_\eta(t, \tau) = \left[\frac{1}{iu_f} \left(\partial_{\bar{t}} - \eta u_f \partial_\xi \right) G_R^<(\xi; \bar{t}, t - \tau) \right]_{\substack{\bar{t}=t \\ \xi=0}}, \qquad (2.131)$$

with

$$G_R^<(\xi; t_1, t_2) = i\langle \psi_R^\dagger(0, t_2)\psi_R(\xi, t_1) \rangle \qquad (2.132)$$

the non-local lesser Green function of the $R-$branch.

We now consider the long-time behavior of $P_\eta(V, t)$. Since the function $\mathcal{F}_\eta(t, \tau)$ does not add any new poles or branch points, we can proceed with the same steps leading to Eq. (2.120). In particular, separating the contributions from $\tau \sim 0$ and $\tau \sim t$, we get

$$P_\eta(V, t) \approx P_{\eta,0}(V, t) + P_{\eta,t}(V, t)$$

$$= P_\eta^\infty(V) + \sum_{n=2}^\infty \frac{\mathcal{P}_{\eta,n}(V)}{t^n} + \frac{\mathcal{M}_\eta^P(V, t)}{t^{\nu+2}}, \qquad (2.133)$$

where

$$P_\eta^\infty(V) = A_\eta^2 P^0 \mathrm{Re} \left[\int_0^\infty G_\infty^<(\tau)\mathcal{F}_1(\tau)G_P^>(\tau) \cos(qV\tau)\, d\tau \right] \qquad (2.134a)$$

is the asymptotic chiral energy current and

$$\mathcal{P}_{\eta,2}(V) = -\frac{\gamma}{2} \left\{ \frac{d^2}{q^2 dV^2} P_\eta^\infty(V) + \frac{P^0}{u_f} \mathrm{Re} \left[\int_0^\infty G_\infty^<(\tau)G_p^>(\tau) \cos(qV\tau) i\tau\, d\tau \right] \right\}, \qquad (2.134b)$$

$$\mathcal{M}_\eta^P(V, t) \approx -\frac{P^0}{2\pi^2 a^2 v_F}[A_\eta^2(\theta_+^2 + \theta_-^2) - \gamma]\left(\frac{a}{u_f} \right)^{\nu_+ + \nu_- + 1} \frac{\cos\left[\frac{\pi}{2}(\nu_+ - \nu_-)\right]}{4^{2\gamma}}$$

$$\times \int_0^\infty \frac{\cos[qV(t - y)]}{[a^2/(2u_f)^2 + y^2]^\gamma}\, dy. \qquad (2.134c)$$

The long-time behavior of the chiral energy current given in Eq. (2.133) has the same structure of the one we found for both the NESF and the charge current: It consists of a steady state value, $P_\eta^\infty(V)$, a universal transient contribution $\propto t^{-2}$ and a non-universal one, $\propto t^{-\nu-2}$. The crucial point is that the exponent of the latter picks up an extra t^{-1} with respect to the non-universal term of the tunneling current, while the universal contribution still remains $\propto t^{-2}$. This results in a enhanced observability of the universal behavior induced by the decay of entanglement between chiral bosonic fields $\hat{\phi}_{f,+}(x)$ and $\hat{\phi}_{f,-}(x)$.

Before focusing on this issue, let us briefly address the asymptotic chiral, $P_\eta(V, t)$, and total, $P^\infty(V) = \sum_\eta P_\eta^\infty(V)$, energy currents. They are shown in
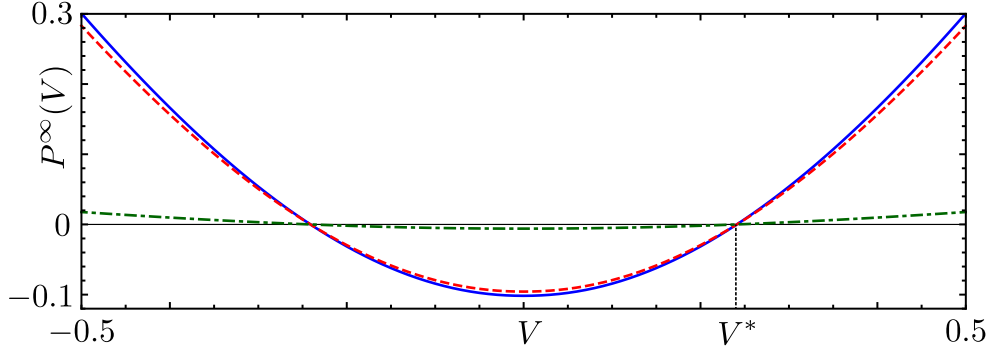
Figure 2.8: Plot of total $P^\infty(V)$ (blue, solid) and chiral $P^\infty_\eta(V)$ (red, dashed for $\eta = +$ and green, dash-dotted for $\eta = -$) energy currents [units $P^0(2\pi^2 a^2 v_F)^{-1}$] as a function of V [units $v_F(qa)^{-1}$] after the quench $K_i = 0.9 \to K_f = 0.6$. Note that $P^\infty_\eta(V^*) = P^\infty(V^*) = 0$ while, $|V| < V^*$, $P^\infty_\eta(V), P^\infty(V) < 0$: For small biases the energy injected by the quench flows *from* the system *to* the probe.

Fig. 2.8. Interestingly, there exists a whole range of biases $|V| < V^*$ for which both $P^\infty_\eta(V)$ and $P_\eta(V,t)$ are negative, implying that the energy is flowing *from* the system *to* the probe. This phenomenon is due to the fact that the quench injects an extensive amount of energy into the LL, resulting in effects similar to an effective heating of the system. Here, $V^* > 0$ is the bias such that $P^\infty_\eta(\pm V^*) = 0$ and a perfect balance between the energy injected by the probe and the one released by the system occurs.

The transient dynamics of $P_\eta(V,t)$ is shown in Fig. 2.10. Clearly, the chiral energy current represents a promising tool to elucidate the universal dynamics of the system. This is due, in essence, to the faster decay of the non-universal transient contribution $\propto t^{-\nu-2}$. Moreover, the excess chiral energy current $\Delta P_\eta(V,t) = P_\eta(V,t) - P^\infty_\eta(V)$ displays a striking dependence on the chirality index η. This fact turns out to help even more in detecting the universal behavior $\propto t^{-2}$. Indeed, as can be seen in Fig. 2.10(a), the non-universal decay mostly affects $\Delta P_+(V,t)$ while $\Delta P_-(V,t)$ exhibits an almost perfect power-law behavior $\propto t^{-2}$, which emerges even at small time scales. Moreover, within the time-range we are interested in, one has $|\Delta P_-(V,t)| \gg |\Delta P_+(V,t)|$: The relaxation of the total energy current $P(V,t) = \sum_\eta P_\eta(V,t)$ is thus controlled essentially by the leading universal contribution $\propto t^{-2}$ of $P_-(V,t)$. It is worth noting that this leads to an intriguing effect. Indeed, during the transient, the majority of the *excess* energy current injected from the probe flows in the $\eta = -$ direction. This is in sharp contrast with the steady-state contribution, which is always dominated by the $\eta = +$ chirality (see Fig. 2.8), and with the non-quenched case, where one finds $P_+(V,t) \propto P_-(V,t)$ with $|P_+(V,t)| \geq |P_-(V,t)|$. Moreover, we also stress here that this effect does not exist for the chiral charge currents, which always satisfies $I_+(V,t) \propto I_-(V,t)$ with $|I_+(V,t)| > |I_-(V,t)|$ [see Eq. (2.116)]. This fact becomes even more striking when $V = \pm V^*$. Indeed, in this case, we have $P^\infty_\eta(V^*) = 0$ and then $P_\eta(V^*,t) = \Delta P_\eta(V^*,t)$. In Fig. 2.9 we show the behavior of $P_\eta(V^*,t)$ for the quench protocol $K_i = 0.9 \to K_f = 0.6$, which
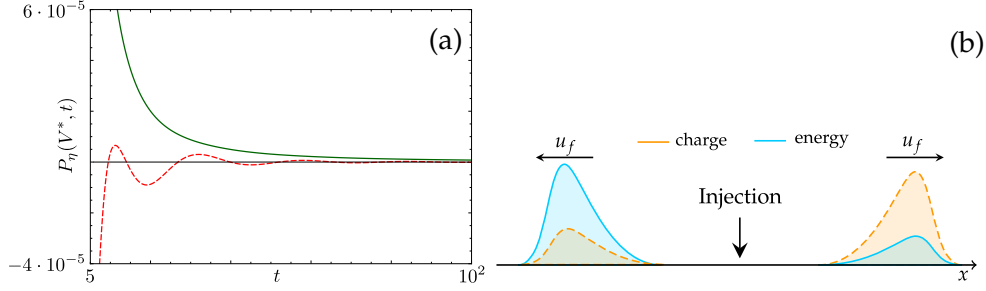
Figure 2.9: Panel (a): Plot of $P_-(V^{*,t})$ (green, solid) and $P_+(V^*,t)$ (red, dashed) [units $P^0(2\pi^2 av_F)^{-1}$] as function of time t [units $(vk_F)^{-1}$] for the quench $K_i = 0.9 \to K_f = 0.6$. Here, $V = 0.1\, v(aq)^{-1}$. Panel (b): Sketch of charge (orange) and energy (blue) currents for an idealized injection of a single right-moving particle. While most of the injected charge flows towards the direction $\eta = +$, the energy travels mainly in the opposite one, $\eta = -1$.

corresponds to a charge fractionalization ratio $R_\eta^Q = 0.8$. This implies that the majority of the injected charge flows in the $\eta = +$ direction. On the other hand, during the entire transient $|P_-(V^*,t)| > |P_+(V^*,t)|$ and thus the injected energy current flows predominantly in the $\eta = -$ direction [see Panel (b) of Fig. 2.9]. We should, however, point out that this behavior is quite peculiar of the regime with $P_\eta(V,t) = 0$ and the region around $V = V^*$ in which it can be observed is quite narrow.

Finally, to further exploit this peculiar chirality-dependence of the excess energy current, we inspect the energy fractionalization ratio

$$R_\eta(V,t) = \frac{P_\eta(V,t)}{\sum_\eta P_\eta(V,t)} \tag{2.135}$$

in the transient regime [133, 134]. Its relaxation towards the steady-state value $R_\eta^\infty = A_\eta^2/(A_+^2 + A_-^2)$ [133, 134] is depicted in Fig. 2.10(b), where we show the behavior of the absolute value of $\Delta R_\eta(V,t) = R_\eta(V,t) - R_\eta^\infty$ for two different set of quench parameters. The universal decay $\propto t^{-2}$ emerges as clearly as in $\Delta P_-(V,t)$. Note that, since $R_\eta(V,t) = 1 - R_{-\eta}(V,t)$, one has $|\Delta R_\eta(V,t)| = |\Delta R_{-\eta}(V,t)|$, i.e. $|\Delta R_\eta(V,t)|$ does not depend on the chirality. Moreover, the fractionalization ratio has the key advantage to be time-independent in the non-quenched case, with $R_\eta(V,t) = R_\eta^\infty\ \forall V,t$. Therefore, the presence of a transient in $R_\eta(V,t)$ is a direct hallmark of the non-equilibrium dynamics of the system settled by the quench. Together with $\Delta P_-(V,t)$, it represents a very promising tool for the investigation of the quench-induced entanglement between counter-propagating chiral fields $\hat{\phi}_{f,\pm}(x)$ and its relaxation in time.

2.5 CONCLUSIONS

In summary, in this Chapter we have discussed the non-equilibrium dynamics of a 1D interacting system after a quantum quench. It has been
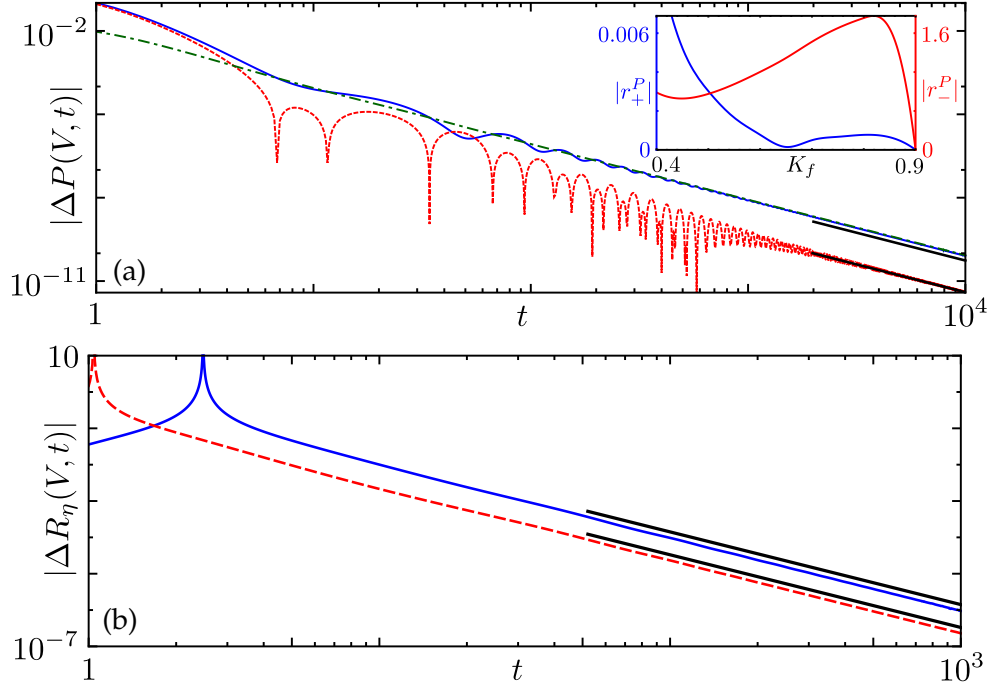
Figure 2.10: Panel (a): Plot of $|\Delta P(V,t)| = |\sum_\eta \Delta P_\eta(V,t)|$ (blue, solid), $|\Delta P_+(V,t)|$ (red, dashed) and $|\Delta P_-(V,t)|$ (green, dash-dotted) [units $P^0(2\pi^2 a v_F)^{-1}$] as function of time t [units $(vk_F)^{-1}$] for the quench $K_i = 0.9 \rightarrow K_f = 0.6$. *Inset*: ratios $|r_\eta^P| = |P_{\eta,2}(V)|/|\mathcal{M}_\eta^P(V,t^*)|$ between coefficients of the leading transient contributions of Eq. (2.133) as function of the post-quench Luttinger parameter K_f for $K_i = 0.9$. As in Fig. 2.7, t^* has been chosen such that $\mathcal{M}_\eta^{V,t^*}|$ is maximum. Note that $|r_+^P| \ll |r_-^P| \sim 1$, which results in an extremely neat signature of the universal behavior in the transient of $P_-(V,t)$. Panel (b): Plot of $|\Delta R_\eta(V,t)|$ as a function of time t [units $(vk_F)^{-1}$] for the quenches $K_i = 0.9 \rightarrow K_f = 0.6$ (blue, solid) and $K_i = 0.8 \rightarrow K_f = 0.4$ (red, dashed). Note that $|\Delta R_\eta(V,t)|$ does not depend on the chirality (see text). In both Panels solid black lines indicate the power law $\propto t^{-2}$ and $V = 0.1\,v(qa)^{-1}$.

shown that an interaction quench results in an initial entanglement between right- and left-moving density excitations, which is encoded in the time evolution of their cross-correlators. This represents a direct fingerprint of the quantum quench and deeply affects the relaxation towards the steady state of the system itself. We have shown this in the specific case of spectral and transport properties of a fermionic 1D system modeled as a spinless LL subject to an interaction quench. In particular, we demonstrated that the entanglement dynamics induces a universal long-time decay $\propto t^{-2}$ in the non-equilibrium spectral function of the LL, whose time-evolution is also affected by other non-universal power laws, with quench-dependent exponents. Interestingly, the universal character clearly emerges by considering charge and energy currents in a transport setup. In particular, fractionalization phenomena, peculiar of 1D interacting systems, can be used to probe the presence of quench-induced entanglement and its relaxation. Among all, the transient dynamics of the energy fractionalization ratio represents a promising tool to observe these universal features. Moreover, we have shown that in the steady state the low-bias power is negative, signaling an energy back-flow from the LL to the probe. When the net exchanged power is zero, a peculiar situation can be achieved in which the largest fraction of charge and the largest fraction of energy propagate in opposite directions.

We expect our discussions to be independent of the precise form of the quench protocol and of the tunneling Hamiltonian. The results contained in this Chapter can elucidate fundamental aspects of non-equilibrium physics settled by a quantum quench and can, in principle, be tested with state-of-the-art implementation of cold atomic systems or solid state devices.

Finally, we have also investigated the robustness of our results in the presence of a finite temperature, showing that the latter turns LL-like power laws into fast exponential decay while the universal power law $\propto t^{-2}$ survives and emerges even clearly [186]. Furthermore, in Ref. [172] we also studied in details how the injection from an extended tunneling region affects the steady-state regime, demonstrating that also in this case charge fractionalization retains no memory of the quench while energy partitioning is strongly modified by the latter.

3

OUT OF EQUILIBRIUM DENSITY DYNAMICS OF A QUENCHED FERMIONIC SYSTEM

In this Chapter we will study effects on quantum quenches in finite-size systems. To do so, in the first part we briefly introduce the formalism allowing to adapt the LL model and the bosonization technique described in Chap. 2 to systems with OBC, following the approach developed by Fabrizio and Gogolin in Ref. [187]. Then, in the second part of the Chapter, we use this formalism to investigate the time evolution of the particle density of a fermionic spinless LL with OBC subject to a finite duration quench of the inter-particle interaction. We focus on how the interplay between the time scale of the quenching protocol and the one introduced by the finite size of the system affects the transient and post-quench dynamics.

As we have discussed in Chap. 1 and in analogy with the Poincaré recurrence theorem (see also Appendix A), the finite size of the system implies a finite recurrence time t_{rec}. The system will never reach a steady state but it will continue to oscillate around a certain configuration [78]. On the other hand, the finiteness in time of the quenching protocol has even more interesting consequences. Indeed, we show that *both* turning on and turning off of the quench ramp create light-cone perturbations in the density, which survive in the post-quench region. The two perturbations, originating from the boundaries [162, 188], travel ballistically through the system with the *instantaneous* velocity of the bosonic excitations of the LL [167] and bounce elastically whenever they reach one of the edges. Furthermore, in the post-quench region, their wavefronts interfere destructively and, thus, the system dynamics is strongly affected by their relative position. Moreover, in spite of the finite size of the system, we find that for slow enough quenches the post-quench average density weakly oscillates in time around the result obtained with a GGE approach. For a fixed quench amplitude, the discrepancy between these two quantities decreases with an oscillatory behavior as a function of the quench duration, with local minima corresponding to a perfect overlap of the two light cones. Finally we obtain that, for a long enough quench, the GGE result approaches the ground state density associated with the final Hamiltonian of the system, showing again a decreasing oscillatory behavior as a function of the quench duration.

This Chapter is based on the results obtained in Ref. [189].

3.1 LUTTINGER LIQUID WITH OPEN BOUNDARY CONDI–TIONS

We start again from the 1D system of spinless fermions described by Eq. (2.1). In contrast to previous Chapter, we now consider a finite system confined within the region $0 \leq x \leq L$, L being the length of the system itself. Thus, instead of Eq. (2.4), we impose OBC on the Fermi field operator $\hat{\Psi}(x)$ [187],

$$\hat{\Psi}(0) = \hat{\Psi}(L) = 0. \tag{3.1}$$

In this case, the non-interacting single-particle energy levels and wave functions are given by

$$\varepsilon(k) = \frac{k^2}{2m}, \qquad \psi_k(x) = \frac{2}{L}\sin(kx), \tag{3.2}$$

respectively, with discretized momentum $k = \pi n/L$ (n being a positive integer). In the zero-temperature ground state of the system, denoted by $|F\rangle$, all the energy levels up to the Fermi energy $E_F = k_F^2 (2m)^{-1}$ are filled. The latter is associated with the Fermi wave vector $k_F = \pi N/L$, with N the total number of particles in the system. Finally, the Fermi operator can be decomposed in Fourier modes as

$$\hat{\Psi}(x) = \frac{2}{L}\sum_{k>0}\sin(kx)\hat{c}_k, \tag{3.3}$$

with $\hat{c}_k$ the annihilation operator of a fermion with momentum k.

LINEARIZATION Following the same steps outlined in Sec. 2.1, we linearize the spectrum of the system $\varepsilon(k)$ around the Fermi energy E_F, as shown in Fig. (3.2). We obtain

$$\varepsilon(k) = E_F + v_F(k - k_F), \tag{3.4}$$

which, in this case, is associated with right-moving fermions only. Here, $v_F = d\varepsilon(k)/dk|_{k_F}$ is the Fermi velocity of the system. As in the case with PBC, we extend the the linearized spectrum to $k \in (-\infty, \infty)$, thus introducing an infinite number of occupied fictitious states which can be properly taken into account by looking at the normal ordered value of operators introduced in Eq. (2.7). This allows to write the Fermi field operator of Eq. (3.2) as

$$\hat{\Psi}(x) \approx \hat{\Psi}_R(x) + \hat{\Psi}_L(x), \tag{3.5}$$

Here, we have introduced right ($r = R$, $\epsilon_R = 1$) and left ($r = L$, $\epsilon_L = -1$) moving fields,

$$\hat{\Psi}_r(x) = \frac{-i}{\sqrt{2L}}\sum_{k=-\infty}^{\infty} e^{i\epsilon_r kx}\hat{c}_k. \tag{3.6}$$

Note that, in sharp contrast with the fields encountered in Sec. 2.1, these fields have periodicity $2L$, i.e. $\hat{\Psi}_r(x) = \hat{\Psi}_r(x + 2L)$, and are not independent. Indeed,

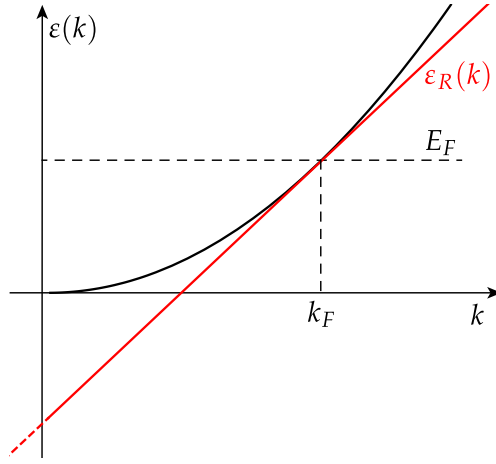$$\hat{\Psi}_L(x) = -\hat{\Psi}_R(-x). \tag{3.7}$$

Figure 3.1: Linearization procedure of the original single-particle spectrum $\varepsilon(k)$ (black curve) around the Fermi energy E_F in the LL model with OBC. The red line represents the dispersion relation of the linearized spectrum, associated with right-moving fermions. The dashed region signals the infinite number of occupied fictitious states introduced in the linearization process.

The degrees of freedom of the system are thus halved as a consequence of the constraint imposed by OBC. By fictitiously extending the domain of $\hat{\Psi}_R(x)$ to $-L \leq x \leq L$, it is then possible to rewrite the whole Fermi field operator of Eq. (3.5) in terms of the right-mover field only,

$$\hat{\Psi}(x) \approx \hat{\Psi}_R(x) - \hat{\Psi}_R(-x). \tag{3.8}$$

At this point, the "extended" right-mover field can be bosonized in the same way we discussed in the PBC case and, thus,[1]

$$\hat{\Psi}_R(x) = \frac{\hat{F}}{\sqrt{2\pi a}} e^{ik_F x} e^{-i\hat{\Phi}(x)}, \tag{3.9}$$

with

$$\hat{\Phi}(x) = i \sum_{q>0} \sqrt{\frac{\pi}{qL}} e^{-aq/2} \left(e^{iqx} \hat{b}_q - e^{-iqx} \hat{b}_q^\dagger \right) \tag{3.10}$$

the bosonic field operator associated with right-moving fermions. Here, a is a small-length cutoff, $q = \pi n_q / L$ (n_q being a positive integer), the bosonic annihilation (creation) operator $\hat{b}_q^{(\dagger)}$ are defined as

$$\hat{b}_q = \sqrt{\frac{\pi}{qL}} \sum_k \hat{c}_{k-q}^\dagger \hat{c}_k, \qquad \hat{b}_q^\dagger = \sqrt{\frac{\pi}{qL}} \sum_k \hat{c}_{k+q}^\dagger \hat{c}_k \tag{3.11}$$

and $\hat{F}$ is a Klein factor satisfying the same identities of Eq. (2.14). In contrast to the previous Section, in which we performed the limit $L \to \infty$, here we are

---

1 In the following definition of bosonic field and operators we will omit the branch index R since, as we have seen, it is the only one present when OBC are assumed.

interested in the case with a finite L. In this case, the commutation relations of Eq. (2.15) reads

$$\left[\hat{\Phi}(x), \hat{\Phi}(y)\right] = 2i \arctan\left\{\frac{\sin[\pi(x-y)/L]}{e^{\pi a/L} - \cos[\pi(x-y)/L]}\right\}. \tag{3.12}$$

Following Sec. 2.1, we now rewrite the kinetic contribution to the Hamiltonian of the linearized model in terms of bosonic operators. We obtain

$$\hat{H}_0 = v_F \int_{-L/2}^{L/2} dx\, \hat{\Psi}_R^\dagger(x)(-i\partial_x)\hat{\Psi}_R(x) \tag{3.13a}$$

$$= \sum_{q>0} v_F q\, \hat{b}_q^\dagger \hat{b}_q + \hat{H}_{0,N}, \tag{3.13b}$$

with $\hat{H}_{0,N} = \frac{\pi v_F \hat{N}^2}{2L}$ the zero-mode contribution and $\hat{N} = \sum_k\, :c_k^\dagger c_k:$ the particle number operator [2]. On the other hand, the particle density operator associated with right-movers is given by

$$\hat{\rho}_R(x) =: \hat{\Psi}_R(x)\hat{\Psi}_R(x) := \frac{\hat{N}}{2L} - \frac{\partial_x \hat{\Phi}(x)}{2\pi} \tag{3.14a}$$

$$= \frac{\hat{N}}{2L} + \frac{1}{2\pi}\sum_{q>0}\sqrt{\frac{\pi q}{L}}e^{-aq/2}\left(e^{iqx}\hat{b}_q + e^{-iqx}\hat{b}_q^\dagger\right) \tag{3.14b}$$

TOTAL DENSITY OPERATOR   Of particular interest for rest of this Chapter will be the total particle density operator,

$$\hat{\rho}(x) =: \hat{\Psi}^\dagger(x)\hat{\Psi}(x) := \hat{\rho}_{LW}(x) + \hat{\rho}_F(x), \tag{3.15}$$

where we used the identity of Eq. (3.8). Here we distinguish two different terms, which can be rewritten using Eq. (3.9) and (3.14). In particular,

$$\hat{\rho}_{LW}(x) = \hat{\rho}_R(x) + \hat{\rho}_R(-x) = \frac{\hat{N}}{L} + \frac{\partial_x \hat{\Phi}_a(x)}{\pi} \tag{3.16a}$$

is the *long-wave* contribution and

$$\hat{\rho}_F(x) = - :\hat{\Psi}_R^\dagger(x)\hat{\Psi}_R(-x): - :\hat{\Psi}_R^\dagger(-x)\hat{\Psi}_R(x):$$

$$= -\frac{1}{\pi a}\cos\left[2k_F x - 2\hat{\Phi}_a(x) - 2f(x)\right] \tag{3.16b}$$

is the so called *Friedel* contribution [19, 187, 190, 191], which arises due to the presence of OBC. Here, we used Eq. (2.41) and we have introduced the antisymmetric component of the bosonic field,

$$\hat{\Phi}_a(x) = \frac{1}{2}\left[\hat{\Phi}(-x) - \hat{\Phi}(x)\right] = \sum_{q>0}\sqrt{\frac{\pi}{qL}}e^{-aq/2}\sin(qx)\left(\hat{b}_q + \hat{b}_q^\dagger\right), \tag{3.17}$$

and the function [see the commutator in Eq. (3.12)]

$$f(x) = \frac{1}{4i}\left[\hat{\Phi}(x), \hat{\Phi}(-x)\right] = \frac{1}{2}\arctan\left[\frac{\sin(2\pi x/L)}{e^{\pi a/L} - \cos(2\pi x/L)}\right]. \tag{3.18}$$

---

[2] Again, as already explained in Sec. 2.1, here and in the following we neglect terms in the Hamiltonian linear in $\hat{N}$.

As clearly emerges from Eq. (3.16b), the Friedel term oscillates with a period which depends on the total number of particle N. Collecting all the above results, one obtains for the total particle density operator

$$\hat{\rho}(x) = \frac{\hat{N}}{L} \left\{ 1 - \cos\left[\frac{2\pi\hat{N}}{L}x - 2\hat{\Phi}_a(x) - 2f(x) \right] \right\} + \frac{1}{\pi}\partial_x\hat{\Phi}_a(x), \qquad (3.19)$$

where we made the identification $a \rightarrow \pi N/L$. The latter is necessary in order to have $\langle \hat{\rho}(0) \rangle = \langle \hat{\rho}(L) \rangle = 0$. Note that this *ad hoc* constraint can be derived more rigorously following a point-splitting procedure, which however leads to the same results [192, 193].

INTERACTIONS   We now turn to the interacting model. Looking at Eq. (2.19) and using the connection between right- and left-movers shown in Eq. (3.7), one obtains

$$\hat{H}_{\text{int}} = \hat{H}_{\text{int}}^{(2)} + \hat{H}_{\text{int}}^{(4)} = \pi \int_{-L}^{L} dx \left[g_4 : \hat{\rho}_R(x)\hat{\rho}_R(x) : + g_2 : \hat{\rho}_R(x)\hat{\rho}_R(-x) : \right].$$
$$(3.20)$$

Note that, although we started from a system with local interactions, the presence of OBC results in the non-locality of the term $\propto g_2$. Nevertheless, the total Hamiltonian $\hat{H}$ is still quadratic in bosonic operators and can thus be diagonalized. In particular, from Eqs. (3.10) and (3.14) one obtains

$$\hat{H} = \hat{H}_{\text{bos}} + \hat{H}_N, \qquad (3.21)$$

with

$$\hat{H}_{\text{bos}} = \sum_{q>0} q \left[(v_F + g_4)\, \hat{b}_q^\dagger \hat{b}_q + \frac{g_2}{2} \left(\hat{b}_q \hat{b}_q + \hat{b}^\dagger \hat{b}_q^\dagger \right) \right], \qquad (3.22a)$$

$$\hat{H}_N = \frac{\pi u_N}{2L}\hat{N}^2, \qquad \text{where } u_N = v_F + g_4 + g_2. \qquad (3.22b)$$

The bosonic Hamiltonian $\hat{H}_{\text{bos}}$ is very similar to the one obtained with PBC - see Eq. (2.21a) - and can be diagonalized by the same Bogolubov transformation,

$$\hat{B}_q = A_+\hat{b}_q + A_-\hat{b}_q^\dagger, \qquad \text{with } A_\pm = \frac{1}{2}\left(\frac{1}{\sqrt{K}} \pm \sqrt{K} \right). \qquad (3.23)$$

We recall that the Luttinger parameter

$$K = \sqrt{\frac{v_F - g_2 + g_4}{v_F + g_2 + g_4}} \qquad (3.24)$$

is defined in such a way that $K = 1$ represents the non-interacting regime, while one finds $K < 1$ ($K > 1$) in the presence of repulsive (attractive) interactions. After the Bogolubov transformation of Eq. (3.23), the diagonalized bosonic Hamiltonian reads

$$\hat{H}_{\text{bos}} = u \sum_{q>0} q\hat{B}_q^\dagger \hat{B}_q, \qquad (3.25)$$

with

$$u = \sqrt{(v_F + g_4)^2 - (g_2)^2} \tag{3.26}$$

the renormalized velocity of elementary excitations of the system. For the sake of simplicity, in the following we will focus on the Galilean invariant case [61–63] with $g_2 = g_4 = g$. Here, one finds

$$K = \left(1 + \frac{2g}{v_F}\right)^{-\frac{1}{2}} \quad \text{and} \quad u = \frac{v_F}{K}. \tag{3.27}$$

To conclude, for future convenience we now rewrite the bosonic field $\hat{\Phi}(x)$ and its antisymmetric component $\hat{\Phi}_a(x)$ in terms of the new bosonic operators introduced in Eq. (3.23). We obtain

$$\hat{\Phi}(x) = \frac{i}{\sqrt{K}} \sum_{q>0} \sqrt{\frac{\pi}{qL}} e^{-aq/2} \left[\cos(qx) + iK\sin(qx)\right] \hat{B}_q + \text{H.c.}, \tag{3.28}$$

$$\hat{\Phi}_a(x) = \sqrt{K} \sum_{q>0} \sqrt{\frac{\pi}{qL}} e^{-aq/2} \sin(qx) \left(\hat{B}_q + \hat{B}_q^\dagger\right), \tag{3.29}$$

where in the first equation H.c. denotes the Hermitian conjugate.

3.1.1 Density in an equilibrium spinless Luttinger liquids

Before turning our attention to the behavior of the particle density in an out-of-equilibrium regime, which will be the focus of this Chapter, we briefly examine the equilibrium regime in the zero-temperature limit. To do so, we evaluate the quantum average of the density operator introduced in Eq. (3.19) over the system ground state, denoted by $\langle ... \rangle_0$. We get

$$\rho(x) = \frac{N}{L} \left\{ 1 - \frac{1}{2} \left[e^{i\left(\frac{2\pi N}{L}x - 2f(x)\right)} e^{-2\langle \hat{\Phi}_a^2(x) \rangle_0} + \text{H.c.} \right] \right\}, \tag{3.30}$$

where we exploited Eq. (2.42) to rewrite the average of the exponential term. Using Eq. (3.29) and the fact that $\langle \hat{B}_q^{(\dagger)} \hat{B}_{q'}^{(\dagger)} \rangle_0 = \langle \hat{B}_q^\dagger \hat{B}_{q'} \rangle_0 = 0$ while $\langle \hat{B}_q \hat{B}_{q'}^\dagger \rangle_0 = \delta_{q,q'}$, one finds

$$\langle \hat{\Phi}_a^2(x) \rangle_0 = \frac{\pi K}{L} \sum_{q>0} \frac{e^{-aq}}{q} \sin^2(qx)$$

$$= \frac{K}{2} \log \left[\frac{\sqrt{\sinh^2\left(\frac{\pi a}{2L}\right) + \sin^2\left(\frac{\pi x}{L}\right)}}{\sinh\left(\frac{\pi a}{2L}\right)} \right]. \tag{3.31}$$

The exponential term containing the quantum average thus evaluates to

$$E_{\text{nq}}(x) \equiv e^{-2\langle \hat{\Phi}_a(x) \rangle_0} = \exp\left[-\frac{2\pi K}{L} \sum_{q>0} \frac{e^{-aq}}{q} \sin^2(qx) \right] \equiv [\mathcal{K}(x)]^K, \tag{3.32}$$

where we have introduced the function

$$\mathcal{K}(x) = \frac{\sinh\left(\frac{\pi a}{2L}\right)}{\sqrt{\sinh^2\left(\frac{\pi a}{2L}\right) + \sin^2\left(\frac{\pi x}{L}\right)}}. \tag{3.33}$$

Turning back to Eq. (3.30) and collecting all the above results, we finally obtain

$$\rho(x) = \frac{N}{L} \left\{ 1 - E_{\mathrm{nq}}(x) \cos \left[\frac{2\pi N}{L} x - 2f(x) \right] \right\}. \qquad (3.34)$$

The density profile oscillates around the mean value N/L with a frequency depending on the number of particle in the system and an amplitude modulated by the *envelope function* $E_{\mathrm{nq}}(x)$, as can be seen in Fig. 3.2. Note that these oscillations [19, 190], called *Friedel oscillations*, are present regardless the strength of inter-particle interactions and are due solely to the OBC. In particular, they exhibit N maxima and $N-1$ minima whose positions, x_{max} and x_{min} respectively, are independent of the Luttinger parameter K and are determined by

$$\frac{2\pi N}{L} x_{\mathrm{max}} - 2f(x_{\mathrm{max}}) = \pi(2n+1), \qquad \text{with } 0 \leq n \leq N-1, \qquad (3.35a)$$

$$\frac{2\pi N}{L} x_{\mathrm{min}} - 2f(x_{\mathrm{min}}) = 2\pi m, \qquad \text{with } 1 \leq m \leq N-1. \qquad (3.35b)$$

On the other hand, the envelope function $E_{\mathrm{nq}}(x)$ strongly depends on inter-particle interactions, as can be clearly seen from Fig. 3.2. This function ensures that $\rho(x) = 0$ at the boundaries, since $E_{\mathrm{nq}}(0) = E_{\mathrm{nq}}(L) = 1$, and controls the amplitude of the oscillations in the bulk of the system. In particular, in the latter region $E_{\mathrm{nq}}(x)$ is rather small for $K \sim 1$, leading to a suppression of the Friedel oscillations, while it grows for smaller K. This behavior is due to the fact that for stronger interactions the repulsion among the particles leads to the formation of a correlated state inside the system, the so called *Wigner molecule*, which is the finite size counterpart of the *Wigner crystal* [19, 61, 158, 194–197]. In this regime, the particles tend to arrange into a lattice, with lattice constant $d \sim L/N$. However, due to the finite size of the system, Heisenberg's uncertainty principle implies that particles will continue to oscillate around their equilibrium position and, thus, that a complete crystallization cannot occur.

3.2 QUENCHED LUTTINGER LIQUID WITH OPEN BOUNDARY CONDITIONS

We now move to the out-of-equilibrium situation. In particular, we consider a fermionic spinless LL confined in the region $0 \leq x \leq L$ with OBC, subject to a quench of the inter-particle interaction from an initial value K_i to the final one K_f. Recalling Eqs. (3.21) and (3.25), for $t < 0$ the system is prepared in the ground state of the initial Hamiltonian

$$\hat{H}_i = \sum_{q>0} q \left[(v_F + g_i) \hat{b}_q^\dagger \hat{b}_q + \frac{g_i}{2} \left(\hat{b}_q \hat{b}_q + \hat{b}_q^\dagger \hat{b}_q^\dagger \right) \right] + \hat{H}_N \qquad (3.36a)$$

$$= \sum_{q>0} q u_i \hat{B}_{i,q}^\dagger \hat{B}_{i,q} + \hat{H}_N, \qquad (3.36b)$$
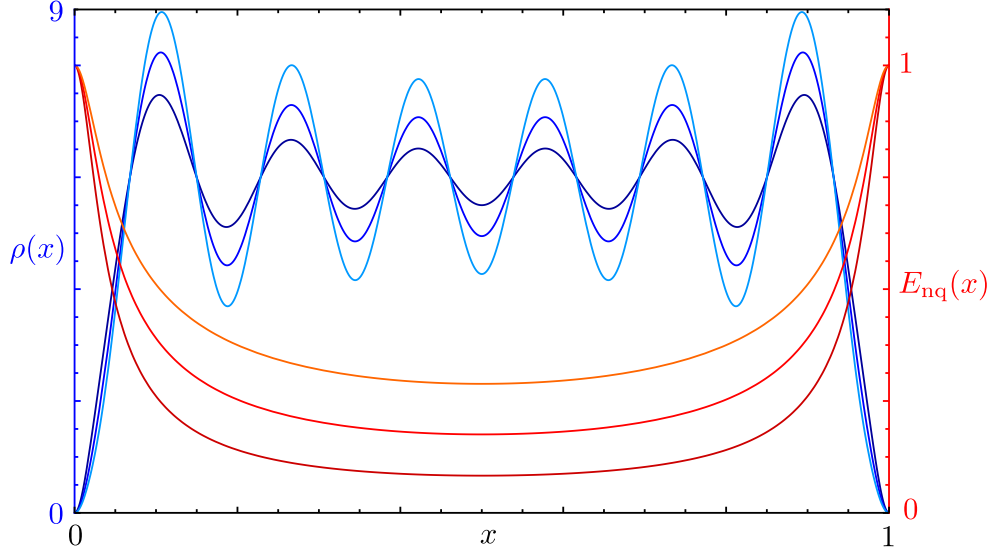
Figure 3.2: Blue curves show the behavior of the particle density $\rho(x)$ (units L^{-1}) as a function of x (units L) for $N = 6$. From darker to lighter blue, $K = 1$, $K = 0.7$, and $K = 0.5$. Red lines represent the envelope function $E_{\mathrm{nq}}(x)$ as a function of x (units L) for $N = 6$ and, from darker to lighter red, $K = 1$, $K = 0.7$, and $K = 0.5$. Here, we fixed $a = L(\pi N)^{-1}$ as explained in the text.

where $\hat{H}_N$ is given in Eq. (3.21), $u_i = v_F/K_i$ and the bosonic operators $\hat{b}_q$ and $\hat{B}_{i,q}$ are connected by the Bogolubov transformation of Eq. (3.23). Therefore, $\hat{B}_{i,q} = A_{i,+}\hat{b}_q + A_{i,-}\hat{b}_q^\dagger$, with

$$A_{i,\pm} = \frac{1}{2}\left(\frac{1}{\sqrt{K_i}} + \sqrt{K_i}\right). \tag{3.37}$$

Then, at $t = 0$ the system undergoes a quench of the inter-particle interaction [167–169, 198] from g_i to g_f with a quenching protocol with amplitude $g_f - g_i = v_F(K_f^{-2} - K_i^{-2})/2$ and with time duration τ. Here, $K_f = (1 + 2g_f/v_F)^{-1/2}$ is the final Luttinger parameter. In this Section, we discuss a generic quench protocol, whose time dependence is described by a function $Q(t)$ such that $Q(t \leq 0) = 0$ and $Q(t \geq \tau) = 1$. Then, in next Sections, we will focus on the specific case of a linear ramp (see Sec. 3.2.1 for details) when more explicit calculations are required. In terms of the initial bosonic operators $\hat{B}_{i,q}$, the time-dependent Hamiltonian can be written as

$$\hat{H}(t) = \sum_{q>0} q\left[u(t)\hat{B}_{i,q}^\dagger\hat{B}_{i,q} + \frac{1}{2}g(t)\left(\hat{B}_{i,q}^\dagger\hat{B}_{i,q}^\dagger + \hat{B}_{i,q}\hat{B}_{i,q}\right)\right] + \hat{H}_N + \Omega(t), \tag{3.38}$$

with

$$\Omega(t) = \frac{e^{\pi a/L}}{2(1 - e^{\pi a/L})^2}\frac{u_i\eta}{2}\left(1 - \frac{1}{K_i}\right)Q(t) \tag{3.39a}$$

$$u(t) = u_i\left[1 + \frac{\eta}{2}Q(t)\right], \tag{3.39b}$$

$$g(t) = \frac{u_i\eta}{2}Q(t). \tag{3.39c}$$

Here, we introduced the parameters

$$\eta = \mu^2 - 1 \qquad \text{and} \qquad \mu = \frac{K_i}{K_f}, \tag{3.40}$$

while $\Omega(t)$ represents the energy mismatch of the instantaneous ground state of $\hat{H}(t)$ at time t with respect to the initial one. The time evolution of initial bosonic operators can be directly obtained by solving the Heisenberg equation of motion [168, 169, 198]

$$i\partial_t \hat{B}_{i,q}(t) = \left[\hat{H}(t), \hat{B}_{i,q}(t)\right] = qu(t)\hat{B}_{i,q}(t) + qg(t)\hat{B}_{i,q}^\dagger. \tag{3.41}$$

The solution of this equation has the form

$$\hat{B}_{i,q}(t) = f(q,t)\hat{B}_{i,q} - h^*(q,t)\hat{B}_{i,q}^\dagger, \tag{3.42}$$

with bosonic operators on the right hand side evaluated at $t = 0$ and the functions $f(q,t)$ and $h(q,t)$ carrying all the time dependence. Due to bosonic commutation rules, the latter have to satisfy the relation $|f(q,t)|^2 - |h(q,t)|^2 = 1$, $\forall q, t$. The equation of motion of Eq. (3.41) can thus be translated in the following system of coupled differential equations for the functions $f(q,t)$ and $h(q,t)$ [169, 198]

$$i\begin{bmatrix} \dot{f}(q,t) \\ \dot{h}(q,t) \end{bmatrix} = q\begin{bmatrix} u(t) & g(t) \\ -g(t) & -u(t) \end{bmatrix}\begin{bmatrix} f(q,t) \\ h(q,t) \end{bmatrix}, \tag{3.43}$$

with the initial condition $f(q,0) = 1$ and $h(q,0) = 0$. Here, the dot indicates the derivate with respect to time. To solve this system it is convenient to move to the basis defined by the functions

$$D(q,t) = f(q,t) - h(q,t), \tag{3.44a}$$
$$S(q,t) = f(q,t) + h(q,t). \tag{3.44b}$$

In this new basis, using the explicit expressions for $u(t)$ and $g(t)$ given in Eqs. (3.39b) and (3.39c), one can rewrite the original system of Eq. (3.43) as

$$\ddot{D}(q,t) + [q\bar{u}(t)]^2 D(q,t) = 0, \tag{3.45a}$$
$$\dot{D}(q,t) + iqu_i S(q,t) = 0, \tag{3.45b}$$

with initial conditions $D(q,0) = S(q,0) = 1$ and $\dot{D}(q,0) = -iqv_i$. Here,

$$\bar{u}(t) = u_i\gamma(t), \qquad \text{with } \gamma(t) = \sqrt{1 + \eta Q(t)}, \tag{3.46}$$

is the *instantaneous* bosonic modes velocity. Indeed, at any time $\bar{t}$ the system Hamiltonian of Eq. (3.38) is diagonal in the instantaneous bosonic operators $\hat{B}_{\bar{t},q}$ [167] ,

$$\hat{H}_{\text{bos}}(\bar{t}) = \sum_{q>0} q\bar{u}(\bar{t})\hat{B}_{\bar{t},q}^\dagger \hat{B}_{\bar{t},q}, \tag{3.47}$$

with $\bar{u}(\bar{t})$ given precisely by Eq. (3.46). Here, $\hat{B}_{q,\bar{t}} = A_{\bar{t},+}\hat{b}_q + A_{\bar{t},-}\hat{b}_q^\dagger$, with coefficients $A_{\bar{t},\pm} = \{[\gamma(\bar{t})]^{-1/2} \pm [\gamma(\bar{t})]^{1/2}\}/2$.

Once solved Eq. (3.45a) for the function $D(q,t)$, one immediately obtains $S(q,t)$ by differentiation and then, from Eq. (3.44), the coefficients $f(q,t)$ and $h(q,t)$. Thus, in the following we will focus only on solving Eq. (3.45a).

3.2.1 Linear quench

The model developed so far is valid for any arbitrary quenching protocol $Q(t)$ with $Q(t \leq 0) = 0$ and $Q(t \geq \tau) = 1$. In order to obtain explicit results, we now specialize the discussion by choosing a quench with a linear ramp defined as [169, 198]

$$Q(t) = \begin{cases} 0 & \text{for } t < 0 \text{ (region I)}, \\ t/\tau & \text{for } 0 \leq t \leq \tau \text{ (region II)}, \\ 1 & \text{for } t > \tau \text{ (region III)}. \end{cases} \tag{3.48}$$

With this protocol Eq. (3.45a) for $D(q,t)$ can be solved in the three regions introduced by Eq. (3.48), with properly matching conditions on the boundaries of each region. In particular, one obtains [167, 189]

$$D^{\text{I}}(q,t) = e^{-iu_i t}, \tag{3.49a}$$

$$D^{\text{II}}(q,t) = \frac{\pi \Delta_q \gamma(t)}{\sqrt{3}} \left\{ \mathcal{A}(\Delta_q) J_{-\frac{1}{3}} \left[\Delta_q \gamma(t)^3 \right] + \mathcal{B}(\Delta_q) J_{\frac{1}{3}} \left[\Delta_q \gamma(t)^3 \right] \right\}, \tag{3.49b}$$

$$D^{\text{III}}(q,t) = \frac{\pi \Delta_q \mu}{\sqrt{3}} \left\{ \mathcal{C}(\Delta_q, \mu) \cos \left[q v_f (t - \tau) \right] - \mathcal{S}(\Delta_q, \mu) \sin \left[q v_f (t - \tau) \right] \right\}. \tag{3.49c}$$

Here, $J_\nu(x)$ are Bessel functions of the first kind of order ν [142]. Furthermore, we have the coefficients

$$\mathcal{A}(\Delta_q) = J_{-\frac{2}{3}}(\Delta_q) + i J_{\frac{1}{3}}(\Delta_q), \tag{3.50a}$$

$$\mathcal{B}(\Delta_q) = J_{\frac{2}{3}}(\Delta_q) - i J_{-\frac{1}{3}}(\Delta_q), \tag{3.50b}$$

$$\mathcal{C}(\Delta_q, \mu) = \mathcal{A}(\Delta_q) J_{-\frac{1}{3}} \left(\Delta_q \mu^3 \right) + \mathcal{B}(\Delta_q) J_{\frac{1}{3}} \left(\Delta_q \mu^3 \right), \tag{3.50c}$$

$$\mathcal{S}(\Delta_q, \mu) = \mathcal{A}(\Delta_q) J_{\frac{2}{3}} \left(\Delta_q \mu^3 \right) - \mathcal{B}(\Delta_q) J_{-\frac{2}{3}} \left(\Delta_q \mu^3 \right), \tag{3.50d}$$

where we have introduced the parameter

$$\Delta_q = \frac{2}{3} \frac{q u_i \tau}{\eta}, \tag{3.51}$$

with η defined in Eq. (3.40). Although Eq. (3.49) provides the exact solution to the non-equilibrium problem over the whole range of time, in order to get more physical insight it is convenient to analyze the two opposite limits of a sudden and a (nearly-)adiabatic quench [15, 33, 169]. These regimes are controlled by the value of the parameter Δ_q introduced in Eq. (3.51). In particular, we have that $\Delta_q \ll 1 \; \forall q$ defines the sudden quench limit, while the opposite condition $\Delta_q \gg 1 \; \forall q$ determines the adiabatic one. Since $\Delta_q \propto q$, the validity of the sudden approximation strongly depends on the highest-momentum cutoff of the theory q_c, while the adiabatic one is cutoff indepen-

dent. For a quench with fixed amplitude $g_f - g_i$, the above conditions can be recast in terms of the ramp time duration

$$\tau \ll \tau_{\text{sq}} \equiv \frac{3|\eta|}{2q_c v_i} \quad \rightarrow \quad \text{sudden quench limit,} \qquad (3.52a)$$

$$\tau \gg \tau_{\text{ad}} \equiv \frac{3L|\eta|}{2\pi v_i} \quad \rightarrow \quad \text{adiabatic quench limit.} \qquad (3.52b)$$

We will discuss a more physical interpretation of these bounds in Sec. 3.3.

The value of τ_{sq} and τ_{ad} in real systems strongly depends on their nature. For example, assuming a system of length $L = 100$ nm with $N = 10$ particles and identifying $q_c = k_F$, we obtain that in a cold fermionic gas (with $v_F \sim 1$ m/s) one has $\tau_{\text{ad}} \sim 10^{-7}|\eta|$ s and $\tau_{\text{sq}} \sim 10^{-8}|\eta|$ s, respectively, while for a carbon nanotube (with $v_F = 10^6$ m/s) one gets $\tau_{\text{ad}} \sim 10^{-13}|\eta|$ s and $\tau_{\text{sq}} \sim 10^{-14}|\eta|$ s. Since for not too strong quenches $|\eta| \sim 1$, from the above values the importance of studying adiabatic quenches should be evident, especially in the solid state realm.

SUDDEN QUENCH LIMIT In the sudden quench case [15, 33, 102], region II collapses and only regions I and III has to be considered and properly connected. Therefore, by expanding Eq. (3.49c) for $\tau \to 0$, i.e. to the zeroth order in Δ_q, one obtains (for $t > 0^+$)

$$D_{\text{sq}}^{\text{III}}(q,t) = \cos[qv_f(t - \tau)] - i\mu^{-1}\sin[qv_f(t - \tau)]. \qquad (3.53)$$

ADIABATIC QUENCH LIMIT On the other hand, in the limit $\tau \gg \tau_{\text{ad}}$ an asymptotic expansion [199] to the first order in Δ_q^{-1} of Eqs. (3.49b, 3.49c) gives

$$D_{\text{ad}}^{\text{II}}(q,t) \approx \frac{1}{\sqrt{\gamma(t)}} \left\{ e^{-i[\Delta_q(\gamma(t)^3 - 1)]} + \frac{1}{6\Delta_q}\sin\left[\Delta_q\left(\gamma(t)^3 - 1\right)\right] \right\} \qquad (3.54a)$$

and

$$D_{\text{ad}}^{\text{III}}(q,t) \approx \frac{1}{24\mu^{5/2}qv_f} \left\{ \mathcal{C}_{\text{ad}}(\Delta_q, \mu)\cos\left[qv_f(t - \tau)\right] \right.$$
$$\left. - \mathcal{S}_{\text{ad}}(\Delta_q, \mu)\sin\left[qv_f(t - \tau)\right] \right\}, \qquad (3.54b)$$

respectively. Here,

$$\mathcal{C}_{\text{ad}}(\Delta_q, \mu) = 4\mu^2 qv_f\left[6\cos\bar{\Delta}_q + (\Delta_q^{-1} - 6i)\sin\bar{\Delta}_q\right], \qquad (3.55a)$$

$$\mathcal{S}_{\text{ad}}(\Delta_q, \mu) = 4qv_i\left[\left(\Delta_q^{-1} - \mu^3\Delta_q^{-1} + 6i\mu^3\right)\cos\bar{\Delta}_q + \left(6\mu^3 - i\Delta_q^{-1}\right)\sin\bar{\Delta}_q\right], \qquad (3.55b)$$

and $\bar{\Delta}_q = \Delta_q(\mu^3 - 1)$. Substituting Eq. (3.55) in Eq. (3.54b), the latter can be further simplified to

$$
D_{\text{ad}}^{\text{III}}(q,t) \approx \frac{1}{\sqrt{\mu}} \left\{ e^{-i[\bar{\Delta}_q + qu_f(t-\tau)]} + \frac{1}{6\Delta_q} \sin\left[\bar{\Delta}_q + qu_f(t-\tau)\right] \right.
$$
$$
\left. - \frac{e^{-i\bar{\Delta}_q}}{6\Delta_q\mu^3} \sin\left[qu_f(t-\tau)\right] \right\}.
\tag{3.56}
$$

3.2.2 Generalized Gibbs ensemble for a Luttinger liquid with a finite duration quench

Similarly to what we did in Sec. 2.2.1, we can introduce the GGE locally describing the steady state to which the quenched LL should relax in the long-time limit. Indeed, in spite of the finiteness of the system size and the resulting recurring behavior, it is of great importance to understand the role played by the GGE also when the thermodynamic limit does not hold. As we shall see later in this Chapter for the specific case of the particle density, it provides a "zero-order" approximation above which light-cone perturbations propagate.

As in the PBC case of Sec. 2.2.1, the density matrix associated to the GGE ensemble is

$$
\hat{\rho}_{\text{GGE}} = \frac{1}{Z_{\text{GGE}}} e^{-\sum_q \lambda_q \hat{I}_q},
\tag{3.57}
$$

with $Z_{\text{GGE}} = \text{Tr}\left[\exp\left(-\sum_q \lambda_q \hat{I}_q\right)\right]$ (see Secs. 1.4.2 and 2.2.1). However, unlike the sudden quench case we examined before, the values of the Lagrange multipliers $\{\lambda_q\}$ are determined by imposing the conservation of the set of integrals of motion $\{\hat{I}_q\}$ *after* the transient, i.e. for $t \geq \tau$. Therefore, we require that

$$
\langle \hat{I}_q(\tau) \rangle_i = \langle \hat{I}_q \rangle_{\text{GGE}} = \frac{1}{e^{\lambda_q} - 1}, \qquad \forall q.
\tag{3.58}
$$

Since the final Hamiltonian $\hat{H}_f = \hat{H}(t \geq \tau)$ is quadratic, the paper by Barthel and Schollwöck [57] suggests that a convenient choice for the quantities $\{\hat{I}_q\}$ are the operators diagonalizing $\hat{H}_f$ itself, $\hat{I}_q = \hat{B}_{f,q}^\dagger \hat{B}_{f,q}$. The final bosonic operator $\hat{B}_{f,q}$ are connected to the non-interacting bosonic ones $\hat{b}_q$ by the Bogulobov transformation [see Eq. (3.23)]

$$
\hat{B}_{f,q} = A_{f,+} \hat{b}_q + A_{f,-} \hat{b}_q^\dagger, \qquad \text{with } A_{f,\pm} = \frac{1}{2}\left(\frac{1}{\sqrt{K_f}} + \sqrt{K}\right).
\tag{3.59}
$$

Moreover, the following relation between $\hat{B}_{i,q}$ and $\hat{B}_{f,q}$ is extremely useful for explicit calculations,

$$
\hat{B}_{f,q} = \chi_+ \hat{B}_{i,q} + \chi_- \hat{B}_{i,q}^\dagger, \qquad \text{with } \chi_\pm = \frac{1}{2}\left(\mu^{-1/2} \pm \mu^{1/2}\right).
\tag{3.60}
$$

Indeed, exploiting the latter identity one obtains

$$
\langle \hat{I}_q(\tau) \rangle_i = \mathscr{F}(\Delta_q, \mu) - \frac{1}{2},
\tag{3.61}
$$

with

$$\mathcal{F}(\Delta_q, \mu) = \frac{\pi^2 \Delta_q^2 \mu^3}{12} \left[|\mathcal{C}(\Delta_q, \mu)|^2 + |\mathcal{S}(\Delta_q, \mu)|^2 \right] \tag{3.62}$$

and $\mathcal{C}(\Delta_q, \mu)$, $\mathcal{S}(\Delta_q, \mu)$ given, for the general case, in Eq. (3.50).

3.3 DYNAMICS OF THE FERMIONIC DENSITY

In previous Sections we have introduced all the tools needed to address the time evolution of the particle density of the system during and after the interaction quench. To do so, as usual, it is convenient to work in the Heisenberg picture. Therefore, in the zero-temperature limit, the averages should be performed over the ground state of the initial Hamiltonian, $\hat{H}_i$, and will be denoted by $\langle ... \rangle_i$. The time-dependent particle density operator of Eq. (3.15) thus becomes

$$\hat{\rho}(x,t) = \hat{\rho}_{\text{LW}}(x,t) + \hat{\rho}_F(x,t), \tag{3.63}$$

with

$$\hat{\rho}_{\text{LW}}(x,t) = \frac{\hat{N}}{L} + \frac{\partial_x \hat{\Phi}_a(x,t)}{\pi} \tag{3.64a}$$

$$\hat{\rho}_F(x,t) = -\frac{1}{\pi a} \cos \left[2k_F x - \hat{\Phi}_a(x,t) - 2f(x) \right]. \tag{3.64b}$$

Here,

$$\hat{\Phi}_a(x,t) = \sqrt{K} \sum_{q>0} \sqrt{\frac{\pi}{qL}} e^{-aq/2} \sin(qx) \left[\hat{B}_{i,q}(t) + \hat{B}_{i,q}^\dagger(t) \right], \tag{3.65}$$

with the time evolution of the bosonic operators $\hat{B}_{i,q}(t)$ determined by Eq. (3.42). Following the same steps of Sec. 3.1.1, we obtain

$$\rho(x,t) = \langle \hat{\rho}(x,t) \rangle_i = \frac{N}{L} \left\{ 1 - E(x,t) \cos \left[\frac{2\pi N}{L} - 2f(x) \right] \right\}. \tag{3.66}$$

Interestingly, all the time dependence is contained in the envelope function only,

$$E(x,t) = \exp \left[\frac{2\pi K_i}{L} \sum_{q>0} \frac{e^{-aq}}{q} \sin^2(qx) |D(q,t)|^2 \right]. \tag{3.67}$$

As shown in Fig. 3.3, the main features of density dynamics are well captured by the envelope function $E(x,t)$ alone. Thus, in the following, we can focus on this quantity only. Note that, for $t > \tau$, $E(x,t)$ – along with the density $\rho(x,t)$ – is a periodic function with period $\mathcal{T} = L/u_f$, i.e. $E(x,t+\mathcal{T}) = E(x,t)$. This is a direct consequence of the so called *quantum recurrence theorem* for systems with a discrete energy spectrum [78] (see Appendix A for details).
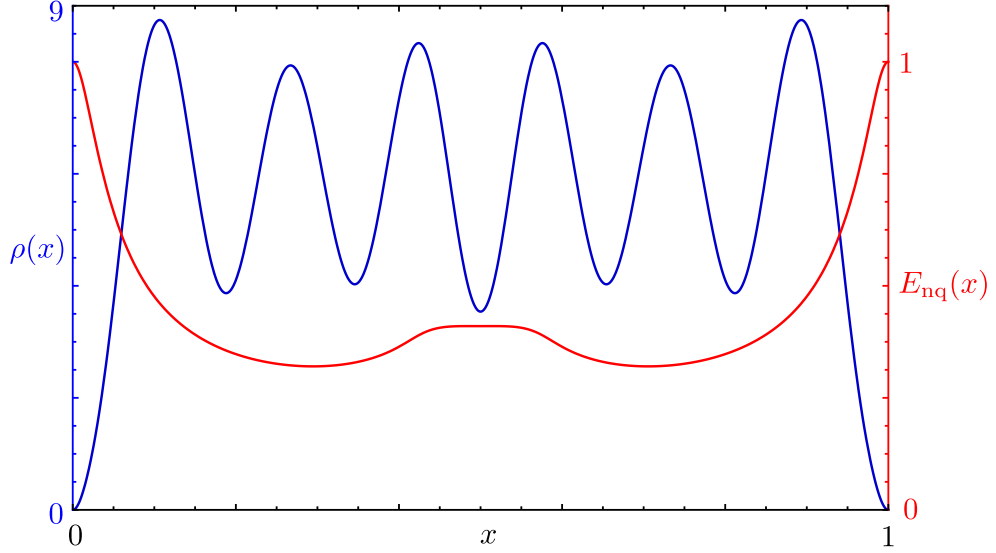
Figure 3.3: The blue curve shows the behavior of the time-dependent particle density $\rho(x,t)$ (units L^{-1}) as a function of x (units L) for $N = 6$ after a quench from $K_i = 0.9$ to $K_f = 0.5$ with duration $\tau = 5 \cdot 10^{-1} \, Lv_F^{-1}$, while the red line displays the envelope function $E(x,t)$ as a function of x (units L) for the same parameters. As can be clearly seen, the time-dependent features of $\rho(x,t)$ are directly induced by $E(x,t)$. Here, we choose $t = 0.3 \, Lv_F^{-1}$ and fix $a = L(\pi N)^{-1}$.

3.3.1 Density evaluated within generalized Gibbs ensemble picture

Before analyzing in details the dynamics of the average density obtained in Eq. (3.66), it is instructive to evaluate the same quantity within the framework of the GGE introduced in Sec. 3.2.2. To do so, we assume our LL, with Luttinger parameter K_f, to be prepared in a state described by the density matrix $\hat{\rho}_{\mathrm{GGE}}$ given in Eq. (3.57). Following the same procedure described in Sec. 3.1.1 for the zero-temperature equilibrium case with the only substitution $\hat{B}_q \to \hat{B}_{f,q}$ and using Eq. (3.61) to perform quantum averages of bosonic operators, we obtain

$$\langle \hat{\rho}(x) \rangle_{(\mathrm{GGE})} = \frac{N}{L} \left\{ 1 - E^{(\mathrm{GGE})}(x) \cos \left[2k_F x - 2f(x) \right] \right\}, \qquad (3.68)$$

with

$$E^{(\mathrm{GGE})}(x) = \exp \left[-\frac{4\pi K_f}{L} \sum_{q>0} \frac{e^{-\pi a/L}}{q} \sin^2(qx) \mathscr{F}(\Delta_q, \mu) \right]. \qquad (3.69)$$

As stated above, since the system possesses a finite length and thus a discrete energy spectrum, an asymptotic steady state for $t > \tau$ will never be reached and the average of a generic observable, such as the density, will continue to oscillate around a certain value with the recurrence time $\mathcal{T}$ [78]. Thus, we do not expect that the GGE approach can capture all the details of the density dynamics. However, in the post-quench region for $x \ll v_f t$ and $L - x \ll v_f t$, i.e. around the system edges, one can neglect the spatial

parts in the dynamical term of Eq. (3.67) obtaining, as we shall see later, that $E(x,t) \to E^{(\mathrm{GGE})}(x)$ [3]. This simply means that the GGE result provides, in a way, the "bulk" value over which dynamical perturbations propagate.

SUDDEN QUENCH LIMIT In the sudden quench limit, using Eq. (3.53), we can expand Eq. (3.69) to the zeroth order in Δ_q, obtaining

$$E_{\mathrm{sq}}^{(\mathrm{GGE})}(x) = [\mathcal{K}(x)]^{\frac{K_f^2 + K_i^2}{2K_i}}, \qquad (3.70)$$

with $\mathcal{K}(x)$ introduced in Eq. (3.33). Note that $E_{\mathrm{sq}}^{(\mathrm{GGE})}(x)$ has the same functional form of the non-quenched LL case – see Eq. (3.32) – with an effective Luttinger parameter $(K_f^2 + K_i^2)/2K_i$.

ADIABATIC QUENCH LIMIT On the other hand, using Eq. (3.54b), one obtains the following asymptotic expansion for $t \geq \tau$ in the adiabatic quench limit, valid up to the first order in Δ_q^{-1},

$$E_{\mathrm{ad}}^{(\mathrm{GGE})}(x) = [\mathcal{K}(x)]^{K_f} \left[1 - \frac{K_f L(1 - \mu^{-1})}{24\pi\ell_0\mu^2} C(x,d) \right]. \qquad (3.71)$$

Here, $d = \ell_0(\mu^3 - 1)$, $\ell_0 = 2u_i\tau/3\eta$ (whose physical interpretation will be clarified in Sec. 3.3.4) and

$$C(x,y) = 2\mathcal{D}(y) - \mathcal{D}(y + x) - \mathcal{D}(y - x), \qquad (3.72)$$

with

$$\mathcal{D}(y) = \mathrm{Im}\left[\mathrm{Li}_2\left(e^{-\alpha\pi/L + 2\pi i y/L} \right) \right], \qquad (3.73)$$

where $\mathrm{Li}_2(x)$ is the dilogarithm function [142].

3.3.2 Dynamics of the envelope function $E(x,t)$

Let us go back to Eq. (3.67) and analyze the dynamics of the envelope function $E(x,t)$ during and after the interaction quench. In order to better highlight its behavior, we focus on the quantity $\delta E(x,t) = E(x,t) - E_{\mathrm{nq},i}(x)$, where $E_{\mathrm{nq},i}(x)$ represents the zero-temperature envelope function of a non-quenched LL with Luttinger parameter K_i – see Eq. (3.32). Figure 3.4 shows $\delta E(x,t)$ for a quench from $K_i = 0.9$ to $K_f = 0.7$ for two opposite situations. In Panel (a) we have chosen $\tau > \tau_{\mathrm{ad}}$, corresponding to an adiabatic quench, while in Panel (b) the sudden quench regime, with $\tau \ll \tau_{\mathrm{sq}}$, is shown. In the adiabatic case two different phases can be clearly distinguished: As soon as the quench begins, in addition to an overall growth of the envelope function over time, a perturbation starts propagating from the edges through the system [162, 188]. Note that, since the edges play here a special role breaking the translational invariance of the system, it is quite natural that excitations

---

[3] The same result holds when the thermodynamic limit $L \to \infty$, keeping N/L fixed, is performed.
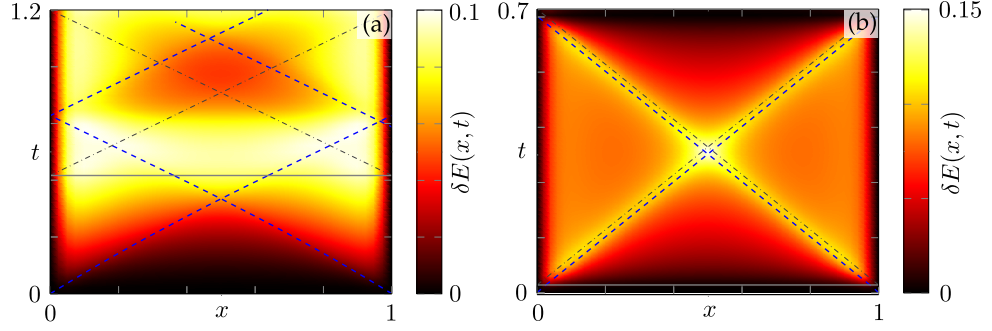
Figure 3.4: Density plot of $\delta E(x,t) = E(x,t) - E_{\mathrm{nq},i}(x)$ as a function of x (units L) and t (units Lv_F^{-1}) for a quench from $K_i = 0.9$ to $K_f = 0.7$. The dashed blue lines represent LC1, while the dash-dotted black ones highlight LC2. The solid gray line denotes the end of the ramp. Ramp time: $\tau = 0.5$ [Panel (a)] and $\tau = 0.02$ [Panel (b)] (units Lv_F^{-1}). Here, we set $a/L = 0.05$.

due to the quench begin their journey from these points. This identifies a first LC (LC1) which travels in an accelerated fashion for $0 \leq t \leq \tau$ – see the dashed lines in Fig. 3.4 highlighting the wavefront of the perturbation. In the post-quench regime, for $t > \tau$, a second LC (LC2) emerges from the edges of the system – see dash-dotted lines in Fig. 3.4 – and both LC1 and LC2 propagate at constant velocity u_f. The two LCs travel ballistically through the system and bounce elastically whenever they reach one of its boundary. The same situation formally occurs also in the case of a sudden quench, depicted in Panel (b), only that to all extents LC1 and LC2 merge and the ramp dynamics is indistinguishable due to its shortness. We will now proceed discussing the two limits in more detail.

3.3.3 Sudden quench

In the sudden quench limit $\tau \to 0$, from Eqs. (3.53) and (3.67), the following analytic expression for $E(x,t)$ can be found

$$
E(x,t) = E_{\mathrm{sq}}^{(\mathrm{GGE})}(x) \left[\frac{\mathcal{K}(u_f t)}{\sqrt{\mathcal{K}(x - u_f t)\mathcal{K}(x + u_f t)}} \right]^{\frac{K_i^2 - K_f^2}{2K_i^2}} , \tag{3.74}
$$

where the GGE envelope function $E_{\mathrm{sq}}^{(\mathrm{GGE})}(x)$ is given in Eq. (3.70). From the denominator of the term in squared brackets of Eq. (3.74), it follows that in this regime LC1 and LC2 merge and only a single LC perturbation with counter-propagating branches moving at constant velocity u_f can be detected, as shown for instance in the example of Fig. 3.5(a).

In Fig. 3.5(b) we analyze the relative difference $|E(x,t) - E_{\mathrm{sq}}^{(\mathrm{GGE})}(x)| / E_{\mathrm{sq}}^{(\mathrm{GGE})}(x)$ between $E(x,t)$ and the GGE envelope function $E_{\mathrm{sq}}^{(\mathrm{GGE})}(x)$. It is clear that, in the sudden quench limit, the envelope function $E(x,t)$ largely fluctuates around the GGE result apart from the regions $x \ll L/2$ and $L - x \ll L/2$
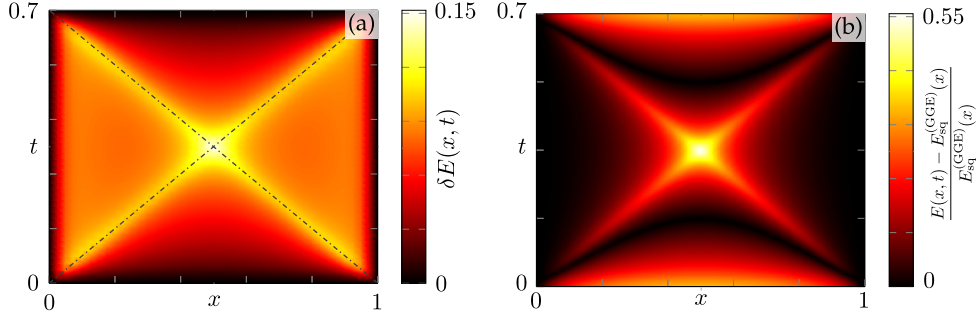
Figure 3.5: Panel (a): Density plot of $\delta E(x,t) = E(x,t) - E_{\mathrm{nq},i}(x)$ as a function of x (units L) and t (units Lv_F^{-1}) for a sudden quench from $K_i = 0.9$ to $K_f = 0.7$. Note that only one LC is present. Panel (b): Density plot of the relative difference $|E(x,t) - E_{\mathrm{sq}}^{(\mathrm{GGE})}(x)|/E_{\mathrm{sq}}^{(\mathrm{GGE})}(x)$ as a function of x (units L) and time t (units Lv_F^{-1}) for the same quench of Panel (a). Here, $a/L = 0.05$.

near the edges. Here, comparing Eq. (3.74) and (3.70), one can show that $E(x,t) \to E_{\mathrm{sq}}^{(\mathrm{GGE})}(x)$. In the rest of the system, however, the GGE fails pretty badly in capturing the density dynamics. As discussed in Sec. 3.3.1, this is essentially due to the finite size of the system.

3.3.4 Adiabatic quench

The case of an adiabatic quench is far richer than the sudden quench one. Here, we have to distinguish between two different regimes, namely (i) the "on-ramp" phase with $0 \le t \le \tau$ and (ii) the post-quench phase for $t > \tau$.

(I) ON-RAMP Besides an overall growth of the envelope function over time, this regime is governed by the dynamics of LC1, which can be readily understood when observing that during the ramp, the excitations at time t are harmonic bosons with instantaneous velocity $\bar{u}(t) = u_i \gamma(t)$ – see Eq. (3.46). Therefore, as the system is non-dispersive, it is reasonable to assume that overall the perturbation propagates with the same instantaneous velocity. Since the perturbation detaches from the edges, we can readily find the distance $\ell(t)$ traveled by its branches from the following equation of motion

$$\dot{\ell}(t) = \pm \bar{u}(t), \tag{3.75}$$

where the sign $+$ $(-)$ refers to the branch moving to the left (to the right). The perturbation front originating at $x = 0$ propagates to the right until it eventually reaches $x = L$ for long enough quenches. In the meanwhile, the front originating at $x = L$ propagates to the left (with the same velocity in modulus) until it reaches $x = 0$. Then, they are perfectly reflected by the boundaries and the motion eventually repeats. Since the modulus of the velocities is the same, it follows that the total distance traveled by each of
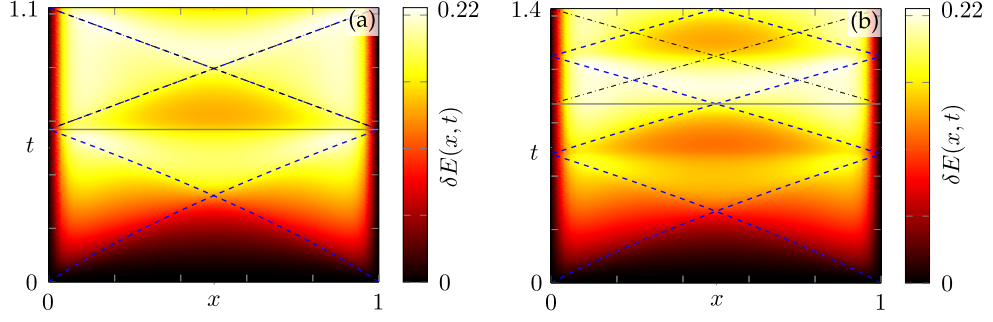
Figure 3.6: Density plot of $\delta E(x,t) = E(x,t) - E_{\mathrm{nq},i}(x)$ as a function of x (units L) and t (units Lv_F^{-1}) for a quench from $K_i = 0.9$ to $K_f = 0.5$. Dashed blue lines represent LC1, while dash-dotted black ones highlight LC2. The solid gray line denotes the end of the ramp. Ramp time: $\tau = \tau_1^{(A)}$ [Panel (a)] and $\tau = \tau_1^{(B)}$ [Panel (b)], see text for details. Here, $\alpha/L = 0.05$.

the wavefronts in the time t can be obtained integrating Eq. (3.75) with the sign $+$ and boundary condition $\ell(0) = 0$,

$$\ell(t) = \ell_0 \left[\left(1 + \frac{\eta t}{\tau} \right)^{\frac{3}{2}} - 1 \right]. \tag{3.76}$$

Here, we recall that $\ell_0 = 2u_i\tau/3\eta$. In passing, we note that the adiabatic condition introduced in Eq. (3.52b) can be rewritten in tems of ℓ_0 as $\ell_0 \gg L$. Of particular interest is the total distance $d = \ell(\tau)$ traveled by the LC1 fronts during the ramp, given by

$$d = \ell_0 \left(\mu^3 - 1 \right), \tag{3.77}$$

with μ defined in Eq. (3.40). Two conditions are notable, namely (A) when LC1 bounces precisely n times in the system during the ramp or (B) when it bounces n times and then reaches $x = L/2$ at $t = \tau$. These conditions are met, respectively, for $\tau = \tau_n^{(A)}$ and $\tau = \tau_n^{(B)}$, given by

$$\tau_n^{(A)} = \frac{3(\mu + 1)}{2(\mu^2 + \mu + 1)} \frac{L}{u_i} n, \tag{3.78}$$

$$\tau_n^{(B)} = \frac{\tau_1^{(A)}}{2} + \tau_n^{(A)}. \tag{3.79}$$

Note that, since $\tau_1^{(A)} = (\mu^3 - 1)\tau_{\mathrm{ad}}/\pi$, unless for very weak quenches, the adiabatic condition in Eq. (3.52b) yields that LC1 bounces at least once off the system boundaries. The dynamics described above is illustrated in Fig. 3.6. When $\tau = \tau_n^{(A)}$, LC1 and LC2 propagate together after the quench [see Panel (a)], while when $\tau = \tau_n^{(B)}$ LC1 and LC2 begin their post-quench evolution being maximally distant [see Panel (b)].

In the adiabatic regime, using Eqs. (3.54a) and (3.67) and expanding to lowest order in the small parameter L/ℓ_0 one can obtain an approximate analytic expression for the envelope function,

$$E(x,t) \approx [\mathcal{K}(x)]^{\bar{K}(t)} \left[1 - \frac{(1-\mu^{-1})L\bar{K}(t)}{24\pi\ell_0\mu^2}C(x,d) \right]$$
$$\times \left[1 - \frac{L\bar{K}(t)}{12\pi\ell_0}C(x,\ell(t)) \right], \tag{3.80}$$

with $\mathcal{K}(x)$ defined in Eq. (3.33), $\bar{K}(t) = K_i/\gamma(t)$ [with $\bar{K}(\tau) = K_f$] and $C(x,y)$ defined in Eq. (3.72). In particular, the term containing $C(x,\ell(t))$ describes the motion of LC1 through the system. Indeed, from the structure of Eq. (3.72) it emerges that two perturbations propagate to the left and to the right, respectively, with a law of motion precisely dictated by $\ell(t)$, as anticipated. A most notable feature here is the presence of an effective *instantaneous* value of the interaction parameter $\bar{K}(t)$, which interpolates between K_i at $t = 0$ and K_f at $t = \tau$.

(II) POST-QUENCH Employing Eqs. (3.54b), (3.67), and (3.71) one can obtain the following approximated analytical expression for the envelope function in the post-quench region

$$E(x,t) \approx E_{\text{ad}}^{(\text{GGE})}(x) \left[1 - \frac{LK_f}{12\pi\ell_0}C(x,v_f(t-\tau)+d) \right.$$
$$\left. + \frac{LK_f^4}{12\pi\ell_0 K_i^3}C(x,v_f(t-\tau)) \right], \tag{3.81}$$

with $E_{\text{ad}}^{(\text{GGE})}(x)$ given in Eq. (3.71) and corresponding to the lowest order expansion in L/ℓ_0 of the GGE envelope function of Eq. (3.69). Here, all expressions have been expanded up to the first order in L/ℓ_0. Two LCs are now present, both propagating at constant speed u_f. One is the continuation of the LC originated at $t = 0$ (LC1), while the second one (LC2) arises from the edges of the system as soon as the quench ramp stops. The amplitude of LC2 with respect to LC1 is modulated by the factor K_f^3/K_i^3. As a consequence, for a quench with $K_f < K_i$, LC1 predominates and the best condition to observe both LC1 and LC2 for $t \geq \tau$ is for rather weak quenches, i.e. for $K_f \lesssim K_i$. The presence of these two LCs is clearly visible in Fig. 3.7, which shows a quench from $K_i = 1$ to $K_f = 0.8$ with ramp time $\tau = 0.2\,Lv_F^{-1}$.

From Eq. (3.81) one can notice that the time-dependent factors modulate $E(x,t)$ around the GGE envelope function $E_{\text{ad}}^{(\text{GGE})}(x)$. Therefore, $E(x,t)$ (and thus the density profile) fluctuates around the envelope obtained within the GGE approach, with an amplitude governed by the ratio L/ℓ_0. The amplitude of such fluctuations then decreases as the quench becomes slower. Although in a finite system no steady distribution can, in principle, be achieved after a quench, it however seems that the more LC1 can travel along the system, the larger a sort of effective equilibration occurs and the better the agreement with the result obtained in the GGE picture becomes.
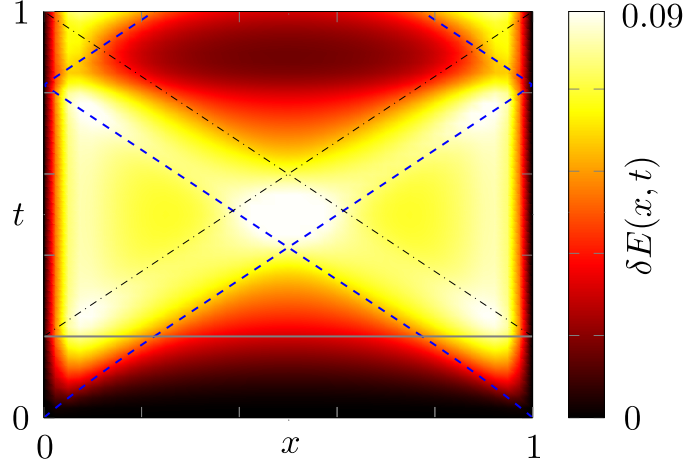
Figure 3.7: Density plot of $\delta E(x,t) = E(x,t) - E_{\mathrm{nq},i}(x)$ as a function of x (units L) and t (units Lv_F^{-1}) for a quench from $K_i = 1$ to $K_f = 0.8$ and ramp time $\tau = 0.2\,Lv_F^{-1}$. The interplay between two LCs, LC1 and LC2, is clearly visible.
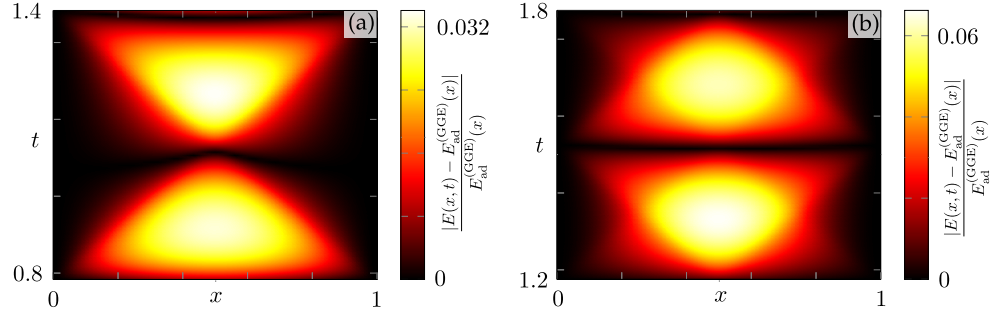

Figure 3.8: Density plot of the relative difference $|E(x,t) - E_{\mathrm{ad}}^{(\mathrm{GGE})}(x)|/E_{\mathrm{ad}}^{(\mathrm{GGE})}(x)$ as a function of x (units L) and t (units L/v_F) for a quench from $K_i = 0.9$ to $K_f = 0.7$. Ramp time: $\tau = \tau_1^{(\mathrm{A})}$ [Panel (a)] and $\tau = \tau_1^{(\mathrm{B})}$ [Panel (b)]. Here, $\alpha/L = 0.05$.

The discrepancy between the exact time-dependent envelope and the GGE result is analyzed in Fig. 3.8. Here, we plot the relative difference $|E(x,t) - E_{\mathrm{ad}}^{(\mathrm{GGE})}(x)|/E_{\mathrm{ad}}^{(\mathrm{GGE})}(x)$ as a function of x and t over a period $\mathcal{T}$, for different values of τ. As a general feature, comparing the situation for $\tau = \tau_n^{(\mathrm{A})}$ and $\tau = \tau_n^{(\mathrm{B})}$ shows that, in the case of an integer number of bounces of LC1 in the system during the ramp, the envelope $E(x,t)$ is overall closer to the GGE limit with respect to the case when a half more bounce occurs, when the distance from the GGE result is maximal. This fact can be explained in terms of a destructive interference between LC1 and LC2 when they overlap. Indeed, since they enter Eq. (3.81) with an opposite sign, their superposition lead to an overall suppression of the perturbation over the GGE envelope. It can also be seen that around the system edges $E(x,t)$ approaches almost perfectly $E_{\mathrm{ad}}^{(\mathrm{GGE})}(x)$, as predicted for the general case below Eq. (3.69).
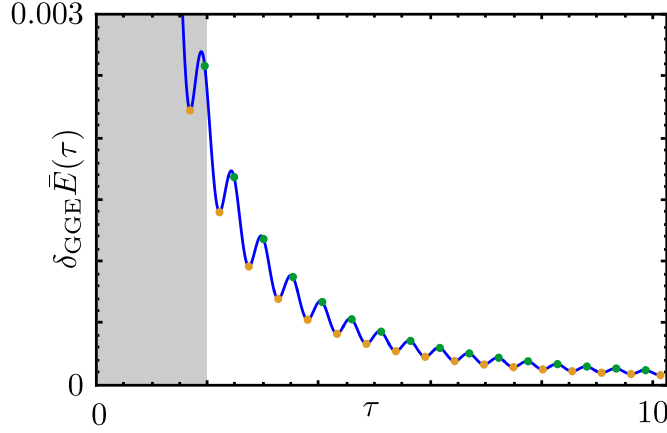
Figure 3.9: Plot of $\delta_{\mathrm{GGE}}\bar{E}(\tau)$ as a function of τ (units Lv_F^{-1}) for a quench from $K_i = 0.9$ to $K_i = 0.4$. The orange dots on the curve represent the sequence $\tau_n^{(A)}$, while the blue ones show the sequence $\tau_n^{(A)}$. The shaded area denotes the non-adiabatic regime in which the result of Eq. (3.81) does not hold. Here, $\alpha/L = 0.05$.

In order to better characterize the behavior discussed above from a quantitative point of view, we study the relative difference between the particle density averaged over one period $\mathcal{T}$, $\bar{E}_\tau(x)$, and the GGE prediction, both evaluated at $x = L/2$ and as a function of the quench duration τ,

$$\delta_{\mathrm{GGE}}\bar{E}(\tau) = \frac{\left| \bar{E}_\tau(L/2) - E^{(\mathrm{GGE})}(L/2) \right|}{E^{(\mathrm{GGE})}(L/2)}, \qquad (3.82)$$

with

$$\bar{E}_\tau(L/2) = \frac{1}{\mathcal{T}} \int_\tau^{\tau+\mathcal{T}} E(L/2, t)\, dt. \qquad (3.83)$$

For the sake of simplicity in the above formula we have chosen $x = L/2$ since it is the point in which one observes the largest discrepancy between $E(x, t)$ and $E^{(\mathrm{GGE})}(x)$. We checked that a similar behavior occurs also for all $x \in [0, L]$. Our results are shown in Fig. 3.9, where clearly emerges that the approach to the GGE envelope function features a non-monotonic oscillating behavior, directly linked to the relative positions of the two LCs. In particular, in the adiabatic regime $\tau \gg \tau_{\mathrm{ad}}$, configurations with a perfect overlap correspond to local minima of $\delta_{\mathrm{GGE}}\bar{E}(\tau)$, while the latter exhibits a local maximum whenever the LCs are maximally distant. When $\ell_0 \lesssim L$, the approximation of Eq. (3.81) ceases to be valid – see the shaded area in Fig. 3.9. In this regime, it is difficult to obtain analytic expressions and one has to resort to an explicit evaluation of Eq. (3.67). Numerical analysis shows that as the adiabatic regime is left the difference between $E(x, t)$ and $E^{(\mathrm{GGE})}(x)$ increases monotonously until the sudden quench regime is reached.
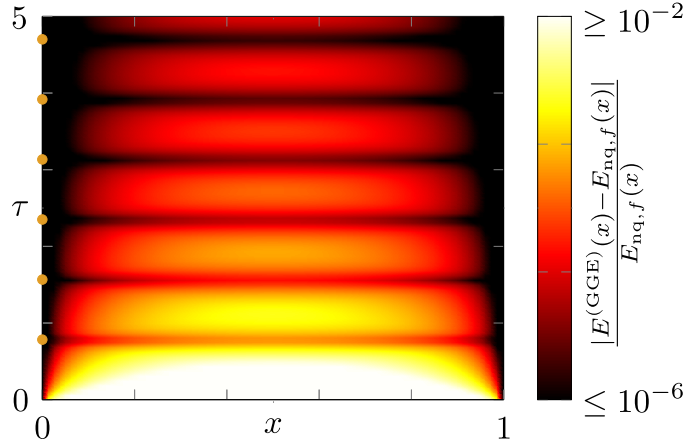
Figure 3.10: Density plot of the relative difference $|E^{(\text{GGE})}(x) - E_{\text{nq},f}(x)|/E_{\text{nq},f}(x)$ as a function of x (units L) and τ (units L/v_F) for a quench from $K_i = 0.9$ to $K_i = 0.7$. The orange dots on the $y-$axis represent the sequence $\tau_n^{(\text{A})}$, with $n \in \{1,...,5\}$. Here, $\alpha/L = 0.05$.

3.3.5 Comparison with the GGE

As seen above, in general $E(x,t)$ fluctuates around a static envelope function obtained assuming a steady distribution for the system in the GGE picture. On the other hand, a naive expectation would be that once a quench is performed, the density would tend to oscillate around the one corresponding to the final Hamiltonian, i.e. that the envelope function would be $E(x,t) \approx E_{\text{nq},f}(x)$, with $E_{\text{nq},f}(x)$ given in Eq. (3.32) for $K = K_f$. In general, this is not the case. However, as can be seen from Eq. (3.71), for very slow quenches with $L/\ell_0 \to 0$ we find that $E_{\text{ad}}^{(\text{GGE})}(x) \to E_{\text{nq},f}(x)$. One can thus conclude that an adiabatic quench with a linear ramp may drive the system towards a state with a particle density which weakly fluctuates around what essentially is the ground state distribution corresponding to the final Hamiltonian. On the other hand, the situation is completely different in the limit of a sudden quench: Here $E_{\text{sq}}^{(\text{GGE})}(x)$ has the same power-law form of $E_{\text{nq},f}(x)$ but with a very different exponent – see Eq.(3.70).

Figure 3.10 shows the relative difference $|E^{(\text{GGE})}(x) - E_{\text{nq},f}(x)|/E_{\text{nq},f}(x)$ as a function of x and τ. The overall picture confirms the trend sketched in the discussion above. It is suggestive to notice that as τ is increased, the relative difference does not decrease monotonically but exhibits an oscillatory behavior, with again local minima corresponding to $\tau = \tau_n^{(\text{A})}$ and local maxima located at $\tau = \tau_n^{(\text{B})}$, further confirming the importance of the LCs dynamics in defining the post-quench behavior.

3.4 CONCLUSIONS

In this Chapter we have studied the time dynamics of the particle density of a spinless fermionic LL with OBC during and after a finite duration quench of the inter-particle interaction. Due to its finite size, the system never reaches a steady state but continues to oscillate around a certain configuration. In the adiabatic quench limit, the dynamics of the particle density is strongly affected by the presence of *two* LC perturbations, one originating as soon as the quench begins and the other arising when the quench stops. These perturbations originate from the edges and propagate ballistically through the system with the instantaneous velocity of the LL bosonic excitations, bouncing elastically whenever they reach one of the boundary. For peculiar values of the length of the quench ramp, the two LCs can interfere destructively and the particle density maximally approaches the behavior predicted by a GGE calculation throughout the entire system. Furthermore, for adiabatic quenches the density evaluated in the GGE picture tends to the fermionic density of the ground state of the final Hamiltonian. In the sudden quench limit, on the other hand, the two LCs are indistinguishable, leading to maximal discrepancy with respect to the GGE limit in the central region of the system. Indeed, regardless the length of the quench ramp, the exact density profile at the edges closely matches the density calculated within the GGE for most of the post-quench regime.

To conclude, we note that often the particle density, on which we focused in this Chapter, is not sufficient to detect the emergence of correlated structures [194, 200], such Wigner molecules in finite systems [157, 158, 194] or Wigner crystals in a periodic ones [156, 159, 191]. For this reason, in future work, it would be of great interest to investigate also the behavior of higher-order density correlation functions after a quantum quench, since the latter are more reliable tools to reveal correlation effects [194, 200].

4 | NON-MONOTONIC RESPONSE AND LIGHT-CONE FREEZING IN GAPLESS-TO-GAPPED QUANTUM QUENCHES

In previous Chapters we have focused on interaction quenches in Luttinger liquids. Of course, they are not the only quench mechanisms that can be performed. For example, many important results about non-equilibrium behavior of integrable quantum systems have been obtained by quenching the transverse magnetic field in the 1D Ising model [18, 47, 106, 107, 173, 177, 201–205]. Furthermore, in non-interacting fermionic topological systems, quantum quenches of various parameters between gapped phases characterized by different Chern numbers have also been studied [206–209]. However, not much attention has been devoted so far to the study of quantum quenches between gapless and gapped states. A notable exception is represented by quantum quenches from a Luttinger liquid to a sine-Gordon model [103, 210–218] where, for example, it has been shown that any local charge density inhomogeneity is strongly enhanced after the quantum quench [213]. However, the characterization of the main features of gapless-to-gapped quantum quenches is still incomplete.

In this Chapter, we will focus on two different and paradigmatic examples of gapless 1D systems which get partially or completely gapped by a change in the parameters of their Hamiltonian. Namely, a SOC quantum system in the presence of an applied magnetic field [219–222] and a chain of spinless 1D fermions. For the latter, the gapping quench mechanism is either induced by a staggered potential (SP) or by the sudden switch-on of fermion-fermion interactions [223]. When the quench does not involve interactions, we consider both lattice models and their continuum counterparts, which describe low-energy sectors of a wide class of 1D systems. Here, we study, in the thermodynamic limit, how these systems respond to the quench by investigating the behavior of the (staggered) magnetization of SOC (SP) system along the direction of the quenched field. We demonstrate that these quantities exhibit, surprisingly, a maximum for a finite value of the gap opening mechanism and tends to the gapless, pre-quench value when strong quenches are performed. The same behavior characterizes a scenario in which a gap is opened by fermion-fermion interactions. Here, we also depart from the study of integrable systems undertaken so far, by considering both the integrable and non-integrable regimes. In the latter case, however, the results should be intended as valid in a long lived pre-thermal state only since, as we have seen in Chap. 1, the breaking of integrability would finally lead to thermalization in the asymptotic time-limit. In order to interpret the re-

sults, we study the time evolution of systems correlation functions associated with the (staggered) magnetization in the continuous non-interacting models. We show that for small quenches the latter display a neat propagation of a LC conveying the information of the quench through the system while for large quenches the LC freezes. In particular, in the non-interacting systems we demonstrate that correlation functions evolve according to a Klein-Gordon (KG) equation in which a competition between a mass and a source term occurs. The very same behavior emerges also when interactions are quenched in a lattice model, providing a strong evidence that the freezing of the LC is responsible of the non-monotonous behavior of observables also in such quenched systems. We finally conclude by analyzing the generality of our results. In particular, we study their robustness in the presence of finite duration quenches and we show that they even survive in systems with dimensionality higher than one.

This Chapter is based on the results obtained in Ref. [224].

4.1 INTRODUCTION TO SPIN–ORBIT COUPLED SYSTEMS

The focus of this Chapter will be mainly on 1D SOC coupled systems in the presence of an external magnetic field. In recent years they have triggered lots of theoretical research since they allow to experimentally engineer helical liquids [150, 220–222, 225–228]. The latter are fermionic 1D systems which exhibit the so-called *spin-momentum locking*: Fermions with opposite spin (with respect to a given quantization axis) propagate in opposite directions. Other important systems in which helical liquids arise are carbon nanotubes subject to an electric field [229, 230] or edge states of two-dimensional topological insulators [148, 150, 231–234]. The great interest towards helical liquids is due to the fact that they represent a very promising platform for both Spintronics [235–238] and Topological Quantum Computation [239–241]. Indeed, the spin-momentum locking provides an efficient method to manipulate spin currents and to create spin diodes [222, 227, 242]. On the other hand, when a helical liquid is proximity-coupled with a $s-$wave superconductor a Majorana fermion bound state, characterized by a peculiar non-abelian statistics, emerges at the boundaries of the system [241, 243–245].

From standard Electrodynamics it is well known that a charged particle, with mass m and charge q, moving with momentum k in an electric field E experiences an effective magnetic field $B_{\text{eff}} = E \times k / mc^2$ in its rest reference frame, which couples to its magnetic moment $\mathfrak{m} = \text{sign}(q) g_s \mu_B \sigma / 2$ [246]. Here, g_s is the $g-$factor of the particle ($g_s \approx 2$ for the electron), $\mu_B = 9.27 \times 10^{-24}\,\text{J}\,\text{T}^{-1}$ is the Bohr magneton, c is the speed of light and σ is the vector of Pauli matrices. Classically, this *spin-orbit coupling* (SOC) results in an interaction term $H_{\text{SO}} \sim \mathfrak{m} \cdot B_{\text{eff}} = (2mc^2)^{-1} g_s \mu_B \text{sign}(q)(E \times k) \cdot \sigma$.

In crystalline structures a very similar phenomenon occurs when electrons move in an electric field given by $E = -\nabla V$. Here, V contains both the crys-
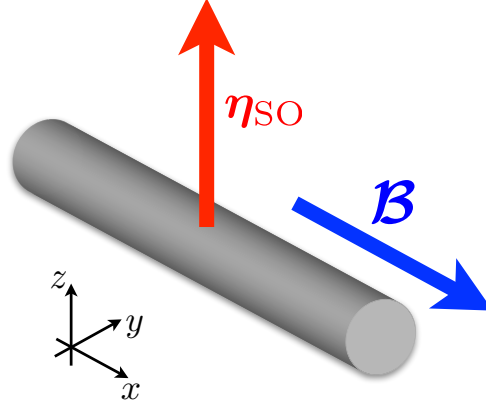
Figure 4.1: Spin-orbit coupled quantum wire with spin-orbit interaction characterized by the vector $\boldsymbol{\eta}_{\text{SO}}$ along the quantization axis z and subject to an external magnetic field parallel to the wire and orthogonal to $\boldsymbol{\eta}_{\text{SO}}$.

tal potential and all the contributions due to confinement, impurities or external electric fields. In this case, the effective magnetic field is $\boldsymbol{B}_{\text{eff}}(\boldsymbol{k}) = -\mu_B(\nabla V \times \boldsymbol{k})/mc^2$. It is possible to show that time reversal symmetry, which is preserved in a system with SOC, requires that $\boldsymbol{B}_{\text{eff}}(\boldsymbol{k}) = -\boldsymbol{B}_{\text{eff}}(-\boldsymbol{k})$. Therefore, it is possible to have $\boldsymbol{B}_{\text{eff}}(\boldsymbol{k}) \neq 0$ only in systems that lack spatial inversion symmetry. This fact is of great importance in low-dimensional systems, such as 2D degenerate electron gases (2DEGs) or 1D quantum wires, which are realized by means of external potentials, leading to a breaking of the so-called structural inversion asymmetry (SIA). This effect has been studied for the first time by Rashba and coworkers in the context of a 2DEG [247, 248] and, as a consequence, the resulting Hamiltonian is known in literature as Rashba Hamiltonian.

In the following Sections, in which we will briefly discuss experimental realizations of SOC systems, we temporarily restore the use of $\hbar$.

4.1.1 Spin–orbit coupled quantum wires

For the purposes of the present Thesis, we now focus on the 1D case only. Here, the Rashba Hamiltonian is given by [222, 226, 249–251]

$$\hat{H}_R = \hat{k}_x \hat{\sigma} \cdot \hat{\boldsymbol{\eta}}_{\text{SO}},\tag{4.1}$$

with $\hat{k}_x$ the component of the momentum along the wire direction, x, and $\boldsymbol{\eta}_{\text{SO}}$ a vector lying in the $y-z$ plane which fully characterizes the SOC interaction in the system. For the sake of simplicity, we assume $\boldsymbol{\eta}_{\text{SO}}$ to be along the z axis, which we also choose as quantization axis. The most intriguing features of the model emerge when an external magnetic field $\boldsymbol{B}$ is applied in a direction orthogonal to $\boldsymbol{B}_{\text{eff}}$, for example along the wire direction, x, as shown in Fig. 4.1

The single-particle Hamiltonian describing the model is thus

$$\hat{H} = \frac{\hbar^2 \hat{k}_x^2}{2m} + \frac{1}{2}g\mu_B \mathcal{B}\hat{\sigma}^x - \eta_{\text{SO}}\hat{k}_x\hat{\sigma}^z.\tag{4.2}$$
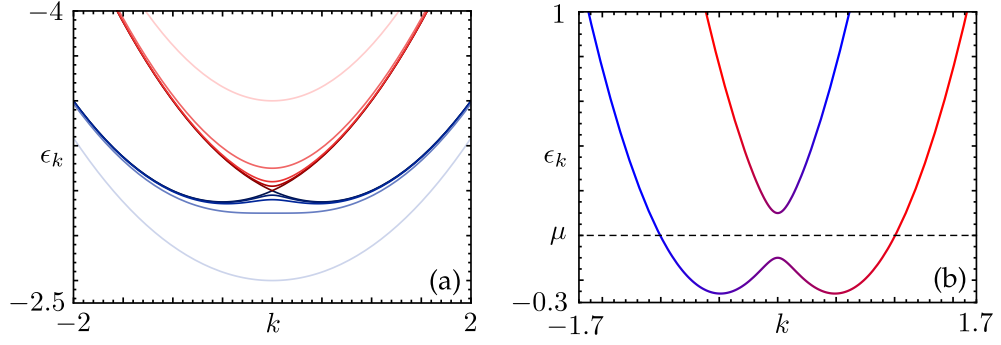
Figure 4.2: Panel (a): valence (blue curves) and conductance (red curves) energy bands $\epsilon_{\pm,k}$ (units ε_0) of the single-particle Hamiltonian of Eq. (4.3) as a function of k (units ℓ^{-1}) for different values of B (units ε_0^{-1}). In particular, from darker to lighter colors $B = 0$, $B = 0.1$, $B = 0.2$, $B = 0.5$, and $B = 2$. Panel (b): spin-resolved energy bands $\epsilon_{\pm,k}$ (units ε_0) as a function of k (units ℓ^{-1}) for $B = 0.1$. Red is associated with spin up electrons while blue to spin down ones. When the chemical potential of the system μ is inside the Zeeman gap only two Fermi points are present and the system behaves effectively as a 1D helical liquid.

In order to make our discussion more general, it is useful to introduce a typical length scale of the system, ℓ, which can be for instance the length of the system or the lattice spacing, and work with a dimensionless version of the above Hamiltonian,

$$\hat{H} = \hat{k}_x^2 + B\hat{\sigma}^x - \alpha\hat{k}_x\hat{\sigma}^z. \tag{4.3}$$

Here, $k_x\ell \to k_x$, with the new k_x dimensionless, energy is measured in units of $\varepsilon_0 = \hbar^2(2m\ell^2)^{-1}$ and we have introduced the parameters

$$B = \frac{g\mu_B\mathcal{B}}{2\varepsilon_0}, \qquad \alpha = \frac{\eta_{\text{SO}}}{\varepsilon_0\ell}. \tag{4.4}$$

The energy bands of the system are

$$\epsilon_{\pm,k} = k^2 \pm D_k, \qquad \text{with } D_k = \sqrt{\alpha^2k^2 + B^2}, \tag{4.5}$$

and are shown in Fig. 4.2(a) for different values of B. In particular, for $B < \alpha^2/2$ the lower band $\epsilon_{-,k}$ has a "mexican hat" shape (with two minima at $k = \pm\sqrt{k_{\text{SO}}^2 - B^2/\alpha^2}$ and one local maximum at $k = 0$), while for $B > \alpha^2/2$ it exhibits a single minimum at $k = 0$. This is due to the interplay between the SOC interaction, which shifts the two spin degenerate subbands by $k_{\text{SO}} = \alpha/2$ in opposite directions (to the left for spin down fermions and to the right for spin up ones) and the magnetic field B, which opens a gap in the single-particle spectrum at $k = 0$ of width $\Delta = 2B$ (Zeeman gap), thus breaking the residual spin-degeneracy at this point. The normalized
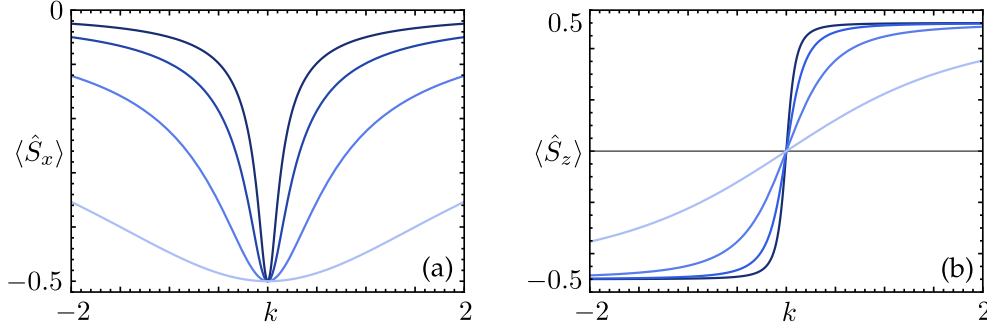
Figure 4.3: In Panel (a) is plotted $\langle \hat{S}_x \rangle_{-,k}$ (units $\hbar$) as a function of k (unit ℓ^{-1}) for different values of the magnetic field B (units ε_0^{-1}): For darker to lighter blue $B = 0.1$, $B = 0.2$, $B = 0.5$, and $B = 2$. In Panel (b) is reported the same as in Panel (a) but for $\langle \hat{S}_z \rangle_{-,k}$ (units $\hbar$).

eigenfunctions of the model, assuming PBC, i.e. $\Psi(x) = \Psi(x + L)$ with $\Psi(x)$ a generic spinor wavefunction and L the length of the system, are[1]

$$\Psi_{+,k}(x) = \frac{1}{(D_k + \alpha k)^2 + B^2} \begin{bmatrix} B \\ D_k + \alpha k \end{bmatrix}, \tag{4.6a}$$

$$\Psi_{-,k}(x) = \frac{1}{(D_k + \alpha k)^2 + B^2} \begin{bmatrix} -D_k - \alpha k \\ B \end{bmatrix}. \tag{4.6b}$$

In the presence of a finite magnetic field B the two bands $\epsilon_{\pm,k}$ have no more definite spin polarization, i.e. spin is no more a good quantum number. This can be clearly seen by investigating the expectation value of the spin projections along the x, y, and z directions. Using the eigenfunctions of Eq. (4.6), we obtain

$$\langle \hat{S}_x \rangle_{-,k} = \frac{\hbar}{2} \langle \Psi_{-,k} | \hat{\sigma}^x | \Psi_{-,k} \rangle = \frac{1}{2} \frac{B}{\sqrt{\alpha^2 k^2 + B^2}}, \tag{4.7a}$$

$$\langle \hat{S}_y \rangle_{-,k} = \frac{\hbar}{2} \langle \Psi_{-,k} | \hat{\sigma}^y | \Psi_{-,k} \rangle = 0, \tag{4.7b}$$

$$\langle \hat{S}_z \rangle_{-,k} = \frac{\hbar}{2} \langle \Psi_{-,k} | \hat{\sigma}^z | \Psi_{-,k} \rangle = \frac{1}{2} \frac{\alpha k}{\sqrt{\alpha^2 k^2 + B^2}}. \tag{4.7c}$$

The behavior of $\langle \hat{S}_x \rangle_{-,k}$ and $\langle \hat{S}_z \rangle_{-,k}$ for different values of B is shown in Fig. 4.3. In particular, the spin polarization of the lower band rotates counterclockwise from the $k > 0$ region to the $k < 0$ one. With similar steps it is possible to show that the opposite holds for the upper band, i.e. here the spin polarization rotates clockwise from $k > 0$ to $k < 0$. This behavior is sketched in Fig. 4.2(b), from which it is also clear why SOC wires allow for the realization of helical liquids: For not too strong magnetic fields, if one sets the chemical potential inside the gap, the system possesses only two conducting channels, one associated with right-moving electrons with (almost) spin up and the other to left-moving electrons with (almost) spin down.
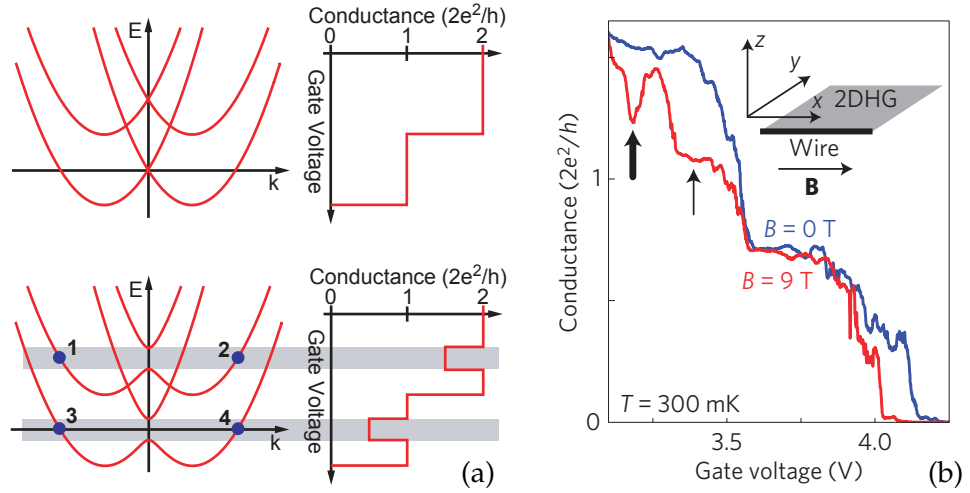
---

1 Note that x and L are given in units ℓ.

Figure 4.4: In Panel (a) are reported the lower energy subbands of a SOC wire and the expected conductance as a function of the gate voltage V_g. In the upper row we show the case with no external magnetic field applied. Here, although the two spin-degenerate subbands are shifted in opposite direction due to the SOC, the conductance behaves as in a standard 1D quantum wire and is quantized in steps of G_0. Things change in the presence of a magnetic field, as depicted in the lower row, where the opening of Zeeman gap results in dips of depth e^2/h in the conductance of the wire whenever the number of conducting channels is reduced. In Panel (b) we show the experimental measure of $G(V_g)$ as a function of V_g with (red curve, $\mathcal{B} = 9\,\text{T}$) and without (blue curve) a magnetic field along the wire direction. The thick black arrow shows the dip due the presence of the Zeeman gap. Figures taken from Ref. [221].

4.1.2 Spin–orbit coupled systems in solid state

In the last ten years SOC systems have been investigate in several different condensed matter setups [220, 221, 252]. The first experimental observation of the Zeeman gap and emergence of the helical regime has been performed by Quay et al. in 2010 [221]. They realized a 1D quantum wire embedded into an AlGaAs/GaAs/AlGaAs quantum well. The reduction of dimensionality from 2D to 1D was realized by means of an electrostatic gate voltage V_g, which leads to the breaking of the SIA and results in a strong SOC interaction within the wire. Moreover, acting on V_g it is possible to modify the electron density inside the wire, i.e. to control the filling of its bands. In order to detect the opening of the Zeeman gap and the emergence of the helical liquid regime, Quay et al. measured the conductance $G(V_g)$ of the wire as a function of V_g. As shown in Fig. 4.4(a), in the absence of the external magnetic field, $G(V_g)$ is quantized in steps of the quantum of conductance $G_0 = 2e^2/h$[19]. However, when a finite magnetic field is present, the halving of channels due to the opening of the Zeeman gap should result in a dip of depth e^2/h for values of V_g such that the chemical potential of the system is inside the gap. The experimental measures of Panel (b) in Fig. 4.4 indeed confirm this picture, although the dip is visible in the second step
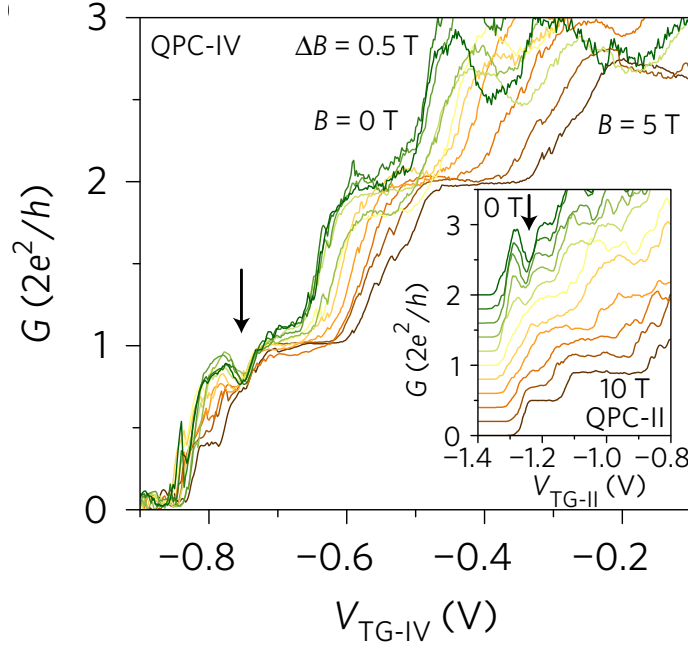
Figure 4.5: Conductance of the InAs nanowire $G(V_{TG})$ as a function of the top-gate voltage V_{TG} for various magnetic fields $\mathcal{B}$, ranging from $\mathcal{B} = 0\,\text{T}$ to $\mathcal{B} = 5\,\text{T}$. The black arrow signals the Zeeman dip occurring when the chemical potential of the wire is tuned inside the Zeeman gap. In the inset the same curves, which have been offset for clarity, are shown but up to a magnetic field of $\mathcal{B} = 10\,\text{T}$. For $\mathcal{B} > 5\,\text{T}$ the dip disappears and steps of height e^2/h emerge. Figure taken from Ref. [220].

only. This has been explained in terms of a very small coupling between the first couple of subbands, which results in a strong suppression of the effects due the interplay between SOC interaction and magnetic field [221].

This latter drawback of the experiment of Quay et al. has been solved in the recent work of Heedt et al. [220], where the conductance of an InAs nanowire has been investigated as a function of a top-gate potential V_{TG} which, also in this case, allows for tuning the chemical potential of the wire. In Fig. 4.5 is reported the measurement of the conductance $G(V_{TG})$ as a function of the gate voltage V_{TG} for various magnetic fields. In contrast to the experiments of Quay et al. [221], the dip due to the halving of the conduction channels occurring inside the Zeeman gap is clearly visible already in the first step of $G(V_{TG})$. As can be seen from the inset of Fig. 4.5, for large magnetic field the dip disappears and steps of height e^2/h emerge in the conductance. This is due to the vanishing of the local maximum of the lower band $\epsilon_{-,k}$, occurring for $B > \alpha^2/2$ [see the discussion below Eq. (4.5)].

4.1.3 Spin–orbit coupled systems in cold atoms

Recently 1D SOC systems have also been engineered in cold atoms [219, 253–255]. Here, SOC interaction can be generated by means of two-photon Raman transitions induced by a pair of laser beams connecting two internal
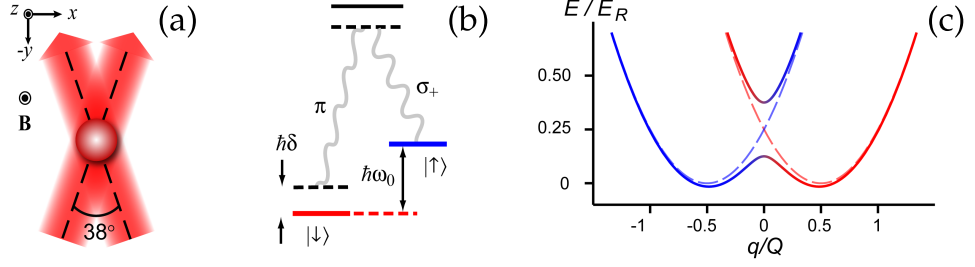
Figure 4.6: In Panel (a) is displayed the setup allowing for the realization of a SOC interaction in a cold atomic system. A pair of laser beams at $\pm 19°$ relative to the $y-$axis couples the internal atomic states $|\uparrow\rangle$ (red) and $|\downarrow\rangle$ (down) displayed in Panel (b). An external bias magnetic field in the z direction provides the quantization axis. The two hyperfine states $|\uparrow\rangle$ and $|\downarrow\rangle$, coupled by the Raman process, are split by an energy $\hbar\omega_0$ while the two-photon transition is detuned by $\hbar\delta$ [Panel (b)]. In Panel (c) we show the energy bands of the system as a function of the quasi-momentum q for $\hbar\delta = 0$ and $\hbar\Omega_R = 0.25E_R$ (solid lines) or $\hbar\Omega_R = 0E_R$ (dashed lines). Figures taken from Ref. [219].

atomic states, associated with pseudo-spin states $|\uparrow\rangle$ and $|\downarrow\rangle$ respectively, as shown in Panels (a) and (b) of Fig. 4.6. In this process a single photon is initially absorbed by an atom from one laser beam and, then, is re-emitted by stimulated emission into the second beam. As a consequence of the entire process, the atom acquires a momentum $\hbar Q e_x$ while changing its spin from $|\downarrow\rangle$ to $|\uparrow\rangle$ and momentum $-\hbar Q e_x$ in the opposite case. Here, e_x is the $x-$axis unit vector. Due to the low temperature of the system, even the momentum of a single optical photon is sufficiently large to provide the link between spin and momentum typical of a SOC system. Indeed, by defining a quasi-momentum $q = k_x + Q/2$ for spin $|\downarrow\rangle$ and $q = k_x - Q/2$ for spin $|\uparrow\rangle$, one obtains the following Hamiltonian [219, 254]

$$\hat{H} = \frac{\hbar^2\hat{k}_x^2}{2m} - \eta\hat{k}_x\hat{\sigma}^y + \frac{1}{2}g\mu_B\mathcal{B}_z\hat{\sigma}^z + +\frac{1}{2}g\mu_B\mathcal{B}_y\hat{\sigma}^y. \tag{4.8}$$

Here, $\eta = \hbar^2 Q(2m)^{-1}$, $\mathcal{B}_z = \hbar\Omega_R(g\mu_B)^{-1}$ and $\mathcal{B}_y = \hbar\delta(g\mu_B)^{-1}$, with Ω_R the two-photon Rabi frequency [256] and δ the two-photon detuning [see Fig. 4.6(b)]. Note that, in contrast with solid state devices, in which the strength of the SOC strongly depends on the material and can hardy be controlled, in cold atoms the latter can be modified at will by properly tuning the parameters of laser beams. Since $\mathcal{B}_y$ is often much smaller than $\mathcal{B}_z$ [219], Eq. (4.8) can be cast in the same form of Eq. (4.2), except for the rotation $z \rightarrow -x$, $y \rightarrow z$, $x \rightarrow -y$, and thus leads to the same energy spectrum with the peculiar spin polarization discussed in Sec. 4.1.1. In particular,

$$\hat{H} \approx \hat{k}_x^2 - \alpha\hat{k}_x\hat{\sigma}^y + B\hat{\sigma}^z, \tag{4.9}$$

where energies are now in units of $\varepsilon_0 = E_R = \hbar^2 Q^2(2m)^{-1}$, $\hat{k}_x Q^{-1} \rightarrow \hat{k}_x$ and

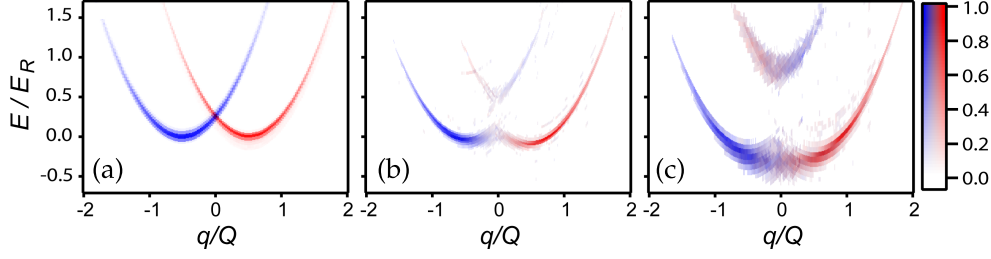$$\alpha = 1, \qquad B = \frac{\hbar\Omega_R}{E_R}, \tag{4.10}$$

Figure 4.7: Spin-resolved energy spectrum for $\hbar\delta = 0.00(3)E_R$ and (a) $\hbar\Omega_R = 0.00(3)E_R$, (b) $\hbar\Omega_R = 0.43(5)E_R$, and (c) $\hbar\Omega_R = 0.9(1)E_R$. Here, red is associated with the $|\downarrow\rangle$ polarization and blue with the $|\uparrow\rangle$ one. Figure taken from Ref. [219].

with $E_R = \hbar^2 Q^2 (2m)^{-1}$ the two-photon recoil energy [219]. In their experiment, Cheuk et al. prepared a system of ^{6}Li atoms in a magnetic trap and cooled it down to a temperature of $T < 0.1T_F$, with T_F the Fermi temperature of the gas [257]. After that, the system is loaded into an optical trap consisting of two orthogonal laser beams. The hyperfine levels are separated thanks to a bias field of 11.6 G along the $z-$axis, which also provides the quantization axis (see Fig. 4.6).

Using a spectroscopic technique based on radio-frequency spin injection of atoms from a free Fermi gas (which acts as a reservoir) into the SOC system and measuring momentum and spin of the atoms by a combination of time of flight and spin-resolved detection, Cheuk et al. succeeded in reconstructing the spin-polarized energy spectrum of the system, reported in Fig. 4.7. The latter perfectly agrees with the theoretically predicted one.

4.2 QUANTUM QUENCH OF A GENERIC GAP OPENING MECHANISM

We now turn to the main point of this Chapter, namely a quantum quench of a term which opens a gap in the single particle spectrum of an initially gapless Hamiltonian. At first we will consider the general case. We will then specialize our discussion to the quench of a magnetic field in a SOC system and of the staggered potential in a free fermionic chain (SP model) in next Sections. Thus, we now focus on a generic gapless Hamiltonian

$$\hat{H}_0 = \sum_k \hat{\Psi}_k^\dagger \hat{\mathcal{H}}_k \hat{\Psi}_k, \tag{4.11}$$

with $\hat{\Psi}_k^\dagger = (\hat{d}_{a,k}^\dagger, \hat{d}_{b,k})$ a two-component momentum resolved Fermi spinor and $\hat{\mathcal{H}}_k$ a family of 2×2 matrices indexed by the (quasi-)momentum k and characterized by a gapless spectrum with a linear crossing. The meaning of the indexes a and b depends on the model and will be clarified later.

Denoting the strength of the gap opening mechanism by Δ, we consider the following time-dependent Hamiltonian

$$\hat{H}(t) = \hat{H}_0 + \hat{H}_{\text{gap}}(t) = \sum_k \hat{\Psi}_k^\dagger \left[\hat{\mathcal{H}}_k + \theta(t) \Delta \hat{\sigma}^x \right] \hat{\Psi}_k, \qquad (4.12)$$

with $\hat{\sigma}_x$ the first Pauli matrix in the usual representation and $\theta(t)$ the Heaviside function. The pre-quench single-mode Hamiltonian $\hat{\mathcal{H}}_k$ can always be written in a diagonal form with eigenvalues $\epsilon_{\pm,0,k}$ such that $\epsilon_{-,0,k} \leq \epsilon_{+,0,k}$, $\forall k$, by means of a unitary transformation [see Eqs. (C.4) and (C.7) of Appendix C]. In particular, for all the cases we will consider later in this Chapter it takes the form

$$\hat{U}_{0,k} = \begin{bmatrix} a_{0,k} & b_{0,k} \\ -b_{0,k}^* & a_{0,k} \end{bmatrix}, \qquad (4.13)$$

where the coefficients $a_{0,k} \in \mathbb{R}$ and $b_{0,k} \in \mathbb{C}$ are determined by Eqs. (C.4) and (C.7). Moreover, $\hat{U}_{0,k} \hat{\mathcal{H}}_k \hat{U}_{0,k}^\dagger = \text{diag}\{\epsilon_{+,0,k}, \epsilon_{-,0,k}\}$. For $t < 0$ the diagonalized Hamiltonian reads

$$\hat{H}(t < 0) = \sum_k \left[\epsilon_{-,0,k} \hat{d}_{v,0,k}^\dagger \hat{d}_{v,0,k} + \epsilon_{+,0,k} \hat{d}_{c,0,k}^\dagger \hat{d}_{c,0,k} \right], \qquad (4.14)$$

where the conduction and valence band operators, $\hat{d}_{c,0,k}$ and $\hat{d}_{v,0,k}$, are defined by

$$\hat{\Phi}_{0,k} = \hat{U}_{0,k} \hat{\Psi}_k = \begin{bmatrix} \hat{d}_{c,0,k} \\ \hat{d}_{v,0,k} \end{bmatrix}. \qquad (4.15)$$

We set the chemical potential to zero and assume the system to be in its pre-quench zero-temperature equilibrium ground state, $|\Phi_0\rangle$. In all the cases we will consider in the following, valence and conduction bands exhibit a linear crossing at zero energy. Therefore, for $t < 0$, the valence band $\epsilon_{-,0,k}$ is filled up to this point and $|\Phi_0\rangle$ is defined as

$$|\Phi_0\rangle = \prod_{k_1}^{k_2} \left(\hat{\Phi}_{0,k}^\dagger \right)_2 |0\rangle = \prod_{k_1}^{k_2} \left(\hat{U}_{0,k}^\dagger \hat{\Psi}_k^\dagger \right)_2 |0\rangle, \qquad (4.16)$$

where $|0\rangle$ is the vacuum of the system and $k_{1,2}$ are determined by imposing that only negative energy states are filled. Here, the subscript 2 means that the second component of the spinor has to be considered.

We now turn to the regime with $t > 0$. The post-quench single-mode Hamiltonian $\hat{\mathcal{H}}_k + \Delta \hat{\sigma}^x$ is diagonalized by the unitary matrix

$$\hat{U}_{1,k} = \begin{bmatrix} a_{1,k} & b_{1,k} \\ -b_{1,k}^* & a_{1,k} \end{bmatrix}, \qquad (4.17)$$

with $a_{1,k} \in \mathbb{R}$ and $b_{1,k} \in \mathbb{C}$ determined again by Eqs. (C.4) and (C.7), and $\hat{U}_{1,k}[\hat{\mathcal{H}}_k + \Delta \hat{\sigma}^x]\hat{U}_{1,k}^\dagger = \text{diag}\{\epsilon_{+,1,k}, \epsilon_{-,1,k}\}$. The total Hamiltonian thus becomes

$$\hat{H}(t > 0) = \hat{H}_{\text{pq}} = \sum_k \left[\epsilon_{-,1,k} \hat{d}_{v,1,k}^\dagger \hat{d}_{v,1,k} + \epsilon_{+,1,k} \hat{d}_{c,1,k}^\dagger \hat{d}_{c,1,k} \right], \qquad (4.18)$$

where $\epsilon_{-,1,k} \leq \epsilon_{+,1,k}$, $\forall k$. The new conduction and valence band fermionic operators, $\hat{d}_{c,1,k}$ and $\hat{d}_{v,1,k}$, are defined as

$$\hat{\Phi}_{1,k} = \hat{U}_{1,k}\hat{\Psi}_k = \begin{bmatrix} \hat{d}_{c,1,k} \\ \hat{d}_{v,1,k} \end{bmatrix}. \tag{4.19}$$

At this point, one immediately obtains the time evolution of the Fermi spinor $\hat{\Psi}_k$ for $t > 0$ in the Heisenberg representation, which is given by the identity

$$\hat{\Psi}_k(t) = \hat{U}_{1,k}^\dagger \text{diag}\left\{e^{-i\epsilon_{+,1,k}t}, e^{-i\epsilon_{-,1,k}t}\right\} \hat{U}_{1,k}\hat{\Psi}_k(0). \tag{4.20}$$

We can now evaluate the response of the system to the quench by inspecting the long-time behavior of the following observable

$$\hat{M}_\Delta(t) = \frac{1}{N}\sum_k \hat{\Psi}_k^\dagger(t)\hat{\sigma}^x\hat{\Psi}(t), \tag{4.21}$$

which corresponds to the (staggered) magnetization along the direction of the applied field in the SOC (SP) system. Here, $N = (2\pi)^{-1}L(|k_1| + |k_2|)$ is the total number of particles in the system and L is its length. Following the discussion in Sec. 1.4.2, the system is expect to relax towards a GGE in which the relevant conserved quantities that should be taken into account are the occupation numbers $\hat{n}_{k,j}$ of the energy levels of the post-quench Hamiltonian, given by

$$\hat{n}_{k,j=1,2} = \left(\hat{\Psi}_k^\dagger \hat{U}_{1,k}^\dagger\right)_j \left(\hat{U}_{1,k}\hat{\Psi}_k\right)_j, \tag{4.22}$$

where j labels the component of the Fermi spinor. To evaluate the asymptotic value of Eq. (4.21) it is therefore sufficient to know the average over the pre-quench ground state $|\Phi_0\rangle$, denoted by $\langle\cdot\rangle_0$, of $\hat{n}_{k,j}$. Indeed, since all the $\hat{n}_{k,j}$ commute with the post-quench Hamiltonian $\hat{H}_{\text{pq}}$, they are conserved for $t > 0$ and, therefore, $\langle\hat{n}_{k,j}\rangle_0 = \langle\hat{n}_{k,j}\rangle_{\text{GGE}}$. We obtain

$$\langle\hat{n}_{k,1}\rangle_0 = \langle\hat{n}_{k,1}\rangle_{\text{GGE}} = |{-a_{1,k}b_{0,k} + a_{0,k}b_{1,k}}|^2 \langle\hat{d}_{v,0,k}^\dagger\hat{d}_{v,0,k}\rangle_0, \tag{4.23a}$$

$$\langle\hat{n}_{k,2}\rangle_0 = \langle\hat{n}_{k,2}\rangle_{\text{GGE}} = |a_{1,k}a_{0,k} + b_{0,k}b_{1,k}^*|^2 \langle\hat{d}_{v,0,k}^\dagger\hat{d}_{v,0,k}\rangle_0, \tag{4.23b}$$

where the averages $\langle\hat{d}_{v,0,k}^\dagger\hat{d}_{v,0,k}\rangle_0$ can be easily evaluated from Eq. (4.16). Using Eq. (4.19) and the fact that $\langle\hat{d}_{c,1,k}^\dagger\hat{d}_{v,1,k}\rangle_{\text{GGE}} = \langle\hat{d}_{v,1,k}^\dagger\hat{d}_{c,1,k}\rangle_{\text{GGE}} = 0$, one gets the steady state magnetization (staggered magnetization) for the SOC (SP) model

$$M_\Delta^{\text{ss}} = \frac{1}{N}\sum_k \langle\hat{\Psi}_k^\dagger\hat{\sigma}^x\hat{\Psi}_k\rangle_{\text{GGE}}$$

$$= \frac{1}{|k_1| + |k_2|}\int_{k_1}^{k_2} dk \left(a_{1,k}b_{1,k} + a_{1,k}b_{1,k}^*\right) \left(\langle\hat{n}_{k,1}\rangle_{\text{GGE}} - \langle\hat{n}_{k,2}\rangle_{\text{GGE}}\right), \tag{4.24}$$

where, in the last step, the thermodynamic limit has been performed.

EFFECTIVE TEMPERATURE PICTURE Since a quantum quench injects an extensive amount of energy in the system, it will be useful to compare our results with the ones obtained within an effective thermal ensemble with effective temperature $\beta_{\text{eff}}^{-1}(\Delta)$. The latter is obtained, for each value of the quench parameter Δ, by solving the following identity

$$\langle \Phi_0(0)|\hat{H}_{\text{pq}}|\Phi_0(0)\rangle = \frac{\text{Tr}\left\{e^{-\beta_{\text{eff}}(\Delta)[\hat{H}_{\text{pq}}-\mu(\Delta)\hat{N}]}\hat{H}_{\text{pq}}\right\}}{\text{Tr}\left\{e^{-\beta_{\text{eff}}(\Delta)[\hat{H}_{\text{pq}}-\mu(\Delta)\hat{N}]}\right\}} \tag{4.25}$$

for $\beta_{\text{eff}}^{-1}(\Delta)$. Here, $\mu(\Delta)$ is the Lagrange multiplier needed for ensuring particle number conservation. The associated effective (staggered) magnetization can thus be obtained as

$$\begin{aligned} M_\Delta^{\text{eff}} &= \frac{1}{N}\sum_k \langle \hat{\Psi}_k^\dagger \hat{\sigma}^x \hat{\Psi}_k \rangle_{\text{eff}} \\ &= \frac{1}{|k_1|+|k_2|}\int_{-\infty}^{\infty} dk \left(a_{1,k}b_{1,k} + a_{1,k}b_{1,k}^*\right)\left(\langle \hat{n}_{k,1}\rangle_{\text{eff}} - \langle \hat{n}_{k,2}\rangle_{\text{eff}}\right), \end{aligned} \tag{4.26}$$

with

$$\langle \hat{O}\rangle_{\text{eff}} = \frac{\text{Tr}\left\{e^{-\beta_{\text{eff}}(\Delta)[\hat{H}_{\text{pq}}-\mu(\Delta)\hat{N}]}\hat{O}\right\}}{\text{Tr}\left\{e^{-\beta_{\text{eff}}(\Delta)[\hat{H}_{\text{pq}}-\mu(\Delta)\hat{N}]}\right\}} \tag{4.27}$$

the average over a canonical thermal ensemble with effective temperature $\beta_{\text{eff}}^{-1}(\Delta)$. In particular,

$$\langle \hat{n}_{k,1}\rangle_{\text{eff}} = \frac{1}{1+e^{\beta_{\text{eff}}(\Delta)[\epsilon_{+,1,k}-\mu(\Delta)]}} \quad \text{and} \quad \langle \hat{n}_{k,2}\rangle_{\text{eff}} = \frac{1}{1+e^{\beta_{\text{eff}}(\Delta)[\epsilon_{-,1,k}-\mu(\Delta)]}}. \tag{4.28}$$

EQUILIBRIUM MAGNETIZATION Finally, we quote here the equilibrium magnetization (staggered magnetization) associated with the post-quench Hamiltonian of the SOC (SP) model,

$$M_\Delta^{\text{eq}} = \frac{1}{N}\sum_k \langle \hat{\Psi}_k^\dagger \hat{\sigma}^x \hat{\Psi}_k \rangle_1 = -\frac{1}{|k_1|+|k_2|}\int_{k_1}^{k_2} dk \left(a_{1,k}b_{1,k} + a_{1,k}b_{1,k}^*\right)\langle \hat{n}_{k,2}\rangle_1, \tag{4.29}$$

where the thermodynamic limit has been performed again and the average $\langle \hat{n}_{k,2}\rangle_1$ is evaluated on the ground state of the post-quench Hamiltonian (with the same number of particles of the pre-quench one),

$$|\Phi_1\rangle = \prod_{k_1}^{k_2}\left(\hat{\Phi}_{1,k}^\dagger\right)_2|0\rangle = \prod_{k_1}^{k_2}\left(\hat{U}_{1,k}^\dagger \hat{\Psi}_k^\dagger\right)_2|0\rangle. \tag{4.30}$$

In next Sections we will explicitly apply the general discussion developed so far to the SOC system and to the 1D chain of spinless fermions with a quenched staggered potential (SP model), both in their lattice and continuum versions. In particular, in order to distinguish between the various

model, in the following we will label them with the aid of an extra index i, defined as

$$\text{SOC} \rightarrow \begin{cases} \text{lattice} & i = 1 \\ \text{continuum} & i = 2 \end{cases} \qquad \text{SP} \rightarrow \begin{cases} \text{lattice} & i = 3 \\ \text{continuum} & i = 4 \end{cases}. \qquad (4.31)$$

4.3 QUENCH IN THE SPIN–ORBIT COUPLED SYSTEM

We start from the SOC model, whose possible realizations in condensed matter systems and cold atoms have been described in Sec. 4.1. The lattice version of its real space Hamiltonian, in the presence of PBC, is given by [255, 258, 259]

$$\hat{H}^{(1)} = \sum_{j=1}^{L} \left\{ \hat{\Psi}_j^{(1)\dagger} \left[2\hat{I}_{2\times2} + B\theta(t)\hat{\sigma}^x \right] \hat{\Psi}_j^{(1)} + \hat{\Psi}_j^{(1)\dagger} \left[\frac{i\alpha}{2}\hat{\sigma}^z - \hat{I}_{2\times2} \right] \hat{\Psi}_{j+1}^{(1)} + \text{H.c.} \right\},$$

$$(4.32)$$

where L is the total length of the system, α the SOC coupling, B the external magnetic field (see Sec. 4.1) and we set the lattice spacing to 1. Here, $\hat{\Psi}_i^{(1)\dagger} = \left(\hat{\psi}_{\uparrow,i}^{(1)\dagger}, \hat{\psi}_{\downarrow,i}^{(1)\dagger} \right)$ is a two-component spinor acting on the $i-$th lattice site, while the two indexes $a = \uparrow$ and $b = \downarrow$ are associated with spin up and spin down fermions, respectively. On the other hand, recalling Eq. (4.3), the single-particle Hamiltonian of the continuum model reads

$$\hat{H}^{(2)} = \int_0^L \hat{\Psi}^{(2)\dagger}(x) \left[-\partial_x^2 - i\alpha\hat{\sigma}^z\partial_x + B\theta(t)\hat{\sigma}^x \right] \hat{\Psi}^{(2)}(x)\,dx, \qquad (4.33)$$

with $\hat{\Psi}^{(2)\dagger}(x) = \left(\hat{\psi}_\uparrow^{(2)\dagger}(x), \hat{\psi}_\downarrow^{(2)\dagger}(x) \right)$.

Since in both the lattice and continuum model the system is translationally-invariant, it is possible to move into momentum space by introducing the Fourier transform of the Fermi spinor

$$\hat{\Psi}_j^{(1)} = \frac{1}{\sqrt{L}} \sum_k e^{ikj}\hat{\Psi}_k^{(1)}, \qquad \hat{\Psi}^{(2)}(x) = \frac{1}{\sqrt{L}} \sum_k e^{ikx}\hat{\Psi}_k^{(2)}, \qquad (4.34)$$

with $k = 2\pi n/L$ (n being an integer). In this case, the time-dependent Hamiltonian of the system can be written exactly in the form of Eq. (4.12)

$$\hat{H}^{(i)}(t) = \sum_k \hat{\Psi}_k^{(i)\dagger} \left[\hat{\mathcal{H}}_k^{(i)} + \theta(t)\Delta^{(i)}\hat{\sigma}^x \right] \hat{\Psi}_k^{(i)}, \qquad (4.35)$$

with $i = \{1, 2\}$, $\Delta^{(i)} = B$ and single-mode Hamiltonians $\hat{\mathcal{H}}_k^{(i)}$ given by

$$\hat{\mathcal{H}}_k^{(1)} = 2[1 - \cos(k)]\hat{I}_{2\times2} + \alpha\sin(k)\hat{\sigma}^z, \qquad \text{with } k \in [-\pi, \pi), \qquad (4.36a)$$

$$\hat{\mathcal{H}}_k^{(2)} = k^2\hat{I}_{2\times2} + \alpha k\hat{\sigma}^z, \qquad (4.36b)$$

for the lattice and the low-energy continuous models, respectively. Although the pre-quench single-mode Hamiltonians $\hat{\mathcal{H}}_k^{(i)}$ are already diagonal, they

can be more conveniently rewritten in terms of conduction and valence band Fermi operators using Eq. (4.13). In this case the coefficients of the unitary matrix $\hat{U}_{0,k}^{(i)}$ are

$$a_{0,k}^{(i)} = [1 - \delta_{k,0}]\theta(k) + \frac{\delta_{k,0}}{\sqrt{2}} \qquad b_{0,k}^{(i)} = [1 - \delta_{k,0}]\theta(-k) + \frac{\delta_{k,0}}{\sqrt{2}}, \qquad (4.37)$$

while the conduction and valence energy bands are

$$\epsilon_{\pm,0,k}^{(1)} = 2[1 - \cos(k)] \pm \alpha|\sin(k)|, \qquad (4.38a)$$

$$\epsilon_{\pm,0,k}^{(2)} = k^2 \pm \alpha|k|. \qquad (4.38b)$$

Finally, filling only states with negative energy results in $k_{1/2}^{(1)} = \mp 2\arctan[\alpha/2]$ and $k_{1/2}^{(2)} = \mp\alpha$.

On the other hand, in the post-quench regime $t > 0$, the unitary matrix $\hat{U}_{1,k}^{(i)}$ which diagonalizes the single-mode Hamitonian $\hat{\mathcal{H}}_k^{(i)} + B\hat{\sigma}^x$ has coefficients

$$a_{1,k}^{(1)} = \frac{B}{\sqrt{\left[D_k^{(1)} - \alpha\sin(k)\right]^2 + B^2}}, \qquad b_{1,k}^{(1)} = \frac{D_k^{(1)} - \alpha\sin(k)}{\sqrt{\left[D_k^{(1)} - \alpha\sin(k)\right]^2 + B^2}},$$

$$(4.39a)$$

$$a_{1,k}^{(2)} = \frac{B}{\sqrt{\left[D_k^{(2)} - \alpha k\right]^2 + B^2}}, \qquad b_{1,k}^{(2)} = \frac{D_k^{(2)} - \alpha k}{\sqrt{\left[D_k^{(2)} - \alpha k\right]^2 + B^2}}, \qquad (4.39b)$$

where $D_k^{(1)} = \sqrt{\alpha^2\sin^2(k) + B^2}$ and $D_k^{(2)} = \sqrt{\alpha^2 k^2 + B^2}$, while the post-quench conduction and valence bands are

$$\epsilon_{\pm,1,k}^{(1)} = 2[1 - \cos(k)] \pm D_k^{(1)}, \qquad (4.40a)$$

$$\epsilon_{\pm,1,k}^{(2)} = k^2 \pm D_k^{(2)}. \qquad (4.40b)$$

From Eq. (4.24) one immediately obtains the steady state magnetization along the direction of the applied magnetic field in the thermodynamic limit,

$$M_B^{\mathrm{ss},(i)} = \frac{2}{\left|k_1^{(i)}\right| + \left|k_2^{(i)}\right|} \left(\int_{k_1^{(i)}}^0 - \int_0^{k_2^{(i)}}\right) dk\, a_{1,k}^{(i)} b_{1,k}^{(i)} \left[\left(a_{1,k}^{(i)}\right)^2 - \left(b_{1,k}^{(i)}\right)^2\right]. \quad (4.41)$$

For the lattice model, using Eq. (4.39a), we have

$$M_B^{\mathrm{ss},(1)} = \frac{1}{\left|k_1^{(1)}\right| + \left|k_2^{(1)}\right|} \frac{B}{2\sqrt{\alpha^2 + B^2}} \log\left(\frac{Z_+}{Z_-}\right), \qquad (4.42)$$

with

$$Z_\pm = (\sqrt{\alpha^2 + B^2} \mp \alpha)^2 \left[\sqrt{\alpha^2 + B^2} \pm \alpha\frac{4 - \alpha^2}{4 + \alpha^2}\right]^2. \qquad (4.43)$$
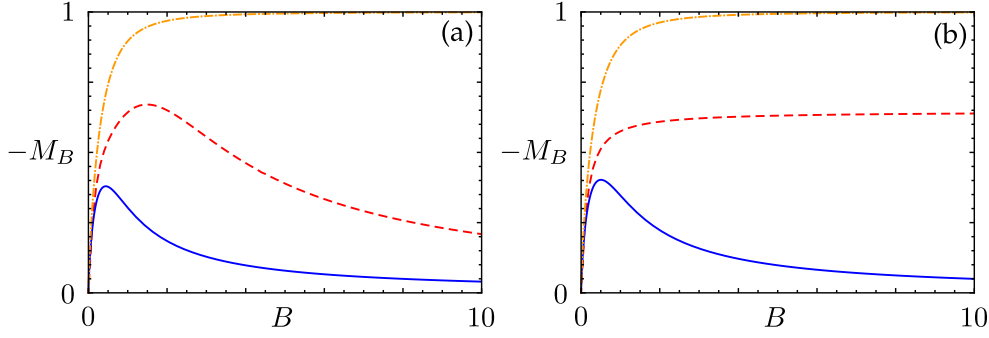
Figure 4.8: Panel (a): steady state magnetization $M_B^{\mathrm{ss},(1)}$ (blue, solid), equilibrium magnetization $M_B^{\mathrm{eq},(1)}$ (orange, dash-dotted) and effective temperature magnetization $M_B^{\mathrm{eff},(1)}$ (red, dashed) as a function of B for the lattice SOC system. Panel (b): same as in Panel (a) but for the continuum SOC model. In both Panels we set $\alpha = 1$.

The behavior of $M_B^{\mathrm{ss},(1)}$ is shown in Panel (a) of Fig. 4.8. On the other hand, for the low-energy continuous model one gets from Eq. (4.39b)

$$M_B^{\mathrm{ss},(2)} = -\frac{B}{4\alpha^2} \log\left[1 + 2\frac{\alpha^4}{B^2} + \frac{\alpha^8}{B^4}\right], \tag{4.44}$$

whose behavior is displayed in Panel (b) of Fig. 4.8.

Before discussing in detail the features of the steady state magnetization $M_\Delta^{\mathrm{ss},(i)}$, it is instructive to briefly address the zero-temperature equilibrium case associated with the post-quench Hamiltonian, shown in Fig. 4.8 as dash-dotted orange lines. From Eq. (4.29) we obtain

$$M_B^{\mathrm{eq},(i)} = -\frac{2}{\left|k_1^{(1)}\right| + \left|k_2^{(1)}\right|} \int_{k_1^{(i)}}^{k_2^{(i)}} dk \, a_{1,k}^{(i)} b_{1,k}^{(i)}. \tag{4.45}$$

In particular, using Eqs. (4.39), the above formula simplifies to

$$M_B^{\mathrm{eq},(1)} = \frac{\mathrm{sgn}(B)}{\left|k_1^{(1)}\right| + \left|k_2^{(1)}\right|} \left[F\left(k_1^{(1)}\,\middle|\, -\frac{\alpha^2}{B^2}\right) - F\left(k_2^{(1)}\,\middle|\, -\frac{\alpha^2}{B^2}\right)\right], \tag{4.46}$$

for the lattice model, with $\mathrm{sgn}(z)$ the sign function and $F(z\,|\,m)$ the incomplete elliptic integral of the first kind [142], and

$$M_B^{\mathrm{eq},(2)} = -\frac{B}{2\alpha^2} \log\left[\frac{-\alpha^2 - \sqrt{\alpha^4 + B^2}}{\alpha^2 - \sqrt{\alpha^4 + B^2}}\right] \tag{4.47}$$

for the low-energy continuous one. In the latter case, as expected, the magnetization grows monotonically as the static external magnetic field is increased until it saturates to $\lim_{B\to\infty} M_B^{\mathrm{eq},(i)} = 1$, where all spins are aligned with the field.

As can be seen from Fig. 4.8, the differences between this behavior and the one of the steady state magnetization after a sudden quench are remarkable:

$M_B^{\text{ss},(i)}$ is non-monotonous as a function of B, increasing up to a maximum before dropping to the pre-quench value (see blue solid lines in Fig. 4.8). A first qualitative interpretation of the phenomenon is the following. For an infinitesimal field B we do not expect any difference between a sudden quench and an adiabatic switching on of the gap opening mechanism, which would result in a magnetization identical to the equilibrium post-quench one. Thus, it is quite natural that for small quenches the systems begins to magnetize. On the other hand, when B strongly exceeds the kinetic energy contribution stemming from $\hat{\mathcal{H}}_k$, the magnetization along the direction of the field B is conserved and hence it remains at the value characterizing the pre-quench ground state. A maximum for a finite value B can thus be expected.

In Fig. 4.8 we also compare the GGE magnetization with the one obtained employing a thermal ensemble with a given effective temperature $\beta_{\text{eff}}^{-1}(B)$, as described in Sec. 4.2 [see, in particular, Eqs. (4.29) and (4.26), respectively]. As clearly emerges from both Panels of Fig. 4.8, this approach is not able to capture the behavior of $M_B^{\text{ss},(i)}$ after a sudden quench. In particular, in the continuum model of Panel (b) the disagreement between the curves is dramatic: the effective temperature picture gives a magnetization which saturates to a non-zero value, similarly to the equilibrium case discussed above although with a smaller saturation value. The failure of the effective temperature approach suggests that the mechanism responsible for the non-monotonic behavior of $M_B^{\text{ss},(i)}$ is not due to effective heating induced by the quench but must be sought in a pure non-equilibrium effect.

4.3.1 Light cone dynamics

To get a deeper understanding of the non-monotonic behavior of the magnetization, we now focus on the continuum SOC model and introduce the one-body correlation function

$$\mathcal{G}^{(2)}(x,t) = \langle \Phi_0^{(2)} | \hat{\Psi}^{(2)\dagger}(x,t)\hat{\sigma}^x\hat{\Psi}^{(2)}(0,t) | \Phi_0^{(2)} \rangle. \tag{4.48}$$

Here, $\hat{\Psi}^{(2)\dagger}(x,t)$ is the space-resolved Fermi spinor introduced in Eq. (4.33) in the Heisenberg picture, while the average is evaluated on the pre-quench equilibrium ground state $|\Phi_0^{(2)}\rangle$. Clearly, $\lim_{x\to 0}\mathcal{G}^{(2)}(x,t) = M^{(2)}(t)$, i.e. it coincides with the time-dependent magnetization of the system.

In order to obtain the time evolution of $\mathcal{G}^{(2)}(x,t)$, we start by deriving the equation of motion of the Fermi field operator $\hat{\Psi}^{(2)}(x,t)$. By using the real-space Hamiltonian of Eq. (4.33) one gets the following Heisenberg equation of motion for the two components of the Fermi spinor,

$$\partial_t\hat{\psi}_\sigma^{(2)}(x,t) = \left(i\partial_x^2 - \sigma\alpha\partial_x\right)\hat{\psi}_\sigma^{(2)}(x,t) - iB\hat{\psi}_{-\sigma}^{(2)}(x,t), \tag{4.49}$$

with $\sigma = \{\uparrow,\downarrow\}$. From the above equation, we can derive the equation of motion for the spin resolved Green's functions,

$$G_{\sigma\sigma'}^{(2)}(x,t) = \langle \hat{\psi}_\sigma^{(2)\dagger}(x,t)\hat{\psi}_{\sigma'}^{(2)}(0,t) \rangle_0. \tag{4.50}$$

As a result, we obtain the following closed set of differential equations

$$\partial_t G^{(2)}_{\uparrow\uparrow}(x,t) = -iB\left[\mathcal{G}^{(2)}_{\uparrow\downarrow}(x,t) - G^{(2)}_{\downarrow\uparrow}(x,t)\right],\tag{4.51a}$$

$$\partial_t G^{(2)}_{\uparrow\downarrow}(x,t) = -iB\left[G^{(2)}_{\uparrow\uparrow}(x,t) - G^{(2)}_{\downarrow\downarrow}(x,t)\right] + 2\alpha\partial_x G^{(2)}_{\uparrow\downarrow}(x,t),\tag{4.51b}$$

$$\partial_t G^{(2)}_{\downarrow\uparrow}(x,t) = +iB\left[G^{(2)}_{\uparrow\uparrow}(x,t) - G^{(2)}_{\downarrow\downarrow}(x,t)\right] - 2\alpha\partial_x G^{(2)}_{\downarrow\uparrow}(x,t),\tag{4.51c}$$

$$\partial_t G^{(2)}_{\downarrow\downarrow}(x,t) = +iB\left[G^{(2)}_{\uparrow\downarrow}(x,t) - G^{(2)}_{\downarrow\uparrow}(x,t)\right].\tag{4.51d}$$

Note that the correlation function of Eq. (4.48) can be written as $\mathcal{G}^{(2)}(x,t) = G^{(2)}_{\uparrow\downarrow}(x,t) + G^{(2)}_{\downarrow\uparrow}(x,t)$. From Eq. (4.51), we thus get

$$\partial_t^2 \mathcal{G}^{(2)}(x,t) = 2\alpha\partial_x\partial_t\left[G^{(2)}_{+-}(x,t) - G^{(2)}_{-+}(x,t)\right]$$
$$= 4\alpha^2\partial_x^2 \mathcal{G}^{(2)}(x,t) - 4i\alpha B\partial_x\left[G^{(2)}_{++}(x,t) - G^{(2)}_{--}(x,t)\right].\tag{4.52}$$

It is now convenient to introduce the function $S(x,t) = \mathcal{G}^{(2)}_{\uparrow\uparrow}(x,t) - G^{(2)}_{\downarrow\downarrow}(x,t)$, whose time derivative satisfies the identity

$$\partial_t S(x,t) = -2iB\left[G^{(2)}_{\uparrow\downarrow}(x,t) - G^{(2)}_{\downarrow\uparrow}(x,t)\right].\tag{4.53}$$

By formally integrating the above equation, one obtains

$$S(x,t) = S(x,0) - 2iB\int_0^t\left[G^{(2)}_{\uparrow\downarrow}(x,t') - G^{(2)}_{\downarrow\uparrow}(x,t')\right]dt'.\tag{4.54}$$

Then, by taking the space derivative of $S(x,t)$ and noting that [see Eqs. (4.51b) and (4.51c)]

$$\partial_x\left[G^{(2)}_{\uparrow\downarrow}(x,t') - G^{(2)}_{\downarrow\uparrow}(x,t')\right] = (2\alpha)^{-1}\partial_t \mathcal{G}^{(2)}(x,t),\tag{4.55}$$

we get

$$\partial_x S(x,t) = \partial_x S(x,0) - i\frac{B}{\alpha}\mathcal{G}^{(2)}(x,t).\tag{4.56}$$

Finally, turning back to Eq. (4.52), we obtain that in the case of a sudden quench $\mathcal{G}^{(2)}(x,t)$ satisfies, for $t > 0$, an inhomogeneous KG equation

$$\left(\partial_x^2 - \frac{1}{4u_2^2}\partial_t^2\right)\mathcal{G}^{(2)}(x,t) = \lambda_2^2\mathcal{G}^{(2)}(x,t) + \lambda_2\phi_2(x),\tag{4.57}$$

where $\lambda_2 = B/u_2$, $u_2 = \alpha$ and

$$\phi_2(x) = i\partial_x\langle\hat{\Psi}^{(2)\dagger}(x,0)\hat{\sigma}^z\hat{\Psi}^{(2)}(0,0)\rangle_0\tag{4.58}$$

$$= 2\left[\frac{1-\cos(\alpha x)}{x^2} - \frac{\alpha\sin(\alpha x)}{x}\right].\tag{4.59}$$

is a source term. Equation (4.57) is the main result of this Section and can be solved by imposing the pre-quench boundary-value condition $\mathcal{G}^{(2)}(x,0) = 0$. One obtains

$$\mathcal{G}^{(2)}(x,t) = \frac{1}{\pi}\left(\int_{k_1^{(2)}}^0 - \int_0^{k_2^{(2)}}\right)dk\, a^{(2)}_{1,k}b^{(2)}_{1,k}\left[\left(a^{(2)}_{1,k}\right)^2 - \left(b^{(2)}_{1,k}\right)^2\right]$$
$$\times \cos(kx)\left[1 - \cos\left(2D^{(2)}_k t\right)\right].\tag{4.60}$$
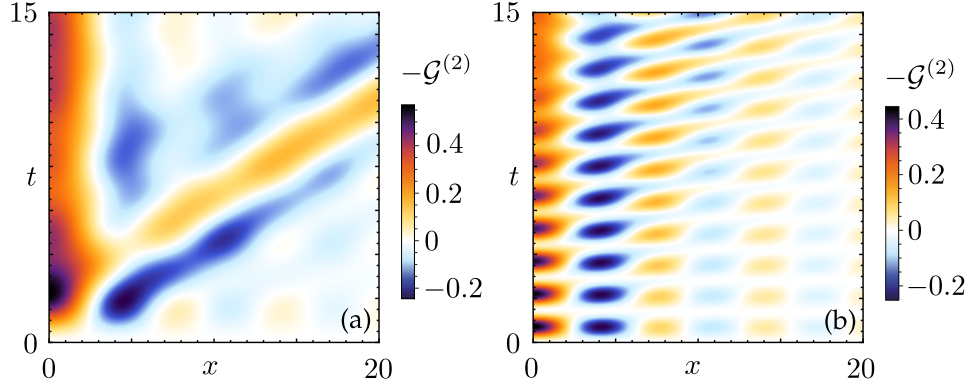
Figure 4.9: Panel (a): Density plot of $-\mathcal{G}^{(2)}(x,t)$ as a function of x and t for $B = 0.3$ and $\alpha = 1$; Panel (b): same as in Panel (a) but for $B = 2$ and $\alpha = 1$.

The analysis of the time evolution of $\mathcal{G}^{(2)}(x,t)$ can shed light on the dynamics leading to the non-monotonous magnetization. Its dynamics is shown in Fig. 4.9, in the case of (a) a small quench with $B = 0.3$ and (b) a large quench with $B = 2$. In the former, the propagation of a LC perturbation arising from the origin can be clearly seen: $\mathcal{G}^{(2)}(x,t)$ exhibits a typical LC behavior [15, 32, 33, 102] (see Chapters 1 and 3) and information of the quench is therefore able to propagate throughout the system. This leaves a finite trail in $x = 0$, which eventually results in a finite value of $M^{(2)}(t)$ at large times. On the other hand, the response of $\mathcal{G}^{(2)}(x,t)$ to the shock induced by a large quench is dramatically different. Indeed, in this regime, $\mathcal{G}^{(2)}(x,t)$ is characterized by weakly damped and almost stationary oscillations both in space and in time, which strongly hinder the propagation of the information through the system and results in both a slowdown and in an overall suppression of the LC. Therefore, the correlation function $\mathcal{G}^{(2)}(x,t)$ oscillates around its pre-quench initial value and, in the long-time limit, remains very close to the latter. This phenomenon can thus be interpreted as an effective freezing of the LC. We attribute the emergence of the non-monotonous behavior of $M_B^{\text{ss},(2)}$ as a function of B to the competition between propagation and freezing regimes. The identification of a freezing regime for large quenches constitutes a crucial result and – as we shall show in the last part of the Chapter – is a quite universal and robust feature of gap-opening sudden quenches. It represents an important new concept in the physics of quantum quenches: Even though the gap is not able to dynamically introduce a length scale in the correlation functions, it dramatically influences the LC propagation.

The above behavior can be explained more formally by inspecting the KG equation of Eq. (4.57), which suggests an interpretation of the propagation and freezing regimes in terms of a simple mechanical model. Indeed, its solutions are driven by a competition between the source term $\propto \lambda_i$ and the mass term $\propto \lambda_i^2$. The former, which in our case contains the information about the quench, induces a finite perturbation in $\mathcal{G}^{(2)}(x,t)$, with an amplitude linearly proportional to B. The mass term, on the other hand,

counter-acts the magnetization and tends to restore the initial configuration of the system in a damped oscillatory way. In a simple mechanical interpretation [260], the KG equation describes the transverse vibrations of a string embedded into an elastic medium with elastic constant $\propto \lambda_2^2$. When the medium is slack, vibrations can propagate almost without disturbance, while in a stiff medium the wave propagation is strongly hindered. The turning point turns out to be for $\lambda_2 \sim 1$, which corresponds to the location of the maximum of $M_B^{\text{ss},(2)}$ shown in Fig. 4.8. Therefore, when the gap becomes comparable to the average kinetic energy scale, the freezing of the LC begins to occur. Thanks to Wick's theorem [19], a similar behavior characterizes all higher order correlators. This issue is relevant since some of those correlators are either easier to numerically evaluate in interacting systems, such as the one we will analyze later in this Chapter, or are experimentally more accessible.

4.3.2 Finite duration quench of the magnetic field

We now investigate if the non-monotonic behavior of the steady state magnetization discussed above survives also in the presence of a quench of the magnetic field with finite duration. In particular, we consider a quench protocol in which the magnetic field is switched on with a linear ramp of duration τ, analogous to the one studied for the interaction quench in Chap. 3. The Hamiltonian of the system is

$$\hat{H}^{(2)} = \sum_k \hat{\Psi}_k^{(2)\dagger} \left[\hat{\mathcal{H}}_k^{(2)} + Q(t)B\hat{\sigma}^x \right] \hat{\Psi}_k^{(2)}, \tag{4.61}$$

with

$$Q(t) = \begin{cases} 0 & \text{for } t < 0 \\ t/\tau & \text{for } 0 \leq t \leq \tau \\ 1 & \text{for } t > \tau \end{cases} . \tag{4.62}$$

During and after the quench, the Heisenberg equation of motion for the components of the Fermi spinor are

$$\partial_t \hat{d}_{\sigma,k}^{(2)}(t) = -i \left[(k^2 + \sigma\alpha k)\hat{d}_{\sigma,k}^{(2)}(t) + Q(t)B\hat{d}_{-\sigma,k}^{(2)}(t) \right], \tag{4.63}$$

where $\sigma = \{\uparrow, \downarrow\}$. To solve this coupled system of differential equations, we take the following ansatz [169]

$$\begin{bmatrix} \hat{d}_{\uparrow,k}^{(2)}(t) \\ \hat{d}_{\downarrow,k}^{(2)}(t) \end{bmatrix} = \begin{bmatrix} f_{\uparrow,k}(t) & g_{\uparrow,k}(t) \\ f_{\downarrow,k}(t) & g_{\downarrow,k}(t) \end{bmatrix} \begin{bmatrix} \hat{d}_{\uparrow,k}^{(2)}(0) \\ \hat{d}_{\downarrow,k}^{(2)}(0) \end{bmatrix} \equiv \hat{V}_k(t) \begin{bmatrix} \hat{d}_{\uparrow,k}^{(2)}(0) \\ \hat{d}_{\downarrow,k}^{(2)}(0) \end{bmatrix}, \tag{4.64}$$

where $\hat{d}_{\sigma,k}^{(2)}(0)$ is the Fermi operator in the Schrödinger picture at $t = 0$. All the time dependence is encoded in the functions $f_{\sigma,k}(t)$ and $g_{\sigma,k}(t)$, which satisfy the initial conditions $f_{\uparrow,k}(0) = g_{\downarrow,k}(0) = 1$ and $f_{\downarrow,k}(0) = g_{\uparrow,k}(0) = 0$. Since anti-commutation relations between the operators $\hat{d}_{\sigma,k}^{(2)}(t)$ must hold during the whole time evolution, we have that $|f_{\sigma,k}(t)|^2 + |g_{\sigma,k}(t)|^2 = 1$, $\forall t$.

By substituting the ansatz of Eq. (4.64) in Eq. (4.63), we obtain two decoupled systems for $f_{\sigma,k}(t)$ and $g_{\sigma,k}(t)$, respectively,

$$i\partial_t \begin{bmatrix} f_{\uparrow,k}(t) \\ f_{\downarrow,k}(t) \end{bmatrix} = \begin{bmatrix} k^2 + \alpha k & Q(t)B \\ Q(t)B & k^2 - \alpha k \end{bmatrix} \begin{bmatrix} f_{\uparrow,k}(t) \\ f_{\downarrow,k}(t) \end{bmatrix}, \tag{4.65a}$$

$$i\partial_t \begin{bmatrix} g_{\uparrow,k}(t) \\ g_{\downarrow,k}(t) \end{bmatrix} = \begin{bmatrix} k^2 + \alpha k & Q(t)B \\ Q(t)B & k^2 - \alpha k \end{bmatrix} \begin{bmatrix} g_{\uparrow,k}(t) \\ g_{\downarrow,k}(t) \end{bmatrix}. \tag{4.65b}$$

These systems can be solved in the same way, given that the appropriate initial conditions are used. In particular, introducing the notation $v = \{f, g\}$, we define the functions [189] (see also Chap. 3)

$$S_{v,k}(t) = v_{\uparrow,k}(t) + v_{\downarrow,k}(t), \qquad D_{v,k}(t) = v_{\uparrow,k}(t) - v_{\downarrow,k}(t). \tag{4.66}$$

Using Eq. (4.65), it is possible to show that they satisfy the following differential equations

$$\begin{cases} i\partial_t S_{v,k}(t) = \left[k^2 + Q(t)B \right] S_{v,k}(t) + \alpha k D_{v,k}(t) \\ i\partial_t D_{v,k}(t) = \left[k^2 - Q(t)B \right] D_{v,k}(t) + \alpha k S_{v,k}(t) \end{cases}. \tag{4.67}$$

Finally, from the above system we derive the following second-order differential equation for $D_{v,k}(t)$

$$\partial_t^2 D_{v,k}(t) + 2ik^2 \partial_t D_{v,k}(t) + \left[B^2 Q^2(t) - k^4 + \alpha^2 k^2 - iB\partial_t Q(t) \right] D_{v,k}(t) = 0, \tag{4.68}$$

which can be analytically solved in every region defined by the quench protocol in Eq. (4.62) using the appropriate matching conditions on the boundaries of each them. Moreover, once we get $D_{v,k}(t)$, the function $S_{v,k}(t)$ is automatically determined by the second equation in Eq. (4.67).

The magnetization along the applied magnetic field can be evaluated within the GGE with a straightforward generalization of procedure described for the sudden quench case. In particular, the quantities conserved after the quench (i.e. for $t > \tau$) are $\langle \hat{n}_{k,j}^{(2)}(\tau) \rangle_0 = \langle \hat{n}_{k,j}^{(2)}(\tau) \rangle_{GGE}$, with

$$\hat{n}_{k,j}^{(2)}(\tau) = \left(\hat{\Phi}_{0,k}^{(2)\dagger} \hat{U}_{0,k}^{(2)} \hat{V}_k^\dagger(\tau) \hat{U}_{1,k}^{(2)\dagger} \right)_j \left(\hat{U}_{1,k}^{(2)} \hat{V}_k(\tau) \hat{U}_{0,k}^{(2)\dagger} \hat{\Phi}_{0,k}^{(2)} \right)_j \tag{4.69}$$

the occupation numbers of the post-quench energy levels and the unitary matrix $\hat{V}_k(t)$ introduced in Eq. (4.64). From the knowledge of $\langle \hat{n}_{k,j}^{(2)}(\tau) \rangle_{GGE}$ and thanks to the fact that

$$\langle \hat{d}_{c,1,k}^{(i)\dagger}(\tau) \hat{d}_{v,1,k}^{(i)}(\tau) \rangle_{GGE} = \langle \hat{d}_{v,1,k}^{(i)\dagger}(\tau) \hat{d}_{c,1,k}^{(i)}(\tau) \rangle_{GGE} = 0, \tag{4.70}$$

one can straightforwardly evaluate the steady state magnetization

$$M_{B;\tau}^{ss,(2)} = \frac{1}{N^{(2)}} \sum_k \langle \hat{\Psi}_k^{(2)\dagger} \hat{\sigma}^x \hat{\Psi}_k^{(2)} \rangle_{GGE}$$

$$= \frac{1}{N^{(2)}} \sum_k \langle \hat{\Phi}_{1,k}^{(2)\dagger}(\tau) \hat{U}_{1,k}^{(2)} \hat{V}_k(\tau) \hat{\sigma}^x \hat{V}_k^\dagger(\tau) \hat{U}_{1,k}^{(2)\dagger} \hat{\Phi}^{(2)}(\tau) \rangle_{GGE}. \tag{4.71}$$

The behavior of $M_{B;\tau}^{ss,(2)}$ for quench protocols with different time duration τ is shown in Fig. 4.10. As one can clearly see, the non-monotonic behavior persists for any finite duration τ. It disappears only in the limit $\tau \to \infty$, in which $M_{B;\tau}^{ss,(2)}$ tends to the (post-quench) equilibrium magnetization.

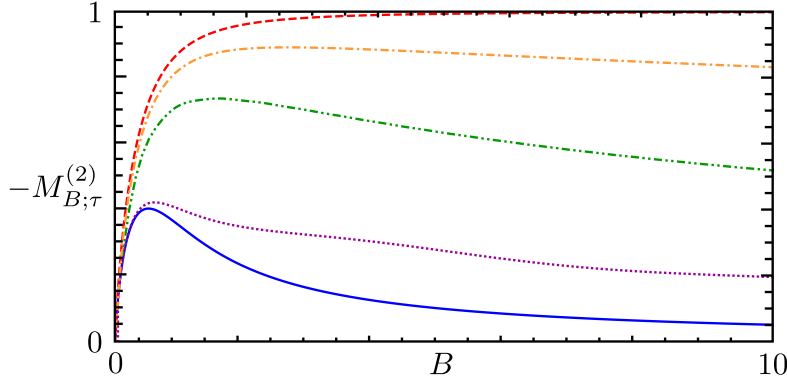**Figure 4.10:** Plot of the steady state magnetization $M^{\mathrm{ss},(2)}_{B,\tau}$ for the continuum SOC model as a function of B and $\alpha = 1$ for different quench protocols with increasingly long switch-on times τ (units $1/\alpha^2$): $\tau = 0$, sudden quench (blue, solid), $\tau = 1$ (purple, dotted), $\tau = 10$ (green, dash-dot-dotted), $\tau = 100$ (yellow, dash-dotted), $\tau = \infty$ – corresponding to the equilibrium magnetization of the post-quench Hamiltonian – (red, dashed).

4.3.3 Robustness against dimensionality

To further support the idea that the emergence of KG physics is robust and represents a generic feature of gap-opening quenches, we checked if it also occurs in higher dimensions. To do so, in this Section we consider the quench of the magnetic field in a 2D Rashba-coupled Fermi gas [261, 262]. The real-space Hamiltonian of the system is

$$\hat{H}^{(2\mathrm{D})}(t) = \int_0^L \int_0^L \hat{\Psi}^\dagger(\boldsymbol{r}) \left[-\nabla_{\boldsymbol{r}}^2 - i\alpha(\hat{\sigma}^x \partial_y - \hat{\sigma}^y \partial_x) \right] \hat{\Psi}(\boldsymbol{r}) \, d\boldsymbol{r}, \qquad (4.72)$$

where $\boldsymbol{r} = (x, y)$ and $\nabla_{\boldsymbol{r}} = (\partial_x, \partial_y)$. By introducing the Fourier transform of the Fermi field $\hat{\Psi}(\boldsymbol{r})$,

$$\hat{\Psi}(\boldsymbol{r}) = \frac{1}{L} \sum_{\boldsymbol{k}} e^{i\boldsymbol{k}\cdot\boldsymbol{r}} \hat{\Psi}_{\boldsymbol{k}}, \qquad (4.73)$$

with discretized (quasi-)momentum $\boldsymbol{k} = (k_x, k_y) = 2\pi L^{-1}(n_x, n_y)$ (n_x and n_y being integer numbers) and L the linear dimension of the system, we can write Eq. (4.72) in Fourier space as

$$\hat{H}^{(2\mathrm{D})}(t) = \sum_{\boldsymbol{k}} \hat{\Psi}^\dagger_{\boldsymbol{k}} [\hat{\mathcal{H}}^{(2\mathrm{D})}_{\boldsymbol{k}} + \theta(t) B \hat{\sigma}^z] \hat{\Psi}_{\boldsymbol{k}}. \qquad (4.74)$$

Here, $\hat{\Psi}^\dagger_{\boldsymbol{k}} = (\hat{d}^\dagger_{\uparrow,\boldsymbol{k}}, \hat{d}^\dagger_{\downarrow,\boldsymbol{k}})$, with $\hat{d}_{\uparrow,\boldsymbol{k}}$ ($\hat{d}_{\downarrow,\boldsymbol{k}}$) fermionic annihilation operators for spin up (down) fermions with momentum $\boldsymbol{k}$ and

$$\hat{\mathcal{H}}^{(2\mathrm{D})}_{\boldsymbol{k}} = \hat{k}\hat{I}_{2\times 2} + \alpha(\hat{\sigma}^x \hat{k}_y - \hat{\sigma}^y \hat{k}_x), \qquad (4.75)$$

with $k = |\boldsymbol{k}| = \sqrt{k_x^2 + k_y^2}$, is the pre-quench Hamiltonian density.

Following the same steps outlined in previous Sections, we begin with the pre-quench case. For $t < 0$ the single-mode Hamiltonian is diagonalized by the unitary matrix

$$\hat{U}_{0,k} = \begin{bmatrix} a_{0,k} & b_{0,k} \\ -b^*_{0,k} & a_{0,k} \end{bmatrix}, \tag{4.76}$$

with

$$a_{0,k} = \frac{1}{\sqrt{2}} \quad \text{and} \quad b_{0,k} = \frac{1}{\sqrt{2}} \frac{k_x + ik_y}{k}. \tag{4.77}$$

The pre-quench conduction and valence fermionic operators are thus given by

$$\hat{\Phi}_{0,k} = \hat{U}_{0,k}\hat{\Psi}_k = \begin{bmatrix} \hat{d}_{c,0,k} \\ \hat{d}_{v,0,k} \end{bmatrix}, \tag{4.78}$$

with associated energy levels

$$\epsilon_{\pm,0,k} = k^2 \pm \alpha k. \tag{4.79}$$

When the energy bands are filled up to the linear crossing at $k = 0$ (i.e. the chemical potential is set to zero) the pre-quench equilibrium ground state $|\Phi_0^{(2D)}\rangle$ is

$$|\Phi_0^{(2D)}\rangle = \prod_{k \leq \alpha} \left(\hat{\Phi}^\dagger_{0,k}\right)_2 |0_{2D}\rangle = \prod_{k \leq \alpha} \left(\hat{U}^\dagger_{0,k}\hat{\Psi}^\dagger_k\right)_2 |0_{2D}\rangle, \tag{4.80}$$

with $|0_{2D}\rangle$ the vacuum of the system. As usual, the subscript 2 means that the second component of the spinor has to be considered.

We now turn to the post-quench regime. For $t > 0$ the unitary matrix diagonalizing the single-mode Hamiltonian $\hat{\mathcal{H}}_k + B\hat{\sigma}^z$ is

$$\hat{U}_{1,k} = \begin{bmatrix} a_{1,k} & b_{1,k} \\ -b^*_{1,k} & a_{1,k} \end{bmatrix}, \tag{4.81}$$

with

$$a_{1,k} = \frac{\alpha k}{\sqrt{(D_k - B)^2 + \alpha^2 k^2}}, \qquad b_{1,k} = \frac{D_k - B}{\sqrt{(D_k - B)^2 + \alpha^2 k^2}} \frac{k_x + ik_y}{k}. \tag{4.82}$$

Here, we have introduced the coefficient $D_k = \sqrt{B^2 + \alpha^2 k^2}$. The post-quench conductance and valence band Fermi operators are

$$\hat{\Phi}_{1,k} = \hat{U}_{1,k}\hat{\Psi}_k = \begin{bmatrix} \hat{d}_{c,1,k} \\ \hat{d}_{v,1,k} \end{bmatrix}, \tag{4.83}$$

with associated energy levels

$$\varepsilon_{\pm,1,k} = (k_x^2 + k_y^2) \pm D_k. \tag{4.84}$$

In order to get the steady state magnetization along the applied magnetic field within the GGE picture, we evaluate the averages of the conserved occupation numbers of the post-quench energy levels,

$$\hat{n}_{k,j=1,2} = \left(\hat{\Psi}^\dagger_k\hat{U}^\dagger_{1,k}\right)_j \left(\hat{U}_{1,k}\hat{\Psi}_k\right)_j, \tag{4.85}$$
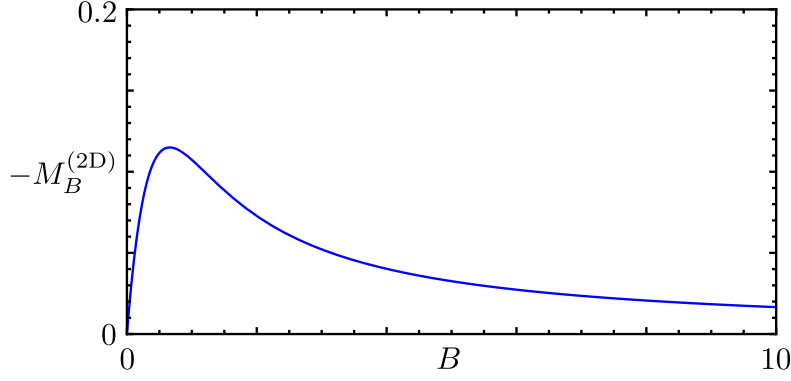
Figure 4.11: Plot of $M^{(2D)}$ for the 2D Rashba-coupled Fermi gas as a function of B for $\alpha = 1$.

over the pre-quench ground state $|\Phi_0^{(2D)}\rangle$. We obtain

$$\langle \hat{n}_{k,1} \rangle_0 = \langle \hat{n}_{k,1} \rangle_{\text{GGE}} = |-a_{1,k}b_{0,k} + a_{0,k}b_{1,k}|^2 \langle \hat{d}_{v,0,k}^\dagger \hat{d}_{v,0,k} \rangle_0, \qquad (4.86a)$$

$$\langle \hat{n}_{k,2} \rangle_0 = \langle \hat{n}_{k,2} \rangle_{\text{GGE}} = |a_{1,k}a_{0,k} + b_{0,k}b_{1,k}^*|^2 \langle \hat{d}_{v,0,k}^\dagger \hat{d}_{v,0,k} \rangle_0. \qquad (4.86b)$$

Since $\langle \hat{d}_{c,1,k}^\dagger \hat{d}_{v,1,k} \rangle_{\text{GGE}} = \langle \hat{d}_{v,1,k}^\dagger \hat{d}_{c,1,k} \rangle_{\text{GGE}} = 0$, the steady state magnetization after the quench evaluates to

$$
\begin{aligned}
M_B^{(2D)} &= \frac{1}{N^{(2D)}} \sum_k \langle \hat{\Psi}_k^\dagger \hat{\sigma}^z \hat{\Psi}_k \rangle_{\text{GGE}} \\
&= \frac{1}{N^{(2D)}} \sum_k \left(a_{1,k}^2 - |b_{1,k}|^2 \right) \left(\langle \hat{n}_{k,1} \rangle_{\text{GGE}} - \langle \hat{n}_k \rangle_{\text{GGE}} \right) \\
&= -\frac{B}{\alpha^2} \left[1 - \frac{B}{\alpha^2} \operatorname{arccot}\left(\frac{B}{\alpha^2} \right) \right],
\end{aligned}
\qquad (4.87)
$$

where in the last step the thermodynamic limit has been performed and we used that $N^{(2D)} = (L\alpha)^2 (4\pi)^{-1}$. As clearly emerges from Fig. 4.11, $M_B^{(2D)}$ exhibits a non-monotonic behavior very similar to the one found in the 1D case.

4.4 QUENCH IN A SPINLESS 1D FERMIONIC CHAIN

At this point one could wonder if the results obtained so far are peculiar to SOC models or if they are present in more general quenches of a gap-opening mechanisms. In order to investigate this issue, in this Section we study two very different quenches in a 1D chain of spinless fermions, namely the quench of a staggered potential δ (SP model) and the one of nearest (and possibly next-to-nearest) neighbor inter-particle interactions. Although these mechanisms open gaps with a very different origin, we will show that the response of the system can be explained again in terms of the competition between a propagation and a freezing regime of the LC effect in suitably chosen correlation functions.

We begin with the real-space lattice Hamiltonian of the spinless fermionic chain,

$$\hat{H}^{(3)}(t) = \hat{H}_0^{(3)} + \hat{H}_{\text{gap}}^{(3)}(t), \tag{4.88}$$

with

$$\hat{H}_0^{(3)} = -J \sum_{j=1}^{L} \left(\hat{c}_j^{(3)\dagger} \hat{c}_{j+1}^{(3)} + \text{H.c.} \right). \tag{4.89}$$

Here, $\hat{c}_j^{(3)}$ are annihilation operators for spinless fermions on the site j of the lattice, L is length of the system and we set the lattice spacing to 1. Introducing the spinor $\hat{\Psi}_k^{(i)\dagger} = \left(\hat{d}_{a,k}^{(i)\dagger}, \hat{d}_{b,k}^{(i)\dagger} \right) = \left(\hat{c}_k^{(i)\dagger}, \hat{c}_{k-\pi}^{(i)\dagger} \right)$, with $\hat{c}_j^{(i)} = \sum_k e^{ikj} \hat{c}_k^{(i)}/\sqrt{L}$ and $i = \{3,4\}$, the pre-quench Hamiltonian can be written in the form of Eq. (4.11),

$$\hat{H}_0^{(i)} = \sum_{k>0} \hat{\Psi}_k^{(i)\dagger} \hat{\mathcal{H}}_k^{(i)} \hat{\Psi}_k^{(i)}, \tag{4.90}$$

where the pre-quench single mode Hamiltonians $\hat{\mathcal{H}}_k^{(i)}$ are

$$\hat{\mathcal{H}}_k^{(3)} = -2J\cos(k)\hat{\sigma}^z, \tag{4.91a}$$

$$\hat{\mathcal{H}}_k^{(4)} = -2J(k - \pi/2)\hat{\sigma}^z, \tag{4.91b}$$

with $k \in [0,\pi)$, for the lattice and the low-energy continuous models, respectively. Note that, to obtain the low-energy theory for the SP model, $i = 4$, we expanded around $k = \pi/2$. In these models fermionic operators $\hat{d}_{a,k}^{(i)}$ and $\hat{d}_{b,k}^{(i)}$ are associated with right and left moving fermions, respectively.

Also in this case the pre-quench single-mode Hamiltonians are diagonal and, again, we can conveniently introduce conduction and valence band Fermi operators using Eq. (4.13). The coefficients of the unitary matrix $\hat{U}_{0,k}^{(i)}$ are

$$a_{0,k}^{(i)} = [1 - \delta_{k,\pi/2}]\theta\left(\frac{\pi}{2} - k\right) + \frac{\delta_{k,\pi/2}}{\sqrt{2}} \tag{4.92a}$$

$$b_{0,k}^{(i)} = [1 - \delta_{k,\pi/2}]\theta\left(k - \frac{\pi}{2}\right) + \frac{\delta_{k,\pi/2}}{\sqrt{2}}, \tag{4.92b}$$

while the pre-quench conductance and valence bands are

$$\epsilon_{\pm,0,k}^{(3)} = \pm 2J|\cos(k)|, \tag{4.93a}$$

$$\epsilon_{\pm,0,k}^{(4)} = \pm 2J|k - \pi/2|. \tag{4.93b}$$

In this model the linear crossing between the energy bands occurs at $k = \pi/2$. Imposing that only states below this point are occupied, one obtains $k_1^{(3)} = k_1^{(4)} = 0$ and $k_2^{(3)} = k_2^{(4)} = \pi$. Note that we are considering a continuum model with the same number of particles of its lattice counterpart.

4.4.1 Quench of a staggered potential

We begin by discussing the SP model, in which a staggered potential is suddenly turned on at $t = 0$. In this case, the gap-opening mechanism Hamiltonian is

$$\hat{H}_{\text{gap}}^{(i)}(t) = -J\delta\theta(t)\sum_{j=1}^{L}(-1)^{j}\left(\hat{c}_{j}^{(i)\dagger}\hat{c}_{j}^{(i)} + \text{H.c.}\right),\tag{4.94}$$

where $\delta = \Delta^{(i)}$ is the strength of the SP. Thus, the time-dependent Hamiltonian of the system takes the form of Eq. (4.12),

$$\hat{H}^{(i)}(t) = \sum_{k>0}\hat{\Psi}_{k}^{(i)\dagger}\left[\hat{\mathcal{H}}_{k}^{(i)} + \theta(t)\delta\hat{\sigma}^{x}\right]\hat{\Psi}_{k}^{(i)}.\tag{4.95}$$

The post-quench single-mode Hamiltonian $\hat{\mathcal{H}}_{k}^{(i)} + \delta\hat{\sigma}^{x}$ can be diagonalized by the unitary matrix $\hat{U}_{1,k}^{(i)}$, whose coefficients are

$$a_{1,k}^{(3)} = \frac{\delta}{\sqrt{\left[\epsilon_{+,1,k}^{(3)} + 2J\cos(k)\right]^{2} + \delta^{2}}},\tag{4.96a}$$

$$b_{1,k}^{(3)} = \frac{\epsilon_{+,1,k}^{(3)} + 2J\cos(k)}{\sqrt{\left[\epsilon_{+,1,k}^{(3)} + 2J\cos(k)\right]^{2} + \delta^{2}}},\tag{4.96b}$$

for the lattice model and

$$a_{1,k}^{(4)} = \frac{\delta}{\sqrt{\left[\epsilon_{+,1,k}^{(4)} + 2J(k - \pi/2)\right]^{2} + \delta^{2}}},\tag{4.97a}$$

$$b_{1,k}^{(4)} = \frac{\epsilon_{+,1,k}^{(4)} + 2J(k - \pi/2)}{\sqrt{\left[\epsilon_{+,1,k}^{(4)} + 2J(k - \pi/2)\right]^{2} + \delta^{2}}},\tag{4.97b}$$

for the continuous one. Here, the post-quench energy bands are

$$\epsilon_{\pm,1,k}^{(3)} = \pm\sqrt{\delta^{2} + 4J^{2}\cos^{2}(k)},\tag{4.98a}$$

$$\epsilon_{\pm,1,k}^{(4)} = \pm\sqrt{\delta^{2} + 4J^{2}(k - \pi/2)^{2}}.\tag{4.98b}$$

Using Eqs. (4.24), (4.23), and (4.92), one finds that the steady state staggered magnetization after the quench evaluates to

$$M_{\delta}^{\text{ss},(i)} = \frac{2}{\pi}\left(\int_{\pi/2}^{\pi} - \int_{0}^{\pi/2}\right)dk\, a_{1,k}^{(i)}b_{1,k}^{(i)}\left[\left(a_{1,k}^{(i)}\right)^{2} - \left(b_{1,k}^{(i)}\right)^{2}\right].\tag{4.99}$$

For the lattice model, using Eq. (4.96), we obtain

$$M_{\delta}^{\text{ss},(3)} = -\frac{2\delta}{\pi\sqrt{\delta^{2} + 4J^{2}}}\text{arctanh}\left(\frac{2J}{\sqrt{\delta^{2} + 4J^{2}}}\right),\tag{4.100}$$
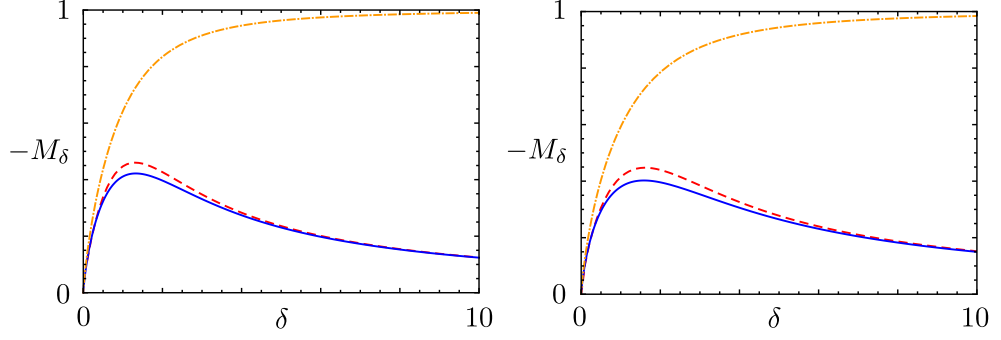
Figure 4.12: Panel (a): steady state staggered magnetization $M_\delta^{\text{ss},(3)}$ (blue, solid), equilibrium staggered magnetization $M_\delta^{\text{eq},(3)}$ (orange, dash-dotted) and effective temperature staggered magnetization $M_\delta^{\text{eff},(3)}$ (red, dashed) as a function of δ for the lattice SP system. Panel (b): same as in Panel (a) but for the continuum SP system. In both Panels we set $J = 1$.

which is shown in Fig. 4.12(a). On the other hand, from Eq. (4.97), one gets for the low-energy continuous model

$$M_\delta^{\text{ss},(4)} = -\frac{\delta}{2\pi J} \ln\left[1 + \left(\frac{\pi J}{\delta}\right)^2\right],$$ (4.101)

displayed in Fig. 4.12(b). Similarly to what we have seen in Sec. 4.3 for the SOC system, also in this model the behavior of the staggered magnetization after a sudden quench, $M_\delta^{\text{ss},(i)}$, strongly differs from the equilibrium one, shown in Fig. 4.12 by dash-dotted orange lines. Indeed, when the system is in the ground state of the post-quench Hamiltonian, the staggered magnetization is obtained from Eq. (4.29) and evaluates to

$$M_\delta^{\text{eq},(i)} = \frac{2}{\pi}\int_0^\pi dk\, a_{1,k}^{(i)} b_{1,k}^{(i)}.$$ (4.102)

In particular, for the lattice model we obtain from Eq. (4.96)

$$M_\delta^{\text{eq},(3)} = -\frac{4KJ^2}{\pi}\left[\frac{1}{\delta^2} - \frac{\delta}{\sqrt{\delta^2 + 4J^2}}\left(\frac{1}{4J^2 + \delta^2}\right)\right],$$ (4.103)

with $K(z)$ the complete elliptic integral of the first kind [142], while for the continuum one we get

$$M_\delta^{\text{eq},(4)} = \frac{\delta}{\pi J}\text{arctanh}\left(\frac{\pi J}{\sqrt{\delta^2 + \pi^2 J^2}}\right).$$ (4.104)

As expected, the staggered magnetization increases monotonically with the strength of the external field up to the saturation value, $\lim_{\delta\to\infty} M_\delta^{\text{eq},(i)} = 1$.

Finally, in Fig. 4.12, we also compare the GGE staggered magnetization, $M_\delta^{\text{ss},(i)}$, with the one obtained with the effective temperature ensemble approach described in Sec. 4.2, $M_\delta^{\text{eff},(i)}$ [see in particular Eq. (4.26)]. In this

case, since the spectrum of the system becomes fully gapped when the staggered potential is turned on, particle number conservation is automatically ensured and the chemical potential $\mu(\delta)$ can be set to zero. In contrast with the previous Section, where we saw that the effective temperature fails to reproduce the behavior of $M_\delta^{\text{ss},(i)}$, in the SP model the agreement between the quenched and the effective thermal magnetization is rather good. This is due to the fact that the fermionic chain of Eq. (4.95) is a very simple model and the quench of the staggered potential has effects similar to an effective heating. Nevertheless, as we will see in the following Section, the transient of the staggered magnetization is again controlled by the very same KG physics we found for the SOC model. Moreover, when the quench of interparticle interactions is considered, the effective temperature picture breaks down while the competition between propagation and freezing regimes of the LC still holds (see Sec. 4.5).

4.4.2 Klein–Gordon physics for the staggered potential model

As anticipated above, we now focus on the dynamics of the continuum SP model towards the GGE state and, in particular, on the time behavior of the one-body correlation function

$$\mathcal{G}^{(4)}(x,t) = \langle \Phi_0^{(4)} | \hat{\Psi}^{(4)\dagger}(x,t) \hat{\sigma}^x \hat{\Psi}^{(4)}(0,t) | \Phi_0^{(4)} \rangle \,, \tag{4.105}$$

with the average evaluated on the pre-quench equilibrium ground state $|\Phi_0^{(4)}\rangle$. Note that $\lim_{x\to 0} \mathcal{G}^{(4)}(x,t) = M^{(4)}(t)$, i.e. for $x = 0$ the correlation function $\mathcal{G}^{(4)}(x,t)$ coincides with the time-dependent staggered magnetization of the system. Here, $\hat{\Psi}^{(4)}(x,t) = \sum_k \hat{\Psi}_k^{(4)}(t) e^{ikx}/\sqrt{L}$ is the space-resolved Fermi spinor, whose time evolution in the Heisenberg picture can be obtained from Eq. (4.20),

$$\hat{\Psi}_k^{(4)}(t) = \hat{U}_{1,k}^{(4)\dagger} \text{diag}\{e^{-i\epsilon_{+,1,k}^{(4)}t}, e^{-i\epsilon_{-,1,k}^{(4)}t}\} \hat{U}_{1,k}^{(4)} \hat{U}_{0,k}^{(4)\dagger} \hat{\Phi}_{0,k}^{(4)}(0), \tag{4.106}$$

with the coefficients of the matrices $\hat{U}_{0,k}^{(4)}$ and $\hat{U}_{1,k}^{(4)}$ given in Eqs. (4.92) and (4.97), respectively.

In principle, the KG equation satisfied by the correlation function $\mathcal{G}^{(4)}(x,t)$ can be obtained following the same steps of the SOC model case, i.e. starting from the equation of motion of the fermionic field $\hat{\Psi}_k(t)$. However, in order to show an alternative and quicker method to obtain it, we derive the equation governing the dynamics of $\mathcal{G}^{(4)}(x,t)$ by a direct calculation. We begin by explicitly evaluating $\mathcal{G}^{(4)}(x,t) = \langle \hat{\Psi}^{(4)\dagger}(x,t) \hat{\sigma}^x \hat{\Psi}^{(4)}(0,t) \rangle$, which can be rewritten as

$$\mathcal{G}^{(4)}(x,t) = \frac{1}{L} \sum_k e^{-ikx} \langle \hat{d}_{b,k}^{(4)\dagger}(t) \hat{d}_{a,k}^{(4)}(t) + \text{H.c.} \rangle_0, \tag{4.107}$$

where the average is evaluated on the ground state of the pre-quench Hamiltonian $\hat{\mathcal{H}}_k^{(4)}$, defined in Eq. (4.16). Using Eqs. (4.92), (4.97) and (4.106), we obtain

$$\langle \hat{d}_{b,k}^{(4)\dagger}(t)\hat{d}_{a,k}^{(4)}(t)\rangle_0 = \frac{1}{8}\langle d_{v,1,k}^{(4)\dagger}d_{v,1,k}^{(4)}\rangle_0\Big[-4\beta_k \mathrm{Im}\{\beta_k\} - ie^{-2it\epsilon_{+,1,k}^{(4)}}\left(1 + \beta_k^2\right)$$
$$- ie^{-2it\epsilon_{-,1,k}^{(4)}}\beta_k^2\left(1 + \beta_k^{*2}\right)\Big], \qquad (4.108)$$

where $\beta_k = \sqrt{2}b_{1,k}^{(4)}$. Substituting in Eq. (4.107) and performing the thermodynamic limit, one has

$$\mathcal{G}^{(4)}(x,t) = -\frac{1}{\pi}\int_0^\pi e^{-ikx}\frac{Jk\delta}{J^2k^2 + \delta^2}\left[1 - \cos\left(2t\epsilon_{+,1,k}^{(4)}\right)\right]dk. \qquad (4.109)$$

Finally, after evaluating the second-order time and space derivatives of $\mathcal{G}^{(4)}(x,t)$,

$$\partial_t^2\mathcal{G}^{(4)}(x,t) = -\frac{4}{\pi}\int_0^\pi e^{-ikx}Jk\delta\cos\left(2t\epsilon_{+,1,k}^{(4)}\right)dk, \qquad (4.110a)$$

$$\partial_x^2\mathcal{G}^{(4)}(x,t) = \frac{1}{\pi}\int_0^\pi e^{-ikx}\frac{Jk^3\delta}{J^2k^2 + \delta^2}\left[1 - \cos\left(2t\epsilon_{+,1,k}^{(4)}\right)\right]dk, \qquad (4.110b)$$

and performing some algebraic manipulations, one can directly verify that the following KG equation is satisfied

$$\left(\partial_x^2 - \frac{1}{4u_4^2}\partial_t^2\right)\mathcal{G}^{(4)}(x,t) = \lambda_4^2\mathcal{G}^{(4)}(x,t) + \lambda_4\phi_4(x), \qquad (4.111)$$

where $u_4 = 2J$, $\lambda_4 = \delta/J$, and the source term $\phi_4(x)$ is

$$\phi_4(x) = 2\frac{\cos(\pi x) + \pi x\sin(\pi x) - 1}{\pi x^2} = i\partial_x\langle\hat{\Psi}^{(4)\dagger}(x,0)\hat{\sigma}^y\hat{\Psi}^{(4)}(0,0)\rangle_0. \quad (4.112)$$

Equation (4.111) is formally identical to Eq. (4.57) and, therefore, the same KG physics discussed in Sec. (4.3.1) also occurs after a quench of the SP in a fermionic chain. Thus, the non-monotonic behavior of the staggered magnetization shown in Fig. (4.12) is due to the competition between two different regimes of the LC generated in $\mathcal{G}^{(4)}(x,t)$ at the instant of the quench, as clearly emerges in Fig. 4.13. For small quenches it freely propagates through the system, carrying the information of the quench and resulting in a finite value of the staggered magnetization $M_\delta^{\mathrm{ss},(4)}$ in the long-time limit. On the other hand, for large quenches the response dynamics of $\mathcal{G}^{(4)}(x,t)$ is governed by damped oscillations, leading to a (partial) restoration of the initial value of staggered magnetization.

4.5 INTERACTION QUENCH IN THE FERMIONIC CHAIN

So far we have only considered non-interacting systems. In this Section we will show that the competition between propagation and freezing regimes
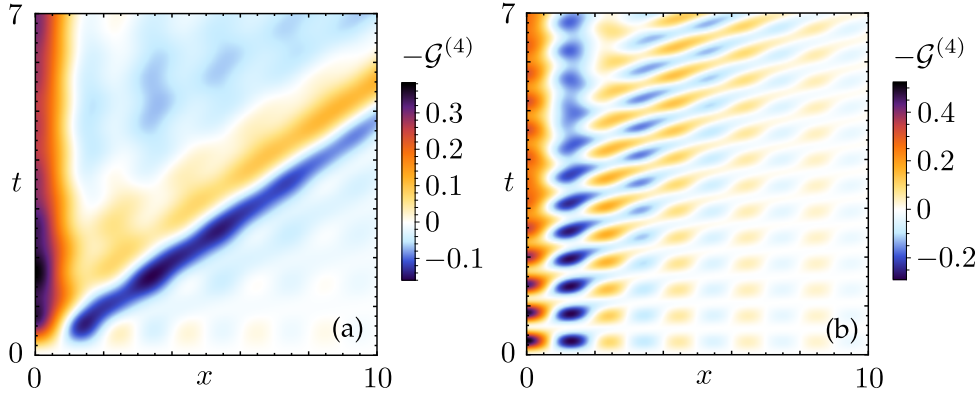
Figure 4.13: Panel (a): Density plot of $-\mathcal{G}^{(4)}(x,t)$ as a function of x and t for $\delta = 0.5$ and $J = 1$; Panel (b): same as in Panel (a) but for $\delta = 5$ and $J = 1$.

of the LC is more generic and applies also to interacting models, even in the absence of integrability[2]. In particular, we turn our attention to the fermionic chain described by the real-space Hamiltonian of Eq. (4.88) where, instead of the SP of the previous Section, the gap-opening mechanism is represented by the turning on at $t = 0$ of nearest-neighbor interactions, with strength $\mathcal{U}(t) = \mathcal{U}\theta(t)$, and/or of next-to-nearest neighbor interactions, with strength $\mathcal{V}(t) = \mathcal{V}\theta(t)$. The real-space time-dependent Hamiltonian is thus

$$\hat{H}^{(i)}(t) = -J\sum_{k}\left[\left(\hat{c}_j^{(i)\dagger}\hat{c}_{j+1}^{(i)} + \text{H.c.}\right) + \mathcal{U}(t)\hat{n}_j^{(i)}\hat{n}_{j+1}^{(i)} + \mathcal{V}(t)\hat{n}_j^{(i)}\hat{n}_{j+2}^{(i)}\right], \quad (4.113)$$

with $\hat{n}_j^{(i)} = \hat{c}_j^{(i)\dagger}\hat{c}_j^{(i)}$ the occupation number operator of the $j-$th site. For $\mathcal{V} = 0$ the post-quench system can be mapped onto the XXZ Heisenberg spin chain which is Bethe-Ansatz solvable (i.e. it is integrable) [61, 263] while for $\mathcal{V} \neq 0$ no solution via the Bethe-Ansatz is known (and is believed to be nonexistent, i.e. the model is non-integrable). Moreover, in the equilibrium regime at $\mathcal{V} = 0$, it is known that for $\mathcal{U}/J < 2$ the system is gapless while for $\mathcal{U}/J > 2$ a gap opens [61]. Note that the gap-opening mechanism considered here is profoundly different from the ones discussed in previous Sections. Indeed, the gap has now a many-body origin and the interacting Hamiltonian cannot be diagonalized analytically. To study the response of the system to the quench of the inter-particle interaction we thus resort to numerical means, employing the density matrix renormalization group (DMRG) technique which, in the limit of an infinite lattice $N \to \infty$ can be conveniently formulated using the language of matrix product states [264–267]. Note that, within the latter method, we have access to finite times only (as the results are obtained by explicit forward time evolution). To push the simulations to larger time scales we employ the ideas developed in Ref. [264]. Of course (like in any finite time simulation) we cannot exclude that the results obtained are not truly steady and that, on some very large time-scale, another

2 The results reported in this Section are the outcome of a collaboration with D. M. Kennes (Columbia University, New York, USA). They have been obtained by means of numerical simulations performed with computing resources granted by RWTH Aachen University, Germany.
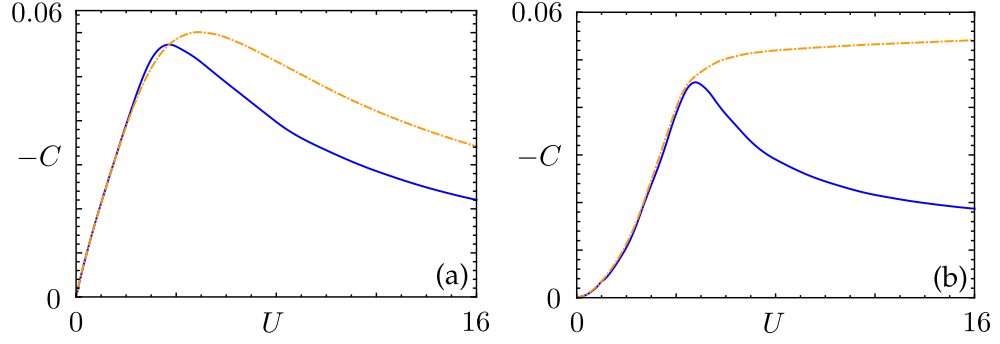
Figure 4.14: Panel (a): steady state magnetization $C_{\mathcal{U}}^{\text{ss}}$ (blue, solid) and effective temperature magnetization $C_{\mathcal{U}}^{\text{eff}}$ (orange, dash-dotted) as a function of U for the interaction-quenched fermionic chain in the presence of nearest-neighbor interaction only. Panel (b): same as in Panel (a) but also in the presence of the quench of next-to-nearest neighbor interactions $\mathcal{V} = \mathcal{U}$. In both Panels we set $J = 1$.

relaxation mechanism sets in. However, we can access time scales on which typical observables appear approximately relaxed on the scale of their respective plots. We might thus only have access to the prethermal state of the system, stipulating that on inaccessible time scales a second regime shows up, which changes the steady state value. Either way the results reported here are then (at least) valid on an extensively long time scale, which would be relevant to experiments.

Since the model is invariant under rotations in the spinor space, the "magnetization" we investigated in previous Sections is no more a good quantity for characterizing the behavior of the system after the quench. We thus analyze the long-time (stationary) limit, $C_{\mathcal{U}}^{\text{ss}} = \lim_{t\to\infty} C(t)$, of the following observable

$$C(t) = \langle (\hat{n}_0^{(3)}(t) - 1/2)(\hat{n}_1^{(3)}(t) - 1/2) \rangle_0 - \langle (\hat{n}_0^{(3)}(0) - 1/2)(\hat{n}_1^{(3)}(0) - 1/2) \rangle_0, \tag{4.114}$$

where $\hat{n}_i^{(3)}(t)$ is the time-resolved occupation number of the $i-$th site and encodes the information about correlations between nearest-neighbor sites. Thus, it well characterizes the response of the system to the interaction quench. Here, $\langle \cdot \rangle_0$ represents the average with respect to the pre-quench ground state, $|\Phi_0^{(3)}\rangle$. Results are shown in Fig. 4.14(a) for the integrable case $\mathcal{V} = 0$. As can be seen (solid line), $C_{\mathcal{U}}^{\text{ss}}$ follows the same qualitative behavior of the magnetization in the reported non-interacting models (see Figs. 4.8 and 4.12), rising for small quenches up to a maximum value. As the gap size increases over the crossover point, $C_{\mathcal{U}}^{\text{ss}}$ begins to decrease and tends (not shown) to the pre-quench value for very large $\mathcal{U}$. As we did in previous Sections, we compare our results to the ones obtained within an effective temperature picture (orange, dash-dotted lines in Fig. 4.14), $C_{\mathcal{U}}^{\text{eff}}$. Although in the integrable case shown in Panel (a) the latter still exhibits a non-monotonic behavior, it fails quite badly to reproduce the actual values of $C_{\mathcal{U}}^{\text{ss}}$.
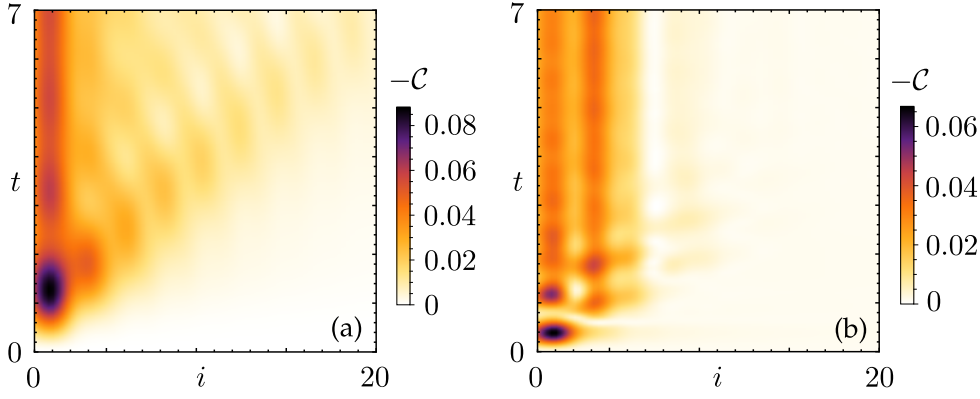
Figure 4.15: Panel (a): Density plot of $-\mathcal{C}(i,t)$ as a function of i and t for $\mathcal{U} = 2$, $\mathcal{V} = 0$ and $J = 1$; Panel (b) same as in Panel (a) but for $\mathcal{U} = 16$, $\mathcal{V} = 0$ and $J = 1$.

The quench of interactions, mixing states in k space, allows to rule out alternative explanations of the non-monotonous behavior of the analyzed quantities, such as a simple dephasing of collections of two-level systems. Even when integrability is lost, as is the case of Fig. 4.14(b) where a quench with $\mathcal{V} = \mathcal{U}$ is shown with a solid line, the qualitative picture remains the same, at least on the accessible time scales. Here, the failure of the description in terms of an effective temperature is particularly evident (see the orange, dash-dotted line), since the latter does not even capture the non-monotonous character of $C_{\mathcal{U}}^{ss}$.

Again, the explanation of the peculiar non-monotonic behavior of $C_{\mathcal{U}}^{ss}$, which characterizes the response of the system to a quench of the inter-particle interaction, can be found by inspecting the transient dynamics of its associated correlation function,

$$\mathcal{C}(i,t) = \langle (\hat{n}_0^{(3)}(t) - 1/2)(\hat{n}_i^{(3)}(t) - 1/2) \rangle_0 - \langle (\hat{n}_0^{(3)}(0) - 1/2)(\hat{n}_i^{(3)}(0) - 1/2) \rangle_0.$$
$$(4.115)$$

Indeed, also in this case a competition between a propagation and a freezing regime for the LC occurs, as clearly emerges from Fig. 4.15. For small quenches with $\mathcal{U}/J \leq 2$ one can observe the propagation of a wavefront carrying the information of the quench throughout the system [Panel (a)]. On the other hand, large quenches with $\mathcal{U}/J > 2$ display a sharp freezing of the LC together with a damped oscillatory behavior due the opening of the gap [Panel (b)]. Thus, the freezing of the LC – and the associated non-monotonic behavior in observables charactering the response of the system to the an external perturbation – is a generic feature of systems subject to quenches opening large gaps in the spectrum, whose appearance seems not essentially related to the particular quench mechanism considered.

4.6 CONCLUSIONS

In conclusion, in this Chapter we have studied the response of two paradigmatic 1D non-interacting models, namely a SOC system and a chain of spinless fermions, to the quench of an external gap-opening mechanism. We inspected observables, that we called magnetizations, which directly characterize the reaction of the system to the latter. In the asymptotic steady state, they show a peculiar non-monotonic behavior as a function of the strength of external field which is a direct consequence of the dynamics of the systems during the transient regime. Indeed, the time evolution of the correlation functions associated with the observables we considered is governed by an inhomogeneous Klein-Gordon equation. Here,a competition between a mass and a source terms occurs and results in two very different dynamical regimes. For small quenches, the information of the quench can freely propagate through the system with a typical LC behavior and leads to a finite magnetization. On the contrary, for large quenches the dynamics of correlation functions features weakly damped oscillations, the LC freezes and the magnetization remains close to its initial pre-quench value. Furthermore, we showed that the very same behavior occurs also when more complicated gap-opening quenches are considered, such as non-sudden protocols in the SOC model or inter-particle interaction quenches in the fermionic chain. The non-monotonic response also persists even when integrability is broken or systems with higher dimensionality are considered.

In all these cases, the non-monotonic behavior of magnetization is the hallmark of the freezing of the LC conveying the information of the quench through the system. This freezing results in a state described by a GGE which differs from effective thermal states, in some cases even dramatically, thus providing an experimentally accessible way to test the GGE physics.

As a limit for the universality of the physics described in this Chapter, it is worth to point out that we do not expect to observe these effects when the gap is opened by merging of crossings, as relevant, for example, for Weyl semimetals [268], or for the models discussed in Refs. [269, 270]. On the other hand, a static fermion-fermion interaction, which could be taken into account, for instance, by means of bosonization [61–63] or DMRG [265, 267], is expected to renormalize the gap opened by the quench to larger values [225, 226]. So, in this case, we argue the described phenomenon to persist with a shifted and renormalized maximum [61].

CONCLUSIONS

The main focus of this Thesis has been the study of one-dimensional (1D) integrable quantum systems out-of-equilibrium. In particular, we investigated the dynamics following a so called quantum quench, consisting in a change in time of one of the system parameters [32, 33]. The general framework of this protocol, which represents a quite natural way to drive a system far from equilibrium and can also be easily implemented in cold atomic gases [34–36, 39, 40, 44, 46], has been described in details in Chap. 1. Here, we briefly summarized the main issues about the equilibration problem in closed quantum systems [16, 18, 45]. We then concentrated on integrable ones which, as their classical counterparts, exhibit peculiar properties due the presence of an extensive set of conserved quantities constraining their dynamics. To take into account this fact, we introduced the Generalized Gibbs Ensemble (GGE), which locally describes the steady state approached by an integrable model after being pushed away from equilibrium [47, 53, 54]. Finally, we have shown that the post-quench relaxation process is conveyed by a typical light cone (LC) spreading of correlation.

In Chap. 2 we investigated how the peculiar properties of the post-quench dynamics of integrable quantum systems, described in Chap. 1, affect spectral and transport properties of Luttinger liquids (LLs), which are briefly introduced at the beginning of the Chapter. Here, we showed that, thanks to the bosonization technique, the low-energy physics of a 1D interacting quantum system can be described in terms of bosonic excitation [61–63]. After a quench of the inter-particle interaction, finite cross-correlations among these bosonic degrees of freedom arise and decay in time with a power law $\propto t^{-2}$. This universal behavior is directly transferred both to spectral properties, where it competes with other typical LL-like power laws, and to transport ones, where it emerges as the dominant contribution to the long-time dynamics. To investigate the latter quantities, we considered a setup in which the system, immediately after the quench, is tunnel-coupled to an external minimally-invasive probe and we focused on charge and energy current. Both these quantities share the same universal power law $\propto t^{-2}$, signaling that it represents an intrinsic property of the relaxation dynamics of LLs. Finally, we inspected how the fractionalization phenomena occurring after the tunneling [123], which is a hallmark of 1D interacting quantum systems, are modified far from equilibrium. We showed that, while the charge fractionalization is unaffected by the quench and depends only on the final Hamiltonian, the behavior of the energy partitioning is a powerful tool to reveal the universal power-law decay.

In Chap. 3 we investigated out-of-equilibrium effects in a finite system. In particular, we studied the dynamics of the particle density in a LL with open boundary conditions (OBC) [187] after an interaction quench with fi-

nite duration. Here, we demonstrated that both the turning on and the turning off of the quench protocol results in the emergence of a pair of counter-propagating LC perturbations in the density, which travel ballistically through the system with the velocity of bosonic excitations that instantaneously diagonalize the system Hamiltonian. These LC perturbations interfere destructively and, thus, the post-quench dynamics is thus strongly affected by their relative position inside the system. In particular, we investigated the deviation of the real-time particle density from the one predicted be the GGE picture, obtaining that it vanishes as the quench duration is increased. However, the behavior is non-monotonic: Indeed, for quench durations such that the two LC perturbations perfectly overlap, a local minimum in the distance from the GGE result occurs, while a local maximum emerges when they are maximally distant from each other.

Finally, in Chap. 4 we studied quench mechanisms which open a gap in the single-particle spectrum of two paradigmatic free fermionic systems. In particular, we considered the quench of a magnetic field in a spin-orbit coupled (SOC) model and the quench of a staggered potential in a chain of spinless fermions. We then characterized the response of both systems by studying the (staggered) magnetization as a function of the strength of the quenched parameter. Here, we observed a peculiar non-monotonic behavior: For small quenches the (staggered) magnetization grows, then it reaches a maximum, and then it starts to decrease for stronger quenches. This phenomenon can not be explained in terms of an effective heating induced by the quench but has its roots in the out-of-equilibrium dynamics of the system. Indeed, we examined in details the time evolution of the correlation functions associated with the (staggered) magnetizations. While for small quenches we found that information spreads through the system with a typical LC behavior, in the opposite case of strong quenches we observed an effective freezing of the LC wavefront. As a consequence the magnetization stays close to its initial value, thus explaining the non-monotonic behavior. In order to study the generality of the phenomenon, we also investigated a more complex gap opening mechanism in the spinless fermionic chain, namely the quench of nearest and, possibly, next-to-nearest neighbor interparticle interactions. In this case we found a very similar non-monotonic behavior in the nearest-neighbor correlation function, which again arises as a consequence of the freezing of the LC propagation in its generalized correlation function.

A | QUANTUM RECURRENCE THEOREM

In this Appendix we discuss the quantum version of the well-know Poincaré recurrence theorem of Classical Mechanics [79, 271]. The latter can be summarized by saying that

every configuration X of a Hamiltonian system enclosed in a finite volume will be repeated with an arbitrary high degree of fidelity after a sufficiently long but finite interval of time.

In 1956 Bocchieri and Loinger demonstrated that a similar theorem holds also for quantum systems with a discrete energy spectrum [78]. In particular,

if we consider a quantum system with discrete energy eigenvalues E_n and denote with $|\psi(t_0)\rangle$ its state in the Schrödinger picture at time t_0, there exists a least one time $\bar{t}$ such that

$$\||\psi(\bar{t})\rangle - |\psi(t_0)\rangle\| < \varepsilon, \tag{A.1}$$

with $\varepsilon > 0$ an arbitrarily small number.

In order to prove this theorem, we start from the general solution of the time-dependent Schrödinger equation, $i\partial_t|\psi(t)\rangle = \hat{H}|\psi(t)\rangle$, which can be written as

$$|\psi(t)\rangle = \sum_{n=0}^{\infty} r_n e^{i\phi_n - iE_n T}|n\rangle, \tag{A.2}$$

with $\hat{H}|n\rangle = E_n|n\rangle$ and r_n positive real numbers such that $\sum_{n=0}^{\infty} r_n^2 = 1$. Using the above equation we get

$$\||\psi(t)\rangle - |\psi(t_0)\rangle\| = 2\sum_{n=0}^{\infty} r_n^2[1 - \cos(E_n\tau)], \tag{A.3}$$

with $\tau = t - t_0$. For a given $\varepsilon > 0$, it is possible to choose a positive integer N such that

$$\sum_{n=N}^{\infty} r_n^2[1 - \cos(E_n\tau)] < \frac{\varepsilon}{2}. \tag{A.4}$$

To complete the proof, it thus sufficient to demonstrate that

$$\sum_{n=0}^{N-1} r_n^2[1 - \cos(E_n\tau)] < \frac{\varepsilon}{2}, \tag{A.5}$$

which can be done in accordance with the theory of almost-periodic functions [78] or by using the classical Poincaré recurrence theorem [80].

B | INTERACTION PICTURE

In this Appendix we briefly review the interaction picture [73, 76]. Let us consider the Hamiltonian

$$\hat{H}(t) = \hat{H}_0(t) + \hat{V}(t), \tag{B.1}$$

with t denoting a possible parametric time dependence, and assume we know all eigenstates and eigenvalues of $\hat{H}_0(t)$, namely $\hat{H}_0(t)|n(t)\rangle = E_n(t)|n(t)\rangle$. The time-evolution operator from t_0 to t associated with $\hat{H}_0(t)$, $\hat{U}_0(t,t_0)$, satisfies the following equation

$$i\frac{d}{dt}\hat{U}_0(t,t_0) = \hat{H}_0(t)\hat{U}_0(t,t_0), \tag{B.2}$$

with initial condition $\hat{U}_0(t_0,t_0) = \hat{I}$ and $\hat{I}$ the identity operator. We can now write the time-evolution operator associated with the total Hamiltonian $\hat{H}(t)$ as

$$\hat{U}(t,t_0) = \hat{U}_0(t,t_0)\hat{U}_I(t,t_0). \tag{B.3}$$

Here, $\hat{U}_I(t,t_0)$ satisfies the differential equation

$$i\frac{d}{dt}\hat{U}_I(t,t_0) = \hat{V}_I(t)\hat{U}_I(t,t_0), \tag{B.4}$$

with initial condition $\hat{U}_I(t_0,t_0) = \hat{I}$ and

$$\hat{V}_I(t) = \hat{U}_0^\dagger(t,t_0)\hat{V}(t)\hat{U}_0(t,t_0) \tag{B.5}$$

the *interaction picture* representation of the operator $\hat{V}(t)$. This equation admits a formal solution of the form

$$\hat{U}_I(t,t_0) = \hat{\mathcal{T}}\left[e^{-i\int_{t_0}^t \hat{V}_I(t')\,dt'}\right], \tag{B.6}$$

with $\hat{\mathcal{T}}$ the time ordering operator. Analogously, we can introduce the interaction picture representation of the state $|\psi(t)\rangle$, which is defined as

$$|\psi_I(t)\rangle = \hat{U}_0^\dagger(t,t_0)|\psi(t)\rangle \tag{B.7}$$

and whose time evolution is entirely governed by the operator $\hat{U}_I(t,t_0)$, i.e.

$$|\psi_I(t)\rangle = \hat{U}_I(t,t_0)|\psi(t_0)\rangle. \tag{B.8}$$

From Eq. (B.8) it follows that, in the interaction picture, the density matrix of the system, $\hat{\rho}(t)$, evolves as

$$\hat{\rho}_I(t) = \hat{U}_I(t,t_0)\hat{\rho}(t_0)\hat{U}_I^\dagger(t,t_0), \tag{B.9}$$

i.e. it only depends on $\hat{V}_I(t)$.

The quantum average over the state described by $\hat{\rho}(t)$ of an generic operator $\hat{O}$ can be evaluated as

$$\langle \hat{O}(t) \rangle = \text{Tr} \left[\hat{\rho}(t) \hat{O} \right] = \text{Tr} \left[\hat{\rho}_I(t) \hat{O}_I(t) \right], \tag{B.10}$$

with

$$\hat{O}_I(t) = \hat{U}_0^\dagger(t, t_0) \hat{O} \hat{U}_0(t, t_0) \tag{B.11}$$

the interaction picture representation of the operator $\hat{O}$. The usefulness of the interaction picture lies in the fact that $\hat{V}(t)$ only affects the time-evolution of $\hat{\rho}_I(t)$, while the dynamics of $\hat{O}_I(t)$ is entirely due to $\hat{H}_0(t)$. Thanks to this property, if $\hat{V}(t)$ represents a small perturbation with respect to $\hat{H}_0(t)$, Eq. (B.6) can be expanded as a Dyson series,

$$\hat{U}_I(t, t_0) = \hat{I} - i \int_{t_0}^t \hat{V}_I(\tau) d\tau - \int_{t_0}^t d\tau \int_{t_0}^\tau d\tau' \hat{V}_I(\tau) \hat{V}_I(\tau') d\tau + \dots \tag{B.12}$$

By recalling Eq. (B.9) and plugging the above expansion in Eq. (B.10), one readily obtains the time-dependent average of $\hat{O}$, for example, to the second-order in the perturbation strength,

$$\langle \hat{O}(t) \rangle = \text{Tr} \left[\hat{\rho}(t_0) \hat{O}_I(t) \right] + i \int_{t_0}^t d\tau \, \text{Tr} \left\{ \left[\hat{\rho}(t_0), \hat{V}_I(\tau) \right] \hat{O}_I(t) \right\}$$

$$- 2\text{Re} \int_{t_0}^t d\tau \int_{t_0}^\tau d\tau' \, \text{Tr} \left\{ \hat{\rho}(t_0) \hat{V}_I(\tau') \left[\hat{V}_I(\tau), \hat{O}(t) \right] \right\}. \tag{B.13}$$

Note that, if $\hat{O}$ is an operator which preserves the particle number, the term linear in $\hat{V}_I$ vanishes.

C | DIAGONALIZATION OF A GENERIC 2 × 2 HERMITIAN MATRIX

In this Appendix we briefly summarize the diagonalization procedure for a generic 2×2 Hermitian matrix,

$$\mathcal{H} = \begin{bmatrix} h_{11} & h_{12} \\ h_{12}^* & h_{22} \end{bmatrix}, \tag{C.1}$$

with $h_{11}, h_{12} \in \mathbb{R}$ and $h_{12} \in \mathbb{C}$. We first focus on the case $h_{12} \neq 0$. Then, the eigenvalues of $\mathcal{H}$ are

$$\epsilon_\pm = \frac{1}{2}(h_{11} + h_{22}) \pm D, \tag{C.2}$$

where

$$D = \sqrt{(h_{11} - h_{22})^2 + 4|h_{12}|^2}/2. \tag{C.3}$$

The Hamiltonian of Eq. (C.1) can be diagonalized by means of the unitary matrix U,

$$U\mathcal{H}U^\dagger = \begin{bmatrix} \epsilon_+ & 0 \\ 0 & \epsilon_- \end{bmatrix}, \tag{C.4}$$

with

$$U = \begin{bmatrix} A_- & -A_- \frac{\epsilon_- - h_{22}}{h_{12}^*} \\ -A_+ \frac{\epsilon_+ - h_{11}}{h_{12}} & A_+ \end{bmatrix} \tag{C.5}$$

and $\varepsilon_+ > \varepsilon_-$. Here, we have introduced the coefficients

$$A_+ = \frac{|h_{12}|}{\sqrt{(\epsilon_+ - h_{11})^2 + |h_{12}|^2}}, \tag{C.6a}$$

$$A_- = \frac{|h_{12}|}{\sqrt{(\epsilon_- - h_{22})^2 + |h_{12}|^2}}. \tag{C.6b}$$

On the other hand, in the case $h_{12} = 0$, the unitary matrix U that transforms $\mathcal{H}$ in the diagonal form of Eq. (C.4), i.e. with $\epsilon_+ > \epsilon_-$, is

$$U = \begin{cases} I_{2\times2}\theta(h_{11} - h_{22}) + i\sigma^y\theta(h_{22} - h_{11}), & \text{if } h_{11} \neq h_{22}, \\ \frac{1}{\sqrt{2}}(I + i\sigma^y), & \text{if } h_{11} = h_{22}, \end{cases} \tag{C.7}$$

with $I_{2\times2}$ the 2×2 identity matrix and σ^y the y Pauli matrix in the usual representation.

BIBLIOGRAPHY

[1] A. Altland and B. D. Simons, *Condensed matter field theory* (Cambridge University Press, 2010).

[2] R. Balescu, *Equilibrium and non-equilibrium statistical mechanics* (Wiley, 1975).

[3] E. Fermi, *Thermodynamics* (Dover Publications, 1956).

[4] W. Ebeling and I. M. Sokolov, *Statistical thermodynamics and stochastic theory of nonlinear systems far from equilibrium* (World Scientific Publishing Company, 2005).

[5] K. Huang, *Statistical mechanics* (John Wiley & Sons, 1987).

[6] L. E. Reichl, *A modern course in statistical physics* (Wiley-VCH, 2016).

[7] A. Arrizabalaga, J. Smit, and A. Tranberg, "Equilibration in φ^4 theory in $3 + 1$ dimensions", Phys. Rev. D **72**, 025014 (2005).

[8] J. Berges, S. Borsányi, and C. Wetterich, "Prethermalization", Phys. Rev. Lett. **93**, 142002 (2004).

[9] L. Kofman, A. Linde, and A. A. Starobinsky, "Reheating after Inflation", Phys. Rev. Lett. **73**, 3195–3198 (1994).

[10] D. Podolsky, G. N. Felder, L. Kofman, and M. Peloso, "Equation of state and beginning of thermalization after preheating", Phys. Rev. D **73**, 023501 (2006).

[11] G. S. Engel, T. R. Calhoun, E. L. Read, T.-K. Ahn, T. Mančal, Y.-C. Cheng, R. E. Blankenship, and G. R. Fleming, "Evidence for wave-like energy transfer through quantum coherence in photosynthetic systems", Nature **446**, 782 EP - (2007).

[12] A. Imamoglu and K. B. Whaley, "Photoactivated biological processes as quantum measurements", Phys. Rev. E **91**, 022714 (2015).

[13] D. N. Basov, R. D. Averitt, D. van der Marel, M. Dressel, and K. Haule, "Electrodynamics of correlated electron materials", Rev. Mod. Phys. **83**, 471–541 (2011).

[14] P. Braun-Munzinger, D. Magestro, K. Redlich, and J. Stachel, "Hadron production in Au–Au collisions at RHIC", Physics Letters B **518**, 41–46 (2001).

[15] M. A. Cazalilla and M.-C. Chung, "Quantum quenches in the luttinger model and its close relatives", Journal of Statistical Mechanics: Theory and Experiment **2016**, 064004 (2016).

[16] L. D'Alessio, Y. Kafri, A. Polkovnikov, and M. Rigol, "From quantum chaos and eigenstate thermalization to statistical mechanics and thermodynamics", Advances in Physics **65**, 239–362 (2016).

[17] J. Eisert, M. Friesdorf, and C. Gogolin, "Quantum many-body systems out of equilibrium", Nat. Phys. **11**, 124–130 (2015).

[18] F. H. L. Essler and M. Fagotti, "Quench dynamics and relaxation in isolated integrable quantum spin chains", Journal of Statistical Mechanics: Theory and Experiment **2016**, 064002 (2016).

[19] G. Giuliani and G. Vignale, *Quantum theory of the electron liquid* (Cambridge University Press, 2008).

[20] G. Grosso and G. Pastori Parravici, *Solid state physics* (Academic Press, 2014).

[21] H. Haug and A.-P. Jauho, *Quantum kinetics in transport and optics of semiconductor* (Springer, 2008).

[22] M. A. Nielsen and I. L. Chuang, *Quantum information and quantum information* (Cambridge University Press, 2010).

[23] L. D. Landau and E. M. Lifshitz, *Statistical Physics. Part 1* (Butterworth-Heinemann, 1980).

[24] L. D. Landau and E. M. Lifshitz, *Statistical Physics. Part 2* (Butterworth-Heinemann, 1980).

[25] C. Giannetti, M. Capone, D. Fausti, M. Fabrizio, F. Parmigiani, and D. Mihailovic, "Ultrafast optical spectroscopy of strongly correlated materials and high-temperature superconductors: a non-equilibrium approach", Advances in Physics **65**, 58–238 (2016), eprint: https://doi.org/10.1080/00018732.2016.1194044.

[26] M. Bukov, L. D'Alessio, and A. Polkovnikov, "Universal high-frequency behavior of periodically driven systems: from dynamical stabilization to floquet engineering", Advances in Physics **64**, 139–226 (2015), eprint: https://doi.org/10.1080/00018732.2015.1055918.

[27] S. Diehl, A. Micheli, A. Kantian, B. Kraus, H. P. Büchler, and P. Zoller, "Quantum states and phases in driven open quantum systems with cold atoms", Nature Physics **4**, 878 EP - (2008).

[28] T. Li, Z.-X. Gong, Z.-Q. Yin, H. T. Quan, X. Yin, P. Zhang, L.-M. Duan, and X. Zhang, "Space-time crystals of trapped ions", Phys. Rev. Lett. **109**, 163001 (2012).

[29] R. Moessner and S. L. Sondhi, "Equilibration and order in quantum floquet matter", Nature Physics **13**, 424 EP - (2017).

[30] F. Wilczek, "Quantum time crystals", Phys. Rev. Lett. **109**, 160401 (2012).

[31] N. Y. Yao, A. C. Potter, I.-D. Potirniche, and A. Vishwanath, "Discrete time crystals: rigidity, criticality, and realizations", Phys. Rev. Lett. **118**, 030401 (2017).

[32] P. Calabrese and J. Cardy, "Time dependence of correlation functions following a quantum quench", Phys. Rev. Lett. **96**, 136801 (2006).

[33] M. A. Cazalilla, "Effect of suddenly turning on interactions in the luttinger model", Phys. Rev. Lett. **97**, 156403 (2006).

[34] I. Bloch, "Ultracold quantum gases in optical lattices", Nat. Phys. **1**, 23 (2005).

[35] I. Bloch, J. Dalibard, and W. Zwerger, "Many-body physics with ultracold gases", Rev. Mod. Phys. **80**, 885–964 (2008).

[36] I. Bloch, J. Dalibard, and S. Nascimbène, "Quantum simulations with ultracold quantum gases", Nat. Phys. **8**, 267 (2012).

[37] M. Greiner, O. Mandel, T. Esslinger, T. W. Hansch, and I. Bloch, "Quantum phase transition from a superfluid to a mott insulator in a gas of ultracold atoms", Nature **415**, 39–44 (2002).

[38] T. Kinoshita, T. Wenger, and D. S. Weiss, "Observation of a one-dimensional Tonks-Girardeau gas", Science **305**, 1125–1128 (2004), eprint: http://science.sciencemag.org/content/305/5687/1125.full.pdf.

[39] T. Kinoshita, T. Wenger, and D. S. Weiss, "A quantum Newton's cradle", Nature **440**, 900–903 (2006).

[40] T. Langen, R. Geiger, and J. Schmiedmayer, "Ultracold atoms out of equilibrium", Annual Review of Condensed Matter Physics **6**, 201–217 (2015).

[41] T. Langen, S. Erne, R. Geiger, B. Rauer, T. Schweigler, M. Kuhnert, W. Rohringer, I. E. Mazets, T. Gasenzer, and J. Schmiedmayer, "Experimental observation of a generalized Gibbs ensemble", Science **348**, 207–211 (2015), eprint: http://science.sciencemag.org/content/348/6231/207.full.pdf.

[42] T. Langen, R. Geiger, M. Kuhnert, B. Rauer, and J. Schmiedmayer, "Local emergence of thermal correlations in an isolated quantum many-body system", **9**, 640 EP - (2013).

[43] T. Langen, T. Gasenzer, and J. Schmiedmayer, "Prethermalization and universal dynamics in near-integrable quantum systems", Journal of Statistical Mechanics: Theory and Experiment **2016**, 064009 (2016).

[44] B. Paredes, A. Widera, V. Murg, O. Mandel, S. Folling, I. Cirac, G. V. Shlyapnikov, T. W. Hansch, and I. Bloch, "Tonks-girardeau gas of ultracold atoms in an optical lattice", Nature **429**, 277–281 (2004).

[45] A. Polkovnikov, K. Sengupta, A. Silva, and M. Vengalattore, "Colloquium: nonequilibrium dynamics of closed interacting quantum systems", Rev. Mod. Phys. **83**, 863–883 (2011).

[46] S. Trotzky, Y.-A. Chen, A. Flesch, I. P. McCulloch, U. Schollwöck, J. Eisert, and I. Bloch, "Probing the relaxation towards equilibrium in an isolated strongly correlated one-dimensional bose gas", Nature Physics **8**, 325 EP - (2012).

[47] L. Vidmar and M. Rigol, "Generalized Gibbs ensemble in integrable lattice models", Journal of Statistical Mechanics: Theory and Experiment **2016**, 064007 (2016).

[48] J. von Neumann, "Beweis des Ergodensatzes und des H-Theorems in der neuen Mechanik", Zeitschrift für Physik **57**, 30–70 (1929).

[49] J. von Neumann, "Proof of the ergodic theorem and the H-theorem in quantum mechanics", The European Physical Journal H **35**, 201–237 (2010).

[50] J. M. Deutsch, "Quantum statistical mechanics in a closed system", Phys. Rev. A **43**, 2046–2049 (1991).

[51] M. Srednicki, "Chaos and quantum thermalization", Phys. Rev. E **50**, 888–901 (1994).

[52] J.-S. Caux and J. Mossel, "Remarks on the notion of quantum integrability", Journal of Statistical Mechanics: Theory and Experiment **2011**, P02023 (2011).

[53] M. Rigol, V. Dunjko, and M. Olshanii, "Thermalization and its mechanism for generic isolated quantum systems", Nature **452**, 854–858 (2008).

[54] M. Rigol, V. Dunjko, V. Yurovsky, and M. Olshanii, "Relaxation in a completely integrable many-body quantum system: an ab initio study of the dynamics of the highly excited states of 1d lattice hard-core bosons", Phys. Rev. Lett. **98**, 050405 (2007).

[55] M. Cramer, C. M. Dawson, J. Eisert, and T. J. Osborne, "Exact relaxation in a class of nonequilibrium quantum lattice systems", Phys. Rev. Lett. **100**, 030602 (2008).

[56] M. Cramer, A. Flesch, I. P. McCulloch, U. Schollwöck, and J. Eisert, "Exploring local quantum many-body relaxation by atoms in optical superlattices", Phys. Rev. Lett. **101**, 063001 (2008).

[57] T. Barthel and U. Schollwöck, "Dephasing and the steady state in quantum many-particle systems", Phys. Rev. Lett. **100**, 100601 (2008).

[58] M. Cramer and J. Eisert, "A quantum central limit theorem for non-equilibrium systems: exact local relaxation of correlated states", New Journal of Physics **12**, 055020 (2010).

[59] A. M. Kaufman, M. E. Tai, A. Lukin, M. Rispoli, R. Schittko, P. M. Preiss, and M. Greiner, "Quantum thermalization through entanglement in an isolated many-body system", Science **353**, 794–800 (2016), eprint: `http://science.sciencemag.org/content/353/6301/794.full.pdf`.

[60] P. Calabrese and J. Cardy, "Quantum quenches is $1+1$ dimensional conformal field theories", Journal of Statistical Mechanics: Theory and Experiment **2016**, 064003 (2016).

[61] T. Giamarchi, *Quantum physics in one dimension* (Oxford Science Publications, 2004).

[62] J. Voit, "One-dimensional Fermi liquids", Reports on Progress in Physics **58**, 977 (1995).

[63] J. von Delft and H. Schoeller, "Bosonization for beginners — refermionization for experts", Annalen der Physik **7**, 225–305 (1998).

[64] A. L. Fetter and J. D. Walecka, *Quantum theory of many-particle systems* (Dover Publications, 2003).

[65] S. Wall, D. Brida, S. R. Clark, H. P. Ehrke, D. Jaksch, A. Ardavan, S. Bonora, H. Uemura, Y. Takahashi, T. Hasegawa, H. Okamoto, G. Cerullo, and A. Cavalleri, "Quantum interference between charge excitation paths in a solid-state Mott insulator", **7**, 114 EP - (2010).

[66] L. Childress, M. V. Gurudev Dutt, J. M. Taylor, A. S. Zibrov, F. Jelezko, J. Wrachtrup, P. R. Hemmer, and M. D. Lukin, "Coherent dynamics of coupled electron and nuclear spin qubits in diamond", Science **314**, 281–285 (2006), eprint: `http://science.sciencemag.org/content/314/5797/281.full.pdf`.

[67] T. Niemeijer, "Some exact calculations on a chain of spins", Physica **36**, 377–419 (1967).

[68] P. Mazur, "Non-ergodicity of phase functions in certain systems", Physica **43**, 533–545 (1969).

[69] E. Barouch and M. Dresden, "Exact time-dependent analysis for the one-dimensional XY model", Phys. Rev. Lett. **23**, 114–117 (1969).

[70] E. Barouch and B. M. McCoy, "Statistical mechanics of the XY model. iii", Phys. Rev. A **3**, 2137–2140 (1971).

[71] E. Barouch and B. M. McCoy, "Statistical mechanics of the XY model. iii", Phys. Rev. A **3**, 2137–2140 (1971).

[72] M. Inguscio, W. Ketterle, and C. Salomon, eds., *Ultra-cold Fermi gases, Vol. 164 of Proceedings of the International School of Physics "Enrico Fermi"* (IOP Press, 2008).

[73] J. J. Sakurai and J. Napolitano, *Modern quantum mechanics* (Addison-Wesley, 2010).

[74] G. Clos, D. Porras, U. Warring, and T. Schaetz, "Time-resolved observation of thermalization in an isolated quantum system", Phys. Rev. Lett. **117**, 170401 (2016).

[75] C. Neill, P. Roushan, M. Fang, Y. Chen, M. Kolodrubetz, Z. Chen, A. Megrant, R. Barends, B. Campbell, B. Chiaro, A. Dunsworth, E. Jeffrey, J. Kelly, J. Mutus, P. J. J. O'Malley, C. Quintana, D. Sank, A. Vainsencher, J. Wenner, T. C. White, A. Polkovnikov, and J. M. Martinis, "Ergodic dynamics and thermalization in an isolated quantum system", Nature Physics **12**, 1037 EP - (2016).

[76] A. Messiah, *Quantum mechanics* (Dover Publications, 2017).

[77] S. Goldstein, J. L. Lebowitz, R. Tumulka, and N. Zanghì, "Long-time behavior of macroscopic quantum systems", The European Physical Journal H **35**, 173–200 (2010).

[78] P. Bocchieri and A. Loinger, "Quantum recurrence theorem", Phys. Rev. **107**, 337–338 (1957).

[79] H. Poincaré, "Sur le problème des trois corps et les équations de la dynamiques", Acta Math. **13**, 1–270 (1890).

[80] L. S. Schulman, "Note on the quantum recurrence theorem", Phys. Rev. A **18**, 2379–2380 (1978).

[81] S. Ziraldo, "Thermalization and relaxation after a quantum quench in disordered hamiltonians", PhD thesis (SISSA, International School fo Advanced Studies, 2013).

[82] S. Ziraldo, A. Silva, and G. E. Santoro, "Relaxation dynamics of disordered spin chains: localization and the existence of a stationary state", Phys. Rev. Lett. **109**, 247205 (2012).

[83] S. Ziraldo and G. E. Santoro, "Relaxation and thermalization after a quantum quench: why localization is important", Phys. Rev. B **87**, 064201 (2013).

[84] M. Srednicki, "Thermal fluctuations in quantized chaotic systems", Journal of Physics A: Mathematical and General **29**, L75 (1996).

[85] M. Srednicki, "The approach to thermal equilibrium in quantized chaotic systems", Journal of Physics A: Mathematical and General **32**, 1163 (1999).

[86] Y. Alhassid, "The statistical theory of quantum dots", Rev. Mod. Phys. **72**, 895–968 (2000).

[87] M. Gring, M. Kuhnert, T. Langen, T. Kitagawa, B. Rauer, M. Schreitl, I. Mazets, D. A. Smith, E. Demler, and J. Schmiedmayer, "Relaxation and prethermalization in an isolated quantum system", Science **337**, 1318–1322 (2012), eprint: http://science.sciencemag.org/content/337/6100/1318.full.pdf.

[88] E. Haller, R. Hart, M. J. Mark, J. G. Danzl, L. Reichsollner, M. Gustavsson, M. Dalmonte, G. Pupillo, and H.-C. Nagerl, "Pinning quantum phase transition for a luttinger liquid of strongly interacting bosons", Nature **466**, 597–600 (2010).

[89] E. H. Lieb and W. Liniger, "Exact analysis of an interacting bose gas. i. the general solution and the ground state", Phys. Rev. **130**, 1605–1616 (1963).

[90] R. Folman, P. Krüger, J. Schmiedmayer, J. Denschlag, and C. Henkel, "Microscopic atom optics: from wires to an atom chip", in , Vol. 48, edited by B. Bederson and H. Walther, Advances In Atomic, Molecular, and Optical Physics Supplement C (Academic Press, 2002), pp. 263–356.

[91] J. Reichel and V. Vuletic, *Atom chips* (Wiley-VCH, 2011).

[92] R. Grimm, M. Weidemüller, and Y. B. Ovchinnikov, "Optical dipole traps for neutral atoms", in , Vol. 42, edited by B. Bederson and H. Walther, Advances In Atomic, Molecular, and Optical Physics Supplement C (Academic Press, 2000), pp. 95–170.

[93] W. Ketterle, D. Durfee, and D. Stamper-Kurn, "Microscopic atom optics: from wires to an atom chip", in , Vol. 140, edited by M. Inguscio, S. Stringari, and C. Wieman, Proceedings of the International School of Physics "Enrico Fermi" (IOP Press, Amsterdam, 1999), pp. 67–176.

[94] C. Chin, R. Grimm, P. Julienne, and E. Tiesinga, "Feshbach resonances in ultracold gases", Rev. Mod. Phys. **82**, 1225–1286 (2010).

[95] S. Inouye, M. R. Andrews, J. Stenger, H. .-.-J. Miesner, D. M. Stamper-Kurn, and W. Ketterle, "Observation of feshbach resonances in a bose-einstein condensate", Nature **392**, 151–154 (1998).

[96] S. Will, T. Best, U. Schneider, L. Hackermuller, D.-S. Luhmann, and I. Bloch, "Time-resolved observation of coherent multi-body interactions in quantum phase revivals", Nature **465**, 197–201 (2010).

[97] B. Sutherland, *Beautiful models: 70 years of exactly solved quantum many-body* (World Scientific Pub. Co. Inc., 2004).

[98] A. Fuhrmanek, A. M. Lance, C. Tuchendler, P. Grangier, Y. R. P. Sortais, and A. Browaeys, "Imaging a single atom in a time-of-flight experiment", New Journal of Physics **12**, 053028 (2010).

[99] J. Sirker, N. P. Konstantinidis, F. Andraschko, and N. Sedlmayr, "Locality and thermalization in closed quantum systems", Phys. Rev. A **89**, 042104 (2014).

[100] E. T. Jaynes, "Information theory and statistical mechanics", Phys. Rev. **106**, 620–630 (1957).

[101] E. T. Jaynes, "Information theory and statistical mechanics. ii", Phys. Rev. **108**, 171–190 (1957).

[102] A. Iucci and M. A. Cazalilla, "Quantum quench dynamics of the luttinger model", Phys. Rev. A **80**, 063619 (2009).

[103] A. Iucci and M. A. Cazalilla, "Quantum quench dynamics of the sine-gordon model in some solvable limits", New Journal of Physics **12**, 055019 (2010).

[104] M. Kollar and M. Eckstein, "Relaxation of a one-dimensional mott insulator after an interaction quench", Phys. Rev. A **78**, 013626 (2008).

[105] P. Calabrese, F. H. L. Essler, and M. Fagotti, "Quantum quench in the transverse-field ising chain", Phys. Rev. Lett. **106**, 227203 (2011).

[106] P. Calabrese, F. H. L. Essler, and M. Fagotti, "Quantum quench in the transverse field ising chain: i. time evolution of order parameter correlators", Journal of Statistical Mechanics: Theory and Experiment **2012**, P07016 (2012).

[107] P. Calabrese, F. H. L. Essler, and M. Fagotti, "Quantum quenches in the transverse field ising chain: ii. stationary state properties", Journal of Statistical Mechanics: Theory and Experiment **2012**, P07022 (2012).

[108] E. H. Lieb and D. W. Robinson, "The finite group velocity of quantum spin systems", Comm. Math. Phys. **28**, 251–257 (1972).

[109] B. Nachtergaele and R. Sims, "Lieb-robinson bounds and the exponential clustering theorem", Communications in Mathematical Physics **265**, 119–130 (2006).

[110] S. Bravyi, M. B. Hastings, and F. Verstraete, "Lieb-robinson bounds and the generation of correlations and topological quantum order", Phys. Rev. Lett. **97**, 050401 (2006).

[111] S. Hofferberth, I. Lesanovsky, B. Fischer, J. Verdu, and J. Schmiedmayer, "Radiofrequency-dressed-state potentials for neutral atoms", **2**, 710 EP - (2006).

[112] T. Schweigler, V. Kasper, S. Erne, I. Mazets, B. Rauer, F. Cataldini, T. Langen, T. Gasenzer, J. Berges, and J. Schmiedmayer, "Experimental characterization of a quantum many-body system via higher-order correlations", Nature **545**, 323–326 (2017).

[113] T. Schumm, S. Hofferberth, L. M. Andersson, S. Wildermuth, S. Groth, I. Bar-Joseph, J. Schmiedmayer, and P. Krüger, "Matter-wave interferometry in a double well on an atom chip", **1**, 57 EP - (2005).

[114] D. A. Smith, S. Aigner, S. Hofferberth, M. Gring, M. Andersson, S. Wildermuth, P. Krüger, S. Schneider, T. Schumm, and J. Schmiedmayer, "Absorption imaging of ultracold atoms on atom chips", Opt. Express **19**, 8471–8485 (2011).

[115] M. Cheneau, P. Barmettler, D. Poletti, M. Endres, P. Schauß, T. Fukuhara, C. Gross, I. Bloch, C. Kollath, and S. Kuhr, "Light-cone-like spreading of correlations in a quantum many-body system", Nature **481**, 484 EP - (2012).

[116] F. Franchini, *An introduction to integrable techniques for one-dimensional quantum systems* (Springer, 2017).

[117] J. Berges and T. Gasenzer, "Quantum versus classical statistical dynamics of an ultracold bose gas", Phys. Rev. A **76**, 033604 (2007).

[118] S. Huber, M. Buchhold, J. Schmiedmayer, and S. Diehl, *Thermalization dynamics of two correlated bosonic quantum wires after a split*, 2018, arXiv:arXiv:1801.05819.

[119] L. D. Landau, "The theory of Fermi liquids", Sov. Phys. JEPT **3** (1957).

[120] O. M. Auslaender, H. Steinberg, A. Yacoby, Y. Tserkovnyak, B. I. Halperin, K. W. Baldwin, L. N. Pfeiffer, and K. W. West, "Spin-charge separation and localization in one dimension", Science **308**, 88–92 (2005), eprint: http://science.sciencemag.org/content/308/5718/88.full.pdf.

[121] A. Calzona, M. Carrega, G. Dolcetto, and M. Sassetti, "Time-resolved pure spin fractionalization and spin-charge separation in helical Luttinger liquid based devices", Phys. Rev. B **92**, 195414 (2015).

[122] A. Calzona, M. Acciai, M. Carrega, F. Cavaliere, and M. Sassetti, "Time-resolved energy dynamics after single electron injection into an interacting helical liquid", Phys. Rev. B **94**, 035404 (2016).

[123] V. V. Deshpande, M. Bockrath, L. I. Glazman, and A. Yacoby, "Electron liquids and solids in one dimension", Nature **464**, 209 EP - (2010).

[124] H. Inoue, A. Grivnin, N. Ofek, I. Neder, M. Heiblum, V. Umansky, and D. Mahalu, "Charge fractionalization in the integer quantum hall effect", Phys. Rev. Lett. **112**, 166801 (2014).

[125] Y. Jompol, C. J. B. Ford, J. P. Griffiths, I. Farrer, G. A. C. Jones, D. Anderson, D. A. Ritchie, T. W. Silk, and A. J. Schofield, "Probing spin-charge separation in a Tomonaga-Luttinger liquid", Science **325**, 597–601 (2009), eprint: `http://science.sciencemag.org/content/325/5940/597.full.pdf`.

[126] H. Kamata, N. Kumada, M. Hashisaka, K. Muraki, and T. Fujisawa, "Fractionalized wave packets from an artificial Tomonaga–Luttinger liquid", Nature Nanotechnology **9**, 177 EP - (2014).

[127] K. L. Hur, B. I. Halperin, and A. Yacoby, "Charge fractionalization in nonchiral Luttinger systems", Annals of Physics **323**, 3037–3058 (2008).

[128] M. Milletarì and B. Rosenow, "Shot-noise signatures of charge fractionalization in the $\nu = 2$ quantum hall edge", Phys. Rev. Lett. **111**, 136807 (2013).

[129] I. Safi and H. J. Schulz, "Transport in an inhomogeneous interacting one-dimensional system", Phys. Rev. B **52**, R17040–R17043 (1995).

[130] A. Schneider, M. Milletarì, and B. Rosenow, "Transient Features in Charge Fractionalization, Local Equilibration and Non-equilibrium Bosonization", SciPost Phys. **2**, 007 (2017).

[131] H. Steinberg, G. Barak, A. Yacoby, L. N. Pfeiffer, K. W. West, B. I. Halperin, and K. Le Hur, "Charge fractionalization in quantum wires", Nature Physics **4**, 116 EP - (2007).

[132] E. Fradkin, *Condensed matter field theory* (Cambridge University Press, 2013).

[133] M. Acciai, A. Calzona, G. Dolcetto, T. L. Schmidt, and M. Sassetti, "Charge and energy fractionalization mechanism in one-dimensional channels", Phys. Rev. B **96**, 075144 (2017).

[134] T. Karzig, G. Refael, L. I. Glazman, and F. von Oppen, "Energy partitioning of tunneling currents into luttinger liquids", Phys. Rev. Lett. **107**, 176403 (2011).

[135] F. M. Gambetta, F. Cavaliere, R. Citro, and M. Sassetti, "Universal transport dynamics in a quenched tunnel-coupled Luttinger liquid", Phys. Rev. B **94**, 045104 (2016).

[136] A. Calzona, F. M. Gambetta, F. Cavaliere, M. Carrega, and M. Sassetti, "Quench-induced entanglement and relaxation dynamics in Luttinger liquids", Phys. Rev. B **96**, 085423 (2017).

[137] E. Miranda, "Introduction to bosonization", en, Brazilian Journal of Physics **33**, 3–35 (2003).

[138] J. Sólyom, *Fundamentals of the physics of solids: volume 3 - normal, broken-symmetry, and correlated systems* (Springer, 2011).

[139] F. D. M. Haldane, "'luttinger liquid theory' of one-dimensional quantum fluids. i. properties of the luttinger model and their extension to the general 1d interacting spinless fermi gas", Journal of Physics C: Solid State Physics **14**, 2585 (1981).

[140] R. Heidenreich, R. Seiler, and D. A. Uhlenbrock, "The luttinger model", Journal of Statistical Physics **22**, 27–57 (1980).

[141] K. Schönhammer and V. Meden, "Correlation effects in photoemission from low dimensional metals", Journal of Electron Spectroscopy and Related Phenomena **62**, 225–236 (1993).

[142] M. Abramowitz and I. Stegun, *Handbook of mathematical functions* (National Bureau of Standards, 1964).

[143] K.-V. Pham, M. Gabay, and P. Lederer, "Fractional excitations in the luttinger liquid", Phys. Rev. B **61**, 16397–16422 (2000).

[144] C. Blumenstein, J. Schäfer, S. Mietke, S. Meyer, A. Dollinger, M. Lochner, X. Y. Cui, L. Patthey, R. Matzdorf, and R. Claessen, "Atomically controlled quantum chains hosting a Tomonaga–Luttinger liquid", Nature Physics **7**, 776 EP - (2011).

[145] M. Bockrath, D. H. Cobden, J. Lu, A. G. Rinzler, R. E. Smalley, L. Balents, and P. L. McEuen, "Luttinger-liquid behaviour in carbon nanotubes", Nature **397**, 598 EP - (1999).

[146] K. von Klitzing, "The quantized Hall effect", Rev. Mod. Phys. **58**, 519–531 (1986).

[147] H. L. Stormer, "Nobel Lecture: the fractional quantum Hall effect", Rev. Mod. Phys. **71**, 875–889 (1999).

[148] G. Dolcetto, M. Sassetti, and T. L. Schmidt, "Edge physics in two-dimensional topological insulators", Riv. Nuovo Cimento **39**, 113 (2016).

[149] T. Li, P. Wang, H. Fu, L. Du, K. A. Schreiber, X. Mu, X. Liu, G. Sullivan, G. A. Csáthy, X. Lin, and R.-R. Du, "Observation of a helical Luttinger liquid in InAs/GaSb quantum spin Hall edges", Phys. Rev. Lett. **115**, 136804 (2015).

[150] C. Wu, B. A. Bernevig, and S.-C. Zhang, "Helical liquid and the edge of quantum spin Hall systems", Phys. Rev. Lett. **96**, 106401 (2006).

[151] R. Egger and A. O. Gogolin, "Effective low-energy theory for correlated carbon nanotubes", Phys. Rev. Lett. **79**, 5082–5085 (1997).

[152] H. Ishii, H. Kataura, H. Shiozawa, H. Yoshioka, H. Otsubo, Y. Takayama, T. Miyahara, S. Suzuki, Y. Achiba, M. Nakatake, T. Narimura, M. Higashiguchi, K. Shimada, H. Namatame, and M. Taniguchi, "Direct observation of tomonaga–luttinger-liquid state in carbon nanotubes at low temperatures", Nature **426**, 540 EP - (2003).

[153] N. Traverso Ziani, G. Piovano, F. Cavaliere, and M. Sassetti, "Electrical probe for mechanical vibrations in suspended carbon nanotubes", Phys. Rev. B **84**, 155423 (2011).

[154] R. M. Konik and P. Fendley, "Haldane-gapped spin chains as Luttinger liquids: correlation functions at finite field", Phys. Rev. B **66**, 144416 (2002).

[155] M. Oshikawa, M. Yamanaka, and I. Affleck, "Magnetization plateaus in spin chains: "haldane gap" for half-integer spins", Phys. Rev. Lett. **78**, 1984–1987 (1997).

[156] Y. Gindikin and V. A. Sablikov, "Deformed wigner crystal in a one-dimensional quantum dot", Phys. Rev. B **76**, 045122 (2007).

[157] I. Safi and H. J. Schulz, "Interacting electrons with spin in a one-dimensional dirty wire connected to leads", Phys. Rev. B **59**, 3040–3059 (1999).

[158] H. J. Schulz, "Wigner crystal in one dimension", Phys. Rev. Lett. **71**, 1864–1867 (1993).

[159] N. Traverso Ziani, F. Cavaliere, and M. Sassetti, "Signatures of Wigner correlations in the conductance of a one-dimensional quantum dot coupled to an AFM tip", Phys. Rev. B **86**, 125451 (2012).

[160] V. Mastropietro and Z. Wang, "Quantum quench for inhomogeneous states in the nonlocal luttinger model", Phys. Rev. B **91**, 085123 (2015).

[161] N. Nessi and A. Iucci, "Quantum quench dynamics of the Coulomb Luttinger model", Phys. Rev. B **87**, 085137 (2013).

[162] D. M. Kennes and V. Meden, "Luttinger liquid properties of the steady state after a quantum quench", Phys. Rev. B **88**, 165131 (2013).

[163] D. M. Kennes, C. Klöckner, and V. Meden, "Spectral properties of one-dimensional fermi systems after an interaction quench", Phys. Rev. Lett. **113**, 116401 (2014).

[164] E. Perfetto and G. Stefanucci, "On the thermalization of a Luttinger liquid after a sequence of sudden interaction quenches", EPL (Europhysics Letters) **95**, 10006 (2011).

[165] M. Schiró and A. Mitra, "Transient orthogonality catastrophe in a time-dependent nonequilibrium environment", Phys. Rev. Lett. **112**, 246401 (2014).

[166] M. Schiró and A. Mitra, "Transport across an impurity in one-dimensional quantum liquids far from equilibrium", Phys. Rev. B **91**, 235126 (2015).

[167] J.-S. Bernier, R. Citro, C. Kollath, and E. Orignac, "Correlation dynamics during a slow interaction quench in a one-dimensional bose gas", Phys. Rev. Lett. **112**, 065301 (2014).

[168] P. Chudzinski and D. Schuricht, "Time evolution during and after finite-time quantum quenches in Luttinger liquids", Phys. Rev. B **94**, 075129 (2016).

[169] B. Dóra, M. Haque, and G. Zaránd, "Crossover from adiabatic to sudden interaction quench in a Luttinger liquid", Phys. Rev. Lett. **106**, 156406 (2011).

[170] M. Collura, P. Calabrese, and F. H. L. Essler, "Quantum quench within the gapless phase of the spin $-\frac{1}{2}$ Heisenberg XXZ spin chain", Phys. Rev. B **92**, 125131 (2015).

[171] C. Karrasch, J. Rentrop, D. Schuricht, and V. Meden, "Luttinger-liquid universality in the time evolution after an interaction quench", Phys. Rev. Lett. **109**, 126406 (2012).

[172] A. Calzona, F. M. Gambetta, M. Carrega, F. Cavaliere, and M. Sassetti, "Nonequilibrium effects on charge and energy partitioning after an interaction quench", Phys. Rev. B **95**, 085101 (2017).

[173] A. Silva, "Statistics of the work done on a quantum critical system by quenching a control parameter", Phys. Rev. Lett. **101**, 120603 (2008).

[174] S. Sotiriadis, G. Takacs, and G. Mussardo, "Boundary state in an integrable quantum field theory out of equilibrium", Physics Letters B **734**, 52–57 (2014).

[175] V. Meden and K. Schönhammer, "Spectral functions for the tomonaga-luttinger model", Phys. Rev. B **46**, 15753–15760 (1992).

[176] H. T. M. Nghiem and T. A. Costi, "Time evolution of the kondo resonance in response to a quench", Phys. Rev. Lett. **119**, 156601 (2017).

[177] D. Rossini, A. Silva, G. Mussardo, and G. E. Santoro, "Effective thermal dynamics following a quantum quench in a spin chain", Phys. Rev. Lett. **102**, 127204 (2009).

[178] J.-P. Brantut, J. Meineke, D. Stadler, S. Krinner, and T. Esslinger, "Conduction of ultracold fermions through a mesoscopic channel", Science **337**, 1069–1071 (2012), eprint: http://science.sciencemag.org/content/337/6098/1069.full.pdf.

[179] C.-C. Chien, S. Peotta, and M. Di Ventra, "Quantum transport in ultracold atoms", Nature Physics **11**, 998 EP - (2015).

[180] D. Husmann, S. Uchino, S. Krinner, M. Lebrat, T. Giamarchi, T. Esslinger, and J.-P. Brantut, "Connecting strongly correlated superfluids by a quantum point contact", Science **350**, 1498–1501 (2015), eprint: http://science.sciencemag.org/content/350/6267/1498.full.pdf.

[181] S. Krinner, D. Stadler, D. Husmann, J.-P. Brantut, and T. Esslinger, "Observation of quantized conductance in neutral matter", Nature **517**, 64 EP - (2014).

[182] D. Chevallier, J. Rech, T. Jonckheere, C. Wahl, and T. Martin, "Poissonian tunneling through an extended impurity in the quantum hall effect", Phys. Rev. B **82**, 155318 (2010).

[183] G. Dolcetto, S. Barbarino, D. Ferraro, N. Magnoli, and M. Sassetti, "Tunneling between helical edge states through extended contacts", Phys. Rev. B **85**, 195138 (2012).

[184] L. Vannucci, F. Ronetti, G. Dolcetto, M. Carrega, and M. Sassetti, "Interference-induced thermoelectric switching and heat rectification in quantum Hall junctions", Phys. Rev. B **92**, 075446 (2015).

[185] E. Perfetto, G. Stefanucci, H. Kamata, and T. Fujisawa, "Time-resolved charge fractionalization in inhomogeneous luttinger liquids", Phys. Rev. B **89**, 201413 (2014).

[186] A. Calzona, F. M. Gambetta, M. Carrega, F. Cavaliere, T. L. Schmidt, and M. Sassetti, *Universal scaling of quench-induced correlations in a one-dimensional channel at finite temperature*, Submitted to SciPost Physics, 2017, arXiv:1711.02967.

[187] M. Fabrizio and A. O. Gogolin, "Interacting one-dimensional electron gas with open boundaries", Phys. Rev. B **51**, 17827–17841 (1995).

[188] S. R. Manmana, S. Wessel, R. M. Noack, and A. Muramatsu, "Time evolution of correlations in strongly interacting fermions after a quantum quench", Phys. Rev. B **79**, 155104 (2009).

[189] S. Porta, F. M. Gambetta, F. Cavaliere, N. Traverso Ziani, and M. Sassetti, "Out-of-equilibrium density dynamics of a quenched fermionic system", Phys. Rev. B **94**, 085122 (2016).

[190] J. Friedel, "Metallic alloys", Il Nuovo Cimento (1955-1965) **7**, 287–311 (1958).

[191] S. A. Söffing, M. Bortz, I. Schneider, A. Struck, M. Fleischhauer, and S. Eggert, "Wigner crystal versus Friedel oscillations in the one-dimensional Hubbard model", Phys. Rev. B **79**, 195114 (2009).

[192] Y. Gindikin and V. A. Sablikov, "Dynamic correlations of the spinless coulomb luttinger liquid", Phys. Rev. B **65**, 125109 (2002).

[193] V. A. Sablikov and Y. Gindikin, "Effect of short-range electron correlations in dynamic transport in a luttinger liquid", Phys. Rev. B **61**, 12766–12771 (2000).

[194] Gambetta, F. M., Traverso Ziani, N., Cavaliere, F., and Sassetti, M., "Correlation functions for the detection of Wigner molecules in a one-channel Luttinger liquid quantum dot", EPL **107**, 47010 (2014).

[195] S. M. Reimann and M. Manninen, "Electronic structure of quantum dots", Rev. Mod. Phys. **74**, 1283–1342 (2002).

[196] E. Wigner, "On the interaction of electrons in metals", Phys. Rev. **46**, 1002–1011 (1934).

[197] C. Yannouleas and U. Landman, "Symmetry breaking and quantum correlations in finite systems: studies of quantum dots and ultracold bose gases and related nuclear and chemical methods", Reports on Progress in Physics **70**, 2067 (2007).

[198] R. Sachdeva, T. Nag, A. Agarwal, and A. Dutta, "Finite-time interaction quench in a luttinger liquid", Phys. Rev. B **90**, 045421 (2014).

[199] J. D. Murray, *Asymptotic analysis* (Springer-Verlag, 1984).

[200] S. H. Abedinpour, M. Polini, G. Xianlong, and M. P. Tosi, "Emergence of wigner molecules in one-dimensional systems of repulsive fermions under harmonic confinement", Phys. Rev. A **75**, 015602 (2007).

[201] P. Calabrese, F. H. L. Essler, and M. Fagotti, "Quantum quench in the transverse-field ising chain", Phys. Rev. Lett. **106**, 227203 (2011).

[202] F. H. L. Essler, S. Evangelisti, and M. Fagotti, "Dynamical correlations after a quantum quench", Phys. Rev. Lett. **109**, 247206 (2012).

[203] M. Heyl, A. Polkovnikov, and S. Kehrein, "Dynamical quantum phase transitions in the transverse-field ising model", Phys. Rev. Lett. **110**, 135704 (2013).

[204] D. Rossini, S. Suzuki, G. Mussardo, G. E. Santoro, and A. Silva, "Long time dynamics following a quench in an integrable quantum spin chain: local versus nonlocal operators and effective thermal behavior", Phys. Rev. B **82**, 144302 (2010).

[205] D. Schuricht and F. H. L. Essler, "Dynamics in the ising field theory after a quantum quench", Journal of Statistical Mechanics: Theory and Experiment **2012**, P04017 (2012).

[206] J. C. Budich and M. Heyl, "Dynamical topological order parameters far from equilibrium", Phys. Rev. B **93**, 085416 (2016).

[207] M. D. Caio, N. R. Cooper, and M. J. Bhaseen, "Quantum quenches in chern insulators", Phys. Rev. Lett. **115**, 236403 (2015).

[208] M. D. Caio, N. R. Cooper, and M. J. Bhaseen, "Hall response and edge current dynamics in chern insulators out of equilibrium", Phys. Rev. B **94**, 155104 (2016).

[209] S. Vajna and B. Dóra, "Topological classification of dynamical phase transitions", Phys. Rev. B **91**, 155127 (2015).

[210] B. Bertini, D. Schuricht, and F. H. L. Essler, "Quantum quench in the sine-gordon model", Journal of Statistical Mechanics: Theory and Experiment **2014**, P10035 (2014).

[211] A. C. Cubero and D. Schuricht, "Quantum quench in the attractive regime of the sine-Gordon model", Journal of Statistical Mechanics: Theory and Experiment **2017**, 103106 (2017).

[212] E. G. Dalla Torre, E. Demler, and A. Polkovnikov, "Universal rephasing dynamics after a quantum quench via sudden coupling of two initially independent condensates", Phys. Rev. Lett. **110**, 090404 (2013).

[213] M. S. Foster, E. A. Yuzbashyan, and B. L. Altshuler, "Quantum quench in one dimension: coherent inhomogeneity amplification and "Supersolitons"", Phys. Rev. Lett. **105**, 135701 (2010).

[214] M. S. Foster, T. C. Berkelbach, D. R. Reichman, and E. A. Yuzbashyan, "Quantum quench spectroscopy of a Luttinger liquid: ultrarelativistic density wave dynamics due to fractionalization in an *XXZ* chain", Phys. Rev. B **84**, 085146 (2011).

[215] D. Horváth and G. Takács, "Overlaps after quantum quenches in the sine-gordon model", Physics Letters B **771**, 539–545 (2017).

[216] M. Kormos and G. Zaránd, "Quantum quenches in the sine-gordon model: a semiclassical approach", Phys. Rev. E **93**, 062101 (2016).

[217] J. Lancaster, E. Gull, and A. Mitra, "Quenched dynamics in interacting one-dimensional systems: appearance of current-carrying steady states from initial domain wall density profiles", Phys. Rev. B **82**, 235124 (2010).

[218] C. P. Moca, M. Kormos, and G. Zaránd, "Hybrid semiclassical theory of quantum quenches in one-dimensional systems", Phys. Rev. Lett. **119**, 100603 (2017).

[219] L. W. Cheuk, A. T. Sommer, Z. Hadzibabic, T. Yefsah, W. S. Bakr, and M. W. Zwierlein, "Spin-injection spectroscopy of a spin-orbit coupled fermi gas", Phys. Rev. Lett. **109**, 095302 (2012).

[220] S. Heedt, N. Traverso Ziani, F. Crépin, W. Prost, S. Trellenkamp, J. Schubert, D. Grützmacher, B. Trauzettel, and T. Schäpers, "Signatures of interaction-induced helical gaps in nanowire quantum point contacts", Nature Physics **13**, 563 EP - (2017).

[221] C. H. L. Quay, T. L. Hughes, J. A. Sulpizio, L. N. Pfeiffer, K. W. Baldwin, K. W. West, D. Goldhaber-Gordon, and R. de Picciotto, "Observation of a one-dimensional spin–orbit gap in a quantum wire", Nature Physics **6**, 336 EP - (2010).

[222] P. St ředa and P. Šeba, "Antisymmetric spin filtering in one-dimensional electron systems with uniform spin-orbit coupling", Phys. Rev. Lett. **90**, 256601 (2003).

[223] T. Mishra, J. Carrasquilla, and M. Rigol, "Phase diagram of the half-filled one-dimensional *t-V-V'* model", Phys. Rev. B **84**, 115135 (2011).

[224] S. Porta, F. M. Gambetta, N. Traverso Ziani, D. M. Kennes, M. Sassetti, and F. Cavaliere, "Nonmonotonic response and light-cone freezing in fermionic systems under quantum quenches from gapless to gapped or partially gapped states", Phys. Rev. B **97**, 035433 (2018).

[225] B. Braunecker, G. I. Japaridze, J. Klinovaja, and D. Loss, "Spin-selective Peierls transition in interacting one-dimensional conductors with spin-orbit interaction", Phys. Rev. B **82**, 045127 (2010).

[226] T. Meng and D. Loss, "Strongly anisotropic spin response as a signature of the helical regime in Rashba nanowires", Phys. Rev. B **88**, 035437 (2013).

[227] Y. V. Pershin, J. A. Nesteroff, and V. Privman, "Effect of spin-orbit interaction and in-plane magnetic field on the conductance of a quasi-one-dimensional system", Phys. Rev. B **69**, 121306 (2004).

[228] F. M. Gambetta, N. Traverso Ziani, S. Barbarino, F. Cavaliere, and M. Sassetti, "Anomalous Friedel oscillations in a quasihelical quantum dot", Phys. Rev. B **91**, 235421 (2015).

[229] J. Klinovaja, M. J. Schmidt, B. Braunecker, and D. Loss, "Helical modes in carbon nanotubes generated by strong electric fields", Phys. Rev. Lett. **106**, 156809 (2011).

[230] J. Klinovaja, M. J. Schmidt, B. Braunecker, and D. Loss, "Carbon nanotubes in electric and magnetic fields", Phys. Rev. B **84**, 085452 (2011).

[231] B. A. Bernevig and S. Zhang, "Quantum spin Hall effect", Phys. Rev. Lett. **96**, 106802 (2006).

[232] B. A. Bernevig, T. L. Hughes, and S. C. Zhang, "Quantum spin Hall effect and topological phase transition in HgTe quantum wells", Science **314**, 1757–1761 (2006), eprint: http://www.sciencemag.org/content/314/5806/1757.full.pdf.

[233] M. König, S. Wiedmann, C. Brüne, A. Roth, H. Buhmann, L. W. Molenkamp, X. Qi, and S. Zhang, "Quantum spin Hall insulator state in HgTe quantum wells", Science **318**, 766–770 (2007), eprint: http://www.sciencemag.org/content/318/5851/766.full.pdf.

[234] X. L. Qi and S. C. Zhang, "Topological insulators and superconductors", Rev. Mod. Phys. **83**, 1057–1110 (2011).

[235] S. Bandyopadhyay and M. Cahay, *Introduction to spintronics* (CRC Press, 2015).

[236] T. Schäpers, *Semiconductor spintronics* (De Gruyter, 2016).

[237] S. A. Wolf, D. D. Awschalom, R. A. Buhrman, J. M. Daughton, S. von Molnár, M. L. Roukes, A. Y. Chtchelkanova, and D. M. Treger, "Spintronics: a spin-based electronics vision for the future", Science **294**, 1488–1495 (2001).

[238] I. Žutić, J. Fabian, and S. Das Sarma, "Spintronics: fundamentals and applications", Rev. Mod. Phys. **76**, 323–410 (2004).

[239] V. Lahtinen and J. K. Pachos, "A Short Introduction to Topological Quantum Computation", SciPost Phys. **3**, 021 (2017).

[240] C. Nayak, S. H. Simon, A. Stern, M. Freedman, and S. Das Sarma, "Non-abelian anyons and topological quantum computation", Rev. Mod. Phys. **80**, 1083–1159 (2008).

[241] S. D. Sarma, M. Freedman, and C. Nayak, "Majorana zero modes and topological quantum computation", Npj Quantum Information 1, 15001 EP - (2015).

[242] A. Manchon, H. C. Koo, J. Nitta, S. M. Frolov, and R. A. Duine, "New perspectives for rashba spin-orbit coupling", Nat. Mater. 14, 871–882 (2015).

[243] R. M. Lutchyn, J. D. Sau, and S. Das Sarma, "Majorana fermions and a topological phase transition in semiconductor-superconductor heterostructures", Phys. Rev. Lett. 105, 077001 (2010).

[244] V. Mourik, K. Zuo, S. M. Frolov, S. R. Plissard, E. P. A. M. Bakkers, and L. P. Kouwenhoven, "Signatures of Majorana fermions in hybrid superconductor-semiconductor nanowire devices", Science 336, 1003–1007 (2012), eprint: http://www.sciencemag.org/content/336/6084/1003.full.pdf.

[245] Y. Oreg, G. Refael, and F. von Oppen, "Helical liquids and Majorana bound states in quantum wires", Phys. Rev. Lett. 105, 177002 (2010).

[246] D. J. Griffiths, *Introduction to electromagnetism* (Pearson, 2012).

[247] Y. A. Bychkov and E. I. Rashba, "Properties of a 2D electron gas with lifted spectral degeneracy", P. Zh. Eksp. Teor. Fiz. 39, 66–69 (1984).

[248] F. T. Vas'ko, "Spin splitting in the spectrum of two-dimensional electrons due to the surface potential", P. Zh. Eksp. Teor. Fiz. 30, 574–577 (1979).

[249] M. Governale and U. Zülicke, "Spin accumulation in quantum wires with strong rashba spin-orbit coupling", Phys. Rev. B 66, 073311 (2002).

[250] M. Governale, "Quantum dots with rashba spin-orbit coupling", Phys. Rev. Lett. 89, 206802 (2002).

[251] A. V. Moroz and C. H. W. Barnes, "Effect of the spin-orbit interaction on the band structure and conductance of quasi-one-dimensional systems", Phys. Rev. B 60, 14272–14285 (1999).

[252] J. Kammhuber, M. C. Cassidy, F. Pei, M. P. Nowak, A. Vuik, Ö. Gül, D. Car, S. R. Plissard, E. P. A. M. Bakkers, M. Wimmer, and L. P. Kouwenhoven, "Conductance through a helical state in an indium antimonide nanowire", Nature Communications 8, 478 (2017).

[253] V. Galitski and I. B. Spielman, "Spin–orbit coupling in quantum gases", Nature 494, 49 EP - (2013).

[254] Y.-J. Lin, K. Jiménez-García, and I. B. Spielman, "Spin–orbit-coupled Bose–Einstein condensates", Nature 471, 83 EP - (2011).

[255] S. Zhang, W. S. Cole, A. Paramekanti, and N. Trivedi, "Spin-orbit coupling in optical lattices", in *Annual review of cold atoms and molecules* (World Scientific, 2015) Chap. 3, pp. 135–179, eprint: http://www.worldscientific.com/doi/pdf/10.1142/9789814667746_0003.

[256] C. Cohen-Tannoudji and G. G. J. Dupont-Roc, *Atom-photon interactions: basic processes and applications* (Wiley-VCH, 1998).

[257] Z. Hadzibabic, S. Gupta, C. A. Stan, C. H. Schunck, M. W. Zwierlein, K. Dieckmann, and W. Ketterle, "Fiftyfold improvement in the number of quantum degenerate fermionic atoms", Phys. Rev. Lett. **91**, 160401 (2003).

[258] J. E. Birkholz and V. Meden, "Spin–orbit coupling effects in one-dimensional ballistic quantum wires", Journal of Physics: Condensed Matter **20**, 085226 (2008).

[259] F. Mireles and G. Kirczenow, "Ballistic spin-polarized transport and rashba spin precession in semiconductor nanowires", Phys. Rev. B **64**, 024426 (2001).

[260] R. Courant and D. Hilbert, *Methods of mathematical physics* (Wiley-VCH, 1953).

[261] D. Bercioux and P. Lucignano, "Quantum transport in rashba spin–orbit materials: a review", Reports on Progress in Physics **78**, 106001 (2015).

[262] R. Winkler, *Spin-orbit coupling effects in two-dimensional electron and hole systems* (Springer-Verlag Berlin Heidelberg, 2003).

[263] D. M. Kennes, J. C. Pommerening, J. Diekmann, C. Karrasch, and V. Meden, "Small quenches and thermalization", Phys. Rev. B **95**, 035147 (2017).

[264] D. Kennes and C. Karrasch, "Extending the range of real time density matrix renormalization group simulations", Computer Physics Communications **200**, 37–43 (2016).

[265] U. Schollwöck, "The density-matrix renormalization group: a short introduction", Philosophical Transactions of the Royal Society of London A: Mathematical, Physical and Engineering Sciences **369**, 2643–2661 (2011), eprint: http://rsta.royalsocietypublishing.org/content/369/1946/2643.full.pdf.

[266] G. Vidal, "Classical simulation of infinite-size quantum lattice systems in one spatial dimension", Phys. Rev. Lett. **98**, 070201 (2007).

[267] S. R. White, "Density matrix formulation for quantum renormalization groups", Phys. Rev. Lett. **69**, 2863–2866 (1992).

[268] B. Yan and C. Felser, "Topological materials: Weyl semimetals", Annual Review of Condensed Matter Physics **8**, 337–354 (2017), eprint: https://doi.org/10.1146/annurev-conmatphys-031016-025458.

[269] B. Dóra, I. F. Herbut, and R. Moessner, "Coupling, merging, and splitting dirac points by electron-electron interaction", Phys. Rev. B **88**, 075126 (2013).

[270] G. Montambaux, F. Piéchon, J.-N. Fuchs, and M. O. Goerbig, "Merging of Dirac points in a two-dimensional crystal", Phys. Rev. B **80**, 153412 (2009).

[271] A. Fasano and S. Marmi, *Analytical mechanics: an introduction* (Oxford University Press, 2006).

[272] G. I. Japaridze, H. Johannesson, and M. Malard, "Synthetic helical liquid in a quantum wire", Phys. Rev. B **89**, 201403 (2014).

[273] F. Cavaliere, F. M. Gambetta, S. Barbarino, and M. Sassetti, "Crystallization of fractional charges in a strongly interacting quasihelical quantum dot", Phys. Rev. B **92**, 235128 (2015).

[274] F. Cavaliere, F. M. Gambetta, N. Traverso Ziani, and M. Sassetti, "Current noise as a probe for Wigner molecules", Journal of Physics: Condensed Matter **27**, 425301 (2015).

[275] F. Gambetta and S. Porta, "Out-of-equilibrium density dynamics of a spinful Luttinger liquid", Il Nuovo Cimento C **40**, 92 (2017).

[276] A. Calzona, F. M. Gambetta, M. Carrega, F. Cavaliere, and M. Sassetti, *Asymmetries in the spectral density of an interaction-quenched Luttinger liquid*, Submitted as proceedings paper for the conference LT28, 2017.